ISBN 978-82-326-5697-4 (printed ver.)
ISBN 978-82-326-5674-5 (electronic ver.)
ISSN 1503-8181 (printed ver.)
ISSN 2703-8084 (electronic ver.)

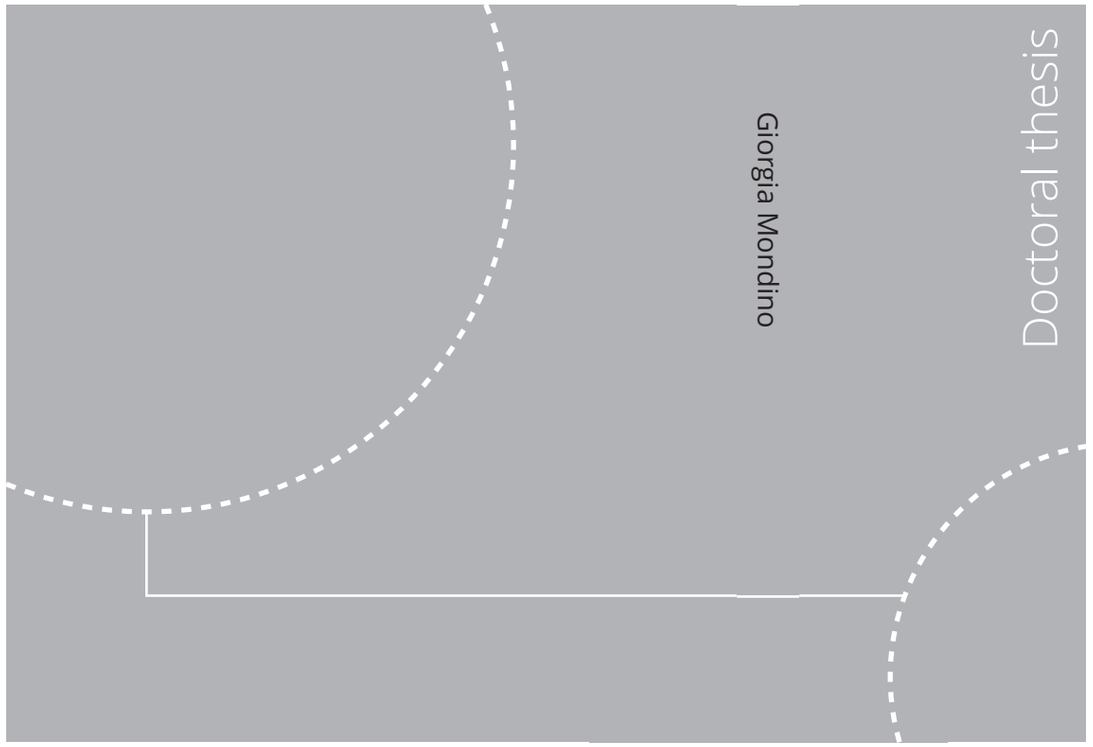

Doctoral theses at NTNU, 2022:90

Giorgia Mondino

Assessment of Moving Bed Temperature Swing Adsorption Process for Post-Combustion CO_2 Capture

NTNU
Norwegian University of
Science and Technology
Thesis for the degree of
Philosophiae Doctor
Faculty of Engineering
Department of Energy and Process Engineering

NTNU
Norwegian University of
Science and Technology

Doctoral theses at NTNU, 2022:90

NTNU

NTNU
Norwegian University of
Science and Technology

Giorgia Mondino

Assessment of Moving Bed Temperature Swing Adsorption Process for Post-Combustion CO_2 Capture

Thesis for the degree of Philosophiae Doctor

Trondheim, April 2022

Norwegian University of Science and Technology
Faculty of Engineering
Department of Energy and Process Engineering

NTNU
Norwegian University of
Science and Technology

NTNU
Norwegian University of Science and Technology

Thesis for the degree of Philosophiae Doctor

Faculty of Engineering
Department of Energy and Process Engineering

ISBN 978-82-326-5697-4 (printed ver.)
ISBN 978-82-326-5674-5 (electronic ver.)
ISSN 1503-8181 (printed ver.)
ISSN 2703-8084 (electronic ver.)

Doctoral theses at NTNU, 2022:90

Printed by Skipnes Kommunikasjon AS

Preface

This thesis is submitted in partial fulfillment of the requirements for the degree of Doctor of Philosophy (Ph.D.) at the Norwegian University of Science and Technology (NTNU). The research described herein was carried out from June 2017 to June 2021 at the Department of Energy and Process Engineering of the Faculty of Engineering, with Associate Professor Lars Olof Nord as main supervisor and Dr. Carlos Adolfo Grande as co-supervisor. The present Ph.D. work was part of the EDeMoTeC project, and was funded by the Norwegian Research Council within the CLIMIT program.

Abstract

In the context of post-combustion CO_2 capture, adsorption-based processes are considered a promising alternative to absorption technologies thanks to their lower environmental impact, absence of corrosion problems, and potentially lower energy requirements. In conventional Temperature Swing Adsorption (TSA) processes, the adsorbent is packed in a series of fixed bed columns that cyclically alternate between the adsorption and regeneration steps to separate the CO_2 from the rest of the flue gas components. One drawback of TSA systems for post-combustion capture is the large temperature swings usually required to achieve high product specifications in terms of both CO_2 purity and recovery. These large temperature swings do not only imply high energy penalties and parasitic losses, but also lead to long cycle times, large system footprints, and low process productivity due to the poor heat transfer within the packed beds.

One way to overcome the aforementioned limitations is by performing the adsorption-desorption cycle in a Moving Bed Temperature Swing Adsorption (MBTSA) system, whereby the adsorbent is circulated through different sections that correspond to each cycle step. The main feature distinguishing moving and fixed bed processes is that the former can be operated at steady state. This is beneficial because it renders complex cycle schedules unnecessary and eliminates the parasitic energy losses associated with intermittent heating/cooling of the heat exchanger walls. The possibility to operate in steady state is also an advantage in terms of internal heat recovery and process integration, which is particularly relevant within post combustion applications where the power cycle can be adapted to supply the heat required by the capture process in an efficient way. In view of its potential advantages, and comparatively lower maturity level, the objective of this thesis is to investigate the application of the MBTSA technology in the context of post-combustion CO_2 capture.

The design of an MBTSA system is a complex task involving a large number of inter-related process parameters such as the choice of adsorbent material, process configuration, operating conditions, and the size and geometry of the components. In this context, process modeling and simulation stands as an essential tool for the conceptualization and analysis of new MBTSA systems. In order to study the performance of the MBTSA technology for different applications, a one-dimensional model of the process was developed. The model was obtained by applying the mass, momentum and energy balances to the different sections of the MBTSA system, and it was implemented in the gPROMS environment. One distinguishing feature of the MBTSA model is that, instead of imposing a fixed wall temperature in the heating and cooling sections, it includes additional

energy balances for the heating/cooling fluid and heat exchanger walls. In addition, the model accounts for the internal heat recovery achieved when coupling the preheating and precooling sections, which is necessary to reduce the external energy duty required by the process.

The performance of the heat exchangers employed to provide and remove heat from the sorbent depends largely on the sorbent-side heat transfer coefficient, as it is the dominating thermal resistance between the gas/solid phases and the heating/cooling fluid. The correct estimation of this parameter is therefore crucial for the design of MBTSA systems. In order to assess the technology with realistic parameters, the heat transfer coefficient on the sorbent side of a lab-scale MBTSA apparatus was measured at different flow rates and temperatures. The heat transfer coefficient increased with the flow rate of adsorbent particles, while no dependence was observed on sorbent temperature. The heat transfer coefficients obtained (70–120 $\mathrm{W/m^2\,K}$) were significantly higher than those typically encountered in fixed bed configurations (10–50 $\mathrm{W/m^2\,K}$). This confirmed that the moving bed configuration has the potential to address one of the main limitations of the fixed bed TSA technology for CO_2 capture, namely, the low process productivity due to the slow heating and cooling of the adsorbent.

The results of the experimental campaign were used to develop a correlation for the sorbent-side Nusselt number as a function of the Péclet number. This correlation was incorporated into the MBTSA computational model, which was then used to design and analyse an MBTSA process for a waste-to-energy plant with a power output of 16.8 $\mathrm{MW_{el}}$, a thermal output of 64.6 $\mathrm{MW_{th}}$, and an exhaust flue gas flow rate of 56 kg/s with 11%vol CO_2 concentration. Despite the low selectivity of the activated carbon adsorbent considered, the proposed MBTSA process reached high CO_2 purity (97.2 %) and capture rate (90.8%). These product specifications were achieved at the expense of adopting a high regeneration temperature (187 °C) and solid-to-gas ratio (11.6 kg of adsorbent per kg of flue gas). Nevertheless, the designed MBTSA system was able to attain high process productivity (181 $\mathrm{kg_{CO_2}/t_{ads}h}$), which can be attributed to the short cycle time associated with the fast heating and cooling of the adsorbent. The results of the waste-to-energy case study indicate that the MBTSA technology is suited to capture CO_2 at high purity and recovery, while achieving higher process productivity than fixed bed TSA processes. In addition, it is believed that the thermal energy required by the proposed MBTSA system may be significantly reduced by replacing the activated carbon material by other adsorbents having higher capacity and selectivity towards CO_2, such as zeolites or metal organic frameworks (MOF).

This thesis also evaluated the suitability of the MBTSA technology in the context of power generation from natural gas. The case study considered was an 800 MW Natural Gas Combined Cycle (NGCC) power plant with an exhaust gas flow rate of 916 kg/s containing 5.15%vol of CO_2. Two different MBTSA capture

processes were proposed: one using a commercial zeolite 13X and other using a novel CPO-27-Ni MOF adsorbent. The two systems were able to meet the target specifications in terms of CO_2 purity ($> 95\%$) and capture rate ($> 90\%$), while achieving higher productivity than conventional fixed bed TSA processes. Even if the separation performance of both processes was similar, the distinct physical properties of the adsorbents led to different system dimensions and operating conditions, demonstrating the flexibility of the MBTSA technology.

In addition, the influence of the capture system and its auxiliaries on the performance of the power plant was analyzed by integrating the MBTSA model with a process model of the NGCC power plant. The simulations showed that the process using CPO-27-Ni required more thermal energy for sorbent regeneration (125.6 vs 100.7 MW_{th}). However, the energy penalty associated with the steam extraction used as thermal input was lower (25.8 vs 29.1 MW_{el}) because the steam extraction was performed at lower temperature and pressure. This advantage was partially offset by the higher pressure drop in the adsorption section of the MOF process, which led to a higher power consumption in the flue-gas booster fans (17.3 vs 10.1 MW_{el}). Despite the distribution of the energy penalties associated with the CPO-27-Ni and zeolite 13X processes was different, the net electric efficiency of the NGCC power plant was very similar in both cases. In particular, both MBTSA capture processes led to a reduction of about 7 percentage points with respect to the reference plant without CO_2 capture.

Moreover, the proposed MBTSA processes were benchmarked against a state-of-the-art absorption process using monoethanolamine (MEA) as solvent. One of the main differences between the amine-based process and the MBTSA systems is that the latter require an additional energy input to dry the flue gas because the adsorbent materials considered (i.e., zeolite 13X and CPO-27-Ni) are incompatible with water. This drying process accounted for the 17% of the energy penalty associated with the MBTSA capture systems. By contrast, the thermal energy required, and hence the power penalty associated with steam extraction, was significantly higher for the MEA process. Despite the breakdown of energy penalties between the MBTSA systems and the MEA process was different, no significant difference was observed in terms of overall power plant performance. In particular, the net electric efficiency of the reference power plant was 63.1%, while the efficiency of the power plant with CO_2 capture was 54.7% for the case of MEA, 56.1% for the MBTSA using CPO-27-Ni, and 56.2% for the MBTSA using zeolite 13X. These results suggest that the MBTSA process applied to NGCC power plants is suitable for capturing CO_2 at high purity and high capture rate, while being competitive with the state-of-the-art MEA capture process in terms of energy penalty. Considering the much earlier stage of development of this technology with respect to the MEA process, the MBTSA seems to offer a large potential for process improvement and should be considered for further development.

Acknowledgements

First and foremost I would like to thank my supervisor Lars O. Nord for accepting me as a Ph.D. student and for guiding me throughout this exciting and challenging journey. This thesis would have not been possible without your constant encouragement and support.

Secondly, I would like to express my deepest gratitude to my co-supervisor Carlos A. Grande, who has been an irreplaceable source of inspiration and motivation with his precious advice and knowledge. I feel privileged for the opportunity I had to work with you during the past years and hope we will have more chances in the coming years.

I am also very grateful to my former boss and now colleague Richard Blom for his invaluable contribution and support in all phases of this project.

A sincere thank as well to my other colleagues at SINTEF Industry for their help in carrying out the experimental work of this thesis and for always welcoming me during my stays in Oslo.

Finally, I take this opportunity to thank the Department of Energy and Process Engineering at NTNU for the technical, financial and administrative support.

Giorgia Mondino

Oslo, 30th December 2021

Contents

Preface i

Abstract iii

Acknowledgements vii

List of Figures xi

List of Tables xiii

Nomenclature xv

1 Introduction 1

1.1 Background and motivation 1

1.2 Objectives 5

1.3 Contributions 6

1.4 Thesis structure 7

1.5 Publications and scientific dissemination 8

1.5.1 Journal articles 8

1.5.2 Conference and seminar presentations 8

2 MBTSA for post-combustion capture 9

2.1 Process description 9

2.2 Performance indicators 10

2.3 Mathematical model 11

2.3.1 Transport equations 12

2.3.2 Transport parameters 14

2.3.3 Adsorption equilibrium 16

2.3.4 Boundary conditions 17

2.3.5 Model implementation 17

3 Experimental determination of heat transfer coefficients 21

3.1 Lab-scale MBTSA apparatus 21

3.2 Experimental procedure 24

3.3 Determination of the heat transfer coefficient 25

3.4 Experimental results 26

4 Waste-to-energy case study using activated carbon **33**
4.1 Definition of the case study . . . 33
4.2 Adsorbent material . . . 34
4.3 Design of the MBTSA process . . . 36
4.4 MBTSA simulation results . . . 37
4.4.1 Concentration and temperature profiles . . . 37
4.4.2 Overall system performance . . . 39
4.5 Chapter summary . . . 41

5 NGCC case study using zeolite 13X **43**
5.1 Definition of the case study . . . 43
5.2 Adsorbent material . . . 44
5.3 Design of the MBTSA process . . . 48
5.4 MBTSA simulation results . . . 50
5.4.1 Concentration and temperature profiles . . . 50
5.4.2 Overall system performance . . . 51
5.5 Integration of NGCC with capture processes . . . 54
5.5.1 Integration with MBTSA process . . . 54
5.5.2 Integration with MEA absorption process . . . 55
5.5.3 Results of the process integration . . . 56
5.6 Chapter summary . . . 59

6 Comparison of MOF CPO27-Ni with zeolite 13X **61**
6.1 Adsorbent material . . . 62
6.2 Design of the MBTSA process . . . 65
6.3 Process simulation results . . . 66
6.3.1 Concentration and temperature profiles . . . 67
6.3.2 Performance of the MBTSA process . . . 70
6.3.3 Integration with NGCC power plant . . . 71
6.4 Chapter summary . . . 73

7 Conclusions and Further Work **75**
7.1 Conclusions . . . 75
7.2 Further work . . . 78

References **81**

A Publications **A1**

List of Figures

2.1 Schematic diagram of the simulated MBTSA process. 10

3.1 Experimental set-up used for heat transfer measurements 22
3.2 Schematic diagram indicating the position of each thermocouple . 27
3.3 Experimental heat transfer coefficients and fitted correlation 28

4.1 CO_2 and N_2 adsorption isotherms for the activated carbon 36
4.2 Concentration and temperature profiles along the MBTSA 40

5.1 Layout of the reference NGCC power plant without CCS 44
5.2 CO_2 and N_2 adsorption isotherms for zeolite 13X 47
5.3 Van't Hoff plot for estimation of isosteric heat of adsorption 48
5.4 Adsorbent loading and molar fraction in the adsorption section . . 52
5.5 Adsorbent loading and molar fraction in the preheating section . . 52
5.6 Adsorbent loading and molar fraction in the desorption section . . 52
5.7 Adsorbent loading and molar fraction in the cooling section 53
5.8 Temperature profiles along the MBTSA system 53
5.9 Layout of the reference NGCC power plant with CCS. 55
5.10 Contributions to the overall duty of the capture processes 58

6.1 SEM pictures of the CPO-27-Ni spheres 62
6.2 CO_2 and N_2 adsorption isotherms for CPO-27-Ni 64
6.3 Simulation results for the adsorption section 68
6.4 Simulation results for the preheating section 68
6.5 Simulation results for the desorption section 69
6.6 Simulation results for the cooling section 69
6.7 Contributions to the overall duty of the capture processes 72

List of Tables

2.1 Boundary Conditions for each section of the MBTSA 19

3.1 Geometry and material properties of the heat exchanger 23
3.2 Physical properties of the activated carbon 24
3.3 Overview of experimental results – part 1 of 3 30
3.4 Overview of experimental results – part 2 of 3 31
3.5 Overview of experimental results – part 3 of 3 32

4.1 Flue gas specifications adopted for the MBTSA simulations 34
4.2 Adsorbent properties adopted for the MBTSA simulations 35
4.3 Virial model parameters of the activated carbon 35
4.4 MBTSA design and process parameters 38
4.5 Summary of the waste-to-energy simulations results 41

5.1 Flue gas specifications adopted for the MBTSA simulation 45
5.2 Summary of technical data of the reference NGCC plant 46
5.3 Adsorbent properties adopted for the MBTSA simulations 47
5.4 Virial model parameters for zeolite 13X 47
5.5 Dimensions and operating conditions of the final MBTSA 49
5.6 Process design and simulation results for the two MBTSA cases . . 51
5.7 Specification of the MEA capture process 56
5.8 Results of the NGCC power plant integration 57

6.1 Adsorbent properties adopted for the MBTSA simulations 63
6.2 Virial model parameters for CPO-27-Ni and zeolite 13X 64
6.3 MBTSA design parameters for CPO-27-Ni and zeolite 13X 65
6.4 MBTSA simulation results for CPO-27-Ni and zeolite 13X 70
6.5 Power plant integration results for CPO-27-Ni and zeolite 13X . . 72

Nomenclature

Latin symbols

a	Fitting constant	-
a'	Particle specific area	$\mathrm{m}^2/\mathrm{m}^3$
A_i	First single-component Virial coefficients	$\mathrm{kg/mol}$
A_{ij}	First multi-component Virial coefficients	$\mathrm{kg/mol}$
$A_{0,i}$	Fitting constants of the first Virial coefficients	$\mathrm{kg/mol}$
$A_{1,i}$	Fitting constants of the first Virial coefficients	$\mathrm{K\,kg/mol}$
$A_{\mathrm{cf,s}}$	Cross-flow area of the sorbent side	m^2
$A_{\mathrm{cf,w}}$	Cross-flow area of the water side	m^2
A_{s}	Heat transfer area of the sorbent side	m^2
A_{w}	Heat transfer area of the water side	m^2
b	Fitting constant	-
B_i	Second single-component Virial coefficients	$\mathrm{kg}^2/\mathrm{mol}^2$
B_{ijk}	Second multi-component Virial coefficients	$\mathrm{kg}^2/\mathrm{mol}^2$
$B_{0,i}$	Fitting constants of the second Virial coefficients	$\mathrm{kg}^2/\mathrm{mol}^2$
$B_{1,i}$	Fitting constants of the second Virial coefficients	$\mathrm{K\,kg}^2/\mathrm{mol}^2$
Bi_i	Biot number of the adsorbent particles for component i	-
$c_{p,\mathrm{f}}$	Specific heat capacity of the heating/cooling fluid	$\mathrm{J/kg\,K}$
$c_{p,\mathrm{g}}$	Specific heat capacity of the gas mixture	$\mathrm{J/kg\,K}$
$c_{p,\mathrm{pk}}$	Specific heat capacity of packing material	$\mathrm{J/kg\,K}$
$c_{p,\mathrm{s}}$	Specific heat capacity of the adsorbent	$\mathrm{J/kg\,K}$
$c_{p,\mathrm{t}}$	Specific heat capacity of the heat exchanger tubes	$\mathrm{J/kg\,K}$
$c_{p,\mathrm{w}}$	Specific heat capacity of water	$\mathrm{J/kg\,K}$
$\hat{c}_p$	Molar heat capacity of the gas mixture at constant pressure	$\mathrm{J/mol\,K}$
$\hat{c}_v$	Molar heat capacity of the gas mixture at constant volume	$\mathrm{J/mol\,K}$
C_i	Third single-component Virial coefficients	$\mathrm{kg}^3/\mathrm{mol}^3$
C_{ijkl}	Third multi-component Virial coefficients	$\mathrm{kg}^3/\mathrm{mol}^3$
$C_{0,i}$	Fitting constants of the third Virial coefficients	$\mathrm{kg}^3/\mathrm{mol}^3$
$C_{1,i}$	Fitting constants of the third Virial coefficients	$\mathrm{K\,kg}^3/\mathrm{mol}^3$
C_i	Molar concentration of component i in the gas phase	$\mathrm{mol}/\mathrm{m}^3$
$C_{\mathrm{p},i}$	Molar concentration of component i in the macropores	$\mathrm{mol}/\mathrm{m}^3$
C_{T}	Total molar concentration of the gas phase	$\mathrm{mol}/\mathrm{m}^3$
d_{p}	Particle diameter	m
$d_{\mathrm{t,ext}}$	Equivalent external diameter of the tubes	m
$d_{\mathrm{t,int}}$	Internal diameter of the tubes	m
D_{c}^0	Micropore limiting diffusivity at infinite temperature	m^2/s

D_{ij}	Binary molecular diffusivity of components (i, j)	m^2/s
$D_{Kn,i}$	Knudsen diffusivity of component i	m^2/s
$D_{m,i}$	Molecular diffusivity of component i	m^2/s
$D_{p,i}$	Macropore diffusivity of component i	m^2/s
$D_{z,i}$	Axial dispersion coefficient of component i	m^2/s
$E_{a,i}$	Activation energy of micropore diffusion of component i	J/mol
h_{gs}	Heat transfer coefficient between gas and solid	$W/m^2\,K$
h_{ft}	Heat transfer coefficient between fluid and tube walls	$W/m^2\,K$
h_{gt}	Heat transfer coefficient between gas and tube walls	$W/m^2\,K$
h_s	Heat transfer coefficient on the sorbent side	$W/m^2\,K$
h_w	Heat transfer coefficient on the water side	$W/m^2\,K$
J_s	Sorbent mass flux	$kg/m^2\,s$
$k_{f,i}$	Film mass transfer coefficient of component i	m/s
k_g	Thermal conductivity of the gas mixture	W/m K
k_w	Thermal conductivity of water	W/m K
$K_{H,i}$	Henry's law constant of component i	mol/kg Pa
$K^{\infty}_{H,i}$	Henry's law constant at infinite temperature	mol/kg Pa
l_t	Length of a single tube	m
$l_{t,tot}$	Total length of the tubes	m
L_x	Tube length along flow direction	m
L_z	Section length along vertical axis	m
$\dot{m}$	Mass flow rate	mol/s
$\dot{m}_s$	Mass flow rate of sorbent	mol/s
$\dot{m}_w$	Mass flow rate of water	mol/s
M_w	Molecular weight	kg/mol
$\dot{n}$	Molar flow rate	mol/s
N_{mod}	Number of heat exchanger modules	-
N_{pass}	Number of passes per module	-
N_t	Number of tubes per module	-
$N_{t,pass}$	Number of tubes per pass	-
Nu	Nusselt number	-
P	Total pressure of the gas mixture	Pa
P_i	Partial pressure of component i	Pa
Pe	Péclet number	-
Pr	Prandtl number	-
q_i	Adsorbed concentration of component i	mol/kg
q_i^*	Adsorbed concentration of component i at equilibrium	mol/kg
$\dot{Q}$	Heat flow rate	W
r_c	Micropore radius	m
r_p	Particle radius	m
r_{pore}	Macropore radius	m

$r_{\mathrm{t,int}}$	Internal radius of the tubes	m
R	Ideal gas constant	J/K mol
R_{t}	Heat transfer resistance of the tubes	K/W
R_{tot}	Total heat transfer resistance	K/W
R_{s}	Heat transfer resistance on the sorbent side	K/W
R_{w}	Heat transfer resistance on the water side	K/W
Re	Reynolds number	-
$s_{\mathrm{t,ext}}$	External side length of the tubes	m
Sc_i	Schmidt number of component i	-
Sh_i	Sherwood number of component i	-
t	Time	s
t_{cycle}	Cycle time of the MBTSA process	s
T	Temperature of the gas	K
T_{f}	Temperature of the heating/cooling fluid	K
T_{s}	Temperature of the sorbent particles	K
T_{t}	Temperature of the heat exchanger tubes wall	K
T_{w}	Temperature of the water	K
u	Superficial velocity of the gas	m/s
u_{f}	Velocity of the heating/cooling fluid	m/s
v_{s}	Velocity of the adsorbent	m/s
v_{w}	Velocity of water	m/s
Y_i	Molar fraction of component i	-
z	Coordinate along the section height	m

Greek symbols

α_{gt}	Ratio of external surface area of tubes to gas-solid volume	$\mathrm{m}^2/\mathrm{m}^3$
$\alpha_{\mathrm{t,ext}}$	Ratio of external surface area of tubes to fluid volume	$\mathrm{m}^2/\mathrm{m}^3$
$\alpha_{\mathrm{t,int}}$	Ratio of internal surface area of tubes to fluid volume	$\mathrm{m}^2/\mathrm{m}^3$
ΔH_i	Heat of adsorption of component i	J/mol
ΔT_{LM}	Logarithmic mean temperature difference	K
ε	Column void fraction	-
ε_{p}	Particle porosity	-
λ_{g}	Axial heat dispersion coefficient of the gas mixture	W/m K
λ_{pk}	Axial heat dispersion coefficient of the packing	W/m K
μ_{g}	Dynamic viscosity of the gas mixture	Pa s
μ_{w}	Dynamic viscosity of water	Pa s
ξ	Packing porosity factor	-
ρ_{f}	Density of the heating/cooling fluid	kg/m^3
ρ_{g}	Density of the gas mixture	kg/m^3
ρ_{p}	Density of the adsorbent particles	kg/m^3

ρ_{pk}	Density of the packing	$\mathrm{kg/m^3}$
ρ_{t}	Density of the heat exchanger tubes	$\mathrm{kg/m^3}$
ρ_{w}	Density of water	$\mathrm{kg/m^3}$
σ_{ij}	Lennard-Jones parameter of binary diffusivity	m
τ_{p}	Particle tortuosity	-
$\Omega_{D_{ij}}$	Dimensionless collision integral of binary diffusivity	-

Abbreviations

CCS	Carbon Capture and Storage
CFDM	Centered Finite Difference Method
CHP	Combined Heat and Power
GHG	Greenhouse Gases
GT	Gas Turbine
HPB	High Pressure Boiler
HPE	High Pressure Economizer
HPS	High Pressure Superheater
HPT	High Pressure Turbine
HRSG	Heat Recovery Steam Generator
HTC	Heat Transfer Coefficient
HX	Heat Exchanger
IEA	International Energy Agency
IPB	Intermediate Pressure Boiler
IPCC	Intergovernmental Panel on Climate Change
IPE	Intermediate Pressure Economizer
IPS	Intermediate Pressure Superheater
IPT	Intermediate Pressure Turbine
LDF	Linear Driving Force
LPB	Low Pressure Boiler
LPE	Low Pressure Economizer
LPS	Low Pressure Superheater
LPT	Low Pressure Turbine
MBTSA	Moving Bed Temperature Swing Adsorption
MEA	Monoethanolamine
MOF	Metal-Organic Framework
NGCC	Natural Gas Combined Cycle
PCC	Post-Combustion Capture
PSA	Pressure Swing Adsorption
RH	Re-Reater
TSA	Temperature Swing Adsorption
VSA	Vacuum Swing Adsorption

Chapter 1

Introduction

1.1 Background and motivation

Since the beginning of the industrial revolution, the emission of significant quantities of greenhouse gases (GHG) deriving from human activities has altered the composition of the atmosphere and contributed to an increase of the global average temperature (IPCC 2018). In particular, anthropogenic emissions of carbon dioxide, resulting primarly from combustion of fossil fuels, are recognized as the main driver for global warming (IPCC 2018). The International Energy Agency assessed that the stabilization of GHGs requires a portfolio of mitigation actions, as a single technology cannot provide sufficient emission reductions (IEA 2019). Such portfolio of approaches includes decarbonizing the electricity generation (i.e., reducing the CO_2 emissions from the energy supply sector), increasing the use of nuclear and renewable energy sources, and increasing energy efficiency.

In particular, carbon capture and storage (CCS) is considered a key technology to drastically reduce the carbon footprint of the power generation sector (IPCC 2005; Liang et al. 2016). CCS is a term describing the route of capturing carbon dioxide from large point sources, compressing it and transporting it to a suitable geological formation for permanent underground storage. When the CO_2 is separated from flue gases of conventional power plants, the technology is referred to as post-combustion capture (PCC) (IPCC 2005). One of the advantages of PCC is that the capture system can be retrofitted to existing plants and it is relatively easy to implement, as it does not affect the core process of the plant (Nord et al. 2020). Although the costs associated with the application of this technology are currently high, post-combustion capture is receiving increased attention because of the realization that many existing power stations will continue to operate for decades (Bui et al. 2018; Nord et al. 2020).

In the context of post-combustion CO_2 capture, adsorption-based processes are considered a promising alternative to the current benchmark technology based on amine solutions, which suffers from high energy consumption and environmental impact, as well as corrosion issues related to solvent degradation (Bui et al. 2018; Sjostrom et al. 2010). Adsorption-based processes make use of porous solids capable of: i) removing the CO_2 from the flue gas by selectively adsorbing it onto their surface and ii) releasing the adsorbed CO_2 when subjected to a change of pressure or temperature. The former property enables the separation of the CO_2 from the

rest of the flue gas components, while the latter is responsible for the regeneration of the adsorbent, enabling a cyclic operation and permitting the recovery of CO_2 in a high purity stream. When the regeneration of the adsorbent is carried out by reducing the pressure of the system, the process is referred to as Pressure Swing Adsorption (PSA) or Vacuum Swing Adsorption (VSA), depending on the operating pressure, while the term Temperature Swing Adsorption (TSA) is used to indicate processes where the adsorbent is regenerated by an increase in temperature upon external heat supply. In large-scale post-combustion capture applications, the CO_2 has to be purified from low-concentration, low-pressure, and high-volume-flow-rate flue gases; and regeneration via temperature swing seems to be the most appropriate option (Ruthven 1984; Wankat 2006; Bui et al. 2018; Sjostrom et al. 2010).

In conventional TSA processes, the adsorbent is normally shaped as beads or pellets and packed in a series of columns that cyclically alternate between the adsorption and regeneration steps. One of the drawbacks of fixed bed processes in applications involving large flow rates, such as post-combustion capture, is the high pressure drop occurring across the packed bed unless the adsorbent pellets are replaced by advanced structured adsorbents (e.g., honeycomb monolith, hollow fibers, spaced sheets)(Akhtar et al. 2014; Rezaei et al. 2010; Masala et al. 2017b; Farmahini et al. 2021). Another important factor hampering the commercialization of TSA systems for post-combustion CO_2 capture is that a large temperature swing is often required (Hefti et al. 2018; Morales-Ospino et al. 2021) to achieve the demanding product specifications in terms of both CO_2 purity and recovery (Joss et al. 2017). These large temperature swings do not only imply high energy penalties and parasitic losses, but also lead to long cycle times due to the poor heat transfer within the packed bed (Bonjour et al. 2004; Plaza et al. 2017; Zanco et al. 2021). This, in turn, results in large sorbent inventories, low process productivity, and large system footprints, which makes conventional TSA processes less competitive with respect to other post-combustion technologies (Bonjour et al. 2005; Rezaei et al. 2010; Zanco et al. 2017; Zanco et al. 2021).

One way to overcome the aforementioned challenges is by performing the adsorption-desorption cycle in a moving bed system, rather than in the traditional fixed bed configurations (Knaebel 2005). In the moving bed process, the temperature swing is achieved by circulating the adsorbent through sections at different temperatures. Each of these sections has a specific purpose and corresponds to a different step: adsorption, desorption and cooling. In contrast to fixed bed processes, in which the same column is operated at variable conditions according to the cycle schedule, each section of the moving bed system can be designed and operated according to its specific purpose. This offers interesting opportunities for system optimization, aiming, for example, to reduce the pressure drop within the adsorption section, or to enhance heat transfer in the desorption and cooling sections, so that a more compact design and higher productivity can be achieved.

Furthermore, the moving bed temperature swing adsorption (MBTSA) process offers the possibility to internally recover part of the heat needed for sorbent regeneration and thus reduce the external energy duty of the process (Knaebel 2005; Kim et al. 2013; Morales-Ospino et al. 2021). Another major feature distinguishing moving bed from fixed bed processes is that the former can be operated at steady state, avoiding complex cycle scheduling (Plaza et al. 2017; Kim et al. 2013) and the parasitic losses associated with intermittent heating/cooling of the heat exchanger walls (Bonjour et al. 2004; Bonjour et al. 2005). The possibility to operate in steady state is also an advantage in terms of process control and integration (Kim et al. 2013), which is particularly relevant within post combustion applications where: (i) the flow rate and composition of flue gases from the upstream power plant can vary over time (Montañés et al. 2018; Rúa et al. 2020), (ii) the power cycle can be appositely modified to supply the heat required by the capture process (Mondino et al. 2019).

The concept of moving bed temperature swing adsorption process was first introduced in the '40s by Berg (1945) for fractionating hydrocarbons. Only recently the same concept has been applied for CO_2 capture purposes, first by Knaebel (2005) who suggested the use of hot flue gas for indirect sorbent heating, and later by Hornbostel and co-workers (M. D. Hornbostel et al. 2013; M. D. Hornbostel et al. 2015; M. Hornbostel 2016), who tested a large bench scale moving bed system employing steam for direct heating of the adsorbent. Pilot-scale design and testing of a moving bed process for CO_2 capture was performed also by Okumura et al. (2014); Okumura et al. (2017), who used an amine impregnated adsorbent regenerated by low-temperature steam in a direct-contact type heat exchanger. The main advantage of direct sorbent heating is that it is possible to achieve fast heat transfer rates due to intense mixing between sorbent particles and heating fluid. However, this type of configuration prevents the use of sorbents materials that are incompatible with the heat transfer fluid and compromises the use of internal heat recovery, which is crucial to minimize the process energy use. In this context, the group of Kim et al. (Kim et al. 2013; Kim et al. 2014; Son et al. 2014) proposed a moving bed process with an internal heat integration scheme, where part of the energy required for sorbent regeneration is recovered from the heat generated during the adsorption step using indirect-contact heat exchangers. The same type of indirect-contact heat exchanger for MBTSA processes was employed in the recent study carried out by Morales-Ospino et al. (2021), who confirmed that internal heat recovery has a great potential to limit the energy penalty of the process.

The success of this heat integration is largely dependent on the performance of the indirect-contact heat exchanger employed to provide and remove heat from the sorbent. In particular, the estimation of the sorbent-side heat transfer coefficient is crucial for the design of the MBTSA system because it represents the limiting thermal resistance between the gas/solid phases and the heating/cooling fluid.

The convective heat transfer to the flowing sorbent is determined by several factors, including the flow pattern, particle mixing, contact area between sorbent and hot surfaces, as well as the sorbent residence time. The effective heat transfer is therefore affected not only by the geometry of the system (e.g., tube arrangements and shape, hydraulic diameters, pitching) or operating conditions (e.g., temperatures of heating/cooling fluid, flow rates), but also by specific properties of the bulk solid that influence its flowability (e.g., particle shape, size, density). Several studies investigated the heat transfer mechanisms in moving bed heat exchangers employing bulk solids as working fluid, both computationally (Campbell 1990; W.-S. Lee et al. 1998; Isaza et al. 2015) and experimentally (Niegsch et al. 1994; Baird et al. 2008; Al-Ansary et al. 2012; Baumann et al. 2015). As an example, the recent works by Qoaider et al. (2017); Dai et al. (2020) analyzed how different materials, including glass beads, corundum, sand, basalt or mixtures thereof, result in different flow characteristics. Other studies focused on different system geometries and configurations, considering for example moving packed beds with and without gas flow (Baird et al. 2008), or comparing horizontal tubes, vertical tubes, parallel plates, and finned tubes (Al-Ansary et al. 2012). The influence of the tube shapes on the local heat transfer has also been investigated by Tian et al. (2020), who compared circular cross-sectioned tubes with elliptical shaped ones. One of the conclusions from the surveyed literature is that the convective heat transfer coefficient of flowing solid particles in moving bed heat exchangers is case-specific and hard to estimate without experimental data (Obuskovic 1988).

Another factor hindering the development of the MBTSA technology is the lack of an established method to design a process for a given flue gas specification. The design of an MBTSA system is a complex task that involves a large number of inter-related process parameters such as the choice of adsorbent material, process configuration, size and geometry of the different components, and operating conditions. In this context, process modeling and simulation is an essential tool for the conceptualization and analysis of new MBTSA systems. Provided that the model captures all relevant physical mechanisms, process simulations can be used to evaluate the system performance under different conditions. This, in turn, can help the designer to gain a better understanding of the process and serve as a basis to improve the design until the desired performance targets are met. In view of these advantages, process simulation has been a popular tool for the design of post-combustion PSA/VSA (Liu et al. 2011; Krishnamurthy et al. 2014; Farmahini et al. 2021) and TSA cycles (Plaza et al. 2017; Joss et al. 2017; Lillia et al. 2018). By contrast, modeling and simulation of MBTSA processes has lagged behind due to the early stage of development of this technology. In fact, only a handful of recent computational studies attempted to model MBTSA processes for post-combustion CO_2 capture (Kim et al. 2013; Son et al. 2014; Morales-Ospino et al. 2021). These works employed sophisticated numerical models to evaluate the performance of the MBTSA technology for different process configurations

and operating conditions. However, one limitation common to these studies is that they did not consider the impact of the capture process on the power plant (Morales-Ospino et al. 2021), or did so in a simplified way that ignored the change in the power plant operating conditions (Kim et al. 2013; Son et al. 2014). As a result of this limitation, it is not possible to establish a fair comparison between the MBTSA processes analyzed in these works and the state-of-the-art amine-based absorption technology (Nord et al. 2020). Indeed, proper benchmarking of different CO_2 capture technologies requires their modeling and simulation in combination with a detailed power plant model (Kvamsdal et al. 2014). However, to the knowledge of the author, the integration of the MBTSA process with a power plant model has not yet been documented.

1.2 Objectives

Considering the knowledge gaps identified in the previous section, the aim of this thesis is to advance the development of the MBTSA process for post-combustion CO_2 capture as alternative to the energy-intensive capture technologies currently in use. In the accomplishment of this main goal, the following objectives were identified:

- Development and implementation of a mathematical model describing the behavior of the MBTSA process. This model will serve as basis for process design and simulation.
- Experimental determination of the convective heat transfer coefficient on an indirect-contact heat exchanger suitable for sorbent heating in MBTSA systems. This heat transfer coefficient shall be used to complement the MBTSA model, thus allowing realistic predictions of the required heat transfer area and associated system footprint.
- Selection of suitable adsorbents for separation of CO_2 from post-combustion flue gases. To this aim, both commercial, as well as novel adsorbent materials shall be considered and compared. The identified adsorbents shall be characterized in terms of their adsorption properties to provide the model parameters required in process simulations.
- Design and analyze MBTSA processes for efficient separation of CO_2 for different post-combustion applications. To this aim two case studies will be considered:
  1. A natural gas combined cycle (NGCC) power plant.
  2. A combined heat and power (CHP) waste-to-energy plant.

  The proposed processes shall be evaluated in terms of process performance indicators including CO_2 purity, capture rate, energy requirement, and system footprint.

- Development and implementation of an NGCC power plant model to be coupled with the MBTSA process model. The integrated model shall be used to investigate the impact of the capture system on the performance of the power plant.
- Comparison of the integrated NGCC-MBTSA process with a reference case consisting of the NGCC power plant coupled with a benchmark absorption process. The aim of this analysis is to evaluate the competitiveness of the MBTSA process with respect to the state-of-the-art capture technology.

1.3 Contributions

The main contributions of this thesis can be summarized as follows:

- A one-dimensional dynamic model based on the transport equations for mass, momentum and energy along the axial direction of the MBTSA system was developed and implemented in the gPROMS software.
- Experimental work was carried out in a lab-scale moving bed apparatus with the aim to determine the heat transfer coefficient within a cross-flow shell-and-tube heat exchanger employed for sorbent heating. A correlation fitting the experimental results was proposed and used to complement the MBTSA process model.
- Two commercial adsorbents, namely activated carbons and zeolite 13X, as well as a novel CPO-27-Ni metal-organic framework (MOF) adsorbent were selected as suitable candidates for the MBTSA capture process. Their affinity towards CO_2 and N_2 was quantified by means of adsorption isotherms measurements at temperature and pressure conditions relevant for post-combustion applications. Model parameters were obtained by fitting the collected experimental data with a Virial isotherm model.
- An MBTSA process using activated carbons was designed for the waste-to-energy case study aiming to achieve high CO_2 purity and capture rate. The proposed MBTSA process was evaluated via numerical simulations in terms of system footprint, process productivity and energy duty.
- Two MBTSA processes using zeolite 13X and CPO-27-Ni MOF were designed for the NGCC case study and compared in terms of their separation and energy performances.
- A plant-level model of a state-of-the-art NGCC power plant was implemented in Thermoflex software and integrated with the MBTSA process model. The integrated model was used to carry out an in-depth analysis of the energy coupling between the MBTSA process and the power plant. The performance of the proposed NGCC-MBTSA systems using zeolite 13X and CPO-27-Ni MOF were compared to an amine-based capture process.

1.4 Thesis structure

This thesis is structured as a monograph that comprises this introduction, five chapters based on the contents of three journal articles, and a final chapter that summarizes the conclusions of this dissertation and proposes directions for further work. A brief summary of the five core chapters is provided below:

Chapter 2 describes the MBTSA process configuration considered in this thesis and provides a definition of the performance indicators used evaluate the process. In addition, the system of partial differential equations and boundary conditions used to model the MBTSA process are presented, and the simulation environment used to solve the model is described.

Chapter 3 documents the experiments performed in a lab-scale moving bed apparatus with the aim to determine the heat transfer coefficient of an activated carbon adsorbent flowing in a cross-flow shell-and-tube heat exchanger. In addition, the results obtained are used to develop a heat transfer correlation that complements the MBTSA model presented in Chapter 2.

Chapter 4 analyzes the suitability of the MBTSA technology to capture CO_2 from the flue gas of a waste-to-energy power plant. To this aim, an MBTSA process using an activated carbon adsorbent is designed and analyzed using the computational model presented in Chapter 2. The proposed MBTSA system is evaluated in terms of different performance indicators, including CO_2 separation performance, system footprint, process productivity and energy duty.

Chapter 5 considers the utilization of the MBTSA technology as an alternative to absorption-based technologies for CO_2 capture in the context of NGCC power plants. To this aim, an MBTSA process using a zeolite 13X adsorbent is designed, and the system behavior is investigated under different operation conditions. Furthermore, the impact of the MBTSA process on plant performance was analyzed by integrating the capture system with a detailed model of the power plant. Finally, the power plant model was coupled with an amine-based absorption process, and the performance of the two capture technologies was compared.

Chapter 6 evaluates the suitability of a novel adsorbent material, namely the CPO-27-Ni MOF, as a candidate for MBTSA post-combustion processes. To this aim, an MBTSA process using the CPO-27-Ni MOF adsorbent is designed for the NGCC case study considered in Chapter 5, and the performance of the capture system is evaluated in terms of different performance indicators. In addition the proposed MBTSA process is integrated with the model of the NGCC power plant to analyze how the presence of the capture process affects the overall performance of the system. Finally, the results obtained for the CPO-27-Ni adsorbent are compared with those obtained with zeolite 13X and benchmarked against the amine-based absorption process.

1.5 Publications and scientific dissemination

1.5.1 Journal articles

The research carried out during this Ph.D. project resulted in three publications in international peer-reviewed journals that are included in this thesis and are subject to evaluation.

1. G. Mondino, C. A. Grande, R. Blom, and L. O. Nord (2019). "Moving Bed Temperature Swing Adsorption for CO_2 Capture from a Natural Gas Combined Cycle Power Plant". *International Journal of Greenhouse Gas Control* 85, pp. 58–70.
2. G. Mondino, A. I. Spjelkavik, T. Didriksen, S. Krishnamurthy, R. E. Stensrød, C. A. Grande, L. O. Nord, and R. Blom (2020). "Production of MOF Adsorbent Spheres and Comparison of Their Performance with Zeolite 13X in a Moving-Bed TSA Process for Postcombustion CO_2 Capture". *Industrial & Engineering Chemistry Research* 59.15, pp. 7198–7211.
3. G. Mondino, C. A. Grande, R. Blom, and L. O. Nord (2021). "Evaluation of MBTSA Technology for CO_2 Capture from Waste-to-Energy Plants". *International Journal of Greenhouse Gas Control* [accepted].

1.5.2 Conference and seminar presentations

A. Moving Bed Temperature Swing Adsorption (MBTSA) for post combustion CO_2 capture. *Poster at the CCS Summer School, organized by IEAGHG.* Trondheim, Norway, June 2018.

B. Design, construction, adsorbents and evaluation of a moving bed temperature swing adsorption (MBTSA) pilot reactor for post combustion CO_2 capture. *Poster at the 14th Greenhouse Gas Control Technologies Conference (GHGT-14), organized by IEAGHG.* Melbourne, Australia, October 2018.

C. Moving bed temperature swing adsorption for CO_2 capture from a natural gas combined cycle power plant. *Oral presentation at the 14th Greenhouse Gas Control Technologies Conference (GHGT-14), organized by IEAGHG.* Melbourne, Australia, October 2018.

D. Moving Bed Temperature Swing Adsorption (MBTSA) for post combustion CO_2 capture. *Poster at the Advanced Process Modelling Forum 2019, organized by Process System Enterprise.* London, UK, March 2019.

E. Moving bed temperature swing adsorption (MBTSA) for CO_2 capture from a natural gas combined cycle power plant. *Poster at The 10th Trondheim Conference on CO2 Capture, Transport and Storage (TCCS-10), organized by SINTEF Energy AS.* Trondheim, Norway, June 2019.

F. Moving bed temperature swing adsorption (MBTSA) technology for post-combustion CO_2 capture. *Oral presentation at the 5th Post Combustion Capture Conference (PCCC-5), organized by IEAGHG.* Kyoto, Japan, Sept. 2019.

Chapter 2

MBTSA for post-combustion CO_2 capture

The present chapter describes the MBTSA process configuration considered in this thesis, as well as the indicators used for performance evaluation. Moreover, a detailed mathematical model of the process is presented, followed by a description of its computer implementation. The model documented herein serves as the basis for the design and performance evaluation of the MBTSA processes analysed in the remaining of this thesis.

2.1 Process description

A schematic diagram of the MBTSA process is shown in Figure 2.1. The system comprises five main sections through which the adsorbent circulates, namely the adsorption, preheating, desorption, precooling and cooling sections. The separation of the CO_2 from the rest of the flue gas takes place within the adsorption section, where the gas flows upwards in a counter-current way with respect to the adsorbent that moves downwards. While the CO_2 is preferentially adsorbed onto the adsorbent, the non-adsorbing gases (i.e., the CO_2-free product) are vented to the atmosphere from the top outlet of the adsorption section. In order to ensure uniform distribution of the sorbent flow, the adsorption section is filled with structured packing consisting of corrugated and perforated metal plates, similar to those used in absorption columns.

The adsorbent reaching the bottom outlet of the adsorption section is loaded with CO_2 and needs to be regenerated. The thermal energy required for sorbent regeneration is provided within the preheating and desorption sections, both operated as indirect-contact heat exchangers. The preheating section is used first to heat the adsorbent to a certain extent by means of internally recovered heat, while the desorption section is used to provide additional heat to the sorbent until reaching the target desorption temperature. The desorbing CO_2 is collected in a CO_2-rich stream at the bottom end of the desorption section. Light vacuum (about 90 kPa) is applied to assist the desorption and direct the desorbing gas towards the extraction point.

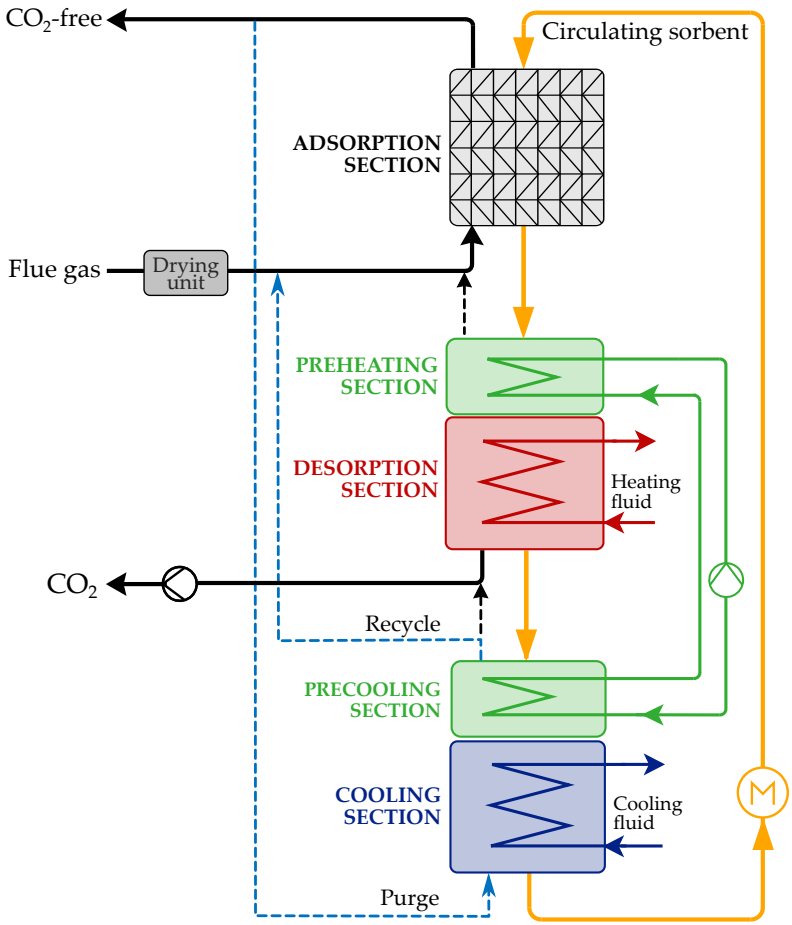

Figure 2.1: Schematic diagram of the simulated MBTSA process.

The remaining sections, precooling and cooling, are used to bring the adsorbent back down to the adsorption temperature. If complete regeneration is not achieved within the desorption section, the remaining CO_2 is recovered by purging the adsorbent in the cooling and precooling sections with a small fraction of the CO_2-free product. Ultimately, the regenerated the adsorbent is transported back to the top of the unit, closing the cycle.

2.2 Performance indicators

The performance of adsorption-based separation processes is usually assessed by means of four main indicators: product purity, product recovery, process productivity and specific energy duty (Yang 1987; Grande 2012). With reference to the MBTSA process for post-combustion CO_2 capture considered in this thesis, see Figure 2.1, these performance indicators are defined as follows.

The CO_2 purity corresponds to the molar fraction of CO_2 in the CO_2-rich product:

$$CO_2 \text{ purity} = \frac{\dot{n}_{CO_2,CO_2\text{-rich gas}}}{\dot{n}_{tot,CO_2\text{-rich gas}}} \cdot 100, \tag{2.1}$$

where $\dot{n}$ denotes the molar flow rate.

The recovery, also referred to as capture rate, is defined as the ratio between the amount of CO_2 in the CO_2-rich product (i.e., moles of CO_2 captured per unit time) and the amount of CO_2 in the flue gas (i.e., amount of CO_2 fed to the system per unit time):

$$CO_2 \text{ recovery} = \frac{\dot{n}_{CO_2,CO_2\text{-rich gas}}}{\dot{n}_{CO_2,\text{flue gas}}} \cdot 100. \tag{2.2}$$

The process productivity, also referred to as adsorbent productivity, is calculated as the ratio between the mass flow rate of CO_2 in the CO_2-rich product and the total sorbent inventory:

$$\text{Productivity} = \frac{\dot{m}_{CO_2,CO_2\text{-rich gas}}}{\dot{m}_s \cdot t_{cycle}}. \tag{2.3}$$

The sorbent inventory is the amount of adsorbent needed to complete a full cycle, and it is given by the product of sorbent flow rate, $\dot{m}_s$, and the total cycle time, t_{cycle}. The latter is obtained as the sum of the residence times in each section.

Lastly, the specific energy duty refers to the amount of energy required to capture one kilogram of CO_2. In this thesis, the specific energy duty was calculated as the ratio between the heat flow rate provided in the desorption section and the amount of CO_2 captured per unit of time,

$$\text{Specific energy duty} = \frac{\dot{Q}_{\text{desorption section}}}{\dot{m}_{CO_2,CO_2\text{-rich gas}}}. \tag{2.4}$$

2.3 Mathematical model

In this work, the MBTSA process is described by means of a one-dimensional mathematical model obtained by applying the mass, momentum and energy balances to the different sections (adsorption, preheating, desorption, precooling and cooling), each of which is connected to the adjacent ones through appropriate boundary conditions. Although the numerical value of certain design parameters (e.g., void fraction, section height, etc.) and operating conditions differ from section to section, the model equations and the underlying assumptions are the same for each section: negligible gradients in the radial direction, constant cross sectional area, constant sorbent velocity, uniform and constant void fraction, and ideal gas behavior in the bulk phase. The resulting set of partial differential equations, together with other supplementary equations and correlations used in the model are given in the following subsections.

2.3.1 Transport equations

Mass balance in the gas phase

The gas phase concentration profiles along the section height are predicted by solving the mass balance in the gas phase for each species:

$$\varepsilon_{\mathrm{c}}\frac{\partial C_i}{\partial t}+\frac{\partial(uC_i)}{\partial z}=\varepsilon_{\mathrm{c}}\frac{\partial}{\partial z}\left(D_{z,i}C_{\mathrm{T}}\frac{\partial Y_i}{\partial z}\right)-\frac{(1-\varepsilon_{\mathrm{c}}-\xi)\,a'k_{\mathrm{f},i}}{\mathrm{Bi}_i/5+1}(C_i-C_{\mathrm{p},i}), \tag{2.5}$$

where the index i corresponds to each component of the gas mixture, t is the time; z the position along the section height; C_i, $C_{\mathrm{p},i}$, and Y_i the concentration in the bulk gas, the concentration in the macropores, and the molar fraction in the bulk gas, respectively; ε_{c} the column void fraction; ξ the volume fraction occupied by structured packing; $D_{z,i}$ the axial dispersion coefficient; u the superficial gas velocity; a' the adsorbent particle specific area; $k_{\mathrm{f},i}$ the film mass transfer coefficient; and Bi_i the Biot number. In addition, C_{T} is the total concentration in the bulk gas, and it is computed with the ideal gas equation of state:

$$C_{\mathrm{T}}=\sum_i C_i=\frac{P}{RT}, \tag{2.6}$$

where P and T are the pressure and temperature in the bulk gas, respectively, and R is the universal gas constant.

Mass balance in the macropores

Using the linear driving force (LDF) approximation to express the mass transfer rate from the bulk gas to the pores, and from the pores to the adsorbed phase, the mass balance in the macropores is given by:

$$\varepsilon_{\mathrm{p}}\frac{\partial C_{\mathrm{p},i}}{\partial t}+v_{\mathrm{s}}\frac{\partial C_{\mathrm{p},i}}{\partial z}=\varepsilon_{\mathrm{p}}\frac{15D_{\mathrm{p},i}}{r_{\mathrm{p}}^2}\frac{\mathrm{Bi}_i}{5+\mathrm{Bi}_i}\left(C_i-C_{\mathrm{p},i}\right)-\rho_{\mathrm{p}}\frac{15D_{\mathrm{c},i}}{r_c^2}\left(q_i^*-q_i\right), \tag{2.7}$$

where r_{p} is the particle radius, $D_{\mathrm{p},i}$ the macropore diffusivity, ρ_{p} the particle density, q_i the adsorbed concentration of component i, and v_{s} the velocity of the adsorbent.

Mass balance in the solid phase

The adsorbent loading profiles are computed from the mass balance in the solid phase:

$$\frac{\partial q_i}{\partial t}+v_{\mathrm{s}}\frac{\partial q_i}{\partial z}=\frac{15D_{\mathrm{c},i}}{r_{\mathrm{c}}^2}\left(q_i^*-q_i\right), \tag{2.8}$$

where $15D_{\mathrm{c},i}/r_{\mathrm{c}}^2$ is treated as a single parameter representing the adsorption rate of component i, and q_i^* is the adsorbed concentration of component i in equilibrium with the corresponding local concentration in the macropore ($C_{\mathrm{p},i}$). The adsorption equilibrium is described using the extension of the Virial isotherm model for multicomponent systems, see Section 2.3.3.

Momentum balance

The pressure gradient along the sections was computed according to:

$$\frac{\partial P}{\partial z} = \frac{150\mu_{\mathrm{g}}(1-\varepsilon_{\mathrm{c}})^2}{\varepsilon_{\mathrm{c}}^3 d_{\mathrm{p}}^2}u + \frac{1.75(1-\varepsilon_{\mathrm{c}})\rho_{\mathrm{g}}}{\varepsilon_{\mathrm{c}}^3 d_{\mathrm{p}}}u|u|, \tag{2.9}$$

where P is the total pressure in the bulk gas, d_{p} is the particle diameter, μ_{g} is the gas viscosity, and ρ_{g} the gas density. This equation was proposed by Ergun (1952) and it is commonly used to estimate pressure losses in packed bed adsorption processes.

Energy balances

The gas and adsorbent temperatures (T and T_{s}) are predicted by solving the energy balances in the gas, Eq. (2.10), and solid phases, Eq. (2.11), respectively.

$$\begin{aligned}\varepsilon_{\mathrm{c}} C_{\mathrm{T}}\hat{c}_v\frac{\partial T}{\partial t} + uC_{\mathrm{T}}\hat{c}_p\frac{\partial T}{\partial z} = \frac{\partial}{\partial z}\left(\lambda_{\mathrm{g}}\frac{\partial T}{\partial z}\right) + \varepsilon_{\mathrm{c}}RT\sum_i\frac{\partial C_i}{\partial t} - \\ (1-\varepsilon_{\mathrm{c}}-\xi)\,a' h_{\mathrm{gs}}\,(T-T_{\mathrm{s}}) - \alpha_{\mathrm{gt}}h_{\mathrm{gt}}\,(T-T_{\mathrm{t}})\end{aligned} \tag{2.10}$$

$$\begin{aligned}\left[(1-\varepsilon_{\mathrm{c}}-\xi)\rho_{\mathrm{p}}c_{p,\mathrm{s}} + \xi\rho_{\mathrm{pk}}c_{p,\mathrm{pk}}\right]\left(\frac{\partial T_{\mathrm{s}}}{\partial t} + v_{\mathrm{s}}\frac{\partial T_{\mathrm{s}}}{\partial z}\right) = \xi\frac{\partial}{\partial z}\left(\lambda_{\mathrm{pk}}\frac{\partial T_{\mathrm{s}}}{\partial z}\right) + \\ (1-\varepsilon_{\mathrm{c}}-\xi)a' h_{\mathrm{gs}}(T-T_{\mathrm{s}}) + (1-\varepsilon_{\mathrm{c}}-\xi)\rho_{\mathrm{p}}\sum_i\left(-\Delta H_i\left[\frac{\partial q_i}{\partial t} + v_{\mathrm{s}}\frac{\partial q_i}{\partial z}\right]\right) + \\ (1-\varepsilon_{\mathrm{c}}-\xi)\varepsilon_{\mathrm{p}}RT_{\mathrm{s}}\sum_i\left[\frac{\partial C_{\mathrm{p},i}}{\partial t} + v_{\mathrm{s}}\frac{\partial C_{\mathrm{p},i}}{\partial z}\right]\end{aligned} \tag{2.11}$$

In the previous equations, ΔH_i represents the heat of adsorption of component i, h_{gs} the film heat transfer coefficient between the gas and the solid, h_{gt} the convective heat transfer coefficient between the gas and the tubes wall, α_{gt} the heat transfer area per unit volume, T_{s} the temperature of the sorbent, T_{t} the temperature of the tubes wall, $\hat{c}_v$ and $\hat{c}_p$ the gas molar heat capacities at constant volume and constant pressure, respectively, $c_{p,\mathrm{s}}$ the specific heat capacity of the sorbent, $c_{p,\mathrm{pk}}$ the specific heat capacity of the packing, ρ_{pk} the density of the packing, λ_{g} and λ_{pk} the heat axial dispersion coefficient of the gas and the packing, respectively, and R the universal gas constant.

In addition, in the sections operated as indirect-contact heat exchanger, the temperature of the tubes wall (T_{t}) and the temperature of the heating/cooling fluid (T_{f}) are respectively given by:

$$\rho_{\mathrm{t}}c_{p,\mathrm{t}}\frac{\partial T_{\mathrm{t}}}{\partial t} = \alpha_{\mathrm{t,ext}}h_{\mathrm{gt}}(T-T_{\mathrm{t}}) - \alpha_{\mathrm{t,int}}h_{\mathrm{ft}}(T_{\mathrm{t}}-T_{\mathrm{f}}) \quad \text{and} \tag{2.12}$$

$$\rho_{\mathrm{f}}c_{p,\mathrm{f}}\frac{\partial T_{\mathrm{f}}}{\partial t} + u_{\mathrm{f}}\rho_{\mathrm{f}}c_{p,\mathrm{f}}\frac{L_z}{L_x}\frac{\partial T_{\mathrm{f}}}{\partial z} = -\alpha_{\mathrm{t,int}}h_{\mathrm{ft}}(T_{\mathrm{f}}-T_{\mathrm{t}}), \tag{2.13}$$

where the subscript t refers to the tubes wall, the subscript f refers to the heating/cooling fluid, $\alpha_{\mathrm{t,ext}}$ and $\alpha_{\mathrm{t,int}}$ are the external and internal heat transfer areas per unit of fluid volume, h_{ft} is the convective heat transfer coefficient between the heating/cooling fluid and the heat exchanger tubes, and the ratio L_x/L_z is the distance travelled by the heating/cooling fluid per unit of height.

Eq. (2.12) was derived assuming that the thermal conduction resistance of the walls is negligible, while taking into account the effect of the thermal capacity of the heat exchanger walls. On the other hand, Eq. (2.13) was derived considering a heat exchanger with a cross-flow shell-and-tube configuration, whereby the heating/cooling fluid flows within horizontal tubes. To this end, the energy balance was applied to a single tube along the direction of the fluid flow (x). The horizontal coordinate (x) was then converted to the axial coordinate along the section (z) by assuming a linear dependence of the tube length (L_x) with respect to the section length (L_z).

2.3.2 Transport parameters

The transport parameters appearing in the mass and energy balance equations are computed using the semi-empirical correlations indicated in this section.

Mass transfer parameters

The axial dispersion coefficients ($D_{z,i}$) controlling the diffusion term of the gas mass balances, Eq. (2.5), are obtained from the correlation proposed by Wakao et al. (1978):

$$D_{z,i} = \frac{D_{\mathrm{m},i}}{\varepsilon_{\mathrm{c}}}(20 + 0.5\ \mathrm{Sc}_i\,\mathrm{Re}), \tag{2.14}$$

where the Schmidt and Reynolds numbers are defined as

$$\mathrm{Sc}_i = \frac{\mu_{\mathrm{g}}\rho_{\mathrm{g}}}{D_{\mathrm{m},i}} \quad \text{and} \quad \mathrm{Re} = \frac{\rho_{\mathrm{g}} u\, d_{\mathrm{p}}}{\mu_{\mathrm{g}}}, \tag{2.15}$$

with ρ_{g} and μ_{g} being the gas density and viscosity, respectively, and d_{p} the particle diameter. The molecular diffusivities ($D_{\mathrm{m},i}$) are approximated with the Wilke correlation (Wilke 1950):

$$D_{\mathrm{m},i} = \frac{1 - Y_i}{\sum_{j\neq i}^{n} \frac{Y_i}{D_{ij}}}. \tag{2.16}$$

where the binary diffusivity (D_{ij}) is given by (Bird et al. 2002):

$$D_{ij} = \frac{0.01883\ T^{3/2}}{P\ \sigma_{ij}^2\ \Omega_{D_{ij}}} \sqrt{\frac{1}{M_{\mathrm{w},i}} + \frac{1}{M_{\mathrm{w},j}}}, \tag{2.17}$$

with M_{w} being the molecular weight of the gas species, σ_{ij} the Lennard-Jones parameter, and $\Omega_{D_{ij}}$ the diffusion collision integral.

The source term of the gas mass balances, Eq. (2.5), involves the film mass transfer coefficients ($k_{\mathrm{f},i}$) and the Biot number of the adsorbent particles (Bi_i). The former is estimated with the Sherwood number correlation proposed by Wakao et al. (1978):

$$\mathrm{Sh}_i = \frac{k_{\mathrm{f},i} d_\mathrm{p}}{D_{\mathrm{m},i}} = 2.0 + 1.1 \mathrm{Re}^{0.6} \mathrm{Sc}_i{}^{1/3}, \tag{2.18}$$

while the Biot number is defined as

$$\mathrm{Bi}_i = \frac{r_\mathrm{p} k_{\mathrm{f},i}}{\varepsilon_\mathrm{p} D_{\mathrm{p},i}}, \tag{2.19}$$

where r_p is the particle radius, ε_p is the particle porosity and $D_{\mathrm{p},i}$ the macropore diffusivity. The macropore diffusivity is computed using the relation proposed by Yang (1987):

$$\frac{1}{D_{\mathrm{p},i}} = \tau_\mathrm{p} \left(\frac{1}{D_{\mathrm{Kn},i}} + \frac{1}{D_{\mathrm{m},i}}, \right) \tag{2.20}$$

where τ_p is the particle tortuosity, and D_Kn is the Knudsen diffusivity, which is computed according to (Ruthven 1984):

$$D_{\mathrm{Kn},i} = \frac{2}{3} r_\mathrm{pore} \sqrt{\frac{8}{\pi} \frac{RT}{M_{\mathrm{w},i}}}. \tag{2.21}$$

Lastly, the rate of adsorption of each component ($15 D_{\mathrm{c},i}/r_\mathrm{c}^2$), appearing in Eq. (2.7) and Eq. (2.8), is assumed to have a dependency on temperature given by an Arrhenius equation:

$$\frac{15 D_{\mathrm{c},i}}{r_\mathrm{c}^2} = \frac{15 D^0_{\mathrm{c},i}}{r_c^2} \exp\left(\frac{-E_{\mathrm{a},i}}{RT} \right), \tag{2.22}$$

where the term $15 D^0_{\mathrm{c},i}/r_\mathrm{c}^2$ represents the adsorption rate at infinite temperature and $E_{\mathrm{a},i}$ the activation energy of micropore/crystal diffusion.

Heat transfer parameters

In analogy with mass dispersion in the gas phase, the axial thermal dispersion coefficient (λ_g) appearing in the gas energy balance, Eq. (2.10), is obtained from the empirical correlation proposed by Wakao et al. (1979):

$$\lambda_\mathrm{g} = k_\mathrm{g} (7 + 0.5 \ \mathrm{Pr}\,\mathrm{Re}), \tag{2.23}$$

where the Prandtl number is defined as

$$\mathrm{Pr} = \frac{c_{p,\mathrm{g}} \mu_\mathrm{g}}{k_\mathrm{g}}, \tag{2.24}$$

with k_g being the gas thermal conductivity. In addition, the convective heat transfer coefficient between gas and solid (h_{gs}) is computed with the Nusselt number correlation proposed by Wakao et al. (1979):

$$\mathrm{Nu} = \frac{h_{gs} d_p}{k_g} = 2.0 + 1.1 \mathrm{Re}^{0.6} \mathrm{Pr}^{1/3}. \tag{2.25}$$

Lastly, the convective heat transfer coefficient between the heat exchanger tubes and the gas (h_{gt}) also needs to be specified. This parameter is case specific as it depends on a number of factors, including the geometry of the heat exchanger, the shape and size of adsorbent particles, and the flow pattern of the adsorbent and gas moving through the system. To the author's knowledge, there are no correlations available to estimate the heat transfer coefficient for flowing adsorbent particles in cross-flow shell-and-tube heat exchangers. To address this limitation, a series of experiments were carried out in a moving bed apparatus with the aim to develop a correlation for the required heat transfer coefficient. The details about this experimental work are presented in Chapter 3.

2.3.3 Adsorption equilibrium

Adsorption equilibrium between the gas in the macropores and the adsorbed phase is described with the multi-component extension of the Virial isotherm model (Taqvi et al. 1997; Talu 1998; Grande et al. 2008; Shen et al. 2010) that takes into account competitive adsorption of the different species in the gas mixture:

$$P_i = \frac{q_i^*}{K_{H,i}} \exp\left[\sum_{j=1}^{N} A_{ij} q_j^* + \sum_{j=1}^{N}\sum_{k=1}^{N} B_{ijk} q_j^* q_k^* + \sum_{j=1}^{N}\sum_{k=1}^{N}\sum_{l=1}^{N} C_{ijkl} q_j^* q_k^* q_l^*\right] \tag{2.26}$$

The mixing Virial coefficients (A_{ij}, B_{ijk}, C_{ijkl}) are calculated based on the pure-component adsorption isotherm parameters as:

$$A_{ij} = \frac{A_i + A_j}{2}, \quad B_{ijk} = \frac{B_i + B_j + B_k}{3} \quad \text{and} \quad C_{ijkl} = \frac{C_i + C_j + C_k + C_l}{4}. \tag{2.27}$$

In turn, the pure-component isotherm parameters are obtained by fitting experimental data to the pure-component Virial equation (Lopes et al. 2009; Grande et al. 2008):

$$P_i = \frac{q_i^*}{K_{H,i}} \exp(A_i q_i^* + B_i q_i^{*2} + C_i q_i^{*3}), \tag{2.28}$$

where subscript i indicates the adsorbate (CO_2 or N_2), P_i is the partial pressure, q_i^* the amount adsorbed at equilibrium, and $K_{H,i}$ the Henry's law constant. The temperature dependence of the Virial coefficients A_i, B_i and C_i was expressed by

$$A_i = A_{0,i} + \frac{A_{1,i}}{T_s}, \quad B_i = B_{0,i} + \frac{B_{1,i}}{T_s}, \quad \text{and} \quad C_i = C_{0,i} + \frac{C_{1,i}}{T_s}; \tag{2.29}$$

while the dependence of the Henry's law constant with temperature was given by the Van't Hoff equation:

$$K_{\mathrm{H},i} = K_{\mathrm{H},i}^{\infty} \exp\left(\frac{-\Delta H_i}{R T_{\mathrm{s}}}\right), \tag{2.30}$$

where $K_{\mathrm{H},i}^{\infty}$ is the adsorption constant at infinite temperature, ΔH_i the heat of adsorption at zero coverage, and R the universal gas constant.

2.3.4 Boundary conditions

To solve the set of partial differential equations given in Section 2.3.1, appropriate boundary conditions need to be provided at the inlet and outlet of each MBTSA section. Table 2.1 contains the complete set of boundary conditions, sorted by section, inlet and outlet position, and corresponding transport equation. Different types of boundary conditions were applied to reflect the actual behavior of the system. For instance, Danckwerts boundary conditions are used for the mass and energy balances of the gas phase when the section is fed with a gas stream. This is the case for the flue gas in the adsorption section or the purge gas in the cooling section. Dirichlet boundary conditions are used to impose the gas velocity at the inlet and the pressure at the outlet of each section. The same type of boundary conditions are applied to specify the temperature and adsorbed concentration of the solid phase. In this case, the values assigned at the inlet correspond to the values computed at the outlet of the previous section. Lastly, zero-gradient conditions are imposed for some of the variables, such as the gas concentration and temperature at the top of each section.

2.3.5 Model implementation

The set of partial differential equations describing the MBTSA is a large-scale system that requires powerful simulation tools to be solved. In this work, the numerical simulations of the MBTSA system were carried out in gPROMS (Process System Enterpise (PSE) 2019), a commercial equation-oriented simulation tool suitable for robustly solving large-scale mathematical problems. In particular, the system of partial differential equations was discretized in space using a centered finite difference method, and the resulting set of differential-algebraic equations was solved with the stiff Radau solver (SRADAU) available in gPROMS. The simulations were performed on a laptop computer with 16 GB of RAM and a 2.80 GHz dual-core Intel i7 processor.

The set of coupled differential equations for each section of the MBTSA system were implemented on gPROMS software and solved simultaneously. For this purpose, the individual section models were connected to each other in a so-called "composite model" flowsheet on gPROMS (Liu et al. 2011). With the gPROMS composite model approach, the different sections of the moving bed communicate

with each other through specifically defined variable-ports. The purpose of these inlet-outlet ports is to transfer certain model variables (e.g. gas and solid phase concentrations, temperature and pressure) at the boundary of the corresponding section-space domain, so that the model instances can exchange information with the adjacent model instances during simulation. As an example, the boundary conditions for the solid phase at the top of the adsorption section (i.e. sorbent inlet), will be assigned based on the variables computed within the cooling section, so that the conditions of the adsorbent leaving the cooling section are used as input at the top of the adsorption section. This allows to take into account for example for a non-complete regeneration of the solid performed in desorption section, which in turns will affect the performance of the adsorption section, and thus the overall process.

Table 2.1: Boundary Conditions (BC) implemented for each section of the MBTSA.

Section	BC at bottom ($z = 0$)	BC at top ($z = L_\mathrm{c}$)	Transport eq.
Adsorption	$-\varepsilon_\mathrm{c} D_{z,i} \frac{\partial C_i}{\partial z} + u\,(C_i - C_{i,\mathrm{in}}^{\mathrm{ads}}) = 0$	$\partial C_i/\partial z = 0$	(2.5)
	–	$\partial C_{\mathrm{p},i}/\partial z = 0$	(2.7)
	–	$q_i = q_{i,\mathrm{in}}^{\mathrm{ads}}$	(2.8)
	$u = u_\mathrm{in}^{\mathrm{ads}}$	$P = P_\mathrm{out}^{\mathrm{ads}}$	(2.9)
	$-\lambda_\mathrm{g} \frac{\partial T}{\partial z} + u\,\hat{c}_p C_\mathrm{T} (T - T_\mathrm{in}^{\mathrm{ads}}) = 0$	$\partial T/\partial z = 0$	(2.10)
	$\partial T_\mathrm{s}/\partial z = 0$	$T_\mathrm{s} = T_{\mathrm{s,in}}^{\mathrm{ads}}$	(2.11)
Preheating	$\partial C_i/\partial z = 0$	$\partial C_i/\partial z = 0$	(2.5)
	–	$\partial C_{\mathrm{p},i}/\partial z = 0$	(2.7)
	–	$q_i = q_{i,\mathrm{in}}^{\mathrm{preh}}$	(2.8)
	$u = 0$	$P = P_\mathrm{out}^{\mathrm{preh}}$	(2.9)
	$\partial T/\partial z = 0$	$\partial T/\partial z = 0$	(2.10)
	$\partial T_\mathrm{s}/\partial z = 0$	$T_\mathrm{s} = T_{\mathrm{s,in}}^{\mathrm{preh}}$	(2.11)
	$T_\mathrm{f} = T_{\mathrm{f,in}}^{\mathrm{preh}}$	$\partial T_\mathrm{f}/\partial z = 0$	(2.13)
Desorption	$\partial C_i/\partial z = 0$	$\partial C_i/\partial z = 0$	(2.5)
	–	$\partial C_{\mathrm{p},i}/\partial z = 0$	(2.7)
	–	$q_i = q_{i,\mathrm{in}}^{\mathrm{des}}$	(2.8)
	$P = P_\mathrm{out}^{\mathrm{des}}$	$u = 0$	(2.9)
	$\partial T/\partial z = 0$	$\partial T/\partial z = 0$	(2.10)
	$\partial T_\mathrm{s}/\partial z = 0$	$T_\mathrm{s} = T_{\mathrm{s,in}}^{\mathrm{des}}$	(2.11)
	$T_\mathrm{f} = T_{\mathrm{f,in}}^{\mathrm{des}}$	$\partial T_\mathrm{f}/\partial z = 0$	(2.13)
Precooling	$-\varepsilon_\mathrm{c} D_{z,i} \frac{\partial C_i}{\partial z} + u\,(C_i - C_{i,\mathrm{in}}^{\mathrm{prec}}) = 0$	$\partial C_i/\partial z = 0$	(2.5)
	–	$\partial C_{\mathrm{p},i}/\partial z = 0$	(2.7)
	–	$q_i = q_{i,\mathrm{in}}^{\mathrm{prec}}$	(2.8)
	$u = u_\mathrm{in}^{\mathrm{prec}}$	$P = P_\mathrm{out}^{\mathrm{prec}}$	(2.9)
	$-\lambda_\mathrm{g} \frac{\partial T}{\partial z} + u\,\hat{c}_p C_\mathrm{T} (T - T_\mathrm{in}^{\mathrm{prec}}) = 0$	$\partial T/\partial z = 0$	(2.10)
	$\partial T_\mathrm{s}/\partial z = 0$	$T_\mathrm{s} = T_{\mathrm{s,in}}^{\mathrm{prec}}$	(2.11)
	$T_\mathrm{f} = T_{\mathrm{f,in}}^{\mathrm{prec}}$	$\partial T_\mathrm{f}/\partial z = 0$	(2.13)
Cooling	$-\varepsilon_\mathrm{c} D_{z,i} \frac{\partial C_i}{\partial z} + u\,(C_i - C_{i,\mathrm{in}}^{\mathrm{cool}}) = 0$	$\partial C_i/\partial z = 0$	(2.5)
	–	$\partial C_{\mathrm{p},i}/\partial z = 0$	(2.7)
	–	$q_i = q_{i,\mathrm{in}}^{\mathrm{cool}}$	(2.8)
	$u = u_\mathrm{in}^{\mathrm{cool}}$	$P = P_\mathrm{out}^{\mathrm{cool}}$	(2.9)
	$-\lambda_\mathrm{g} \frac{\partial T}{\partial z} + u\,\hat{c}_p C_\mathrm{T} (T - T_\mathrm{in}^{\mathrm{cool}})$	$\partial T/\partial z = 0$	(2.10)
	$\partial T_\mathrm{s}/\partial z = 0$	$T_\mathrm{s} = T_{\mathrm{s,in}}^{\mathrm{cool}}$	(2.11)
	$T_\mathrm{f} = T_{\mathrm{f,in}}^{\mathrm{cool}}$	$\partial T_\mathrm{f}/\partial z = 0$	(2.13)

Chapter 3

Experimental determination of heat transfer coefficients

The sorbent-side heat transfer coefficient is a crucial parameter in the design of MBTSA processes for CO_2 capture because it has a great influence on the sizing and performance of the system. However, to the knowledge of the author, there are no studies concerned with the determination of sorbent-side heat transfer coefficients in indirect-contact heat exchangers for MBTSA systems. For this reason, the objective of this chapter was to determine the heat transfer coefficient of an activated carbon adsorbent flowing through a cross-flow shell-and-tube heat exchanger. First, the lab-scale MBTSA apparatus used for this purpose is described. Then, the experimental procedure and the equations used to determine the heat transfer coefficients from the measured data are presented. Finally, the experimental results are discussed and a correlation relating the heat transfer coefficient with the sorbent mass flux is proposed. This correlation complements the MBTSA model documented in Chapter 2 and will be used to assess the heat transfer performance of the MBTSA process for the waste-to-energy case study considered in Chapter 4.

3.1 Lab-scale MBTSA apparatus

A series of experiments were carried out in a lab-scale apparatus replicating a full MBTSA process with the aim to analyze the heat transfer performance of the desorption section. The MBTSA apparatus, schematically shown in Figure 3.1, is composed of three main sections, namely the adsorption, the desorption and the cooling sections, through which the adsorbent circulates in a continuous manner. The adsorbent is released into the adsorption section at a controlled flow rate from a feeding system placed at the top (ZD22B Standard Feeder, ThreeTec, Switzerland). The adsorption section consists of a 1.5 m high, 5 cm internal diameter polycarbonate column filled with structured packing that ensures uniform distribution of the sorbent flow.

Part of the content of this chapter also is reported in G. Mondino, C. A. Grande, R. Blom, and L. O. Nord (2021). "Evaluation of MBTSA Technology for CO_2 Capture from Waste-to-Energy Plants". *International Journal of Greenhouse Gas Control* [accepted]

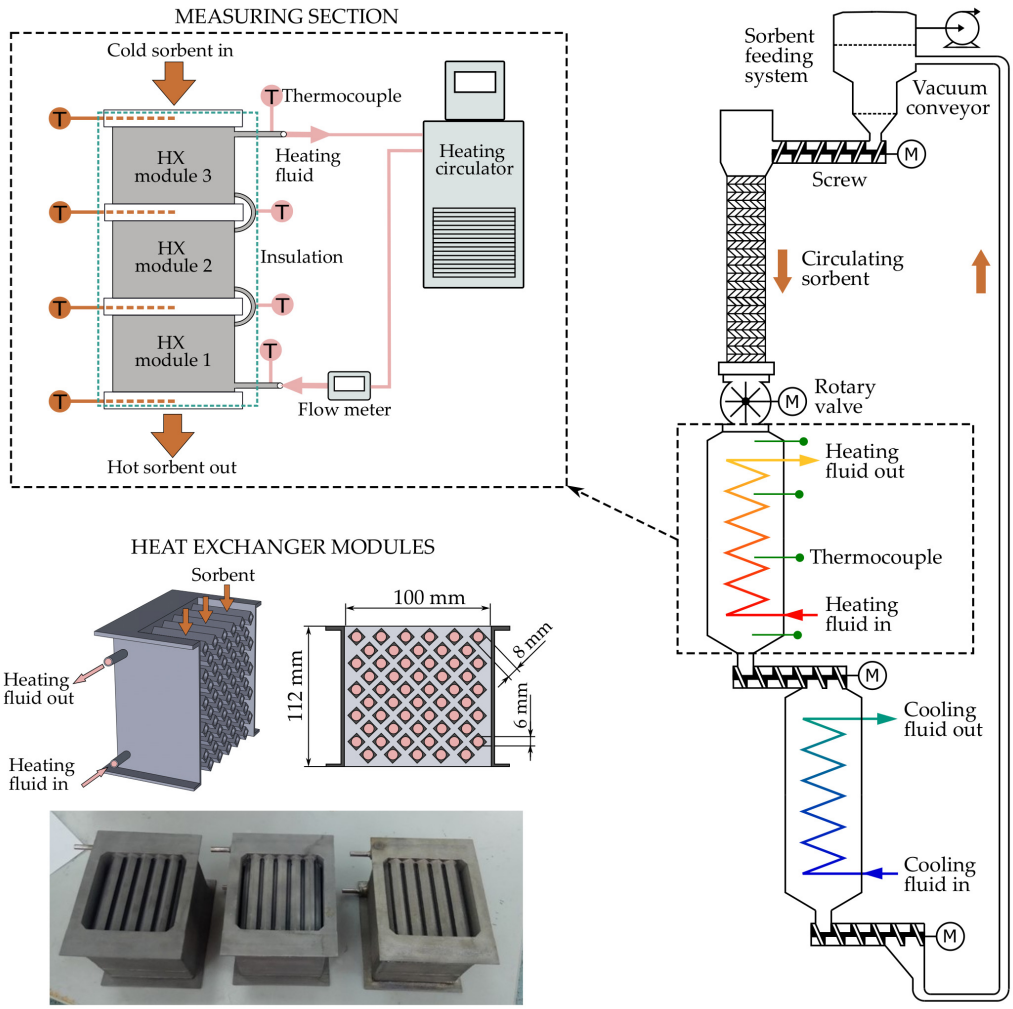

Figure 3.1: Experimental set-up used for heat transfer measurements: schematic diagram of the lab-scale moving bed (right), details on the measuring section (top left) and heat exchanger modules with a sectioned three-dimensional view, a cross-section and a picture of the three modules (bottom left).

After passing through the adsorption section, the sorbent enters a rotary valve (ACS valve, CI series) activated by a three-phase induction motor connected to the power supply by a WEG frequency inverter (CFW500 vector inverter/series). The rotary valve discharges the sorbent into the desorption section indicated as "measuring section" in Figure 3.1. This part consists of a series of three heat exchanger modules (shell-and-tube), in which the sorbent is indirectly heated by a thermal fluid. More specifically, the adsorbent moves downwards in the shell-side of the heat exchanger while the heating media flows within the horizontal tubes in a cross-flow mode. In addition, the lateral surfaces of the heat exchanger modules are insulated with a glass wool layer to limit the heat losses to the surroundings.

Table 3.1: Geometry and material properties of the heat exchanger used for the heat transfer measurements.

Parameter	Symbol	Unit	Value
Number of modules	N_{mod}	-	3
Number of tubes per module	N_{t}	-	55
Number of passes (water side)[a]	N_{pass}	-	5
Number of tubes per pass (water side)	$N_{\mathrm{t,pass}}$	-	11
Internal tube diameter	$d_{\mathrm{t,int}}$	m	0.006
External tube square side	$s_{\mathrm{t,ext}}$	m	0.008
Single tube length	l_{t}	m	0.1
Total tube length	$l_{\mathrm{t,tot}}$	m	16.50
Heat transfer area - water side	A_{w}	m^2	0.311
Heat transfer area - sorbent side	A_{s}	m^2	0.528
Cross flow area - sorbent side[b]	$A_{\mathrm{cf,s}}$	mm^2	6857
Cross flow area - water side[c]	$A_{\mathrm{cf,w}}$	mm^2	311
Tubes material	-	-	TiAl6V4
Specific heat capacity of TiAl6V4	$c_{p,\mathrm{t}}$	$\mathrm{J/kg\,K}$	526
Thermal conductivity of TiAl6V4	k_{t}	$\mathrm{W/m\,K}$	6.6
Density of TiAl6V4	ρ_{t}	$\mathrm{kg/m}^3$	4420

[a] The flow is directed into separate passes by four baffles placed in the lateral heads
[b] Calculated as the volume available for the sorbent flow divided by the module height
[c] Calculated as the internal cross section of a single tube multiplied by the number of tubes per pass

Each heat exchanger module contains a bundle of 55 horizontal tubes through which the heating fluid is distributed in a multi-pass configuration. As shown on the bottom left side of Figure 3.1, the tubes present an inner circular cross section (6 mm in diameter) and an outer squared cross section with a square side of 8 mm. Such configuration and tube shape were adopted to ensure good contact between the sorbent particles and the heating surface, enhancing the heat transfer rate. In particular, staggered horizontal tube arrangements promote a better particle mixing in comparison with vertical tubes or plate configurations (Takeuchi 1996; Baumann et al. 2015; Tian et al. 2020), especially when the tube pitch is narrow (Baumann et al. 2014). Furthermore, using a squared cross-section alleviates the local formation of stagnant and void zones above and below the tubes, respectively. This phenomenon typically occurs on circular tubes and limits the performance of the heat exchanger (Niegsch et al. 1994; Baumann et al. 2015). The numerical values of the geometrical parameters of the heat exchanger are listed in Table 3.1.

Water is used as thermal fluid, supplied by a SE-6 JULABO heating circulator. The temperature of the water at the heat exchanger inlet is controlled by adjusting the set point on the heating circulator. The flow rate is measured with a turbine flow meter (F110P-AU model, HP series, KEM - Germany) installed between the

Table 3.2: Physical properties of the sorbent material.

Parameter	Value	Unit
Adsorbent type	Activated carbon*	–
Particle shape	Spherical beads	–
Particle size	0.5–1.00	mm
Bulk density	452	kg/m^3
Particle density	904	kg/m^3
Heat capacity	880	kJ/kg K

* Provided by Blücher (Germany).

heating circulator and the heat exchanger. The mass flow rate cannot be directly controlled as it depends on the balance between the pressure drop in the circuit and the charateristic of the Julabo circulator pump.

The sorbent temperature is measured with four thermocouples located at different positions within the heat exchangers, see Figure 3.1 (top left). The thermocouples are installed within the spacers separating the modules to ensure a good contact with the bulk of the sorbent flow. Four additional thermocouples are used to measure the water temperature at the inlet and outlet of each heat exchanger module. All thermocouples are connected to a data acquisition system to record the temperature data in a LabVIEW interface (National Instruments 2019). Moreover, a series of powder level sensors are installed within the spacers separating the heat exchanger modules and connected to the LabVIEW program for monitoring the level of adsorbent inside the heat exchangers and ensure that the bed is packed during operation.

The bottom outlet of the heating section is connected to an adjustable transport screw driven by a stepper motor (M1343031, LAM Technologies) that discharges the sorbent into the cooling section. The speed of the screw is adjusted through the LabView program while monitoring the powder level indicators so that the level of adsorbent inside the heat exchanger can be kept as desired.

The cooling section is similar to the heating one, but has only two modules and employs water as cooling media supplied by a Julabo CORIO™ CD-300F Refrigerated Circulator. After passing through the cooling section, the sorbent finally reaches a collector funnel at the bottom of the unit from which it is transported back to the top feeder by means of a vacuum conveyor system.

3.2 Experimental procedure

The heat transfer measurements were carried out using a commercial activated carbon shaped as spherical beads. The material was supplied by Blücher (Germany), and was selected because of its suitable properties for moving bed

applications (i.e., good flowability, particle size between 0.5–1.0 mm, mechanical strength against attrition) as well as commercial availability at large scale. The physical properties of the adsorbent are summarized in Table 3.2. The system was loaded with approximately 10 kg of adsorbent. As previously mentioned, the adsorbent flow rate is controlled by the upper feeding system through a double screw that can be operated at different rotational speeds. As the actual feeding rate does not only depend on the apparatus specifications, but also on the type of sorbent material and its flowing properties, the feeding system was calibrated prior to the experiments. To this aim, the sorbent flow rates were measured at different rotating speeds of the feed screw within the experimental range (7–24 g/s).

All experimental data were collected upon reaching steady state, which was assessed by monitoring the system temperatures via the LabVIEW interface. The sorbent feeding system was activated starting from the lowest flow rate and operated for several minutes until a new steady state was reached. At this point, the temperature measurement were recorded in LabVIEW. The sorbent flow rate was then changed to the next set point and the procedure was repeated. Each data point was obtained by averaging the readings over a period of time to reduce the influence of instantaneous random fluctuations.

3.3 Determination of the heat transfer coefficient

The heat transfer coefficient is determined from the governing equations of the heat exchangers. The main assumptions underlying this analysis are: steady-state operating conditions, one-dimensional flow, negligible changes in the potential and kinetic energy of the fluids, constant transport properties, no fouling on internal heat exchanger surfaces, uniform heat transfer coefficients, and negligible heat loss to the surroundings. The latter assumption was verified by estimating the heat loss due to the natural convection of air on the vertical surfaces exposed to the surrounding. Based on the actual temperature of the exposed insulation layer and the room temperature, the heat loss was estimated to be less than 1 % of the total heat transfer rate in all cases.

Under the assumption of negligible heat loss, the heat transfer from the water is equal to the heat transfer to the sorbent. If, in addition, the specific heat of water is assumed to be constant, the heat flow rate can be calculated from the measured data according to:

$$\dot{Q} = \dot{m}_{\mathrm{w}} c_{p,\mathrm{w}} (T_{\mathrm{w,in}} - T_{\mathrm{w,out}}), \tag{3.1}$$

where the subscript “w” stands for water.

Using the mean logarithmic temperature difference approach (Cengel et al. 1998), the heat transfer rate can be related to the heat transfer resistances as:

$$\dot{Q} = \frac{\Delta T_{\mathrm{LM}}}{R_{\mathrm{tot}}}, \tag{3.2}$$

where R_{tot} is the total heat transfer resistance and ΔT_{LM} is the logarithmic mean temperature difference for the counter-flow arrangement. The total thermal resistance, R_{tot}, is the sum of the contributions due to internal convection (water-side), conduction across the tube walls, and external convection (sorbent-side). The average heat transfer coefficient between the flowing sorbent and the tube walls, h_{s}, can be solved from:

$$R_{\text{tot}} = R_{\text{w}} + R_{\text{t}} + R_{\text{s}} = \frac{1}{A_{\text{w}} h_{\text{w}}} + \frac{\ln(d_{\text{t,ext}}/d_{\text{t,int}})}{2\pi k_{\text{t}} l_{\text{t,tot}}} + \frac{1}{A_{\text{s}} h_{\text{s}}}, \tag{3.3}$$

where the subscript "t" stands for tubes and "s" for sorbent, whereas A_{s} is the heat transfer area on the sorbent side, given by:

$$A_{\text{s}} = 4 s_{\text{t,ext}}\, l_{\text{t}}\, N_{\text{mod}}\, N_{\text{t}}. \tag{3.4}$$

Concerning the internal convective resistance (water side), the heat transfer area A_{w} is calculated directly from the system geometry as:

$$A_{\text{w}} = 2\pi r_{\text{t,int}}^2\, l_{\text{t,tot}}, \tag{3.5}$$

where $l_{\text{t,tot}}$ is the total length of tubes in the heat exchanger and $r_{\text{t,int}}$ is the internal tube diameter. Moreover, the internal heat transfer coefficient, h_{w}, is estimated from an empirical correlation. As the water flow is laminar in all the tests (Reynolds numbers between 1178–1638), the following correlation for internal laminar flow was adopted (Cengel et al. 1998):

$$\text{Nu} = \frac{h_{\text{w}} d_{\text{t,int}}}{k_{\text{w}}} = 3.66 + \frac{0.065(d_{\text{t,int}}/l_{\text{t}})\text{Re}\,\text{Pr}}{1 + 0.04[(d_{\text{t,int}}/l_{\text{t}})\text{Re}\,\text{Pr}]^{2/3}} \tag{3.6}$$

The water conductivity, k_{w}, and the dimensionless numbers appearing in the correlation were evaluated at the bulk mean water temperature (i.e., arithmetic average of the temperature at the inlet and outlet).

Lastly, the tube walls resistance, R_{t}, was directly calculated from the thermal properties of the tube material (TiAl6V4 alloy) and the system geometry. For this purpose, the square profile of the tubes (with a side length $s_{\text{t,ext}}$) was converted into an equivalent circular profile (with diameter $d_{\text{t,ext}}$) with the same cross-sectional area as the actual profile.

3.4 Experimental results

An example of the collected temperature data is shown in Figure 3.2, where the points in the plots correspond to the temperatures sensed by the thermocouples, as specified in the schematic diagram on the right side. It was observed that, in all the experiments performed, the largest adsorbent temperature gain is achieved within

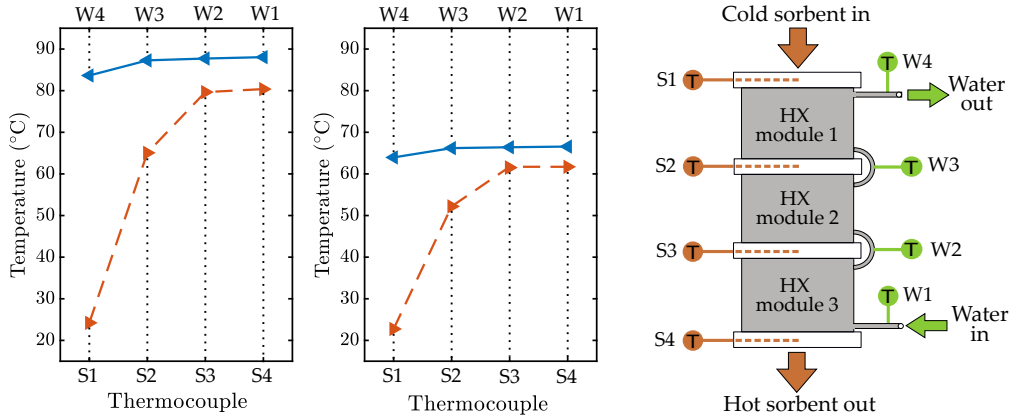

Figure 3.2: On the left, example of experimental results obtained for two test runs: Plot of the measured sorbent and water temperatures. On the right, schematic diagram of the experimental set-up indicating the position of each thermocouple.

the first module, while only a small fraction of heat is exchanged in the second and third modules. Furthermore, the change in temperature experienced by the water, is only a few degrees in the first module and almost negligible in the second and third ones. It was therefore decided to estimate the heat transfer coefficient using only the data corresponding to the first module, where the majority of the heat exchange takes place and the results have the least uncertainty.

The numerical values of the measured temperatures and the thermal parameters used to estimate the heat transfer coefficient are reported in Tables 3.3 to 3.5. The estimated heat transfer rate, $\dot{Q}$, ranged between 249 W and 628 W, corresponding to tests 4 and 9, respectively. With regards to the thermal resistances, the convection on the sorbent-side was always the dominating resistance, ranging between 72 and 82 % of the total thermal resistance, while the conductive resistance of the tube walls ranged between 1.8 and 2.7 %.

The convective heat transfer coefficient on the sorbent side was computed for each operating point according to Eq. (3.3), and the results were plotted against the velocity of the solid particles in Figure 3.3. As expected, the heat transfer coefficient increases with the solid velocity (Niegsch et al. 1994; Al-Ansary et al. 2012; Baumann et al. 2015), while no dependence was observed on the solid temperature. The measured heat transfer coefficients ranged between 69 and 117 $\mathrm{W/m^2\,K}$ with an uncertainty below 8% in all cases, which was evaluated using the law of propagation of uncertainty (Farrance et al. 2012). The trend of the experiments suggests that even higher values might be achieved by operating the system at higher solid velocities. However, this hypothesis could not be verified due to the limitations of the experimental apparatus. In addition, the analysis of the uncertainty.

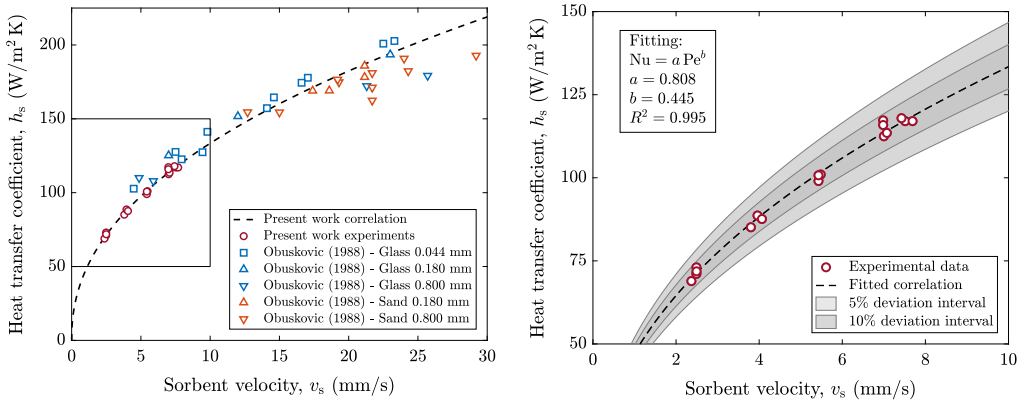

Figure 3.3: Experimental heat transfer coefficients and fitted correlation (right). Comparison of the heat transfer coefficients measured in this work against the values reported by Obuskovic (1988) for a single tube immersed in a moving bed operated with glass and sand particles of different diameters (left).

In order to correlate the experimental results, the heat transfer coefficient and solid velocity were expressed in terms of dimensionless quantities. The dependence of the heat transfer coefficient on: (i) gas thermal conductivity, (ii) bulk density, (iii) sorbent heat capacity, (iv) solid velocity, and (v) tube external side can be expressed as:

$$f(h_s,\, k_g,\, \rho_b,\, c_{p,s},\, v_s,\, s_{t,ext}) = 0. \tag{3.7}$$

Since this relationship involves 6 variables and 4 physical dimensions (i.e., time, length, mass, and temperature), dimensional analysis yields two independent dimensionless groups:

$$g(\mathrm{Nu},\, \mathrm{Pe}) = 0, \tag{3.8}$$

where

$$\mathrm{Nu} = \frac{h_s s_{t,ext}}{k_g} \tag{3.9}$$

is the Nusselt number and

$$\mathrm{Pe} = \frac{\rho_b c_{p,s} v_s s_{t,ext}}{k_g} \tag{3.10}$$

is the Péclet number. The Nusselt and Péclet numbers can be interpreted as the dimensionless heat transfer coefficient and solid velocity, respectively. Using these dimensionless numbers, the experimental results were correlated by means of regression analysis, and the following equation was obtained:

$$\mathrm{Nu} = a\,\mathrm{Pe}^b = 0.808\,\mathrm{Pe}^{0.445}. \tag{3.11}$$

As shown in Figure 3.3 (right), the relative deviation between the heat transfer coefficients determined experimentally and the values predicted by Equation (3.11) is below 5% for all cases. In addition, the coefficient of determination obtained

from the regression analysis is $R^2 = 0.995$. This suggests that the proposed correlation is adequate to predict the heat transfer coefficient for flowing adsorbent particles within cross-flow shell-and-tube heat exchangers, provided that they are geometrically similar and operated within the range of particle velocities considered in these experiments.

In addition, Figure 3.3 (left) compares the heat transfer coefficients measured in this work against those reported by Obuskovic (1988) for a single tube immersed in a moving bed of solid particles. The heat transfer coefficients obtained for the activated carbon particles considered in this work are comparable with those obtained by Obuskovic (1988) for glass and sand particles of different diameters. In addition, the variation of the heat transfer coefficient with the velocity of the solid particles follows the same trend as the data from Obuskovic (1988). In particular, the exponent of the Péclet number obtained in the present work ($b = 0.455$), see Equation (3.11), agrees well with the exponent reported by Obuskovic (1988) for their low-velocity experiments ($b = 0.4$), and with the theoretical value suggested by Mickley et al. (1955) for an homogeneous moving bed of infinitesimally small particles ($b = 0.5$).

Finally, the heat transfer coefficients measured in this work are significantly higher than those typically encountered in fixed bed configurations. For example, Marx et al. (2016) reported heat transfer coefficients between 20 and 40 $\mathrm{W/m^2\,K}$ when performing TSA experiments on a indirectly-heated packed bed filled with a zeolite 13X adsorbent shaped as spherical beads with diameters between 1.6 and 2.0 mm. Similarly, Bonjour et al. (2002) obtained heat transfer values up to 50 $\mathrm{W/m^2\,K}$ when measuring the heat transfer performance of a coaxial packed bed heat exchanger filled with activated carbon beads of 0.65 mm mean diameter. This confirms that the moving bed configuration has the potential to address one of the main limitations of the fixed bed TSA process, namely, the low productivity due to the slow heating and cooling of the adsorbent.

In the next chapter, the MBTSA process model described in Chapter 2 will be complemented with the heat transfer correlation proposed here, and then used to design and analyse a full-scale MBTSA process for CO_2 capture from a waste-to-energy power plant.

Table 3.3: Overview of experimental results – part 1 of 3: measured data and calculated heat transfer parameters.

			Test ID					
			1	2	3	4	5	6
Sorbent								
Flow rate	$\dot{m}_\mathrm{s}$	g/s	7.72	7.72	16.99	7.34	16.82	16.82
Mass flux	J_s	kg/m^{2}s	1.13	1.13	2.48	1.07	2.45	2.45
Velocity	v_s	mm/s	2.49	2.49	5.48	2.37	5.43	5.43
Inlet temp.	$T_\mathrm{s,in}$	°C	25.1	24.2	26.4	22.7	24.9	26.7
Outlet temp.	$T_\mathrm{s,out}$	°C	66.2	65.1	55.8	52.2	45.5	46.0
Water								
Inlet temp.	$T_\mathrm{w,in}$	°C	87.5	87.3	85.7	66.2	65.3	65.3
Outlet temp.	$T_\mathrm{w,out}$	°C	84.2	83.6	80.6	64.0	62.0	62.1
Flow rate	$\dot{m}_\mathrm{w}$	g/s	27.65	25.09	25.21	26.57	26.58	26.58
Velocity	v_w	mm/s	91.88	83.39	83.72	87.16	87.16	87.16
Density	ρ_w	kg/m^3	967	968	968	980	981	981
Viscosity	μ_w	mPa s	0.326	0.326	0.332	0.428	0.433	0.433
Heat capacity	$c_{p,\mathrm{w}}$	J/kg K	4202	4202	4201	4188	4187	4187
Conductivity	k_w	W/m K	0.671	0.671	0.670	0.656	0.656	0.656
Reynolds	Re	-	1638	1483	1466	1198	1185	1185
Prandtl	Pr	-	2.04	2.04	2.08	2.73	2.77	2.77
Nusselt	Nu	-	5.19	5.08	5.09	5.17	5.17	5.17
Heat balance								
Heat load	$\dot{Q}$	W	385.1	383.2	544.6	248.8	361.3	352.7
Mean log ΔT	ΔT_LM	-	37.05	37.82	40.87	25.21	27.54	26.54
HTC water	h_w	W/m^{2}K	581.0	568.0	568.1	565.4	564.9	564.9
HTC sorbent	h_s	W/m^{2}K	73.0	71.1	101.0	68.9	99.0	100.7
Thermal resistances								
Total	R_tot	K/kW	96.19	98.70	75.03	101.30	76.24	75.27
Water side	R_w	K/kW	16.60	16.98	16.98	17.06	17.07	17.07
Tubes walls	R_t	K/kW	1.79	1.79	1.79	1.79	1.79	1.79
Sorbent side	R_s	K/kW	77.80	79.93	56.26	82.45	57.37	56.40
% water side	R_w	%	17.3	17.2	22.6	16.8	22.4	22.7
% tubes walls	R_t	%	1.9	1.8	2.4	1.8	2.3	2.4
% sorbent side	R_s	%	80.9	81.0	75.0	81.4	75.3	74.9

Table 3.4: Overview of experimental results – part 2 of 3: measured data and calculated heat transfer parameters.

			Test ID					
			7	8	9	10	11	12
Sorbent								
Flow rate	$\dot{m}_\mathrm{s}$	g/s	21.70	23.29	23.84	7.73	11.78	12.28
Mass flux	J_s	kg/m^{2}s	3.16	3.40	3.48	1.13	1.72	1.79
Velocity	v_s	mm/s	7.00	7.51	7.69	2.49	3.80	3.96
Inlet temp.	$T_\mathrm{s,in}$	°C	27.7	28.8	26.4	21.2	24.4	22.6
Outlet temp.	$T_\mathrm{s,out}$	°C	43.5	52.0	51.1	66.6	60.8	59.0
Water								
Inlet temp.	$T_\mathrm{w,in}$	°C	64.7	84.7	84.6	87.3	86.7	86.4
Outlet temp.	$T_\mathrm{w,out}$	°C	61.2	79.2	78.9	83.7	82.4	81.8
Flow rate	$\dot{m}_\mathrm{w}$	g/s	26.59	26.51	26.51	25.67	25.68	25.69
Velocity	v_w	mm/s	87.16	87.96	87.96	85.31	85.31	85.31
Density	ρ_w	kg/m^3	981	969	969	968	968	968
Viscosity	μ_w	mPa s	0.435	0.335	0.335	0.326	0.329	0.330
Heat capacity	$c_{p,\mathrm{w}}$	J/kg K	4187	4200	4200	4202	4202	4202
Conductivity	k_w	W/m K	0.655	0.670	0.670	0.671	0.671	0.671
Reynolds	Re	-	1178	1528	1526	1517	1507	1504
Prandtl	Pr	-	2.78	2.10	2.10	2.04	2.06	2.06
Nusselt	Nu	-	5.17	5.14	5.14	5.11	5.11	5.11
Heat balance								
Heat load	$\dot{Q}$	W	387.5	609.4	629.4	386.9	465.1	498.6
Mean log ΔT	ΔT_LM	-	26.88	40.91	42.25	37.82	39.74	41.28
HTC water	h_w	W/m^{2}K	564.7	574.4	574.3	571.0	570.8	570.7
HTC sorbent	h_s	W/m^{2}K	112.5	117.0	117.0	71.9	85.1	88.6
Thermal resistances								
Total	R_tot	K/kW	69.38	67.13	67.13	97.76	85.45	82.79
Water side	R_w	K/kW	17.08	16.79	16.79	16.89	16.90	16.90
Tubes walls	R_t	K/kW	1.79	1.79	1.79	1.79	1.79	1.79
Sorbent side	R_s	K/kW	50.51	48.54	48.54	79.08	66.76	64.10
% water side	R_w	%	24.6	25.0	25.0	17.3	19.8	20.4
% tubes walls	R_t	%	2.6	2.7	2.7	1.8	2.1	2.2
% sorbent side	R_s	%	72.8	72.3	72.3	80.9	78.1	77.4

Table 3.5: Overview of experimental results – part 3 of 3: measured data and calculated heat transfer parameters.

			Test ID				
			13	14	15	16	17
Sorbent							
Flow rate	$\dot{m}_\mathrm{s}$	g/s	21.92	12.60	23.02	21.65	21.65
Mass flux	J_s	kg/m^{2}s	3.20	1.84	3.36	3.16	3.16
Velocity	v_s	mm/s	7.07	4.07	7.43	6.98	6.98
Inlet temp.	$T_\mathrm{s,in}$	°C	26.9	23.2	25.9	31.0	27.5
Outlet temp.	$T_\mathrm{s,out}$	°C	53.5	48.2	41.2	45.8	43.2
Water							
Inlet temp.	$T_\mathrm{w,in}$	°C	84.9	65.7	64.2	64.9	64.5
Outlet temp.	$T_\mathrm{w,out}$	°C	79.4	62.8	60.5	61.7	61.0
Flow rate	$\dot{m}_\mathrm{w}$	g/s	25.70	27.07	27.09	27.08	27.09
Velocity	v_w	mm/s	85.31	88.79	88.79	88.79	88.79
Density	ρ_w	kg/m^3	969	980	981	981	981
Viscosity	μ_w	mPa s	0.334	0.431	0.438	0.435	0.437
Heat capacity	$c_{p,\mathrm{w}}$	J/kg K	4201	4187	4187	4187	4187
Conductivity	k_w	W/m K	0.670	0.656	0.655	0.655	0.655
Reynolds	Re	-	1485	1212	1193	1202	1197
Prandtl	Pr	-	2.09	2.75	2.80	2.78	2.79
Nusselt	Nu	-	5.11	5.19	5.19	5.19	5.19
Heat balance							
Heat load	$\dot{Q}$	W	597.2	323.9	423.5	362.9	396.9
Mean log ΔT	ΔT_LM	-	41.07	27.09	28.37	24.41	26.92
HTC water	h_w	W/m^{2}K	570.4	567.6	567.0	567.3	567.1
HTC sorbent	h_s	W/m^{2}K	113.5	87.6	117.9	117.3	115.9
Thermal resistances							
Total	R_tot	K/kW	68.76	83.65	66.98	67.25	67.83
Water side	R_w	K/kW	16.91	16.99	17.01	17.00	17.01
Tubes walls	R_t	K/kW	1.79	1.79	1.79	1.79	1.79
Sorbent side	R_s	K/kW	50.06	64.86	48.18	48.46	49.03
% water side	R_w	%	24.6	20.3	25.4	25.3	25.1
% tubes walls	R_t	%	2.6	2.1	2.7	2.7	2.6
% sorbent side	R_s	%	72.8	77.5	71.9	72.1	72.3

Chapter 4

Waste-to-energy case study using activated carbon

The production of municipal solid waste is expected to keep increasing as a result of the rapid grow of population and living standards around the world (Kaza et al. 2018). In this context, waste-to-energy plants represent a key technology to manage the increasing quantities of solid waste, reduce the methane emissions associated with landfilled waste, and satisfy the rising energy demand (Brunner et al. 2015). In addition, the integration of waste-to-energy plants with CCS technologies has the potential to make waste a net-zero or even negative emission energy source (Kearns 2019; Haaf et al. 2020; Turan et al. 2021). The aim of the present chapter is to assess the MBTSA technology for CO_2 capture from a waste-to-energy power plant. To this purpose, the computational model presented in Chapter 2 was complemented with the heat transfer correlation proposed in Chapter 3, and used as basis for process simulations. The adsorbent material considered for this application is a commercial activated carbon. The adsorption isotherms for CO_2 and N_2 on the activated carbon were determined experimentally and fitted with a Virial model. Based on adsorbent properties and flue gas specifications, the capture process was designed to achieve high CO_2 purity and recovery. Finally, the proposed MBTSA system was evaluated in terms of different performance parameters, including CO_2 separation performance, system footprint, process productivity and energy duty.

4.1 Definition of the case study

The application considered for the MBTSA process is a combined heat and power waste-to-energy plant with a net power output of 16.8 MW_{el} and a thermal output of 64.6 MW_{th}. The power plant was modeled in Thermoflex software (Thermoflow Inc. 2017) using a built-in waste-to-energy plant model. The flue gas specification required to design the MBTSA process were obtained by simulating the plant at its nominal operating point. In order to reduce the computational

Part of the content of this chapter also is reported in G. Mondino, C. A. Grande, R. Blom, and L. O. Nord (2021). "Evaluation of MBTSA Technology for CO_2 Capture from Waste-to-Energy Plants". *International Journal of Greenhouse Gas Control* [accepted]

Table 4.1: Flue gas specifications adopted for the MBTSA simulations.

Parameter	Value	Unit
Mass flow rate	55.9	kg/s
Temperature	30	°C
Pressure	101.5	kPa
Simplified composition:		
molar fraction of CO_2	11	%
molar fraction of N_2	89	%

effort in the MBTSA simulations, the composition of the exhaust gas was simplified to a binary mixture of N_2 and CO_2, assuming that: (i) the flue gas is dried prior to the capture process, and (ii) O_2 and Ar behave similarly to N_2 in terms of adsorption equilibrium and kinetics (Plaza et al. 2014; Plaza et al. 2017). The resulting flue gas specifications, used as input for designing and simulating the MBTSA process, are listed in Table 4.1.

4.2 Adsorbent material

The adsorbent used for the case study was the same activated carbon (Blücher, Germany) employed in the heat transfer experiments described in Chapter 3. The physical properties of the adsorbent used as basis for the MBTSA process simulations are summarized in Table 4.2. In addition, the adsorption equilibrium data for N_2 and CO_2 were measured experimentally and fitted with a suitable adsorption isotherm model as described below.

Pure-component adsorption isotherms of CO_2 and N_2 were measured on a sample of the activated carbon using a volumetric adsorption apparatus (Belsorp Max, MicrotracBEL, Japan). The data were collected at six different temperatures between 30 and 150 °C. Prior to the measurements, overnight degassing of the sample was performed at 150 °C and vacuum conditions.

The experimental isotherms data were fitted with a Virial model truncated at its second term (Barrer 1981; Grande et al. 2008):

$$P_i = \frac{q_i^*}{K_{\mathrm{H},i}} \exp(A_i q_i^* + B_i q_i^{*2}), \tag{4.1}$$

where the temperature dependency of the parameters is expressed by

$$K_{\mathrm{H},i} = K_{\mathrm{H},i}^{\infty} \exp\left(\frac{-\Delta H_i}{RT}\right), \quad A_i = A_{0,i} + \frac{A_{1,i}}{T}, \quad \text{and} \quad B_i = B_{0,i} + \frac{B_{1,i}}{T}. \tag{4.2}$$

Fitting of the pure component adsorption data was carried out by minimizing an error function with the Nelder-Mead algorithm available in the Scilab environment

Table 4.2: Adsorbent properties adopted for the MBTSA simulations.

Parameter	Value	Unit
Adsorbent type	Activated carbon*	–
Particle shape	Spherical beads	–
Particle diameter	0.70	mm
Particle density	904	kg/m^3
Particle porosity	0.50	–
Heat capacity	880	$kJ/kg\,K$

* Provided by Blücher (Germany)

Table 4.3: Virial model parameters fitting CO_2 and N_2 adsorption isotherms on the activated carbon at temperatures between 30 and 150 °C and pressures up to 105 kPa.

	K_H^∞ $mol/kg\,kPa$	$-\Delta H$ kJ/mol	A_0 kg/mol	A_1 $K\,kg/mol$	B_0 kg^2/mol^2	B_1 $K\,kg^2/mol^2$
CO_2	$2.6969 \cdot 10^{-7}$	30.006	−4.3235	1474.0	1.4239	−465.20
N_2	$5.5486 \cdot 10^{-7}$	21.934	−22.982	7121.1	51.644	−15756

(ESI Group 2017). The error function employed takes into account both the absolute and the relative deviations, and it is defined as (Ribeiro et al. 2008):

$$f_{\text{error}} = w \sum_T \sum_q \left(P_{\text{calc}} - P_{\text{exp}}\right)^2 + (1-w) \sum_T \sum_q \left(\frac{P_{\text{calc}} - P_{\text{exp}}}{P_{\text{calc}}}\right)^2 \tag{4.3}$$

where T refers to each of the isotherms, q refers to the measurement point along the isotherm, P_{exp} and P_{calc} are the equilibrium pressures determined experimentally and calculated with the Virial model, respectively, and w is a weighting factor between zero and one. The obtained fitting parameters are summarized in Table 4.3 and they serve as basis for prediction of adsorption equilibrium in the MBTSA model, where the multicomponent extension of the Virial model is implemented to account for competitive adsorption of the two gases, see Section 2.3.3.

The results of the CO_2 and N_2 isotherms measurements together with the isotherms fitting are shown in Figure 4.1. As expected, the adsorption capacity of CO_2 is higher than that of N_2 in the whole temperature and pressure ranges examined. Nevertheless, the equilibrium selectivity expressed as

$$s_{CO_2/N_2} = \frac{q_{CO_2}/p_{CO_2}}{q_{N_2}/p_{N_2}} \tag{4.4}$$

and calculated at the feed gas conditions (see Table 4.1) is just above 11. This value is significantly lower than that of other widely used CO_2 capture adsorbents,

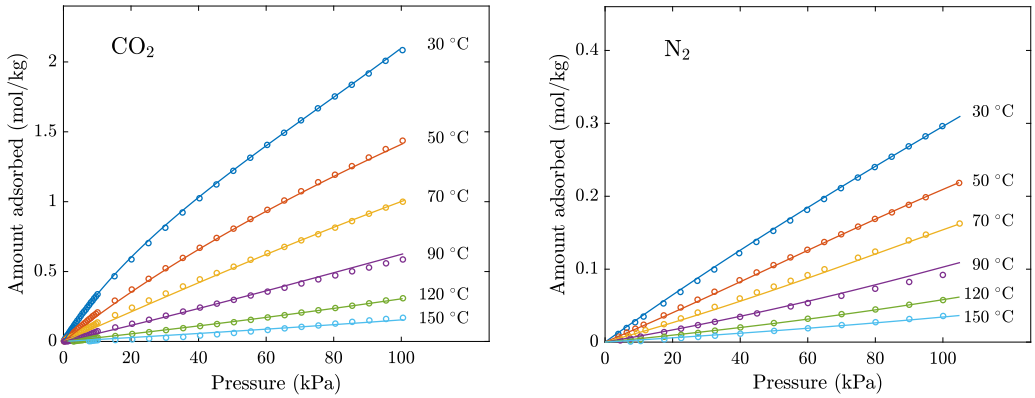

Figure 4.1: CO_2 and N_2 adsorption isotherms on the activated carbon: measured data (dots) and model fitting (continuous lines).

such as 13X and 5A zeolites, for which the selectivity can be as high as 96 and 90, respectively (Merel et al. 2008). Indeed, the CO_2 adsorption capacity at the feed gas conditions (11 kPa and 30 °C) is much lower for the activated carbon evaluated, being less than 0.4 mol/kg, compared to a value larger than 2 mol/kg for the zeolites (Cavenati et al. 2004; Mulloth et al. 1998).

With regards to the heat of adsorption, the values obtained by fitting the CO_2 and N_2 isotherms are in agreement with literature data reported for other carbon adsorbents (Lopes et al. 2009; Plaza et al. 2017; Mondino et al. 2017).

4.3 Design of the MBTSA process

The MBTSA process model documented in Chapter 2 was extended with the heat transfer correlation proposed in Chapter 3 and then used to design an MBTSA process for the present waste-to-energy case study. A set of simulations was performed by varying several model parameters, with the aim to achieve a CO_2 purity of at least 95% and a capture rate higher than 90%, as typically required in CCS applications (Nord et al. 2020; Joss et al. 2017; Plaza et al. 2017).

The simulations were performed by discretizing the axial space domain of each MBTSA section with a second order Centered Finite Difference Method (CFDM). The number of intervals employed to discretize the axial space domain was 600 for the adsorption and precooling sections, 400 for the preheating section, and 140 for the desorption and cooling sections. The space-discretized equations were integrated in time until steady state was reached, and all results presented herein refer to the steady-state solution.

Several design parameters including the system dimensions (height and diameter of each section) and operating conditions (amount of circulating sorbent, adsorption and desorption temperatures, and CO_2 extraction pressure) were ad-

justed until the target CO_2 purity and capture rate were achieved. The design parameters of the final configuration are listed in Table 4.4. A large amount of sorbent (650 kg/s) relative to the flue gas (56 kg/s) was required because of the low CO_2 capacity of the adsorbent. The limited working capacity of the adsorbent was partially compensated by adopting a large temperature swing. In particular, the cooling and regeneration temperatures, i.e., the minimum and maximum temperatures experienced by the adsorbent, were 18 °C and 184 °C, respectively.

With regards to the system dimensions, the length and diameter of the adsorption section were selected as a trade-off to reduce the footprint of the column and limit the gas and sorbent velocities to avoid fluidization, guarantee a sufficient residence time, and limit the pressure drop. The cross section area of the other sections (preheating, desorption, precooling and cooling) was determined by scaling up the heat exchanger modules of the experimental apparatus to the actual sorbent flow rate, while maintaining the same tube shape and diameter (i.e., same heat transfer area per unit volume). The length was then adjusted so that the desired temperatures were reached by the end of the section.

As seen in Table 4.4, the diameter of the sections is significantly larger than their length, which may compromise the assumption of negligible gradients in the radial direction. However, as described in Chapter 2, the adsorption section has a structured packing that helps to maintain uniform distribution of the particles across the section, supporting the one-dimensional flow assumption. Similarly, the heat exchanger tube bundles of the other sections help to guide the flow and achieve a homogeneous heat transfer process, which, in turn, is beneficial to avoid temperature gradients in the radial direction. In any case, the assumption of one-dimensional flow for this configuration is not validated and should be assessed experimentally if the system were to be implemented.

4.4 MBTSA simulation results

The mathematical model describing the MBTSA was used to predict the system behavior in terms of temperature and concentration profiles along the different sections. The simulation results were then used to assess the performance of the process on the basis of separation performance (CO_2 purity and capture rate), energy use and process productivity.

4.4.1 Concentration and temperature profiles

Figure 4.2 shows the computed concentration and temperature profiles along the five MBTSA sections, where the left and right limits of the plot correspond to the bottom of the cooling section and the top of the adsorption section, respectively. In agreement with this representation, the adsorbent flows from the right to the left in each section and the feed gas flows from the left to the right within the adsorption section.

Table 4.4: MBTSA design and process parameters.

Operating conditions		
Sorbent regeneration temperature	184	°C
Sorbent cooling temperature	18	°C
CO_2 extraction pressure	90	kPa
Inlet gas sup. velocity	0.41	m/s
Void fraction in adsorption section	0.7	-
Void fraction in other sections	0.5	-
System dimensions		
Diameter in adsorption section	12.8	m
Diameter in other sections	13.3	m
Height of adsorption section	0.9	m
Height of preheating section	0.4	m
Height of desorption section	0.8	m
Height of precooling section	0.4	m
Height of cooling section	0.6	m
Total height	3.1	m
Sorbent inventory		
Amount of circulating sorbent	650	kg/s
Sorbent mass flux in heat exchangers	4.7	kg/m^2s
Sorbent residence time	4.2	min
Heating/cooling fluids		
Specific heat capacity	4.2	kJ/kg K
Density	1000	kg/m^3
Flow rate in preheat./precool. sections	160.6	kg/s
Flow rate in desorption section	267.6	kg/s
Flow rate in cooling section	267.6	kg/s
Inlet temperature in desorption section	187	°C
Inlet temperature in cooling section	10	°C

As seen in the adsorbent loading profile within the adsorption section, a significant amount of nitrogen is also adsorbed along with the CO_2. This is in agreement with the adsorption equilibrium data and corresponding selectivity, which was estimated to be as low as 11. More specifically, at the bottom end of the adsorption section, i.e., at the gas feeding point, the fraction of nitrogen in the adsorbed phase is approximately 39% of the total, corresponding to a specific loading around 0.26 mol/kg, versus a CO_2 loading of 0.42 mol/kg. Furthermore, as seen in the temperature profile of the adsorption section, the effect of the heat

of adsorption is modest and causes an increase in the adsorbent temperature of about 9 °C. As expected, in the adsorption section the maximum temperature is reached at the gas feeding point, where the adsorption driving force is the highest. The reason for the limited impact of this non-isothermal effect can be attributed to the high sorbent-to-gas ratio associated to the low adsorption capacity.

Most of the adsorbed nitrogen is released from the adsorbed phase as the temperature increases along the preheating section, i.e., moving from right to left along the plot, while the CO_2 loading remains approximately constant due to its stronger affinity on the adsorbent. The gas that is being desorbed within the preheating section is removed from the top and re-mixed with the feed gas (see Figure 2.1). As the N_2 is removed, and the adsorbent temperature increases, the CO_2 fraction in the gas phase gradually increases towards the bottom end of the preheating section. The same trend continues in the desorption section, where the adsorbent temperature is further increased to the target regeneration temperature (184 °C) and CO_2 molar fraction in the gas phase reaches a maximum value of 97.2 % at the bottom end of the section, i.e., the CO_2 extraction point.

As depicted in Figure 4.2, the adsorbent still contains a certain amount of CO_2 (about 0.07 mol/kg) when entering the following section for precooling. To further regenerate the adsorbent and recover this CO_2, a fraction of the CO_2-free product (approximately 15% of the total flow rate on a weight basis) was used to counter-currently purge the adsorbent within the cooling and precooling sections. The use of this purge gas is also important to avoid the formation of low pressure zones induced by the decrease in temperature, thus maintaining the pressure close to atmospheric.

In addition to the gas and sorbent temperature profiles, the bottom plot in Figure 4.2 also shows the temperature of the heating and cooling fluids along the corresponding sections. In an attempt to maximize the internal heat recovery, the flow rate of the heat transfer media was tuned so that its heat capacity rate was as close as possible to that of the sorbent-gas side and the temperature difference along the heat exchanger was approximately constant.

4.4.2 Overall system performance

The MBTSA process was evaluated in terms of the performance indicators defined in Section 2.2, and the results are reported in Table 4.5. In spite of the low adsorbent selectivity, the designed MBTSA process was able to meet the desired target performance in terms of purity and capture rate, the obtained values being 97.2% and 90.8%, respectively. With regards to the energy use, the process requires 5.7 MJ/kg_{CO_2}, which is higher than other values reported in the literature for TSA capture processes achieving high CO_2 purity and recovery. For example, a value of 4.28 MJ/kg_{CO_2} has been reported for a heat-integrated fixed bed TSA system employing zeolite 13X (Joss et al. 2017), while Merel et al. (2008) estimated 4.5 MJ/kg_{CO_2} when using zeolite 5A. A slightly lower value (3.59 MJ/kg_{CO_2}) was

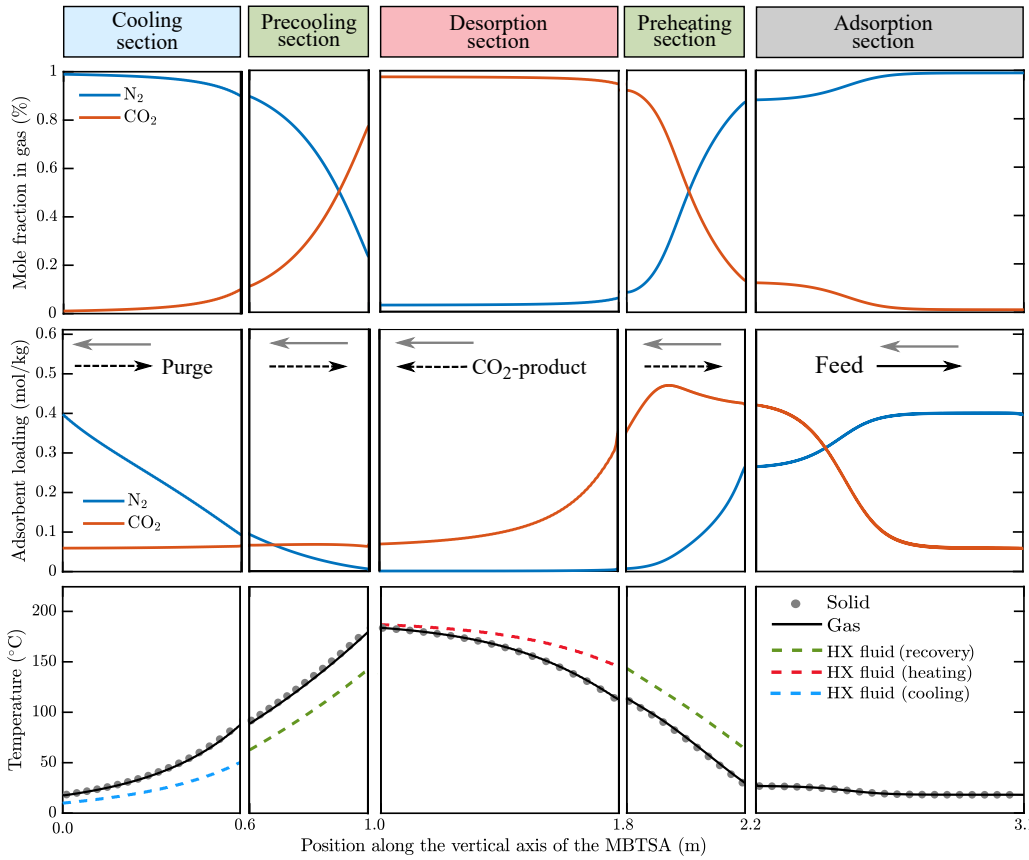

Figure 4.2: Concentration and temperature profiles for each section of the MBTSA system. Position 0 m corresponds to bottom of the cooling section and position 3.1 m to the top of the adsorption section. The black and gray arrows represent the direction of the gas and sorbent flows, respectively.

reported by Plaza et al. (2017) referring to a TSA system based on structured carbon adsorbent and steam stripping. Nevertheless, the specific energy duty estimated in the present study is approximately three times higher than that of a similar MBTSA process previously documented by the authors (Mondino et al. 2019), where zeolite 13X was employed to capture CO_2 from a natural gas combined cycle (Mondino et al. 2019). The relatively higher energy duty can be explained by the much lower working capacity of the activated carbon (0.36 mol/kg) compared to that of the zeolite (2.8 mol/kg) which implies larger sorbent inventory and contributes to the parasitic duty associated to the sorbent heat capacity. In addition, to compensate for the low adsorption capacity towards CO_2, a high desorption temperature was adopted, which also leads to an increase in the process energy requirement.

On the other hand, the simulated process seems to be very promising in terms of productivity, the obtained value being 181 $kg_{CO_2}/t_s h$. Such high process pro-

Table 4.5: Summary of the waste-to-energy simulations results.

Main performance indicators		
CO_2 purity	97.2	%vol
CO_2 capture rate	90.8	%vol
CO_2 captured	8.26	kg/s
Sorbent flow rate	650	kg/s
Process productivity	181	$kg_{CO_2}/t_s h$
Specific energy duty	5.7	MJ/kg_{CO_2}
Heat loads in MBTSA sections		
Preheating (internal recovery)	54.2	MW
Desorption (external heating)	47.0	MW
Precooling (internal recovery)	54.2	MW
Cooling (external cooling)	45.8	MW

ductivity can be attributed to the short cycle time (4.22 min) associated with the fast heating and cooling of the adsorbent. For comparison, Bonjour and coworkers calculated a productivity of 22.4 $kg_{ethane}/t_s h$ for a fixed bed TSA process with indirect heating for gaseous pollutant treatment (Bonjour et al. 2005). In the context of post-combustion CO_2 capture, Plaza et al. (2017) reported a productivity of 35-40 $kg_{CO_2}/t_s h$ when using carbon honeycomb monoliths in a fixed bed process with direct heating, while Joss et al. (2017) obtained a productivity between 30 and 60 $kg_{CO_2}/t_s h$ for an indirect heated TSA process using zeolite 13X achieving similar performance in terms of energy consumption (about 4 MJ/t_{CO_2}), purity (above 95%), and capture rate (above 90%).

4.5 Chapter summary

The application of the MBTSA technology for CO_2 capture from a waste-to-energy power plant was evaluated via process simulations. Input model parameters concerning the adsorbent material were provided by experimentally measuring the adsorption isotherms of a bead-shaped activated carbon. The designed MBTSA process is able to meet the target performance in terms of CO_2 purity (above 95%) and recovery (above 90%). With regards to the energy use, the proposed precooling/preheating sections for internal heat recovery leads to a 53.5% energy saving, reducing the total heat load from 101.3 MW to 45.8 MW. The rather high specific energy duty (5.7 MJ/kg_{CO_2}) can be attributed to the poor performance of the adsorbent in terms of CO_2 working capacity and selectivity. In this respect, significant improvements can be expected by employing adsorbents with higher adsorption capacity towards CO_2 and better selectivity, such as zeolite 13X or MOFs. Furthermore, despite of the large amount of sorbent required,

the obtained system footprint is within reasonable values: the largest diameter among the different MBTSA sections was 13.3 m while the total height of the system was 3.1 m. Particularly promising are the results in terms of process productivity, which was found to be significantly higher than reference values from existing literature, thanks to the short cycle time.

Chapter 5

NGCC case study using Z13X

The present chapter considers the utilization of the MBTSA technology for CO_2 capture as alternative to the commercial absorption-based technologies in the context of NGCC power plants. The adsorbent material employed for this application is a commercially available zeolite 13X. Adsorption equilibrium data of CO_2 and N_2 on the selected adsorbent were determined experimentally and then fitted with a Virial model. After that, the MBTSA system was designed to achieve high CO_2 purity and capture rate, and a series of simulations was carried out to investigate the system behavior under different operating conditions. Furthermore, the effect of implementing the MBTSA process on plant performance was studied by integrating the capture system with a process model of the reference power plant. A detailed analysis of the energy use associated with the capture process auxiliaries was performed. Finally, the power plant model was used to simulate the same NGCC system coupled with a state-of-the-art absorption process, for a direct comparison between the two capture technologies.

5.1 Definition of the case study

The case study considered in this chapter is a natural gas combined cycle power plant with a net power output of nearly 800 MW. The power plant was initially modelled in the GT PRO software (Thermoflow Inc. 2017) to provide the MBTSA model with the input flue gas specifications.

As illustrated in Figure 5.1, the reference NGCC power plant is composed of a topping gas turbine cycle coupled with a bottoming steam cycle. The system was designed with the aim of representing the current state-of-the-art technology in combined cycles, which are engineered to achieve net efficiencies exceeding 63% (Vandervort 2018). For this purpose, a General Electric 9HA.02 model fueled by natural gas was adopted for the Gas Turbine (GT). In addition, a three-pressure-level cycle configuration with reheat was employed for the steam bottoming cycle. As a common measure to increase the power plant efficiency (Fernandez et al.

Part of the content of this chapter also is reported in G. Mondino, C. A. Grande, R. Blom, and L. O. Nord (2019). "Moving Bed Temperature Swing Adsorption for CO_2 Capture from a Natural Gas Combined Cycle Power Plant". *International Journal of Greenhouse Gas Control* 85, pp. 58–70

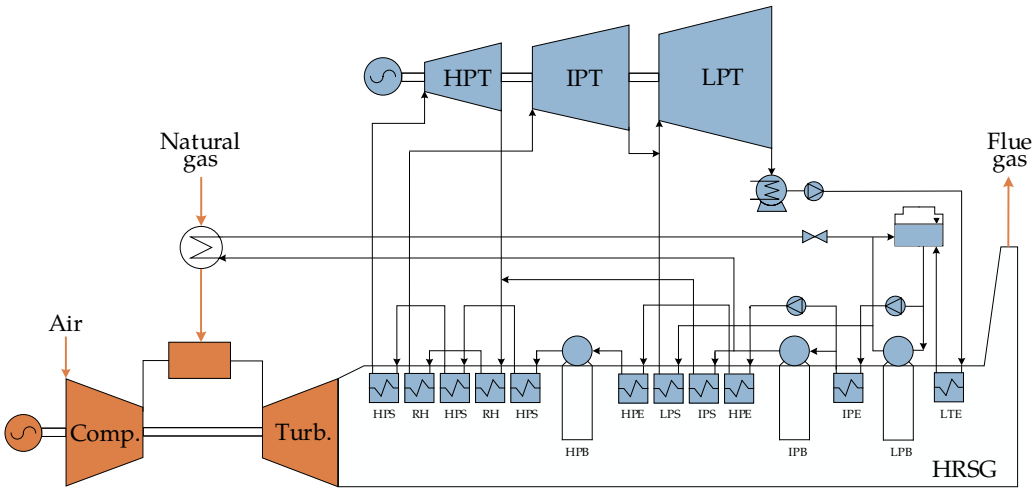

Figure 5.1: Layout of the reference NGCC power plant without CCS. The following abbreviations are used: Comp. for compressor section in gas turbine, Turb. for turbine section in gas turbine, HPT, IPT and LPT for high, intermediate and low pressure steam turbines, respectively, HRSG for heat recovery steam generator, HPS, IPS, LPS for high, intermediate and low pressure superheaters, respectively, HPE, IPE, LPE for the corresponding economizers, HPB, IPB and LPB for the boilers, and RH for the reheater.

2014; Anantharaman et al. 2011), the gas turbine fuel is preheated prior the combustor with part of the steam produced in the intermediate pressure (IP) drum. The main operating conditions and performance parameters of the NGCC are summarized in Table 5.2.

In order to reduce the computational effort of the MBTSA simulations, the composition of the NGCC exhaust gas obtained from the GT PRO model was simplified to a binary mixture of N_2 and CO_2. For this purpose the following assumptions were made: (i) O_2 and Ar present a similar behavior to N_2 with respect to adsorption equilibrium and kinetics (Baksh et al. 1992; Park et al. 2006; Merel et al. 2008) and (ii) the water vapor is removed prior the MBTSA unit. The resulting flue gas specifications, used as input for designing and simulating the MBTSA process, are listed in Table 5.1.

5.2 Adsorbent material

Besides reducing the computational effort of the MBTSA simulations, another reason for considering a dried flue gas is to allow the use of highly selective materials that are incompatible with the presence of water (e.g., zeolites or metal organic frameworks). For the purpose of this study, it was therefore possible to employ a commercial zeolite 13X adsorbent, which is suitable for the NGCC case due to its high CO_2 adsorption capacity at low CO_2 partial pressures and high

Table 5.1: Flue gas specifications adopted for the MBTSA simulations.

Parameter	Value	Unit
Mass flow rate	916	kg/s
Temperature	30	°C
Pressure	1.05	bar
Simplified composition:		
molar fraction of CO_2	5.15	%
molar fraction of N_2	94.85	%

CO_2/N_2 selectivity (Zanco et al. 2018; Hefti et al. 2015; Lillia et al. 2018; Merel et al. 2008). A summary of the adsorbent physical properties used as input to the MBTSA process simulations is provided in Table 5.3. The size of the particles (700 μm diameter) was selected to be higher than few hundreds μm in order to avoid fluidization in the adsorption section of the moving bed, where large flow rates move counter-currently to the adsorbent (Zanco et al. 2018).

In order to provide the MBTSA model with the necessary equilibrium data, the zeolite 13X was characterized in terms of pure-component adsorption isotherms of CO_2 and N_2. The measurements were performed in a volumetric apparatus (Belsorp Max, MicrotracBEL) at seven different temperatures in the range from 10 to 180 °C, and pressures from zero to 1.05 bar. Prior to the measurements, the sample was pre-treated at 320 °C under vacuum for 10 hours to remove any presence of moisture and other impurities.

The results of CO_2 and N_2 isotherms measurements are shown in Figure 5.2. As expected, the adsorption capacity of CO_2 is significantly higher than that of N_2 in the whole temperature and pressure ranges examined. At 30 °C and 0.0515 bar, which corresponds to the CO_2 partial pressure at the feed gas conditions, the equilibrium capacity of CO_2 is 3.5 mol/kg. Conversely, the equilibrium capacity of N_2 at the feed gas conditions (30 °C and 0.996 bar) is only 0.4 mol/kg. This yields a selectivity s_{CO_2/N_2} of 169, which is significantly higher than that of the activated carbons analysed in Section 4.2. The confirmed high equilibrium selectivity of the zeolite 13X is beneficial for the MBTSA process, where high purity of the CO_2 product is desired.

The fitting of the pure-component isotherm data was performed following the same procedure described in Section 4.2 for the case of the activated carbon adsorbent. The values of the parameters obtained by fitting the isotherms with the pure-component Virial model are listed in Table 5.4. As shown in Figure 5.3, the heat of adsorptions obtained by the Virial fitting is in good agreement with the values obtained from the slope of the Van't Hoff plot, where the Henry's law constant are plotted against the reciprocal of temperature (Shen et al. 2010; Ruthven 1984; Yang 1987).

Table 5.2: Summary of technical data of the reference NGCC plant.

Gas cycle		
GT model	GE 9HA.02	–
Fuel type	Natural gas	–
Net fuel energy input	1257.3	MW
GT gross electric power output	555.3	MW
Fuel lower heating value	46280	kJ/kg
Fuel higher heating value	51237	kJ/kg
Fuel temperature at combustor inlet	180	°C
Fuel pressure at combustor inlet	39.29	bar
Fuel flow rate	27.17	kg/s
Air pressure at compressor inlet	1.013	bar
Air temperature at compressor inlet	15	°C
Air humidity at compressor inlet	60	%
Air flow rate	957	kg/s
GT inlet temperature	1504.5	°C
GT exhaust temperature	646.9	°C
GT exhaust pressure	1.051 bar	bar
GT exhaust gas flow rate	984.1	kg/s
Steam cycle		
Number of pressure levels	3	–
ST gross electric power output	246.5	MW
HP turbine inlet temperature	600	°C
HP turbine inlet pressure	186	bar
HP turbine inlet flow rate	126	kg/s
IP turbine inlet temperature	600	°C
IP turbine inlet pressure	30	bar
IP turbine inlet flow rate	142.9	kg/s
LP turbine inlet temperature	72.32	°C
LP turbine inlet pressure	0.3447	bar
LP turbine inlet flow rate	161	kg/s
Condenser pressure	0.0586	bar
Combined cycle		
Gross combined electric power output	801.8	MW
Net power output	792.8	MW
Net electric efficiency	63.05	%
CO_2 emitted	70.82	kg/s

Table 5.3: Adsorbent properties adopted for the MBTSA simulations.

Parameter	Value	Unit
Adsorbent type	Zeolite 13X*	–
Particle shape	Spherical beads	–
Particle diameter	0.70	mm
Particle density	924	kg/m^3
Particle porosity	0.34	–
Heat capacity	880	kJ/kg K

* Provided by CWT (Germany)

Table 5.4: Virial model parameters fitting CO_2 and N_2 adsorption isotherms on zeolite 13X at temperatures between 10 and 180 °C and pressures between 0 and 1.05 bar.

	K_H^∞ mol/kg bar	$-\Delta H$ kJ/mol	A_0 kg/mol	A_1 K kg/mol	B_0 kg^2/mol	B_1 $K\,kg^2/mol^2$
CO_2	1.61935×10^{-5}	44.7838	0.4220	7.8371	−0.0485	34.8669
N_2	5.48207×10^{-5}	22.6591	−13.037	3889.5	24.9613	−7213.8

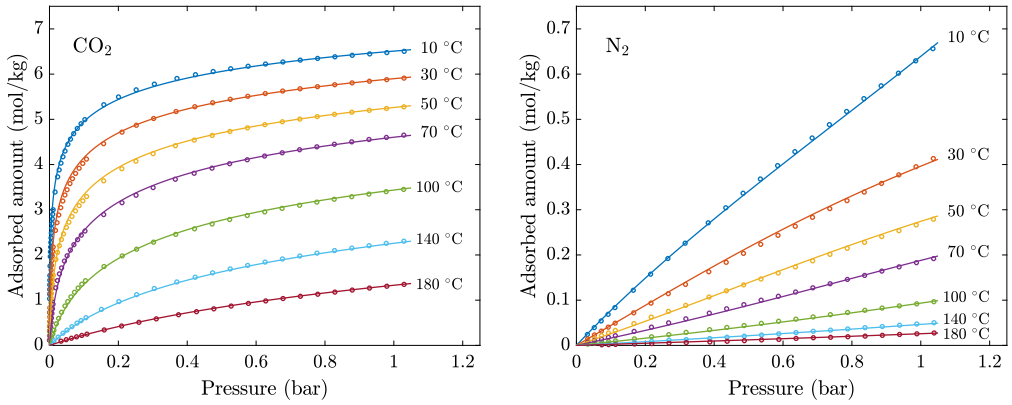

Figure 5.2: CO_2 (left) and N_2 (right) adsorption isotherms on zeolite 13X at temperatures between 10 and 180 °C, and pressures up to 1.05 bar: experimental values (symbols) and fitting with Virial model (lines).

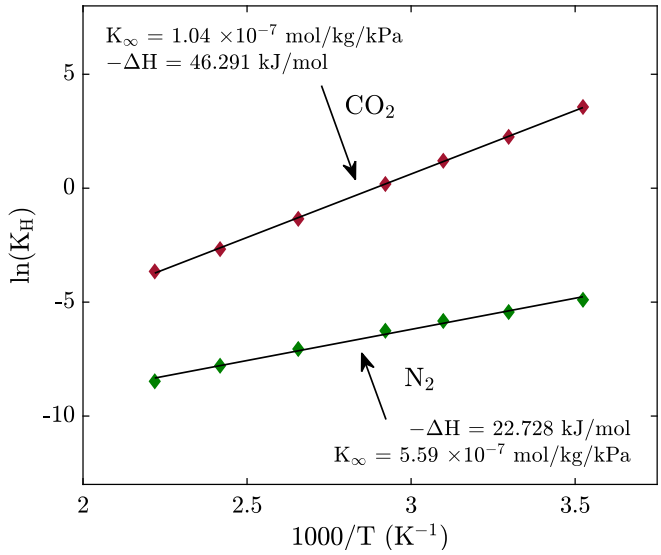

Figure 5.3: Van't Hoff plot for estimation of isosteric heat of adsorption.

5.3 Design of the MBTSA process

This section describes the design an MBTSA process to separate the CO_2 from the flue gas of the reference NGCC plant. The design was carried out targeting at a CO_2 purity of at least 95% and a capture rate higher than 90%, as typically considered for transport and storage application (Nord et al. 2020; Joss et al. 2017; Plaza et al. 2017).

The system was simulated using an earlier version of the MBTSA model documented in Chapter 2 that only takes into consideration four sections (i.e., adsorption, preheating, desorption and cooling). The main difference of this model version is that it does not include the energy equations of the heat transfer fluid, Eq. (2.13), and the heat exchanger walls, Eq. (2.12). Instead, the temperature of the heat transfer surface along the vertical axis is imposed, and a constant value of the gas-to-wall convective heat transfer coefficient is assumed. Furthermore, as the equation of the heat transfer fluid is missing, the energy savings attainable by preheating the adsorbent with the heat recovered form the hot adsorbent entering the cooling section were evaluated by analysing the temperature profiles and heat loads. A graphical procedure was used for this purpose, whereby the hot and cold composite curves were plotted on an temperature-enthalpy diagram (Kim et al. 2013). The minimum amount of external heat required was estimated by moving the cold curve along the enthalpy axis so that a minimum temperature difference is ensured at the pinch point. Considering that a third heat transfer media is needed as intermediate fluid, a conservative value of 20 °C was assumed as the pinch-point temperature difference on both sides (hot and cold).

Table 5.5: Dimensions and operating conditions of the final MBTSA configuration.

	MBTSA section			
	Adsorption	Preheating	Desorption	Cooling
Length of the section (m)	1.5	2	9	12
Number of discretizations	200	100	400	200
Cross sectional area (m^2)	254.5	78.5	78.5	78.5
Hydraulic diameter (m)	0.04	0.10	0.10	0.08
Heat transfer coefficient (W/m^2K)	90	90	90	90
Inlet gas superficial velocity (m/s)	1.50			
Adsorbent residence time (s)	216	207	933	1244

The simulations of the MBTSA system were carried out using a second order Centered Finite Difference Method (CFDM) to discretize the axial coordinate of each section. The number of intervals employed to discretize the axial space domain was 200 for the adsorption and cooling sections, 100 for the preheating, and 400 for the desorption section. The space-discretized equations were integrated in time until steady state was reached, and all results presented herein refer to the steady-state solution.

As starting point for the design, the required adsorbent flow rate was initially estimated based on the CO_2 capacity of the zeolite 13X at the feed gas conditions and the corresponding flow of CO_2 that is to be captured. Due to the large amount of flue gas to be processed (over 900 kg/s) it was decided to employ two MBTSA units, as the gas velocity within the adsorption section must be kept below the minimum fluidization velocity and the size of the column should be limited to realistic values (Kim et al. 2013; Zanco et al. 2018). After that, a set of simulations was performed by varying several design parameters and operating conditions to improve the performance of the system until the target CO_2 purity and recovery were satisfied. The system dimensions and operating conditions adopted for the final configuration are listed in Table 5.5.

5.4 MBTSA simulation results

The MBTSA model was used to predict system behavior in terms of temperature and concentration profiles along the different sections. The simulation results were then used to assess the performance of the process on the basis of separation performance (CO_2 purity and capture rate), energy use and process productivity.

5.4.1 Concentration and temperature profiles

The results of the process simulations in terms of N_2 and CO_2 concentration profiles in each section of the MBTSA are shown in Figures 5.4 to 5.7. The corresponding temperature profiles, for both the gas and solid phases, are shown in Figure 5.8. In each of the figures the horizontal axis represents the position along the height of the corresponding MBTSA section, where the upper and lower limits of the axis corresponds to the top and bottom the section, respectively. The flow directions of gas and sorbent are also shown as green arrows on the plots for the sake of clarity.

In order to limit the increase in temperature caused by the high heat of adsorption of CO_2, which in turn reduces the capacity of the adsorbent, it was decided to operate the adsorption section similarly to the cooling section and remove heat from the sorbent using cooling water. Despite this measure, an increase in temperature of nearly 20 °C still occurs within the adsorption section, see Figure 5.8.

Thanks to the high equilibrium selectivity of the zeolite 13X, the adsorbent leaving the adsorption section contains a nearly negligible amount of N_2 in the adsorbed phase, which has a beneficial effect on the obtainable CO_2 purity. After leaving the adsorption section, the CO_2-loaded adsorbent is heated from 30 °C to approximately 90 °C in the preheating section. The change in temperature is accompanied by a change in the gas phase CO_2/N_2 ratio (see Figure 5.5), since part of the adsorbed CO_2 is released by the adsorbent. However, due to the high CO_2 adsorption capacity, even at high temperatures, the change in adsorbent loading within the preheating section is limited. This means that most of the desorption takes place in the desorption section, where the temperature is further increased to 207 °C. In order to direct the gas flow towards the CO_2 extraction line, and thus avoid upward gas flow within the desorption section, a slightly sub-atmospheric pressure (0.97 bar) is applied at the bottom of the section.

Due to the steepness of the CO_2 isotherm, the adsorbent loading of CO_2 is still significant at the exit of the desorption section (nearly 1 mol/kg). Part of this CO_2 can be removed from the adsorbent and recovered from the top of the cooling section by recirculating a small fraction of the CO_2-free gas to the cooling section (i.e., the purge stream indicated in Figure 2.1). If the gas recirculated through the cooling section is sufficiently small, the gas leaving from the top of the cooling section will contain mostly CO_2 and can be mixed with the CO_2-rich product without excessively reducing its purity.

Table 5.6: Summary of process design and simulation results for the two MBTSA cases.

	Case A	Case B
CO_2 purity	95.1%	95.8%
CO_2 capture rate	96.0%	98.2%
CO_2 working capacity	2.76 mol/kg$_{ads}$	3.28 mol/kg$_{ads}$
Amount of circulating sorbent	570 kg/s	490 kg/s
Regeneration temperature	180 °C	207 °C
Energy required for sorbent regeneration:		
- without heat integration	152.7 MW_{th}	158.7 MW_{th}
- with heat integration	101.2 MW_{th}	100.7 MW_{th}
Specific energy for sorbent regeneration:		
- without heat integration	2.21 MJ/kg$_{CO_2}$	2.24 MJ/kg$_{CO_2}$
- with heat integration	1.46 MJ/kg$_{CO_2}$	1.42 MJ/kg$_{CO_2}$

5.4.2 Overall system performance

The MBTSA process was evaluated in terms of the performance indicators defined in Section 2.2, and the results are reported in Table 5.6. This analysis is presented for two cases employing different sorbent regeneration temperatures, namely 180 °C (Case A) and 207 °C (Case B). As expected, the system behavior is very sensitive to the regeneration temperature, as it directly affects the CO_2 working capacity and thus the amount of adsorbent required. A lower regeneration temperature, which is beneficial when considering heat integration using waste heat from the power plant, implies a less efficient regeneration of the sorbent and thus has to be compensated by increasing the amount of circulating sorbent. Better CO_2 purity and capture rate are obtained in the case of higher regeneration temperature (Case B), which also requires 16.3% less adsorbent. When comparing the total amount of thermal energy required, the case using lower regeneration temperature (Case A) seems to be more efficient. However, due to the difference in CO_2 capture rate, the specific energy consumption of the two cases in terms of energy required per unit mass of CO_2 captured does not differ significantly.

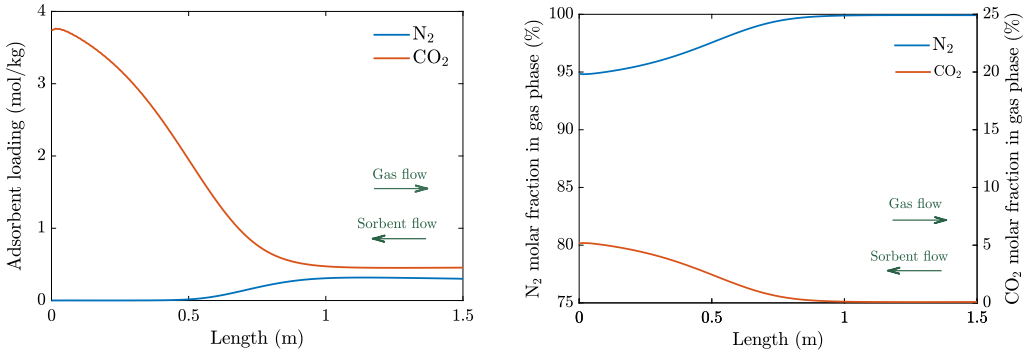

Figure 5.4: Adsorbent loading (left) and molar fraction (right) profiles along the vertical coordinate of the adsorption section.

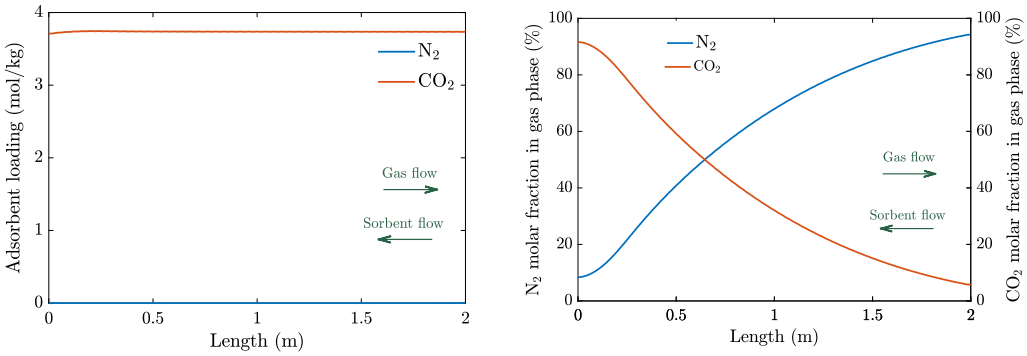

Figure 5.5: Adsorbent loading (left) and molar fraction (right) profiles along the vertical coordinate of the preheating section.

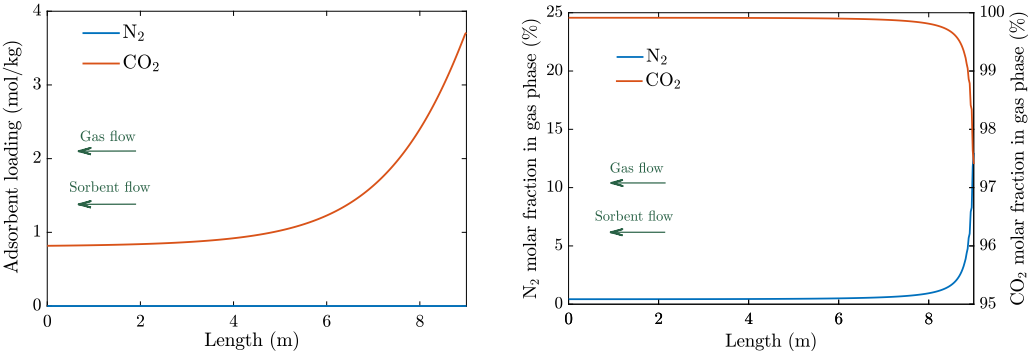

Figure 5.6: Adsorbent loading (left) and molar fraction (right) profiles along the vertical coordinate of the desorption section.

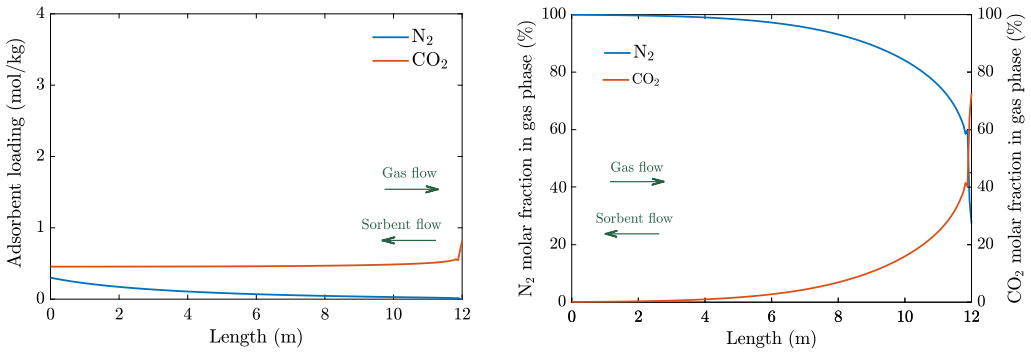

Figure 5.7: Adsorbent loading (left) and molar fraction (right) profiles along the vertical coordinate of the cooling section.

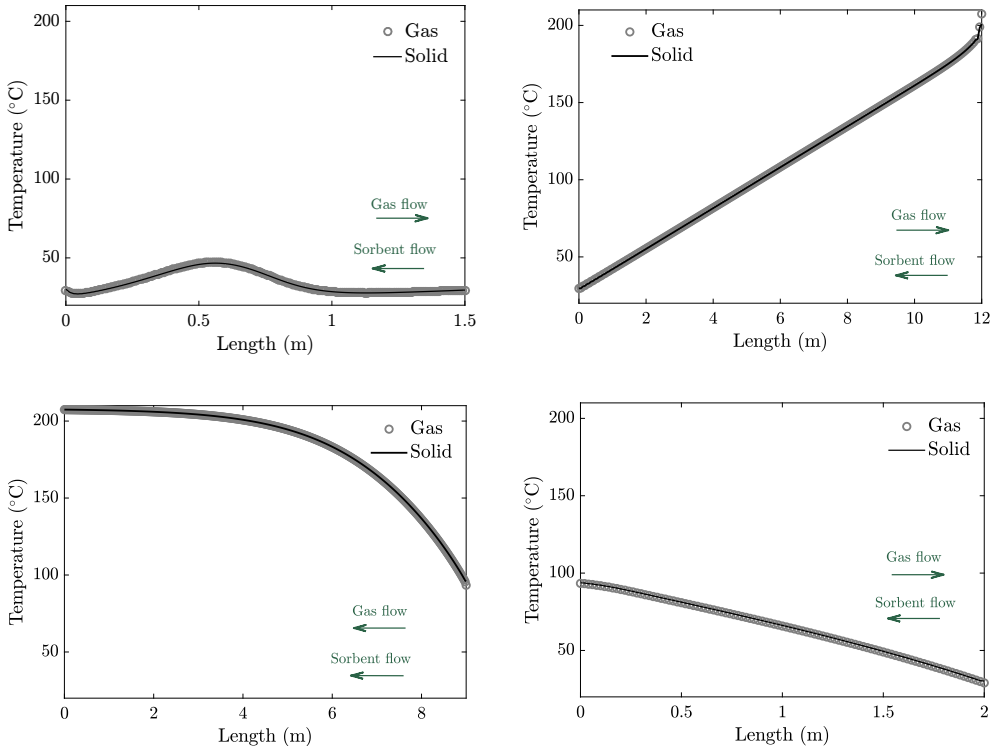

Figure 5.8: Temperature profiles along the vertical coordinate of: adsorption section (top left), cooling section (top right), desorption section (bottom left), cooling section (bottom right).

5.5 Integration of NGCC with capture processes

The last part of this chapter concerns the integration of the proposed MBTSA process with the reference NGCC power plant. First, the approach followed to link the power plant with the MBTSA system and supply the heat required for sorbent regeneration is described. After that, the reference power plant is coupled with an absorption-based process to benchmark the MBTSA system against the state-of-the-art capture technology. Finally, the simulation results comparing the two technologies in terms of their impact on the power plant efficiency are presented.

5.5.1 Integration with MBTSA process

In order to evaluate the impact of the CO_2 capture system on the power plant efficiency, the NGCC model initially developed in GT PRO was exported into Thermoflex and appositely modified to accommodate the capture process. The layout of the NGCC power plant integrated with the MBTSA system is shown in Figure 5.9. The main modifications with respect to the reference case (i.e., the NGCC plant without CO_2 capture, see Figure 5.1) include: (i) the extraction of steam from the IP turbine, needed in the MBTSA for sorbent regeneration, (ii) a drying unit, employed for removing water from the flue gas upstream the MBTSA, (iii) a compressor/fan compensating for the pressure drops of the MBTSA, (iv) an inter-cooled compressor to rise the pressure of the CO_2-rich stream to meet transport specifications, (v) a cooling water circuit that takes into account the cooling demand of the MBTSA system.

The steam extracted from the IP turbine is processed by an indirect-contact, counter-current heat exchanger that mimics the desorption section of the MBTSA system, in terms of heat duty and inlet/outlet temperatures of the flowing sorbent. The condensed water leaving the heat exchanger is returned to the deaerator after appropriate pressure reduction. The amount of steam extracted and the corresponding pressure will therefore be determined based on the heat exchanger duty, while assuring that the condensed outlet temperature corresponds to the deaerator operating temperature. A similar approach is used for simulating the cooling section of the MBTSA process. In this case, cooling water available at the plant side is used to provide the required cooling duty.

The flue gas drying unit consists of three components: (i) a gas-water contact heat exchanger where the flue gas is cooled to 30 °C, (ii) an electric chiller that further reduces the temperature of the flue gas to 16 °C, and (iii) a fan placed upstream the gas-water contact heat exchanger, for overcoming the pressure drops of the drying steps. The flue gas leaving the drying units still contains a small amount of water (approximately 1.8 vol%), which should also be removed. Although this final step was not included in the present work, it was assumed that the remaining water can be removed in a process with limited energy consumption, applying the same approach described by Lillia et al. (2018), where the activated alumina used for adsorbing water is regenerated by the CO_2-free product.

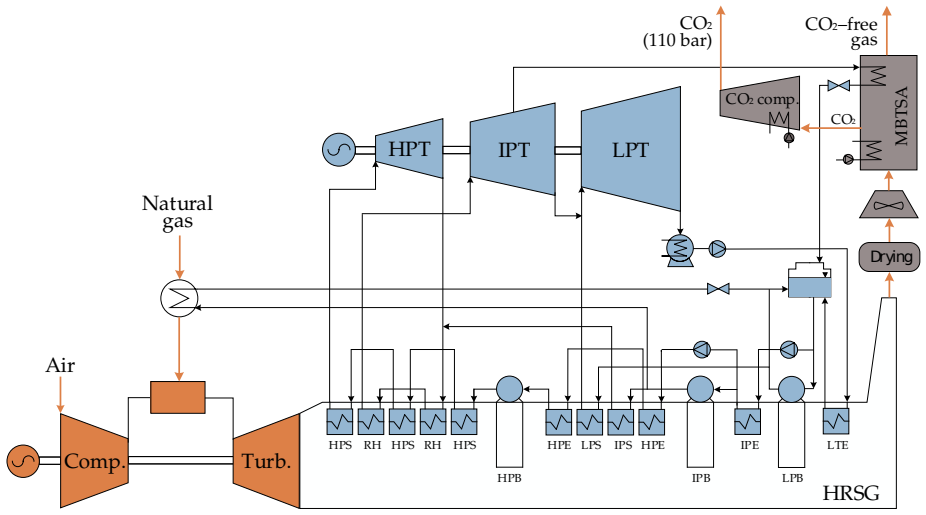

Figure 5.9: Layout of the reference NGCC power plant integrated with the MBTSA process. Comp. for air compressor, Turb. for gas turbine, HPT, IPT and LPT for high, intermediate and low pressure turbines, respectively, HRSG for heat recovery steam generator, HPS, IPS, LPS for high, intermediate and low pressure superheaters, respectively, HPE, IPE, LPE for the corresponding economizers, HPB, IPB and LPB for the boilers, and RH for the reheater.

Lastly, the CO_2 compressor consists of five inter-cooled stages with an isentropic efficiency of 85% for each stage. The inlet conditions (i.e. gas composition, flow rate, temperature and pressure) are set based on the results obtained with the MBTSA simulations. The delivery pressure is assumed to be 110 bar.

5.5.2 Integration with MEA absorption process

One of the aims of this work is to provide a plant-level comparison of the MBTSA process considered in this thesis with the benchmark amine-based capture technology. For this purpose, the reference NGCC model was again exported to Thermoflex and modified to integrate a standard chemical absorption process using monoethanolamine (MEA) as solvent. The model of the absorption process is part of the Thermoflex library and it provides an estimate of the total auxiliary power, heat consumption, and cooling duty required by the process, as well as its impact on the combined cycle efficiency. The input model parameters used to define to MEA-absorption process are listed in Table 5.7. These specifications are representative of a typical MEA process with a specific energy input of 3.95 MJ/kg (Fernandez et al. 2014; Franco et al. 2011; Anantharaman et al. 2011).

Similarly to the the MBTSA system, the implemented absorption process requires a certain amount of heat for solvent regeneration. The regeneration of the solvent takes place in the reboiler, and the heat required is usually provided by condensing steam at a temperature near the boiling temperature of the solvent.

Table 5.7: Specification of the MEA capture process.

Parameter	Value	Unit
Cooler exit temperature	40	°C
CO_2 compressor inlet temperature	40	°C
CO_2 compressor inlet pressure	1.6	bar
CO_2 compressor delivery pressure	110	bar
Number of compressor stages	5	–
Booster fan isentropic efficiency	85	%
Booster fan mech.+ elec. efficiency	95	%
Pumps efficiency	75	%
Total gas pressure drop (in absorber)	0.1	bar
Steam pressure at reboiler inlet	3.05	bar
Steam temperature at reboiler inlet	134	°C
Solvent regeneration specific energy	3.95	MJ/kg

Following the same approach used by Fernandez et al. (2014), the steam required by the reboiler is extracted from the IP turbine and then further conditioned via pressure reduction and attemperation to meet the reboiler operating conditions. The condensate exiting the reboiler is pumped back to the feed water tank.

5.5.3 Results of the process integration

The main results of the NGCC power plant simulations are summarized in Table 5.8, where the following five cases are presented: (i) the NGCC without CO_2 capture as reference case, (ii) the NGCC coupled with a MEA capture process characterized by 90% capture rate, which corresponds to the minimum target process specification, (iii) the NGCC coupled with a MEA capture process with a 95% capture rate, for comparison with the MBTSA system, (iv) the NGCC integrated with the MBTSA case using 180 °C as regeneration temperature (previously referred as Case A), (v) the NGCC integrated with the MBTSA case using 207 °C as regeneration temperature (previously referred as Case B). By comparing the investigated cases, the table shows how the different capture systems affect the power plant performance in terms of net electric efficiency, including a detailed list of the energy use associated to the capture process and power plant auxiliaries.

While the gas cycle is not affected by the capture process, as its operating conditions remain unchanged, the steam cycle suffers from a reduction in power output due to the steam extraction used to satisfy the heat demand of the capture process. With regards to the MEA cases, low pressure steam is sufficient to provide the required heat, as the reboiler is operated at relatively low temperature (134 °C steam inlet temperature). On the contrary, the MBTSA process requires higher steam extraction pressures, depending on the sorbent regeneration temperature,

Table 5.8: Results of the NGCC power plant integration with the MBTSA and comparison with the MEA capture process.

	Without capture	MEA Case A	MEA Case B	MBTSA Case A	MBTSA Case B
Capture efficiency (%)	-	90.0	95.0	96.0	98.2
CO_2 captured (t/h)	-	229.4	242.2	243.2	248.8
CO_2 emitted (t/h)	253.4	23.9	11.2	10.1	4.6
Specific emissions (kg/MWh)	316.0	32.5	15.3	13.2	6.0
GT gross electric power output (MW)	555.3	555.3	555.3	555.3	555.3
ST gross electric power output (MW)	246.5	182.2	178.5	214.8	211.3
Gross power output (MW)	801.8	737.5	733.9	770.1	766.7
Net power output (MW)	792.7	693.1	688.1	692.9	689.0
Net electric efficiency (% LHV)	63.1	55.1	54.7	56.2	55.9
Details on the steam extraction:					
Steam extraction temperature (°C)		292	292	395	465
Steam extraction pressure (bar)		3.62	3.62	8.17	13.16
Steam extracted flow (kg/s)		106.8	101.2	38.0	35.9
Heat input (MW)		251.7	265.7	101.2	100.7
Detailed plant auxiliaries:					
Gas turbine auxiliaries (MW)	1.071	1.071	1.071	1.071	1.071
Condenser c.w. pump (MW)	0.728	0.423	0.384	0.559	0.569
Condensate forwarding pump (MW)	0.419	0.162	0.147	0.322	0.327
HP feedwater pump (MW)	4.604	4.609	4.609	4.605	4.605
IP feedwater pump (MW)	1.317	1.316	1.316	1.316	1.316
Steam turbine auxiliaries (MW)	0.518	0.383	0.375	0.451	0.444
Miscellaneous auxiliaries (MW)	0.401	0.369	0.367	0.385	0.383
Total CO_2 capture auxiliaries (MW)	0	36.090	37.459	54.493	54.728
Total plant auxiliaries (MW)	9.057	44.422	45.729	63.246	63.490
Detailed CO_2 capture auxiliaries:					
Booster fan(s) (MW)		10.827	10.827	10.023	10.008
Electric chiller (MW)				15.330	15.330
Intercooled compressor (MW)		20.479	21.617	28.824	29.077
Cooling water pump (MW)		2.165	2.252	0.316	0.315
Solvent circulation pump (MW)		1.973	2.082		
Condensate pump (MW)		0.014	0.015		
Others (MW)		0.632	0.667		

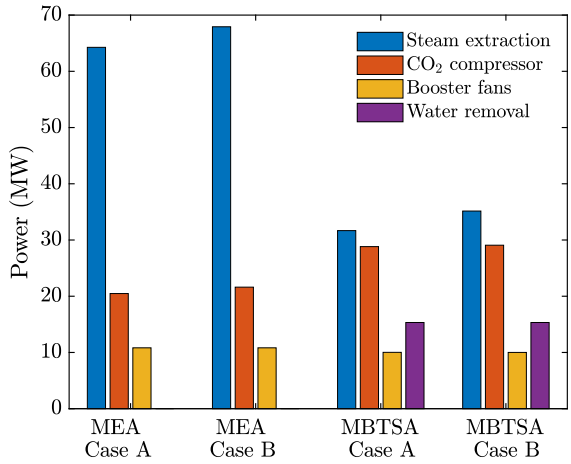

Figure 5.10: Individual contribution to the overall duty of the four capture processes.

in order to ensure that the minimum pinch point within the heat exchanger is satisfied. Although the MEA process requires steam at lower pressure, which is beneficial for the steam cycle performance, the total amount of heat to be provided by the steam is 2.5 times higher than for the MBTSA process.

The overall reduction in power output due to steam bleeding is smaller for the MBTSA than for the MEA process, confirming that the thermal energy requirement for regeneration is a crucial process parameter to consider when selecting a capture technology (Fernandez et al. 2014). However, when comparing the net electric efficiency of the power plant, no significant difference is observed between the two technologies. In particular, a reduction of about 7 and 8 percentage points is caused by the integration of the MBTSA and the MEA processes, respectively. The reason for this is the higher energy required by the CO_2 capture auxiliaries of the MBTSA. In this respect, the higher energy consumption of the MBTSA is associated mainly to: (i) the use of the electric chiller for water removal and (ii) the CO_2 compressor, which uses approximately twice as much energy compared to the MEA case due to the lower CO_2 inlet pressure and the higher inlet temperature (180 °C, against 40 °C for the MEA process). A graphical representation of how the individual factors contribute to the total reduction in the net electric efficiency for each case is shown in Figure 5.10. In this figure, the power loss due to steam extraction is calculated as the difference between the power output of the steam turbine in the reference NGCC without CO_2 capture and the NGCC with the corresponding capture system.

In terms of net electric efficiency, the values obtained for the MEA process are in line with the results of similar studies available in literature (Lillia et al. 2018; Fernandez et al. 2014). In particular, Fernandez et al. (2014) estimated an 8.4 percentage points reduction, versus the 8.0 and 8.4 of this study, corresponding to MEA cases A and B, respectively. As expected, the higher energy penalty

is associated to the MEA process with the higher capture rate (Case B). By increasing the capture rate, the heat input of the extracted steam also increases, with a negative effect on the power output.

With respect to the MBTSA processes, better performance in terms of net electric efficiency is obtained for Case A, in which the steam extracting pressure is lower, with a beneficial effect on the power output of the steam turbines. Despite the worse performance in term of net electric efficiency, Case B of the MBTSA process outperforms the other four cases evaluated with regards to the amount of CO_2 emitted by the power plant.

5.6 Chapter summary

The application of the MBTSA technology for CO_2 capture from a NGCC power plant was evaluated. The performances of the MBTSA process in terms of CO_2 capture rate and CO_2 purity were assessed via dynamic simulations performed in gPROMS software. Input model parameters concerning the adsorbent material were provided by experimentally measuring adsorption isotherms on a pelletized sample of zeolite 13X. When designing the MBTSA process, two cases employing different regeneration temperatures (180 °C for Case A and 207 °C for Case B) were compared. In both cases the proposed system was able to meet the process target specifications. In particular the obtained CO_2 purities were 95.1% and 95.8% for Case A and Case B respectively, with corresponding capture rates of 96.0% and 98.2%. Based on the performed MBTSA simulations, the thermal energy required for sorbent regeneration was also estimated. Promising results are obtained when considering internal heat recovery, through which approximately 35% of the total energy required can be saved.

In addition, a more comprehensive analysis of the energy consumption associated to the CO_2 capture process was performed by implementing a Thermoflex model of the NGCC integrated with the capture process. Besides accounting for the effect of steam extraction on the overall power plant performance, the developed model allows a detailed analysis of the energy penalties associated to the various CO_2 capture auxiliaries (e.g., booster fans, CO_2 compressor, and electric chiller for water removal from flue gas). For the sake of comparison, the application of a benchmark absorption-based capture system was also considered by suitably modifying the Thermoflex model of the reference NGCC. Interestingly, no significant difference is observed in terms of overall power plant efficiency between the proposed MBTSA system and the MEA process. More specifically, the overall power plant efficiency decreases from 63.1% to 55.1% for the case of the MEA, and from 63.1% to 56.2% when applying the MBTSA capture process. While the MBTSA requires less steam when compared to the MEA system, the latter presents a lower energy penalty associated to the CO_2 capture auxiliaries, compensating the higher effect associated to steam extraction.

Chapter 6

Comparison of MOF CPO27-Ni and zeolite 13X

Metal-organic frameworks (MOFs) are a class of microporous materials with the potential to improve the performance of adsorption-based separation technologies, compared to more traditional materials such as activated carbons and zeolites (Hefti et al. 2016; Danaci et al. 2020; Mondino et al. 2020). The large structural and chemical diversity of MOFs make them suitable for a wide variety of potential applications, including gas storage (Rosi et al. 2003; Morris et al. 2008), gas separation (Bastin et al. 2008; Agueda et al. 2015; Adil et al. 2017), heat pumps and chillers (De Lange et al. 2015; Teo et al. 2018), and catalysis (Jiao et al. 2018). Yet, the use of MOFs is negligible commercially, partly due to upscaling and cost issues, and on the more technical side, lack of testing of shaped MOFs under realistic conditions (Hefti et al. 2016; Mondino et al. 2020).

In the context of CO_2 capture, the potential of MOFs has been explored in a number of recent studies focusing on fixed bed PSA (Danaci et al. 2020; Masala et al. 2017a) and TSA cycles (Hefti et al. 2016; Mason et al. 2011; Zhang et al. 2014). However, to the knowledge of the author, the use of MOFs for MBTSA post-combustion capture processes has not been documented yet. In view of this knowledge gap, the objective of this chapter is to evaluate the suitability of a novel adsorbent material, namely the CPO-27-Ni MOF, as a candidate for MBTSA capture processes.

The analysis is carried out considering the same NGCC case study described in the previous chapter. First, the adsorption equilibrium properties of the CPO-27-Ni are determined experimentally and fitted with the Virial model. The fitted isotherm parameters are then used as input to design an MBTSA process for the given flue gas specifications. The proposed MBTSA system is evaluated in terms of different performance parameters, including CO_2 purity and recovery, system footprint, and energy duty. After that, the MBTSA process is integrated with the model of the reference NGCC power plant to analyze how the presence of the

Part of the content of this chapter also is reported in G. Mondino, A. I. Spjelkavik, T. Didriksen, S. Krishnamurthy, R. E. Stensrød, C. A. Grande, L. O. Nord, and R. Blom (2020). "Production of MOF Adsorbent Spheres and Comparison of Their Performance with Zeolite 13X in a Moving-Bed TSA Process for Postcombustion CO_2 Capture". *Industrial & Engineering Chemistry Research* 59.15, pp. 7198–7211

capture system affects the performance of the power plant. Finally, the results obtained for the CPO-27-Ni adsorbent are compared with those obtained with the zeolite 13X and benchmarked against the state-of-the-art MEA capture process.

6.1 Adsorbent material

The adsorbent material considered in this chapter is a CPO-27-Ni metal organic framework (MOF) synthesized at SINTEF laboratories in Oslo. The material was produced in the form of spherical beads with a suitable size for MBTSA systems, as depicted in the Scanning Electron Microscopy (SEM) pictures of Figure 6.1. The physical properties of the adsorbent used as basis for the MBTSA process simulations are summarized in Table 6.1. Further details about the synthesis, shaping and characterization of the adsorbent are available in Mondino et al. (2020) and references cited therein.

In order to provide the MBTSA model with the equilibrium properties of the material, the adsorption isotherms of CO_2 and N_2 on the CPO-27-Ni MOF were measured and fitted with a suitable adsorption isotherm model as described below. The pure-component equilibrium data were collected from zero to one bar

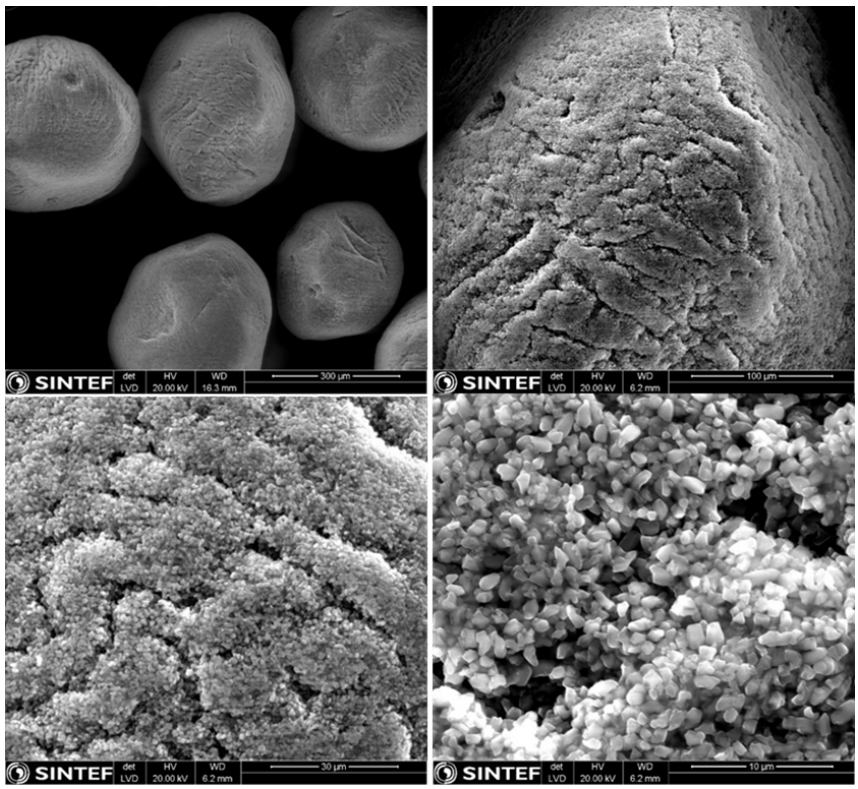

Figure 6.1: SEM pictures at increasing magnification of the CPO-27-Ni spheres.

Table 6.1: Adsorbent properties adopted for the MBTSA simulations.

Parameter	Value		Unit
Adsorbent type	CPO-27-Ni[a]	Zeolite 13X[b]	–
Particle shape	Spherical beads	Spherical beads	–
Particle diameter	0.70	0.70	mm
Particle density	739	924	kg/m^3
Particle porosity	0.38	0.34	–
Heat capacity	880	880	kJ/kg K

[a] Synthesized and shaped at Sintef (Norway)
[b] Provided by CWT (Germany)

at different temperatures between 30 and 120 °C using a commercial volumetric BELSORP Max instrument (BEL, Japan). Sample activation was carried out overnight with an external pretreatment unit (BELPREP II vac) at 120 °C under vacuum followed by a short pretreatment (2 hours) with the BELSORP Max instrument as part of the isotherm measurement procedure.

The results of adsorption equilibrium measurements on the CPO-27-Ni spheres are shown in Figure 6.2, where the isotherms of zeolite 13X at 30 °C are also included for the sake of comparison. The highest measured CO_2 uptake on the MOF (corresponding to 1 bar and 30 °C) is larger than that of the zeolite at the same conditions. However, the situation is reversed at low partial pressures (<0.2 bar), which are more relevant for post-combustion capture applications where the adsorption of CO_2 is typically carried out at low temperature and low CO_2 partial pressures. In particular, the CO_2/N_2 selectivity of the CPO-27-Ni at the feed gas conditions (calculated according to Eq. (4.4)) is significantly lower than that of the zeolite 13X (54 versus 169). On the other hand, CPO-27-Ni adsorbs significantly less CO_2 than zeolite 13X also at high temperatures and close-to-atmospheric pressure (i.e., at desorption conditions in a temperature swing cycle). This means that, for a given desorption temperature, a higher level of regeneration can be achieved with the MOF.

Figure 6.2 also shows the results of the fitting with the Virial model obtained by simultaneous nonlinear regression of the data in the whole temperature range. Details on the methodology used for isotherm fitting is provided in Section 4.2. The fitted parameters are listed in Table 6.2, where the corresponding values of the zeolite 13X are also reported for the sake of comparison. The obtained heat of adsorption of CO_2 is lower for CPO-27-Ni (37.4 kJ/mol) than for zeolite 13X (44.8 kJ/mol), which is beneficial in terms of limiting the energy requirement of the capture process. The estimated heat of adsorption for the CPO-27-Ni spheres is close to previously reported values of 38-39 kJ/mol for powder samples of the same material (Dietzel et al. 2009; Queen et al. 2014).

Table 6.2: Virial model parameters fitting the CO_2 and N_2 equilibrium isotherms for CPO-27-Ni and zeolite 13X adsorbents.

		CPO-27-Ni		Zeolite 13X	
		CO_2	N_2	CO_2	N_2
K_H^∞	mol/kg bar	2.000×10^{-5}	2.975×10^{-5}	1.619×10^{-5}	5.482×10^{-5}
ΔH	kJ/mol	-37.390	-25.867	-44.7838	-22.6591
A_0	kg/mol	-0.7550	-2.1534	0.4220	-13.037
A_1	K kg/mol	279.022	679.71	7.8371	3889.5
B_0	kg^2/mol^2	0.5048	0.000	-0.0485	24.9613
B_1	$K\,kg^2/mol^2$	-165.45	0.000	34.8669	-7213.8
C_0	kg^3/mol^3	-0.0406	0.000	–	–
C_1	$K\,kg^3/mol^3$	14.930	0.000	–	–

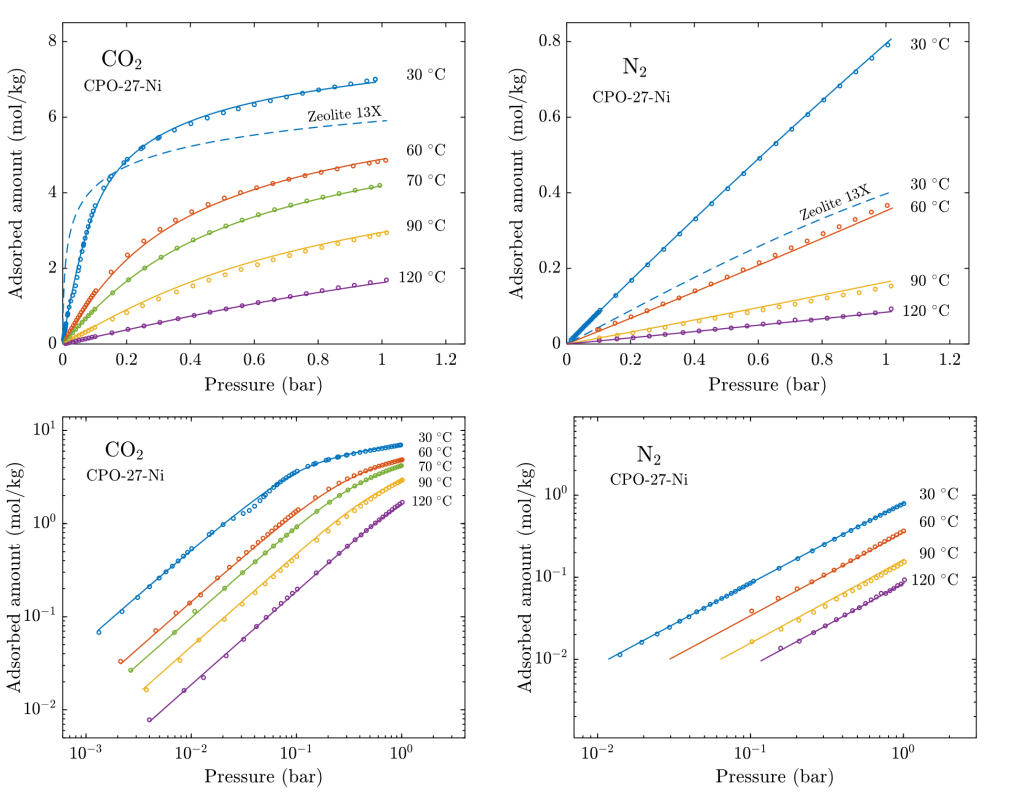

Figure 6.2: Adsorption isotherms of CO_2 and N_2 on CPO-27-Ni spheres in linear (top) and logarithmic scale (bottom).

6.2 Design of the MBTSA process

The objective of this section is to design an MBTSA capture system using the CPO-27-Ni MOF adsorbent. The case study considered is the same power plant analyzed Chapter 5, namely a 800 MW NGCC power plant with an exhaust gas flow rate of 916 kg/s containing 5.15%vol of CO_2 (see Table 5.1). The MBTSA process was simulated with the same modeling approach described in Section 5.3. In this case, the number of intervals used to discretize the axial space domain was 400 for the adsorption and desorption sections, 100 for the preheating, and 300 for the cooling section.

As basis for the design of the MBTSA with CPO-27-Ni, the process developed in Section 5.3 using zeolite 13X was taken as the initial configuration. A series of simulations was then performed by iteratively adjusting certain design parameters until the desired process performance was achieved. In this respect, a minimum of 95% CO_2 purity and 90% CO_2 capture rate were set as targets. Also in this case, the use of two MBTSA units was adopted due to the large amount of flue gas to be treated. The list of design parameters that were modified and the final values corresponding to the simulations presented in the following section are reported in Table 6.3. The values of the original parameters from the zeolite case are also reported in Table 6.3 for comparison.

In terms of constraints to be taken into account when adjusting the operating conditions, a major difference between the zeolite and the MOF cases concerns the choice of regeneration temperature; while no limitation was imposed in the zeolite

Table 6.3: Main design parameters and operating conditions used in the simulations of the MBTSA process. Values referred to a single MBTSA unit.

	CPO-27-Ni	Zeolite 13X
Height of adsorption section (m)	3.5	1.5
Cross sectional area in adsorption section (m^2)	254.5	254.5
Column void fraction in adsorption section (-)	0.8	0.8
Cross sectional area in other sections (m^2)	78.5	78.5
Column void fraction in adsorption section (-)	0.6	0.6
Height of preheating section (m)	3	2
Height of desorption section (m)	6	9
Height of cooling section (m)	10	12
Adsorbent residence time / cycle time (min)	25.7	43.3
CO_2 extraction pressure (bar)	0.97	0.97
Amount of circulating sorbent (kg/s)	350	245
Regeneration temperature (°C)	132	207

study, a temperature of 132 °C was set as the maximum desorption temperature for the CPO-27-Ni case to avoid potential degradation of the adsorbent. As suggested by the isotherm plots depicted in Figure 6.2, this means that the adsorbent will still contain a significant amount of CO_2 adsorbed (above 1 mol/kg) when leaving the desorption section. In other words, only part of the captured CO_2 will be recovered as a result of a temperature increase occurring within the desorption section. However, the remaining CO_2 can be recovered by further purging the adsorbent while traversing the subsequent cooling section. For this purpose, a small fraction (approximately 5%wt) of the CO_2-free product leaving the adsorption section is recirculated to the cooling section, where it flows counter-currently to the adsorbent inducing further desorption of CO_2, see Figure 2.1.

The flow of recirculated gas through the cooling section also serves to maintain the pressure inside the column close to atmospheric pressure, as the cooling of the adsorbent would otherwise promote adsorption of the surrounding gas, and thus a decrease in pressure in the bulk phase. As a result of this recirculation through the cooling section, a small gas stream (approximately 7%wt of the feed gas) containing a certain amount of CO_2 is released from the top of the cooling section. As seen in Figure 2.1 (dashed blue lines), the released gas is recycled and mixed with the flue gas feeding the adsorption section with the aim to the CO_2 recovery of the process. As a result of this measure, the CO_2 partial pressure in the feed gas is also increased. For simplicity, it is assumed that the recycled gas is cooled down to the feed gas temperature before mixing. A similar strategy was adopted in the zeolite case, with the difference that the gas released at the top of the cooling section (dashed black line in Figure 2.1) was directly mixed with the CO_2 product obtained from the desorption section, rather than being mixed with the feed gas.

6.3 Process simulation results

This section present the results of the MBTSA simulations in terms of: (i) temperature and concentration profiles along the adsorption, preheating, desorption and cooling sections and (ii) overall process performance indicators. In addition, the performance of the MBTSA systems designed for the CPO-27-Ni and zeolite 13X adsorbents is compared in terms of purity, recovery and energy use. Finally, the impact of the capture process on the performance of the reference NGCC power plant is analysed and compared against a MEA absorption process. To this purpose, the proposed MBTSA process was integrated with the NGCC power plant model following the methodology described in Section 5.5.

6.3.1 Concentration and temperature profiles

The simulation results in terms of concentration and temperature profiles along the height of each moving bed section are shown in Figures 6.3 to 6.6 and compared with the profiles obtained using zeolite 13X. One of the main differences between the two cases concerns the shape of the concentration profiles in the adsorption section. As CPO-27-Ni presents a more spread profile, it was necessary to increase the length of the adsorption to 3.5 m (versus the original 1.5 m of the zeolite case), leading to higher pressure drops. The reason for this is related to the difference in the CO_2 adsorption isotherms of the two adsorbents at the feed gas conditions, which are steeper for the zeolite.

Another difference that is noticeable in Figure 6.3 is the higher amount of N_2 co-adsorbing with CO_2 on CPO-27-Ni. This is a result of the lower equilibrium selectivity of CPO-27-Ni compared to zeolite 13X. However, this does not affect the purity of the CO_2 product because most the N_2 desorption occurs within the preheating section (Figure 6.4). Here, as the adsorbent moves downwards, it undergoes a first increase in temperature, which induces a shift in adsorption equilibrium. Most of the adsorbed N_2 is released to the gas phase and removed at the top of the section, while the CO_2 concentration in the gas phase increases without a significant change in the adsorbed concentration. Similarly to the gas recovered from the cooling section, the gas released from the preheating section is recycled to feed gas (shown as dashed black line in Figure 2.1). The flow rate of the recycle stream is a approximately 1%wt of the total feed gas.

The majority of CO_2 is then desorbed as a result of further heating of the adsorbent occurring in the desorption section (Figure 6.5). By setting a mild vacuum (0.97 bar) as evacuation pressure, the released gas is collected at the bottom, where high CO_2 purity is achieved. Lastly, the adsorbent is cooled as it traverses the cooling section (Figure 6.6). Here, a small stream of nearly pure N_2 recirculated from the adsorption section is used as purge gas to further regenerate the adsorbent from the remaining CO_2. As previously mentioned, the fraction of recirculated gas is approximately 5% of the total CO_2-free gas leaving the adsorption section.

As shown in Figures 6.3 to 6.6 and reported in Table 6.3, the advantage of the zeolite of having a shorter adsorption section is offset by the need for longer cooling and desorption sections, due to their higher regeneration temperature. In fact, with respect to sorbent inventory, the process using zeolite is outperformed by CPO-27-Ni: despite circulating a lower amount of material in terms of kg/s, the total amount of adsorbent required (i.e., the amount of adsorbent that is processed in one cycle) is 43% higher due to the much longer residence time of the zeolite.

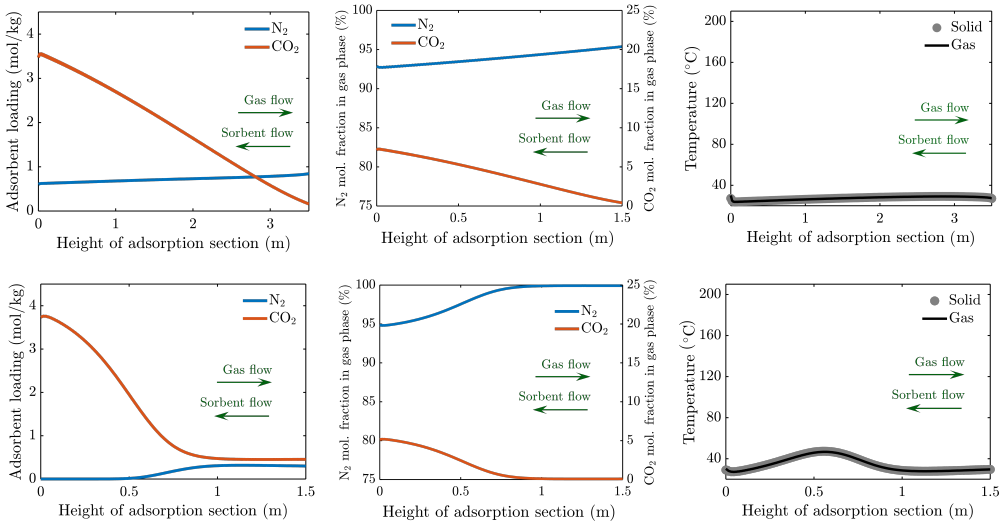

Figure 6.3: Adsorbent loading, molar fractions and temperature profiles along the height of the adsorption section of the moving bed using CPO-27-Ni spheres (top plots) and zeolite 13X (bottom plots). The flue gas flows counter-currently to the adsorbent: position zero corresponds to the bottom of the section, i.e. flue gas inlet and adsorbent outlet.

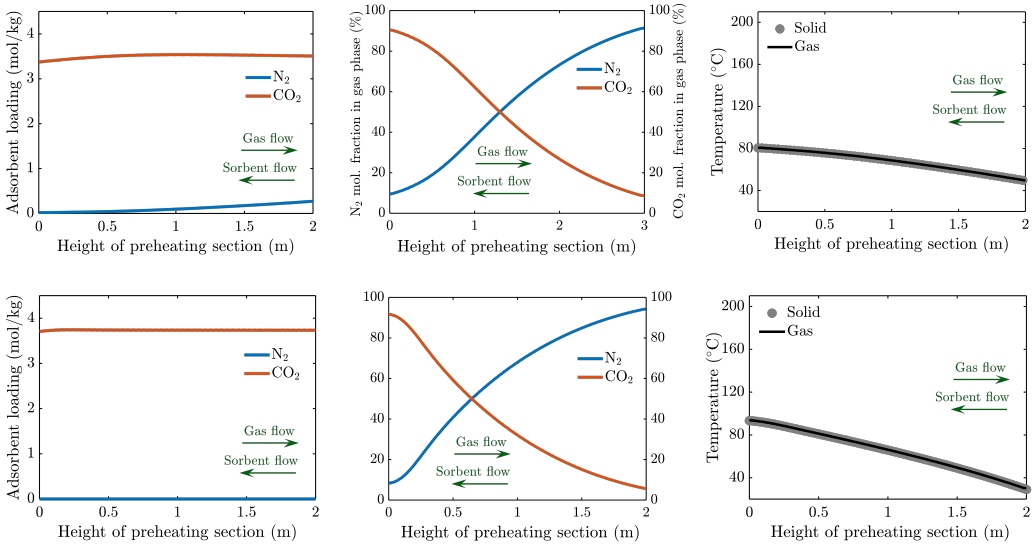

Figure 6.4: Adsorbent loading, molar fractions and temperature profiles along the preheating section of the moving bed using CPO-27-Ni (top plots) and zeolite 13X (bottom plots). Position zero corresponds to outlet of the adsorbent (bottom of the section).

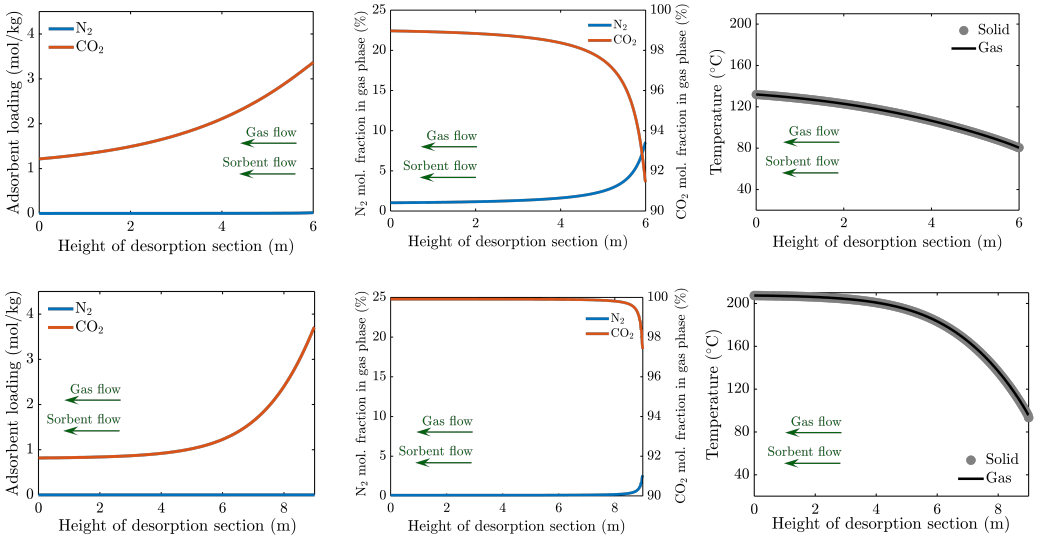

Figure 6.5: Adsorbent loading, molar fractions and temperature profiles along the desorption section of the moving bed (top plots) and zeolite 13X (bottom plots). The flue gas flows co-currently to the adsorbent: Position zero corresponds to the bottom of the section, i.e. the CO_2 extraction point, and sorbent outlet.

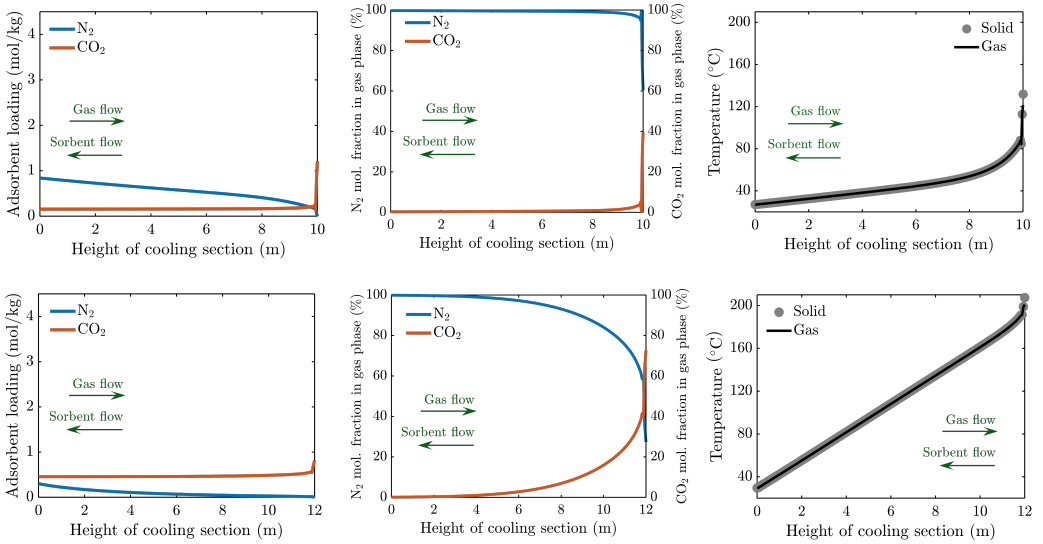

Figure 6.6: Adsorbent loading, molar fractions and temperature profiles along the cooling section of the moving bed using CPO-27-Ni spheres (top plots) and zeolite 13X (bottom plots). Position zero corresponds to the bottom of the section, i.e. the inlet of recirculation gas and sorbent outlet.

6.3.2 Performance of the MBTSA process

The performance of the MBTSA system using CPO-27-Ni was assessed in terms of CO_2 purity, capture rate, and energy use, and the values obtained are reported in Table 6.4. The results concerning the MBTSA process using zeolite 13X (see Section 5.4) are also included for the sake of comparison. Notably, both the MOF- and zeolite-based processes are able to meet the target performance in terms of purity and capture rate. In particular, the MBTSA process using CPO-27-Ni achieved a higher purity (98.9%) than that obtained with the zeolite (95.8%). Conversely, the capture rate of the MBTSA using CPO-27-Ni (92.6%) is somewhat lower than that of the zeolite-based process (98.2%). Moreover, the productivity of the MOF- and zeolite-based processes was 222 and 200 $kg_{CO_2}/t_s h$, respectively, which is significantly higher than that of conventional fixed bed processes (Plaza et al. 2017; Joss et al. 2017)

With regards to the thermal energy required for sorbent regeneration, the process using zeolite 13X consumes only 10% more heat, despite the significantly higher regeneration temperature (207 versus 132 °C). This indicates that the effect of the higher temperature swing is partially offset by the much lower adsorbent flow rate (490 versus 700 kg/s). Interesting results are found also in terms of specific energy use. In particular, the amount of heat per unit of CO_2 captured required by the CPO-27-Ni (2.15 MJ/kg_{CO_2}) is slightly lower than the corresponding value of the zeolite-based system (2.24 MJ/kg_{CO_2}). However, when part of the heat is internally recovered, the situation is reversed and the process employing zeolite 13X becomes more energy-efficient, consuming 1.42 MJ/kg_{CO_2} versus the 1.89 MJ/kg_{CO_2} of the MOF-based process. The reason for this is that the process using zeolite 13X offers a higher potential for heat integration due to its higher regeneration temperature.

Table 6.4: MBTSA process simulation results for CPO-27-Ni and zeolite 13X.

	CPO-27-Ni	Zeolite 13X
CO_2 purity	98.9%	95.8%
CO_2 capture rate	92.6%	98.2%
Process productivity	222 $kg_{CO_2}/t_s h$	200 $kg_{CO_2}/t_s h$
Amount of circulating sorbent	700 kg/s	490 kg/s
Regeneration temperature	132 °C	207 °C
Energy required for sorbent regeneration:		
- without heat integration	142.9 MW_{th}	158.7 MW_{th}
- with heat integration	125.6 MW_{th}	100.7 MW_{th}
Specific energy for sorbent regeneration:		
- without heat integration	2.15 MJ/kg_{CO_2}	2.24 MJ/kg_{CO_2}
- with heat integration	1.89 MJ/kg_{CO_2}	1.42 MJ/kg_{CO_2}

6.3.3 Integration with NGCC power plant

On the basis of the results obtained with the MBTSA simulations, the amount of thermal energy required for sorbent regeneration was computed and used as input to the NGCC model simulations. The results of the MBTSA and power plant integration are summarized in Figure 6.7 and Table 6.5. The CPO-27-Ni case is compared with the reference moving bed process using zeolite 13X, the benchmark amine-based process, and the reference NGCC plant without capture.

As shown graphically in Figure 6.7, one of the main differences between the moving bed and amine-based systems is the additional energy penalty associated with the drying of the flue gas for the MBTSA cases. This drying process is required because the selected adsorbents (zeolite 13X and CPO-27-Ni) are incompatible with a high water content in the flue gas. In particular, the drying process accounts for approximately 17% of the total energy penalty of the capture system. Another factor playing in favor of the MEA process is the slightly higher pressure at which CO_2 is separated, which implies lower power consumption in the CO_2 compressor. On the other hand, the MBTSA processes present a significantly lower heat demand for sorbent regeneration and hence a lower power loss associated with the steam extraction.

When comparing the zeolite-based process with the MOF-based process, the higher energy penalty due to the pressure drops in the CPO-27-Ni system is compensated by the smaller power output penalty associated with steam bleeding. In fact, despite requiring a slightly higher amount of energy for sorbent regeneration (both in terms of total heat input and specific heat per kg of CO_2 captured), the process using CPO-27-Ni allows extraction of steam at lower temperature and pressure, which is beneficial for the performance of the steam cycle (see Table 6.5).

Although the breakdown of the total energy penalty associated with the CO_2 capture process differs from case to case (see Figure 6.7), the overall performance of the NGCC power plant in terms of net electric efficiency is very similar in all cases. In particular, both MBTSA capture processes lead to a reduction of about 7 percentage points with respect to the reference plant without capture, while the amine-based process causes a reduction of 8 percentage points.

Table 6.5: Main simulation results of MBTSA with CPO-27-Ni and integration of capture process with NGCC power plant.

	Reference NGCC	NGCC with MEA process	NGCC with zeolite 13X	NGCC with CPO-27-Ni
CO_2 purity (%)	–	99.9	95.8	98.9
CO_2 recovery (%)	–	95.0	98.2	92.6
Heat input to capture unit (MW_{th})	–	266	101	125
Specific heat input (MJ_{th}/kg_{CO_2})	–	3.95	1.42	1.89
CO_2 captured (t_{CO_2}/h)	–	242	249	240
CO_2 emitted (t_{CO_2}/h)	253	11.2	4.6	18.8
Specific emissions (kg_{CO_2}/MWh)	316	15	6	24
NGCC gross power output (MW_{el})	802	734	767	773
GT gross power output (MW_{el})	555	555	555	555
ST gross power output (MW_{el})	246	179	211	218
Steam extraction flow rate (kg/s)	–	107	35.9	50.4
Steam extraction temperature (°C)	–	292	465	277
Steam extraction pressure (bar)	–	3.22	12.3	2.66
CO_2 capture auxiliaries (MW_{el})	–	37.5	54.7	60.1
NGCC net electric efficiency	**63.1**	**54.7**	**55.9**	**56.1**

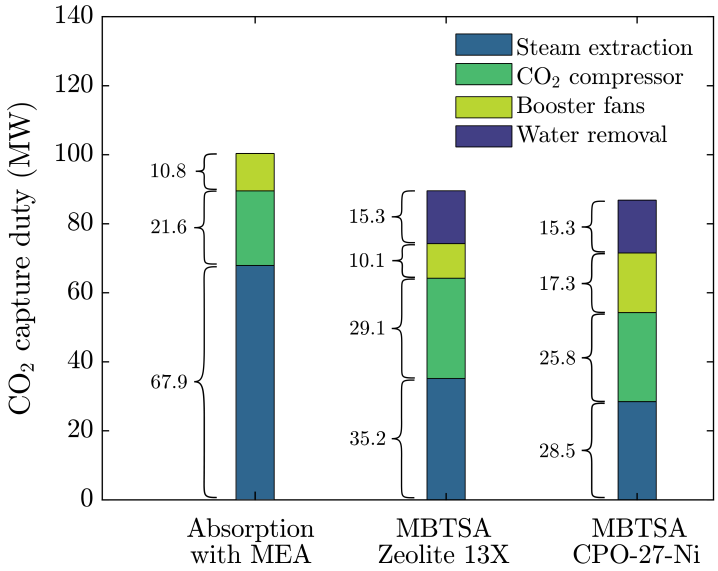

Figure 6.7: Individual contributions to the overall capture duty. Comparison of the MBTSA process with CPO-27-Ni, MBTSA with zeolite 13X and amine-based process.

6.4 Chapter summary

The suitability of a novel adsorbent material, namely CPO-27-Ni MOF, as a candidate for MBTSA capture processes was evaluated and compared to the commercial zeolite 13X studied in the previous chapter. A sample of the selected adsorbent, shaped as spherical beads of suitable size for moving bed systems (700 μm), was characterized in terms of adsorption equilibrium properties towards CO_2 and N_2. Based on the measured isotherms, the CO_2/N_2 equilibrium selectivity was calculated at conditions representative of an NGCC flue gas, and the value obtained was three times lower than that of the reference zeolite.

Despite its lower selectivity, process simulation results showed that the MBTSA system using CPO-27-Ni is able to achieve the design targets for CO_2 purity and recovery (i.e., higher than 95% and 90%, respectively), while using slightly less thermal energy compared to the zeolite-based process. The reason for this is that the zeolite 13X needs to be regenerated at a significantly higher temperature due to its stronger affinity for CO_2. In particular, the specific energy consumption of the MBTSA process using the CPO-27-Ni is 2.15 MJ/kg_{CO_2}, while the corresponding value for zeolite 13X is 2.24 MJ/kg_{CO_2}. However, if part of the thermal energy is provided by internal heat recovery, the zeolite-based process becomes more energy efficient, consuming 1.42 MJ/kg_{CO_2} against the 1.89 MJ/kg_{CO_2} required by the MOF-based system.

In addition, a more in-depth analysis of the capture process energy consumption was performed by integrating a model of the reference NGCC power plant with the two capture processes. Besides accounting for the effect of steam bleeding on the overall power plant performance, the integrated model allows a detailed analysis of the energy penalties associated to the various CO_2 capture auxiliaries (e.g., booster fans, CO_2 compressor, and water removal). The numerical simulations showed that, despite requiring a slightly higher amount of energy for sorbent regeneration, the process using CPO-27-Ni allows extraction of steam at a lower temperature and pressure, which is beneficial for the performance of the steam cycle. However, this advantage is partially offset by the higher pressure drop associated with the additional length required in the adsorption section, which in turn leads to a higher power consumption in the flue gas booster fans. Although the distribution of the energy penalties is different between the MOF- and the zeolite-based processes, the overall performance of the NGCC power plant in terms of net electric efficiency is very similar in both cases. In particular, both MBTSA capture processes lead to a reduction of about 7 percentage points with respect to the reference plant without capture, which is comparable to a solvent-based MEA process.

Chapter 7

Conclusions and Further Work

7.1 Conclusions

This Ph.D. thesis studied the suitability of the MBTSA technology for CO_2 capture as an alternative to the energy-intensive post-combustion technologies currently in use. For this purpose, a mathematical model of the MBTSA process was developed and utilized to design MBTSA systems for two applications: (i) a waste-to-energy CHP plant and (ii) a NGCC power plant. The proposed MBTSA processes were assessed in terms of different performance indicators, including separation performance, energy consumption, and system footprint. In addition, the results were benchmarked against conventional fixed bed adsorption processes and the state-of-the-art amine-based absorption technology.

The MBTSA model developed during the course of this Ph.D. project was obtained by applying the mass, momentum and energy balances to the different sections of the system. The resulting set of partial differential equations and boundary conditions were implemented in the gPROMS environment and solved simultaneously using the composite model approach. One distinguishing feature of the MBTSA model is that, instead of imposing a fixed wall temperature in the heating and cooling sections, it includes additional energy balances for the heating/cooling fluid and heat exchanger wall. This approach enables the prediction of the temperature of the gas, adsorbent, wall, and heat transfer fluid along system, which is necessary to obtain an accurate estimation of the heating and cooling duties required to operate the process. Furthermore, the MBTSA model also accounts for the internal heat recovery achieved by coupling the preheating and precooling sections, which, in turn, allows for a realistic estimation of the external energy duty required by the capture process.

The performance of the indirect-contact heat exchangers employed to provide and remove heat from the sorbent depends largely on the sorbent-side heat transfer coefficient, as it is the limiting thermal resistance between the gas/solid phases and the heating/cooling fluid. The correct estimation of this parameter is therefore crucial for the design of an MBTSA system. Nevertheless, the author could not find any heat transfer correlation suitable for the heat exchanger configuration and operating conditions considered in this work. For this reason, a series of experiments were performed to determine the heat transfer coefficient

of an activated carbon adsorbent flowing in the cross-flow shell-and-tube heat exchanger of a lab-scale moving bed apparatus. The analysis of the results revealed a direct dependence between the heat transfer coefficient and the sorbent flow rate, while no dependence was observed on the sorbent temperature. The trend of the experimental results suggested that operating the system at higher sorbent flow rates could lead to even higher heat transfer coefficients. However, this hypothesis could not be verified due to the limitations of the experimental apparatus. In any case, the heat transfer coefficients obtained (70–120 $W/m^2\,K$) were significantly higher than those typically encountered in fixed bed configurations (10–50 $W/m^2\,K$). This confirmed that the moving bed configuration has the potential to address one of the main limitations of the fixed bed TSA process, namely, the low productivity due to the slow heating and cooling of the adsorbent.

The results of the experimental campaign were used to develop a correlation for the sorbent-side Nusselt number as a function of the Péclet number. This correlation was incorporated into the MBTSA computational model, which was then used to design and analyse an MBTSA process for an industrial-scale application. The case study considered was a waste-to-energy CHP plant with a power output of 16.8 MW_{el}, a thermal output of 64.6 MW_{th}, and an exhaust flue gas flow rate of 56 kg/s with 11%vol CO_2 concentration. The adsorbent material was the same commercial activated carbon used in the heat transfer experiments. Despite the low selectivity of the adsorbent, the proposed MBTSA process was able to achieve high CO_2 purity (97.2 %) and capture rate (90.8%), at the expense of adopting a high regeneration temperature (187 °C) and solid-to-gas ratio (11.6 kg of adsorbent per kg of flue gas). These two factors led to a rather high energy consumption (5.7 MJ/kg_{CO_2}) compared with the values reported in literature for other adsorbents. Nevertheless, the designed MBTSA system was able to achieve high process productivity (181 $kg_{CO_2}/t_{ads}h$). This can be attributed to the fast temperature swings associated with the high sorbent-side heat transfer coefficient of the moving bed configuration. Overall, the results of the waste-to-energy case study indicated that the MBTSA technology is suited to capture CO_2 at high purity and recovery, while achieving higher process productivity than fixed bed TSA processes. However, the energy performance of the capture process was relatively poor, especially considering that 53.5% of the heat required to regenerate the adsorbent was provided by internal heat recovery. In this regard, it is believed that the thermal energy required by the proposed MBTSA system may be significantly reduced by replacing the activated carbon material by other adsorbents having higher capacity and selectivity towards CO_2, such as zeolites or MOFs.

Moreover, this thesis evaluated the suitability of the MBTSA technology in the context of power generation from natural gas. The case study considered was a 800 MW NGCC power plant with an exhaust gas of 916 kg/s containing 5.15%vol of CO_2. Two different MBTSA capture processes were proposed: one using a commercial zeolite 13X and other using a novel CPO-27-Ni MOF adsorbent. The two

systems were able to meet the target specifications in terms of CO_2 purity ($> 95\%$) and capture rate ($> 90\%$), while achieving higher productivity than conventional fixed bed TSA processes. Even if the separation performance of both processes was similar, the distinct physical properties of the adsorbent materials led to different system dimensions and operating conditions, demonstrating the flexibility of the MBTSA technology. One important difference between the two processes was the choice of regeneration temperature. The maximum desorption temperature of the CPO-27-Ni process was limited to 132 °C to avoid potential degradation of the adsorbent. Conversely, adsorbent degradation was not a concern in the zeolite 13X case, and the regeneration temperature was set to 207 °C. This selection, together with the adoption of internal heat recovery, had a marked impact on the energy use of the processes. In particular, the amount of heat per unit of CO_2 captured required by the CPO-27-Ni process (2.15 MJ/kg_{CO_2}) was slightly lower than the corresponding value of the zeolite-based system (2.24 MJ/kg_{CO_2}). However, when part of the heat was internally recovered, the situation was reversed and the process employing zeolite 13X became more energy-efficient, consuming 1.42 MJ/kg_{CO_2} versus the 1.89 MJ/kg_{CO_2} of the MOF-based process. The reason for this is that the process using zeolite 13X offers a higher potential for heat integration due to its higher regeneration temperature.

One could argue that the preceding energy analysis and comparison between processes is not fair because: (i) it ignores that the heat required by the capture processes is provided at different temperatures and (ii) it does not account for the additional power required to compensate the pressure drop across the MBTSA sections, or to rise the pressure of the CO_2-rich stream to meet transport specifications. To address these limitations, the influence of the capture system on power plant performance was analyzed by integrating the MBTSA with a process model of the NGCC power plant. Besides accounting for the effect of steam extraction on the net electric efficiency of the power plant, the NGCC process model enabled the evaluation of the energy penalties associated to the various CO_2 capture auxiliaries (e.g., booster fans, CO_2 compressor, and electric chiller for water removal from flue gas). The numerical simulations showed that, even if the process using the CPO-27-Ni adsorbent required more thermal energy for sorbent regeneration (125.6 vs 100.7 MW_{th}), the energy penalty associated with steam extraction was smaller (25.8 vs 29.1 MW_{el}) because the steam extraction was performed at lower temperature and pressure. However, this advantage was partially offset by the higher pressure drop associated with the additional length required in the adsorption section of the CPO-27-Ni process, which in turn led to a higher power consumption in the flue-gas booster fans (17.3 vs 10.1 MW_{el}). Although the distribution of the energy penalties was different between the MOF- and the zeolite-based processes, the overall performance of the NGCC power plant in terms of net electric efficiency was very similar in both cases. In particular, both MBTSA capture processes led to a reduction of about 7 percentage points

with respect to the reference plant without CO_2 capture.

Moreover, the zeolite- and MOF-based MBTSA processes were benchmarked against the state-of-the-art MEA absorption technology. One of the main differences between the moving bed and amine-based systems was the additional energy penalty associated with the drying of the flue gas for the MBTSA cases. This drying process was required because the selected adsorbents (zeolite 13X and CPO-27-Ni) are incompatible with a high water content in the flue gas. In particular, the drying process represented approximately 17% of the total energy penalty of the capture system. Another advantage of the MEA process was the slightly higher pressure at which CO_2 is separated, which led to lower power consumption in the CO_2 compressor. By contrast, the thermal energy required, and hence the power loss associated with steam extraction, was significantly lower for both MBTSA processes. Even if the breakdown of the total energy penalty differed between the MBTSA systems and the MEA process, no significant difference was observed in terms of overall power plant efficiency. In particular, the net electric efficiency of the reference power plant was 63.1%, while the efficiency of the power plant with CO_2 capture was 54.7% for the case of MEA, 56.1% for the MBTSA using CPO-27-Ni, and 56.2% for the MBTSA using zeolite 13X.

In conclusion, the simulation results suggest that the MBTSA process applied to NGCC power plants is suitable for capturing CO_2 at high purity and high capture rate, while being competitive with the state-of-the-art capture process in terms of energy penalty. Considering the much earlier stage of development of this technology with respect to the MEA process, the MBTSA seems to offer a large potential for process improvement and should be considered for further development.

7.2 Further work

The MBTSA systems analyzed in this thesis were designed by adjusting the process parameters and operating conditions in an iterative manner until a satisfactory performance was achieved. Besides being time-consuming, this manual design approach relies heavily on the previous experience of the designer and it is likely to overlook potential interaction between variables that could lead to better process performance. In this respect, systematic exploration of the design space is a promising way to decrease the time required for design, achieve higher process performance, and acquire a better understanding of the performance envelope with respect to the decision variables. In particular, extensive parametric analysis applied to the current MBTSA model could help to identify which are the most influential parameters, quantify the potential for improvement in terms of different performance indicators, and guide the path towards the development of an automatic optimization strategy.

Future work may also be devoted to assess the performance of the MBTSA process for other adsorbent materials than those considered in this thesis. In addition, the developed MBTSA model could be extended to explore other configurations and operation strategies that may enable the separation of the CO_2 in a more energy-efficient way. As an example, the use of a lower operating pressure within the desorption section might be considered as a measure to improve sorbent regeneration and cyclic adsorption capacity. Furthermore, the application of the MBTSA as a CO_2 capture technology could be evaluated for other hard-to-carbonize industries such as cement and steel manufacturing.

References

Adil, K., Y. Belmabkhout, R. S. Pillai, A. Cadiau, P. M. Bhatt, A. H. Assen, G. Maurin, and M. Eddaoudi (2017). "Gas/Vapour Separation Using Ultra-Microporous Metal-Organic Frameworks: Insights into the Structure/Separation Relationship". *Chemical Society Reviews* 46.11, pp. 3402–3430.

Agueda, V. I., J. A. Delgado, M. A. Uguina, P. Brea, A. I. Spjelkavik, R. Blom, and C. Grande (2015). "Adsorption and Diffusion of H_2, N_2, CO, CH_4 and CO_2 in UTSA-16 Metal-Organic Framework Extrudates". *Chemical Engineering Science* 124, pp. 159–169.

Akhtar, F., L. Andersson, S. Ogunwumi, N. Hedin, and L. Bergström (2014). "Structuring Adsorbents and Catalysts by Processing of Porous Powders". *Journal of the European Ceramic Society* 34.7, pp. 1643–1666.

Anantharaman, R., O. Bolland, N. Booth, E. van Dorst, C. Ekstrom, E. S. Fernandez, and F. Franco (2011). "CESAR-D2.4.3-APPROVED-European Best Practice Guidelines for CO_2 Capture Technologies - EBTF". Ed. by E. Macchi, G. Manzolini, D. Nikolic, A. Pfeffer, M. Prins, S. Rezvani, and L. Robinson.

Al-Ansary, H., A. El-Leathy, Z. Al-Suhaibani, S. Jeter, D. Sadowski, A. Alrished, and M. Golob (2012). "Experimental Study of a Sand–Air Heat Exchanger for Use With a High-Temperature Solar Gas Turbine System". *Journal of Solar Energy Engineering* 134.4.

Baird, M. H. I., N. V. Rama Rao, E. Tackie, and A. Vahed (2008). "Heat Transfer to a Moving Packed Bed of Nickel Pellets". *The Canadian Journal of Chemical Engineering* 86.2, pp. 142–150.

Baksh, M. S. A., E. S. Kikkinides, and R. T. Yang (1992). "Lithium Type X Zeolite as a Superior Sorbent for Air Separation". *Separation Science and Technology* 27.3, pp. 277–294.

Barrer, R. M. (1981). "Sorption in Porous Crystals: Equilibria and their Interpretation". *Journal of Chemical Technology and Biotechnology* 31.1, pp. 71–85.

Bastin, L., P. S. Bárcia, E. J. Hurtado, J. A. Silva, A. E. Rodrigues, and B. Chen (2008). "A Microporous Metal-Organic Framework for Separation of CO_2/N_2 and CO_2/CH_4 by Fixed-Bed Adsorption". *The Journal of Physical Chemistry C* 112.5, pp. 1575–1581.

Baumann, T. and S. Zunft (2015). "Development and Performance Assessment of a Moving Bed Heat Exchanger for Solar Central Receiver Power Plants". *Energy Procedia* 69, pp. 748–757.

Baumann, T., S. Zunft, and R. Tamme (2014). "Moving Bed Heat Exchangers for use With Heat Storage in Concentrating Solar Plants: a Multiphase Model". *Heat transfer engineering* 35.3, pp. 224–231.

Berg, C. H. O. (1945). "Adsorption Process and Apparatus". US2519873A.

Bird, R. B., W. E. Stewart, and E. N. Lightfoot (2002). *Transport Phenomena*. 2nd edition. Wiley, New York.

Bonjour, J., L. A. O. Rocha, A. Bejan, and F. Meunier (2004). "Dendritic Fins Optimization for a Coaxial Two-stream Heat Exchanger". *International Journal of Heat and Mass Transfer* 47.1, pp. 111–124.

Bonjour, J., J.-B. Chalfen, and F. Meunier (2002). "Temperature Swing Adsorption Process with Indirect Cooling and Heating". *Industrial & engineering chemistry research* 41.23, pp. 5802–5811.

Bonjour, J., M. Clausse, and F. Meunier (2005). "A TSA Process with Indirect Heating and Cooling: Parametric Analysis and Scaling-up to Practical Sizes". *Chemical Engineering and Processing: Process Intensification* 44.9, pp. 969–977.

Brunner, P. H. and H. Rechberger (2015). "Waste to Energy – Key Element for Sustainable Waste Management". *Waste management* 37, pp. 3–12.

Bui, M., C. S. Adjiman, A. Bardow, E. J. Anthony, A. Boston, S. Brown, P. S. Fennell, S. Fuss, A. Galindo, and L. A. Hackett (2018). "Carbon Capture and Storage (CCS): the Way Forward". *Energy & Environmental Science* 11.5, pp. 1062–1176.

Campbell, C. S. (1990). "Rapid Granular Flows". *Annual Review of Fluid Mechanics* 22.1, pp. 57–90.

Cavenati, S., C. A. Grande, and A. E. Rodrigues (2004). "Adsorption Equilibrium of Methane, Carbon Dioxide, and Nitrogen on Zeolite 13X at High Pressures". *Journal of Chemical & Engineering Data* 49.4, pp. 1095–1101.

Cengel, Y. A., S. Klein, and W. Beckman (1998). *Heat Transfer: a Practical Approach*. 2nd edition. Vol. 141. WBC McGraw-Hill Boston.

Dai, Y. L., X. J. Liu, and D. Xia (2020). "Flow Characteristics of Three Typical Granular Materials in Near 2D Moving Beds". *Powder Technology* 373, pp. 220–231.

Danaci, D., M. Bui, N. Mac Dowell, and C. Petit (2020). "Exploring the Limits of Adsorption-based CO_2 Capture Using MOFs with PVSA – From Molecular Design to Process Economics". *Molecular Systems Design & Engineering* 5.1, pp. 212–231.

De Lange, M. F., T. Zeng, T. J. H. Vlugt, J. Gascon, and F. Kapteijn (2015). "Manufacture of Dense CAU-10-H Coatings for Application in Adsorption Driven Heat Pumps: Optimization and Characterization". *CrystEngComm* 17.31, pp. 5911–5920.

Dietzel, P. D. C., V. Besikiotis, and R. Blom (2009). "Application of Metal-Organic Frameworks with Coordinatively Unsaturated Metal Sites in Stor-

age and Separation of Methane and Carbon Dioxide". *Journal of Materials Chemistry* 19.39, pp. 7362–7370.

Ergun, S. (1952). "Fluid Flow Through Packed Columns". *Chemical Engineering Progress* 48, pp. 89–94.

ESI Group (2017). *Scilab Version 6.0*.

Farmahini, A. H., S. Krishnamurthy, D. Friedrich, S. Brandani, and L. Sarkisov (2021). "Performance-based Screening of Porous Materials for Carbon Capture". *Chemical Reviews* 121.17, pp. 10666–10741.

Farrance, I. and R. Frenkel (2012). "Uncertainty of Measurement: a Review of the Rules for Calculating Uncertainty Components Through Functional Relationships". *The Clinical Biochemist Reviews* 33.2, p. 49.

Fernandez, E. S., E. Goetheer, G. Manzolini, E. Macchi, S. Rezvani, and T. Vlugt (2014). "Thermodynamic assessment of amine based CO_2 Capture technologies in power plants based on European Benchmarking Task Force methodology". *Fuel* 129, pp. 318–329.

Franco, F., R. Anantharaman, O. Bolland, N. Booth, E. van Dorst, C. Ekstrom, E. Fernandes, E. Macchi, G. Manzolini, D. Nicolic, A. Pfeffer, M. Prins, S. Rezvani, and L. Robinson (2011). *Test Cases and Preliminary Benchmarking Results from the Three Projects*. Tech. rep. Alstom UK.

Grande, C. A. (2012). "Advances in Pressure Swing Adsorption for Gas Separation". *International Scholarly Research Notices* 2012.

Grande, C. A., F. V. S. Lopes, A. M. Ribeiro, J. M. Loureiro, and A. E. Rodrigues (2008). "Adsorption of Off-Gases from Steam Methane Reforming (H_2, CO_2, CH_4, CO and N_2) on Activated Carbon". *Separation Science and Technology* 43.6, pp. 1338–1364.

Haaf, M., R. Anantharaman, S. Roussanaly, J. Ströhle, and B. Epple (2020). "CO_2 Capture from Waste-to-energy Plants: Techno-economic Assessment of Novel Integration Concepts of Calcium Looping Technology". *Resources, Conservation and Recycling* 162, p. 104973.

Hefti, M., L. Joss, Z. Bjelobrk, and M. Mazzotti (2016). "On the Potential of Phase-Change Adsorbents for CO_2 Capture by Temperature Swing Adsorption". *Faraday discussions* 192, pp. 153–179.

Hefti, M., D. Marx, L. Joss, and M. Mazzotti (2015). "Adsorption Equilibrium of Binary Mixtures of Carbon Dioxide and Nitrogen on Zeolites ZSM-5 and 13X". *Microporous and Mesoporous Materials* 215, pp. 215–228.

Hefti, M. and M. Mazzotti (2018). "Postcombustion CO2 capture from wet flue gas by temperature swing adsorption". *Industrial & Engineering Chemistry Research* 57.45, pp. 15542–15555.

Hornbostel, M. (2016). *Pilot-Scale Evaluation of an Advanced Carbon Sorbent-Based Process for Post-Combustion Carbon Capture*. Report. SRI International, Menlo Park, CA (United States).

Hornbostel, M. D., J. Bao, G. Krishnan, A. Nagar, I. Jayaweera, T. Kobayashi, A. Sanjurjo, J. Sweeney, D. Carruthers, and M. A. Petruska (2013). "Character-

istics of an Advanced Carbon Sorbent for CO_2 Capture". *Carbon* 56, pp. 77–85.

Hornbostel, M. D., G. N. Krishnan, and A. Sanjurjo (2015). "Falling Microbead Counter-Flow Process for Separating Gas Mixtures". US9168484B1.

IEA (2019). *World Energy Outlook 2019*. IEA, Paris.

IPCC (2005). *IPCC Special Report on Carbon Dioxide Capture and Storage*. Metz, Bert and Davidson, Ogunlade and De Coninck, HC and Loos, Manuela and Meyer, Leo.

IPCC (2018). *Summary for Policymakers. In: Global Warming of 1.5° C. An IPCC Special Report on the Impacts of Global Warming of 1.5° C above Pre-industrial Levels and Related Global Greenhouse Gas Emission Pathways, in the Context of Strengthening the Global Response to the Threat of Climate Change, Sustainable Development, and Efforts to Eradicate Poverty*. V. Masson-Delmotte, P. Zhai, H. O. Pörtner, D. Roberts, J. Skea, P. R. Shukla, A. Pirani, W. Moufouma-Okia, C. Péan, R. Pidcock, S. Connors, J. B. R. Matthews, Y. Chen, X. Zhou, M. I. Gomis, E. Lonnoy, T. Maycock, M. Tignor, T. Waterfield (eds.). World Meteorological Organization, Geneva, Switzerland.

Isaza, P. A., W. D. Warnica, and M. Bussmann (2015). "Co-current Parallel-plate Moving Bed Heat Exchanger: An Analytical Solution". *International Journal of Heat and Mass Transfer* 87, pp. 616–624.

Jiao, L., Y. Wang, H.-L. Jiang, and Q. Xu (2018). "Metal-Organic Frameworks as Platforms for Catalytic Applications". *Advanced Materials* 30.37, p. 1703663.

Joss, L., M. Gazzani, and M. Mazzotti (2017). "Rational Design of Temperature Swing Adsorption Cycles for Post-combustion CO_2 Capture". *Chemical Engineering Science* 158, pp. 381–394.

Kaza, S., L. Yao, P. Bhada-Tata, and F. Van Woerden (2018). *What a Waste 2.0: a Global Snapshot of Solid Waste Management to 2050*. World Bank Publications.

Kearns, D. T. (2019). *Waste-to-Energy with CCS: A Pathway to Carbon-Negative Power Generation*.

Kim, K., Y.-K. Park, J. Park, E. Jung, H. Seo, H. Kim, and K. S. Lee (2014). "Performance Comparison of Moving and Fluidized bed Sorption Systems for an Energy-efficient Solid Sorbent-Based Carbon Capture Process". *Energy Procedia* 63, pp. 1151–1161.

Kim, K., Y. Son, W. B. Lee, and K. S. Lee (2013). "Moving Bed Adsorption Process with Internal Heat Integration for Carbon Dioxide Capture". *International Journal of Greenhouse Gas Control* 17, pp. 13–24.

Knaebel, K. S. (2005). "Temperature Swing Adsorption System". US8353978B2.

Krishnamurthy, S., R. Haghpanah, A. Rajendran, and S. Farooq (2014). "Simulation and Optimization of a Dual-adsorbent, Two-bed Vacuum Swing Adsorption Process for CO_2 Capture from Wet Flue Gas". *Industrial & Engineering Chemistry Research* 53.37, pp. 14462–14473.

Kvamsdal, H. M., I. Kim, P. Van Os, C. Pevida, M.-B. Hägg, J. Brown, L. Robinson, and P. Feron (2014). "HiPerCap: a New FP7 Project for Development and Assessment of Novel and Emerging Post-combustion CO_2 Capture Technologies". *Energy Procedia* 63, pp. 6166–6172.

Lee, W.-S., S.-K. Youn, and S.-I. Park (1998). "Finite Element Analysis of the Flow and Heat Transfer of Solid Particles in Moving Beds". *International journal of energy research* 22.13, pp. 1145–1155.

Liang, Z., K. Fu, R. Idem, and P. Tontiwachwuthikul (2016). "Review on Current Advances, Future Challenges and Consideration Issues for Post-combustion CO_2 Capture Using Amine-based Absorbents". *Chinese Journal of Chemical Engineering* 24.2, pp. 278–288.

Lillia, S., D. Bonalumi, C. Grande, and G. Manzolini (2018). "A Comprehensive Modeling of the Hybrid Temperature Electric Swing Adsorption Process for CO_2 Capture". *International Journal of Greenhouse Gas Control* 74, pp. 155–173.

Liu, Z., C. A. Grande, P. Li, J. Yu, and A. E. Rodrigues (2011). "Multi-bed Vacuum Pressure Swing Adsorption for Carbon Dioxide Capture from Flue Gas". *Separation and Purification Technology* 81.3, pp. 307–317.

Lopes, F. V. S., C. A. Grande, A. M. Ribeiro, E. L. Oliveira, J. M. Loureiro, and A. E. Rodrigues (2009). "Enhancing Capacity of Activated Carbons for Hydrogen Purification". *Industrial & engineering chemistry research* 48.8, pp. 3978–3990.

Marx, D., L. Joss, M. Hefti, and M. Mazzotti (2016). "Temperature Swing Adsorption for Postcombustion CO_2 Capture: Single- and Multi-column Experiments and Simulations". *Industrial & Engineering Chemistry Research* 55.5, pp. 1401–1412.

Masala, A., J. G. Vitillo, G. Mondino, C. A. Grande, R. Blom, M. Manzoli, M. Marshall, and S. Bordiga (2017a). "CO_2 Capture in Dry and Wet Conditions in UTSA-16 Metal-Organic Framework". *ACS applied materials & interfaces* 9.1, pp. 455–463.

Masala, A., J. G. Vitillo, G. Mondino, G. Martra, R. Blom, C. A. Grande, and S. Bordiga (2017b). "Conductive ZSM-5-based Adsorbent for CO_2 Capture: Active Phase vs Monolith". *Industrial & Engineering Chemistry Research* 56.30, pp. 8485–8498.

Mason, J. A., K. Sumida, Z. R. Herm, R. Krishna, and J. R. Long (2011). "Evaluating Metal-Organic Frameworks for Post-combustion Carbon Dioxide Capture via Temperature Swing Adsorption". *Energy & Environmental Science* 4.8, pp. 3030–3040.

Merel, J., M. Clausse, and F. Meunier (2008). "Experimental Investigation on CO_2 Post-combustion Capture by Indirect Thermal Swing Adsorption Using 13X and 5A Zeolites". *Industrial & Engineering Chemistry Research* 47.1, pp. 209–215.

Mickley, H. S. and D. F. Fairbanks (1955). "Mechanism of Heat Transfer to Fluidized beds". *AIChE Journal* 1.3, pp. 374–384.

Mondino, G., C. A. Grande, and R. Blom (2017). "Effect of Gas Recycling on the Performance of a Moving Bed Temperature-Swing (MBTSA) Process for CO_2 Capture in a Coal Fired Power Plant Context". *Energies* 10.6, p. 745.

Mondino, G., C. A. Grande, R. Blom, and L. O. Nord (2019). "Moving Bed Temperature Swing Adsorption for CO_2 Capture from a Natural Gas Combined Cycle Power Plant". *International Journal of Greenhouse Gas Control* 85, pp. 58–70.

Mondino, G., C. A. Grande, R. Blom, and L. O. Nord (2021). "Evaluation of MBTSA Technology for CO_2 Capture from Waste-to-Energy Plants". *International Journal of Greenhouse Gas Control* [accepted].

Mondino, G., A. I. Spjelkavik, T. Didriksen, S. Krishnamurthy, R. E. Stensrød, C. A. Grande, L. O. Nord, and R. Blom (2020). "Production of MOF Adsorbent Spheres and Comparison of Their Performance with Zeolite 13X in a Moving-Bed TSA Process for Postcombustion CO_2 Capture". *Industrial & Engineering Chemistry Research* 59.15, pp. 7198–7211.

Montañés, R. M., N. E. Flø, and L. O. Nord (2018). "Experimental Results of Transient Testing at the Amine Plant at Technology Centre Mongstad: Open-loop Responses and Performance of Decentralized Control Structures for Load Changes". *International Journal of Greenhouse Gas Control* 73, pp. 42–59.

Morales-Ospino, R., V. N. Santos, A. R. Lima Jr, A. E. B. Torres, E. Vilarrasa-García, M. Bastos-Neto, C. L. Cavalcante Jr, D. C. S. Azevedo, C. R. M. Marques, and T. F. de Aquino (2021). "Parametric Analysis of a Moving Bed Temperature Swing Adsorption (MBTSA) Process for Postcombustion CO_2 Capture". *Industrial & Engineering Chemistry Research*.

Morris, R. E. and P. S. Wheatley (2008). "Gas Storage in Nanoporous Materials". *Angewandte Chemie International Edition* 47.27, pp. 4966–4981.

Mulloth, L. M. and J. E. Finn (1998). *Carbon Dioxide Adsorption on a 5A Zeolite Designed for CO_2 Removal in Spacecraft Cabins*. Tech. rep. National Aeronautics and Space Administration, Ames Research Center.

National Instruments (2019). *LabVIEW*.

Niegsch, J., D. Köneke, and P.-M. Weinspach (1994). "Heat Transfer and Flow of Bulk Solids in a Moving Bed". *Chemical Engineering and Processing: Process Intensification* 33.2, pp. 73–89.

Nord, L. O. and O. Bolland (2020). *Carbon Dioxide Emission Management in Power Generation*. 1st edition. John Wiley & Sons.

Obuskovic, N. S. (1988). "Heat Transfer Between Moving Beds of Solids and a Vertical Tube". PhD thesis. Oregon State University.

Okumura, T., T. Ogino, S. Nishibe, Y. Nonaka, T. Shoji, and T. Higashi (2014). "CO_2 Capture Test for A Moving-bed System Utilizi g Low-temperature Steam". *Energy Procedia* 63, pp. 2249–2254.

Okumura, T., K. Yoshizawa, S. Nishibe, H. Iwasaki, M. Kazari, and T. Hori (2017). "Parametric Testing of a Pilot-scale Design for a Moving-bed CO_2 Capture System Using Low-temperature Steam". *Energy Procedia* 114, pp. 2322–2329.

Park, Y.-J., S.-J. Lee, J.-H. Moon, D.-K. Choi, and C.-H. Lee (2006). "Adsorption equilibria of O_2, N_2, and Ar on carbon molecular sieve and zeolites 10X, 13X, and LiX". *Journal of Chemical and Data, Engineering* 51.3, pp. 1001–1008.

Plaza, M. G., A. S. González, C. Pevida, and F. Rubiera (2014). "Influence of Water Vapor on CO_2 Adsorption Using a Biomass-based Carbon". *Industrial & Engineering Chemistry Research* 53.40, pp. 15488–15499.

Plaza, M. G., F. Rubiera, and C. Pevida (2017). "Evaluating the Feasibility of a TSA Process Based on Steam Stripping in Combination with Structured Carbon Adsorbents to Capture CO_2 from a Coal Power Plant". *Energy & Fuels* 31.9, pp. 9760–9775.

Process System Enterpise (PSE) (2019). *gPROMS Model Builder Version 6.0*.

Qoaider, L., Q. Thabit, and S. Kiwan (2017). "Performance Assessment of a Moving-bed Heat Exchanger with a Sensible Heat Transfer Medium for Solar Central Receiver Power Plants". *8th International Renewable Energy Congress (IREC)*, pp. 1–5.

Queen, W. L., M. R. Hudson, E. D. Bloch, J. A. Mason, M. I. Gonzalez, J. S. Lee, D. Gygi, J. D. Howe, K. Lee, T. A. Darwish, et al. (2014). "Comprehensive Study of Carbon Dioxide Adsorption in the Metal-Organic Frameworks M_2(dobdc) (M = Mg, Mn, Fe, Co, Ni, Cu, Zn)". *Chemical Science* 5.12, pp. 4569–4581.

Rezaei, F. and P. Webley (2010). "Structured Adsorbents in Gas Separation Processes". *Separation and Purification Technology* 70.3, pp. 243–256.

Ribeiro, A. M., T. P. Sauer, C. A. Grande, R. F. P. M. Moreira, J. M. Loureiro, and A. E. Rodrigues (2008). "Adsorption Equilibrium and Kinetics of Water Vapor on Different Adsorbents". *Ind. Eng. Chem. Res* 47, pp. 7019–7026.

Rosi, N. L., J. Eckert, M. Eddaoudi, D. T. Vodak, J. Kim, M. O'Keeffe, and O. M. Yaghi (2003). "Hydrogen Storage in Microporous Metal-Organic Frameworks". *Science* 300.5622, pp. 1127–1129.

Rúa, J., M. Bui, L. O. Nord, and N. Mac Dowell (2020). "Does CCS Reduce Power Generation Flexibility? A Dynamic Study of Combined Cycles with Post-combustion CO_2 Capture". *International Journal of Greenhouse Gas Control* 95, p. 102984.

Ruthven, D. M. (1984). *Principles of Adsorption and Adsorption Processes*. 1st edition. John Wiley & Sons.

Shen, C., C. A. Grande, P. Li, J. Yu, and A. E. Rodrigues (2010). "Adsorption Equilibria and Kinetics of CO_2 and N_2 on Activated Carbon Beads". *Chemical Engineering Journal* 160.2, pp. 398–407.

Sjostrom, S. and H. Krutka (2010). "Evaluation of Solid Sorbents as a Retrofit Technology for CO_2 Capture". *Fuel* 89.6, pp. 1298–1306.

Son, Y., K. Kim, and K. S. Lee (2014). "Feasibility Study of a Moving-Bed Adsorption Process with Heat Integration for CO_2 Capture through Energy Evaluation and Optimization". *Energy & Fuels* 28.12, pp. 7599–7608.

Takeuchi, H. (1996). "Particles Flow Pattern and Local Heat Transfer Around Tube in Moving Bed". *AIChE journal* 42.6, pp. 1621–1626.

Talu, O. (1998). "Needs, Status, Techniques and Problems with Binary Gas Adsorption Experiments". *Advances in Colloid and Interface Science* 76, pp. 227–269.

Taqvi, S. M. and M. D. LeVan (1997). "Virial Description of Two-component Adsorption on Homogeneous and Heterogeneous Surfaces". *Industrial & Engineering Chemistry Research* 36.6, pp. 2197–2206.

Teo, H. W. B., A. Chakraborty, and S. Kayal (2018). "Formic Acid Modulated (FAM) Aluminium Fumarate MOF for Improved Isotherms and Kinetics with Water Adsorption: Cooling/Heat Pump Applications". *Microporous and Mesoporous Materials* 272, pp. 109–116.

Thermoflow Inc. (2017). *Thermoflow Version 27*.

Tian, X., J. Yang, Z. Guo, Q. Wang, and B. Sunden (2020). "Numerical Study of Heat Transfer in Gravity-Driven Particle Flow around Tubes with Different Shapes". *Energies* 13.8.

Turan, G., A. Zapantis, D. Kearns, E. Tamme, C. Staib, T. Zhang, J. Burrows, A. Gillespie, I. Havercroft, D. Rassool, C. Consoli, and H. Liu (2021). *Global Status of CCS 2021*. Tech. rep. Global CCS Institute, Melbourne, Australia.

Vandervort, C. (2018). "Advancements in H Class Gas Turbines and Combined Cycle Power Plants". *ASME Turbo Expo 2018: Turbomachinery Technical Conference and Exposition*.

Wakao, N. and T. Funazkri (1978). "Effect of Fluid Dispersion Coefficients on Particle-to-fluid Mass Transfer Coefficients in Packed Beds: Correlation of Sherwood Numbers". *Chemical Engineering Science* 33.10, pp. 1375–1384.

Wakao, N., S. Kaguei, and T. Funazkri (1979). "Effect of Fluid Dispersion Coefficients on Particle-to-fluid Heat transfer Coefficients in Packed beds: Correlation of Nusselt Numbers". *Chemical engineering science* 34.3, pp. 325–336.

Wankat, P. C. (2006). *Separation Process Engineering*. 2nd edition. Pearson Education.

Wilke, C. R. (1950). "Diffusional Properties of Multicomponent Gases". *Chemical Engineering Progress* 46.2, pp. 95–104.

Yang, R. T. (1987). *Gas Separation by Adsorption Processes*. 1st edition. Butterworth.

Zanco, S. E., M. Ambrosetti, G. Groppi, E. Tronconi, and M. Mazzotti (2021). "Heat Transfer Intensification with Packed Open-cell Foams in TSA Processes for CO_2 Capture". *Chemical Engineering Journal*, p. 131000.

Zanco, S. E., M. Mazzotti, M. Gazzani, M. C. Romano, and I. Martínez (2018). "CO_2 Capture via Temperature Swing Adsorption". *AIChE Journal* 64.5, pp. 1744–1759.

Zanco, S. E., L. Joss, M. Hefti, M. Gazzani, and M. Mazzotti (2017). "Addressing the Criticalities for the Deployment of Adsorption-based CO_2 Capture Processes". *Energy Procedia* 114, pp. 2497–2505.

Zhang, Z., Z.-Z. Yao, S. Xiang, and B. Chen (2014). "Perspective of Microporous Metal–Organic Frameworks for CO_2 Capture and Separation". *Energy & Environmental Science* 7.9, pp. 2868–2899.

Appendix A

Publications

Publication I

G. Mondino, C. A. Grande, R. Blom, and L. O. Nord (2019). "Moving Bed Temperature Swing Adsorption for CO_2 Capture from a Natural Gas Combined Cycle Power Plant". *International Journal of Greenhouse Gas Control* 85, pp. 58–70.

Publication II

G. Mondino, A. I. Spjelkavik, T. Didriksen, S. Krishnamurthy, R. E. Stensrød, C. A. Grande, L. O. Nord, and R. Blom (2020). "Production of MOF Adsorbent Spheres and Comparison of Their Performance with Zeolite 13X in a Moving-Bed TSA Process for Postcombustion CO_2 Capture". *Industrial & Engineering Chemistry Research* 59.15, pp. 7198–7211.

Publication III

G. Mondino, C. A. Grande, R. Blom, and L. O. Nord (2021). "Evaluation of MBTSA Technology for CO_2 Capture from Waste-to-Energy Plants". *International Journal of Greenhouse Gas Control* [accepted].

International Journal of Greenhouse Gas Control 85 (2019) 58–70

Contents lists available at ScienceDirect

International Journal of Greenhouse Gas Control

journal homepage: www.elsevier.com/locate/ijggc

Moving bed temperature swing adsorption for CO_2 capture from a natural gas combined cycle power plant

Giorgia Mondino[a,*], Carlos A. Grande[b], Richard Blom[b], Lars O. Nord[a]

[a] NTNU – Norwegian University of Science and Technology, Department of Energy and Process Engineering, Trondheim, Norway
[b] SINTEF Industry, P.O. Box 124, Blindern, N0314 Oslo, Norway

ARTICLE INFO

Keywords:
TSA
MBTSA
NGCC
Post-combustion
PCC
CCS
Zeolite 13X

ABSTRACT

The present work considers the utilization of a moving bed temperature swing adsorption (MBTSA) process for CO_2 capture as alternative to the commercial absorption-based technologies, in the context of natural gas combined cycle (NGCC) power plants. A detailed mathematical model consisting of energy, mass and momentum balances was implemented in gPROMS software, in order to investigate the system behavior under different operating conditions and design parameters. Results show that under the simulated process conditions, the system is suitable for capturing CO_2 at high purity and high capture rate. Promising results are obtained also in terms of process energy duty, by performing a preliminary analysis that takes into account the heat required for sorbent regeneration. Furthermore, the effect of implementing the MBTSA process on plant performance was studied, by integrating the capture system with a process model of the reference power plant. A detailed analysis of the energy use associated with the capture process auxiliaries was performed. Finally, the power plant model was used to simulate the same NGCC system coupled with a state-of-the-art absorption process, for a direct comparison between the two capture technologies.

1. Introduction

In post-combustion CO_2 capture, adsorption processes are considered a promising alternative to the commercial absorption-based technology, which suffers from high costs and high energy penalties (Liang et al., 2016). While requiring further developments as a CO_2 capture technology, solid sorbents are already commercially used in a wide range of applications, from air separation, to hydrogen purification, gas drying and methane purification (Ruthven, 1984). In all these processes, the adsorbent material is used in a cyclic manner, switching between adsorption and desorption steps, where the latter (i.e. sorbent regeneration) is performed either by a change in pressure (Pressure Swing/Vacuum Pressure Swing) or in temperature (Temperature Swing). The same concept can be employed for post-combustion CO_2 capture, provided that the adsorbent is selective toward CO_2 at the flue gas conditions.

The main issue with conventional temperature swing adsorption (TSA) processes, where the adsorbent is packed in large columns, is the long cycle time associated to the heating and cooling steps, which can take several hours (Plaza et al., 2017). One way to overcome this issue, thus significantly improving the efficiency of the separation process, is to employ the moving bed temperature swing adsorption (MBTSA) concept, in which the adsorbent circulates through different sections, always operated at the same conditions for their specific purpose: adsorption, desorption, or cooling.

The MBTSA process has been previously suggested for CO_2 capture by Knaebel (2009) and SRI International (Hornbostel et al., 2013), who respectively used zeolites and activated carbons as adsorbent materials. The same concept has been lately proposed as a viable option for post-combustion capture by Kim et al. (Kim et al., 2013, 2014; Son et al., 2014), who investigate the possibility of reducing the energy penalty of the process by internal heat integration.

At GHGT-13 we presented a simplified assessment of the MBTSA process in the Natural Gas Combined Cycle (NGCC) context (Grande et al., 2017). More recently we have carried out a more comprehensive study of the MBTSA process using the composite model approach in gPROMS software (gPROMS, 2016) to simultaneously simulate the different sections composing the MBTSA (Mondino et al., 2017). The composite model was used to investigate the application of the MBTSA for CO_2 from a coal fired power plant. Based on the detailed model for the coal case (Mondino et al., 2017), the present work aims to give a more thorough assessment of the performance of an MBTSA process in the NGCC context. For this purpose, the configuration of the system is adapted to the NGCC case study, which differs from the coal fired

* Corresponding author.
E-mail address: giorgia.mondino@ntnu.no (G. Mondino).

https://doi.org/10.1016/j.ijggc.2019.03.021
Received 3 October 2018; Received in revised form 27 February 2019; Accepted 21 March 2019
Available online 08 April 2019

Nomenclature

A	first Virial coefficient (kg mol^{-1})
a'	particle specific area (m^2 m^{-3})
B	second Virial coefficient (kg^2 mol^{-1})
Bi	Biot number
$C_{p,g}$	gas mixture mass specific heat at constant pressure (J kg^{-1} K^{-1})
c_p	gas mixture molar specific heat at constant pressure (J mol^{-1} K^{-1})
$c_{p,pack}$	specific heat capacity of packing material (J kg^{-1} K^{-1})
$c_{p,s}$	specific heat capacity of the adsorbent (J kg^{-1} K^{-1})
c_v	gas mixture molar specific heat at constant volume (J mol^{-1} K^{-1})
$C_{b,i}$	molar concentration of component i in the macropores (mol m^{-3})
C_i	molar concentration of component i (mol m^{-3})
C_T	total gas concentration (mol m^{-3})
D_c	micropore effective diffusivity of component i (m^2 s^{-1})
D_c^0	micropore limiting diffusivity at infinite temperature (m^2 s^{-1})
D_{ij}	binary molecular diffusivity (m^2 s^{-1})
D_h	hydraulic diameter (m)
D_m	molecular diffusivity (m^2 s^{-1})
$D_{p,i}$	macropore diffusivity of component i (m^2 s^{-1})
D_z	axial dispersion coefficient (m^2 s^{-1})
d_p	particle diameter (m)
E_a	activation energy of micropore diffusion (kJ/mol)
k_g	thermal conductivity of the gas (W m^{-1} K^{-1})
K_i	equilibrium constant of component i *(mol kg−1 kPa−1)*
K_i^∞	equilibrium constant at infinite temperature (mol kg−1 kPa^{-1})
h_f	film heat transfer coefficient between the gas and the solid (J s^{-1} m^{-2} K^{-1})
$h_{g,hx}$	film heat transfer coefficient between the gas and the wall (J s^{-1} m^{-2} K^{-1})
K_m	film mass transfer coefficient (m s^{-1})
M_w	molecular weight (g mol^{-1})
q_i	adsorbed phase concentration of component i (mol/kg)
R	ideal gas constant (J K^{-1} mol^{-1})
r_c	crystals radius (m)
R_p	particle radius (m)
P_i	partial pressure of component i (kPa)
T	temperature of the gas (K)
T_s	temperature of the solid (K)
T_hx	temperature of the wall (K)
u	superficial velocity of the gas (m s^{-1})
v_{solid}	velocity of the solid (m s^{-1})
Y_i	molar fraction of component i

Greek letters

ΔH	isosteric heat of adsorption (kJ/mol)
ε	bed void fraction
ε_p	particle porosity
λ	heat axial dispersion coefficient (J m^{-1} s^{-1} K^{-1})
μ_g	gas viscosity (Pa s)
ξ	packing porosity factor
ρ_g	gas density (kg m^{-3})
ρ_p	particle density (kg m^{-3})
ρ_{pack}	packing density (kg m^{-3})
$\Omega_{D_{ij}}$	dimensionless collision integral of binary diffusivity

power plant in terms of flue gas conditions (temperature, pressure, flow rate and composition). Due to the lower CO_2 partial pressure in the flue gas, the use of zeolites is considered, as zeolites present a significantly higher selectivity towards CO_2 compared to activated carbons (Chue et al., 1995).

Adsorption equilibrium data was experimentally measured for the selected adsorbent and fitted with a mathematical model in order to provide the required model parameters. A set of simulations was performed by varying several design parameters and operating conditions, as well as adjusting the system configuration, in order to reach the desired product gas specifications, in terms of CO_2 purity and capture rate. Furthermore, the amount of energy required for sorbent regeneration was evaluated by applying the energy balance across the preheating and desorption sections of the moving bed, where the adsorbent was heated to the regeneration temperature. The use of steam from the power plant was considered for this purpose, in addition to a heat integration scheme that reduces the need of external heat by recovering heat within the MBTSA system.

In order to evaluate the impact of the CO_2 capture system on the power plant efficiency, Thermoflex software was used (Thermoflow Version, 2017). A computational model of the NGCC power plant able to accommodate the capture system was built, and full plant-analysis performed. The power plant model was also used to simulate the same NGCC system without CO_2 capture unit, as reference case, as well as a NGCC system coupled with a state-of-the-art absorption process, for a direct comparison between the two capture technologies.

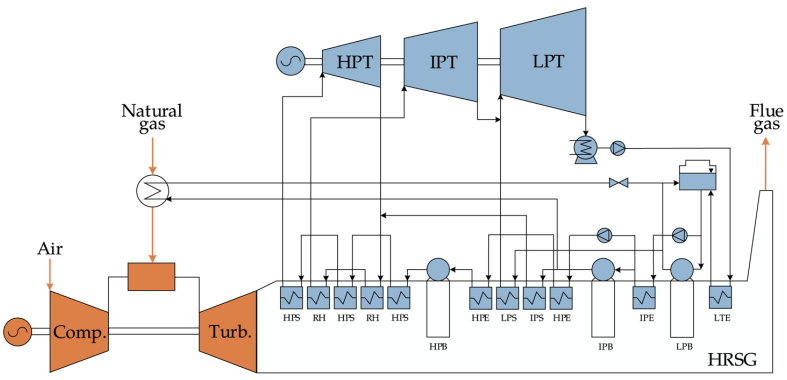

Fig. 1. Layout of the reference NGCC power plant without CCS, where the following abbreviations are used: Comp. for compressor section in gas turbine; Turb. for turbine section in gas turbine, HPT, IPT and LPT for high, intermediate and low pressure steam turbines, respectively; HRSG for heat recovery steam generator; HPS, IPS, LPS for high, intermediate and low pressure superheaters, respectively; HPE, IPE, LPE for the corresponding economizers; HPB, IPB and LPB for the boilers; and RH for the reheater.

2. Framework for the process simulations

The application considered for the MBTSA capture process consists of an NGCC with a net power output of nearly 800 MW. The power plant was initially modeled through GT PRO software (Thermoflow package (Thermoflow Version, 2017)), in order to provide the input data for the MBTSA model, in terms of flue gas specifications.

The NGCC object of this study was designed with the aim of representing the current state-of-the-art technology in combined cycles, which are engineered to achieve net efficiencies exceeding 63% LHV based (Vandervort, 2018). For this purpose, the General Electric 9HA.02 model was adopted for the Gas Turbine (GT), fueled by natural gas. Details on the natural gas compositions and heating values are listed in Appendix A6 .

A three pressure levels and reheat type steam cycle configuration was employed. As a common measure to increase the power plant efficiency (Fernandez et al., 2014; Anantharaman et al., 2011), the fuel is preheated prior the combustor with part of the steam produced in the intermediate pressure (IP) drum. The resulting plant layout is shown in Fig. 1, while a summary of the main operating conditions and performance parameters is presented in Table 1.

The next paragraphs contain a description of the MBTSA process and model approach, followed by a description of the adsorbent material employed and characterized. Furthermore, details are given on how the MBTSA model results were used as basis for the integration of the capture process with the power plant for full-plant analysis. Finally, some details are given concerning the comparison of the MBTSA process with an amine-based CO_2 capture process.

2.1. The MBTSA process and model simulations

A schematic diagram of an MBTSA system is shown in Fig. 2. As shown in the figure, the MBTSA system is composed of the following three main sections through which the pelletized adsorbent circulates: the adsorption section at the top (black in the figure), the desorption section (red in the figure) and the cooling section at the bottom (blue in the figure).

In the adsorption section the adsorbent particles falls counter-currently to the flue gas, capturing the incoming CO_2. The adsorbent leaving from the bottom of the adsorption section is loaded with CO_2 extracted from the flue gas and continues into the desorption (regeneration) section. In the desorption section, heat is transferred to the adsorbent promoting desorption of CO_2 that is further assisted by light vacuum for extraction. In this work it is assumed that the desorption section is operated as an indirect-contact heat exchanger where steam from the power plant is used as heat transfer fluid.

The unloaded adsorbent is then cooled down in the cooling section and transported back to the top of the reactor, ready to start a new cycle. As shown in the figure, preheating and precooling sections can also be employed in order to recover part of the heat from the hot powder leaving the desorption section for preheating the powder leaving the adsorption section.

The mathematical model describing the MBTSA (Fig. 2) consists of a set of partial differential equations (unsteady and one dimensional) obtained by applying the mass, energy and momentum balance to the individual sections (adsorption, desorption and cooling section).

One of the main differences compared to a fixed-bed adsorption model is given by the terms containing v_{solid} (i.e. velocity of the solid) appearing in the mass and energy balance equations, which represent the contribution due to the movement of the adsorbent along the axial coordinate. It should be noted that, unlikely fixed bed adsorption systems, the counter current moving bed can be operated at steady state. Although a dynamic model is used for simulations, only the steady-state behaviors is investigated in this study, and all results presented were obtained during steady-state.

The set of coupled differential equations, implemented on gPROMS software for each section of the moving bed, has to be solved simultaneously for continuous process simulations. For this purpose, the individual units were connected to each other in a so-called “composite model” flowsheet on gPROMS (Liu et al., 2011). With the gPROMS composite model approach, the different sections of the moving bed communicate with each other through specifically defined variable-ports. The purpose of these inlet-outlet ports is to transfer certain model variables (e.g. gas and solid phase concentrations, temperature and pressure) at the boundary of the corresponding section-space domain, so that the model instances can exchange information with the adjacent model instances during simulation. As an example, the boundary conditions for the solid phase at the top of the adsorption section (i.e. sorbent inlet), will be assigned based on the variables computed within the cooling section, so that the conditions of the adsorbent leaving the cooling section are used as input at the top of the adsorption section. This allows to take into account for example for a non-complete regeneration of the solid performed in desorption section, which in turns will affect the performance of the adsorption section, and thus the overall process. More details on the modeling approach and underlying assumptions can be found in Appendix B.

The simulations were performed by discretizing the axial space domain of each process sections with the centered finite difference method (CFDM), with second order approximation. The number of intervals employed to discretize the axial space domain was 200 for the adsorption and the cooling sections, 100 for the preheating and 400 for the desorption section.

A set of simulations was performed by varying several design parameters and operating conditions, as well as adjusting the system configuration, in order to improve the process performances, with the aim of obtaining high CO_2 purity and capture rate. The following values were set as minimum targets, based on the typical specifications required for CO_2 transport and storage: 95% CO_2 purity and 90% CO_2 capture rate.

Furthermore, the total amount of energy required for sorbent

Table 1
Summary of technical data of the reference NGCC plant.

Gas cycle	
GT model	GE 9HA.02
Fuel type	Natural gas
Net fuel energy input (MW)	1257.3
GT gross electric power output (MW)	555.3
Fuel temperature at combustor inlet (°C)	180
Fuel pressure at combustor inlet (bar)	39.29
Fuel flow (kg/s)	27.17
Air temperature at compressor inlet (°C)	15
Air flow (kg/s)	957
GT inlet temperature (°C)	1504.5
GT exhaust temperature (°C)	646.9
GT exhaust pressure (bar)	1.051 bar
GT exhaust gas flow (kg/s)	984.1
Steam cycle	
Number of pressure levels	3
ST gross electric power output (MW)	246.5
HP turbine inlet temperature (°C)	600
HP turbine pressure (bar)	186
HP turbine inlet flow (kg/s)	126
IP turbine inlet temperature (°C)	600
IP turbine inlet pressure (bar)	30
IP turbine inlet flow (kg/s)	142.9
LP turbine inlet temperature (°C)	72.32
LP turbine pressure (bar)	0.3447
LP turbine inlet flow (kg/s)	161
Condenser pressure (bar)	0.0586
Combined cycle	
Gross combined electric power output (MW)	801.8
Net power output (MW)	792.8
Net electric efficiency	63.05
CO_2 emitted (kg/s)	70.82

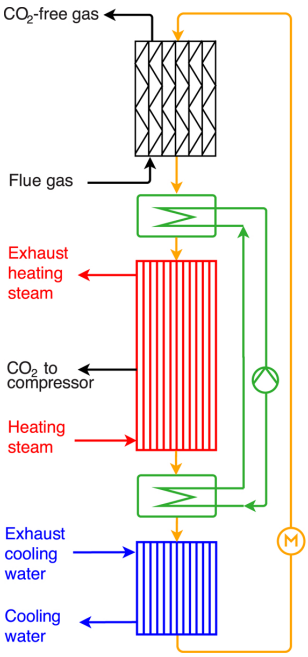

Mass balance in the gas phase

$$\varepsilon_c \frac{\partial C_i}{\partial t} = \varepsilon_c \frac{\partial}{\partial z}\left(D_z C_T \frac{\partial Y_i}{\partial z}\right) - \frac{\partial (u C_i)}{\partial z} - \frac{(1-\varepsilon_c-\xi)a' K_m}{Bi/5+1}(C_i - C_{b,i})$$

Mass balance in macropores of the adsorbent (LDF description)

$$\varepsilon_p \frac{\partial C_{b,i}}{\partial t} = \varepsilon_p \frac{15 D_{p,i}}{R_p{}^2} \frac{Bi_i}{5+Bi_i}(C_i - C_{b,i}) - \rho_p\left(\frac{\partial q_i}{\partial t} + v_{solid}\frac{\partial q_i}{\partial z}\right) - v_{solid}\frac{\partial C_{b,i}}{\partial z}$$

Mass balance in micropores of the adsorbent

$$\frac{\partial q_i}{\partial t} + v_{solid}\frac{\partial q_i}{\partial z} = \frac{15 D_{c,i}}{r_c{}^2}(q_i^* - q_i)$$

Adsorption isotherm (extension of Virial isotherm for multicomponent adsorption isotherm)

$$P_i = \frac{q_i^*}{K_i} exp\left[\sum_{j=1}^{N} A_{ij} q_j^* + \sum_{j=1}^{N}\sum_{k=1}^{N} B_{ijk} q_j^* q_k^* + \sum_{j=1}^{N}\sum_{k=1}^{N}\sum_{l=1}^{N} C_{ijkl}\, q_j^* q_k^* q_l^*\right] \qquad K_i = K_i^{\infty} exp\left(\frac{-\Delta H_i}{R_g T_s}\right)$$

$$A_i = A_{0,i} + \frac{A_{1,i}}{T_s}; \qquad A_{ij} = \frac{A_i + A_j}{2}; \qquad B_i = B_{0,i} + \frac{B_{1,i}}{T_s} \qquad B_{ijk} = \frac{B_i + B_j + B_k}{3}$$

Energy balance in the gas phase

$$\varepsilon_c C_T c_v \frac{\partial T}{\partial t} = \frac{\partial}{\partial z}\left(\lambda \frac{\partial T}{\partial z}\right) - u C_T c_p \frac{\partial T}{\partial z} + \varepsilon_c RT \sum \frac{\partial C}{\partial t} - (1-\varepsilon_c-\xi)a' h_f (T - T_s) - \frac{4\, h_{g,hx}}{D_h}(T - T_{hx})$$

Energy balance in the solid phase

$$\left[(1-\varepsilon_c-\xi)\rho_p c_{ps} + \xi \rho_{pack} c_{ppack}\right]\left(\frac{\partial T_s}{\partial t} + v_{solid}\frac{\partial T_s}{\partial z}\right) = \xi \frac{\partial}{\partial z}\left(\lambda_{pack}\frac{\partial T_s}{\partial z}\right) + (1-\varepsilon_c-\xi)a' h_f (T_g - T_s)$$
$$+(1-\varepsilon_c-\xi)\rho_p \sum\left(-\Delta H_i\left[\frac{\partial q_i}{\partial t} + v_{solid}\frac{\partial q_i}{\partial z}\right]\right) + (1-\varepsilon_c-\xi)\varepsilon_p RT_s \sum\left[\frac{\partial C_{b,i}}{\partial t} + v_{solid}\frac{\partial C_{b,i}}{\partial z}\right]$$

Fig. 2. Schematic diagram of the MBTSA (right) and summary of model equations.

Table 2
Main input parameters adopted in the MBTSA simulations: specifications of the NGCC exhaust gas and adsorbent properties.

Flue gas at MBTSA inlet	
Temperature	30 °C
Pressure	1.05 bar
Flowrate	916 kg/s
Composition	
CO_2	5.15 vol%
N_2	94.85 vol%
Adsorbent properties	
Adsorbent type	Zeolite 13X
Particles shape	Spheres
Particles diameter	700 μm
Particle porosity	0.5
Particle density	1100 kg/m^3
Heat capacity	880 kJ/(kg K)

regeneration was evaluated by applying the energy balance across the preheating and desorption sections, where the adsorbent is heated to the regeneration temperature. The amount of thermal energy that can be recovered by transferring heat from the hot adsorbent leaving the desorption section to the adsorbent that has to be regenerated, was estimated by analyzing the temperature profiles along the heating and cooling sections, and the corresponding heat exchanged. A graphical procedure was used for this purpose, by plotting the hot and cold composite curves on an temperature-enthalpy diagram. The minimum amount of external heat required was estimated by moving the cold curve along the enthalpy axis so that a minimum temperature difference is ensured at the pinch point. As conservative assumption, considering that a third heat transfer media is used for transferring the recoverable heat, a value of 20 °C was assumed as ΔT minimum on both sides (hot and cold). With the same approach, the amount of external heat required was estimated in order to provide the input for process integration with the power plant.

As previously mentioned, the characteristics of the flue gas considered for the application of the MBTSA in this work refer to an NGCC power plant. In order to reduce the computational effort in the MBTSA simulations, the composition of the exhaust gas, obtained with the NGCC model in GT PRO software, was simplified to a binary mixture of N_2 and CO_2. For this purpose the following assumptions were made: O_2 and Ar behave similarly to N_2 (Baksh et al., 1992; Park et al., 2006; Merel et al., 2008), and the water vapor is removed prior the MBTSA unit. The resulting flue gas specifications, used as input for designing and simulating the MBTSA process, are listed in Table 2.

2.2. The adsorbent material

Besides reducing the computational effort of the MBTSA simulations, another reason for considering dried flue gas is to avoid limiting the choice of the adsorbent to those materials having low affinity towards water, such as activated carbons. For the purpose of this study, it was therefore possible to employ a Zeolite 13X, which is suitable for the NGCC case, for its high CO_2 adsorption capacity at low CO_2 partial pressures and high CO_2/N_2 selectivity (Zanco et al., 2018; Hefti et al., 2015; Lillia et al., 2018; Merel et al., 2008).

A sample of Zeolite 13X, pelletized into spherical particles of 700 μm diameter, was purchased by CWK, Germany. The size of the particles was chosen to be higher than few hundreds μm in order to avoid fluidization in the adsorption section of the moving bed, where large flow rates move counter currently to the adsorbent.

In order to provide the MBTSA model with the necessary data of the adsorbent, the purchased Zeolite 13X was characterized in terms of pure components adsorption isotherms of CO_2 and N_2. The measurements were performed in a volumetric apparatus (Belsorp Max, MicrotracBEL) at seven different temperatures in the range of 10–180 °C, up to 1.05 bar. Prior to the measurements the sample was regenerated at 320 °C under vacuum for 10 h, in order to remove any presence of impurities or moisture adsorbed.

Fitting of the experimental data was performed using the Virial model (Taqvi and LeVan, 1997; Shen et al., 2012; Barrer, 1981), which provides the parameters to use as input for the multicomponent adsorption equations implemented in the MBTSA model. Details on the methods used for the isotherms fitting can be found elsewhere (Mondino et al., 2017). In order to account for competitive adsorption of the two gases, the extension of the Virial model for multicomponent adsorption equilibrium (Ribeiro et al., 2008; Shen et al., 2010) was implemented in the MBTSA simulations, as shown in Fig. 2.

2.3. Integration of the MBTSA process and the power plant

In order to evaluate the impact of the CO_2 capture system on the power plant efficiency, the NGCC model initially developed in GT PRO was exported into Thermoflex and appositely modified in order to accommodate the capture process. The reason for using Thermoflex is that, compared to GT PRO, it allows a higher degree of model customization.

The layout of the NGCC power plant integrated with the MBTSA system is shown in Fig. 3. The main modifications with respect to the reference case (NGCC plant without CO_2 capture, shown in Fig. 1) include: (i) the extraction of steam from the IP turbine, needed in the MBTSA for sorbent regeneration, (ii) a drying unit, employed for removing water from the flue gas upstream the MBTSA, (iii) a compressor/fan compensating for the pressure drops of the MBTSA, (iv) a CO_2 compressor, (v) a cooling water circuit that takes into account the cooling demand of the MBTSA system.

The extracted steam is processed by an indirect counter current heat exchanger that mimics the desorption section of the MBTSA, in terms of inlet/outlet temperatures of the cold fluid and heat duty. The condensed water leaving the heat exchanger is returned to the deaerator after appropriate pressure reduction. The amount of steam extracted and the corresponding pressure will therefore be determined based on the heat exchanger duty, while assuring that the condensed outlet temperature corresponds to the deaerator operating temperature. A similar approach is used for simulating the cooling part of the MBTSA process, where cooling water is used, implying the use of a circulating pump.

The drying unit consists of three components: (i) a gas-water contact heat exchanger where the flue gas is cooled to 30 °C, (ii) an electric chiller that further reduces the temperature of the flue gas to 16 °C, (iii) a fan placed upstream the gas-water contact heat exchanger, for overcoming the pressure drops of the drying steps. The flue gas leaving the drying units still contains a small amount of water (approximately 1.8 mol%), which should also be removed. Although this final step was not included in the present work, it was assumed that the remaining water can be removed in a process with limited energy consumption, applying the same approach described by Lillia et al. (2018), where the activated alumina used for adsorbing water is regenerated by the CO_2-free product of the capture process.

Lastly, the CO_2 compressor consists in five inter-cooled stages characterized by an isentropic efficiency of 85% for each stage. The inlet conditions (i.e. gas composition, flow rate, temperature and pressure) are set based on the results obtained with the MBTSA simulations. The delivery pressure is assumed to be 110 bar.

2.4. Comparison with an amine based capture process

One of the aims of this work is to provide a plant-level comparison of the developed MBTSA process with the benchmark amine based capture technology. For this purpose, the reference NGCC model was again modified in Thermoflex software (Thermoflow Version, 2017), which provides a built-in model of a standard chemical absorption process using MEA (MonoEthanolAmine) as solvent. Together with certain user-inputs, the built-in model provides an estimate of the total auxiliary power, heat consumption, and cooling duty required by the process, as well as its impact on the combined cycle efficiency.

The main input that were provided to the software when implementing this model are representative of a typical MEA process with a specific energy input of 3.95 MJ/kg (Fernandez et al., 2014; Franco et al., 2011; Anantharaman et al., 2011). A comprehensive list of process parameters adopted is can be found in Appendix A7 .

The implemented absorption process requires a certain amount of steam for covering the heat duty of the reboiler. Using the same approach used by Fernandez et al. (2014), the necessary steam is extracted at a pressure close to the steam condensing pressure in the reboiler and further conditioned for reboiler use. The condensate from the reboiler is pumped back to the feed water tank.

3. Results and discussion

3.1. Adsorption equilibrium of CO_2 and N_2 on Zeolite 13X

The results of CO_2 and N_2 isotherms measurements, performed on the Zeolite 13X in a wide range of temperature (10–180 °C), are shown in Fig. 4, together with the isotherms fitting, given by the Virial model (solid lines). As expected, the adsorption capacity of CO_2 is significantly higher than the adsorption capacity of N_2, in the whole temperature

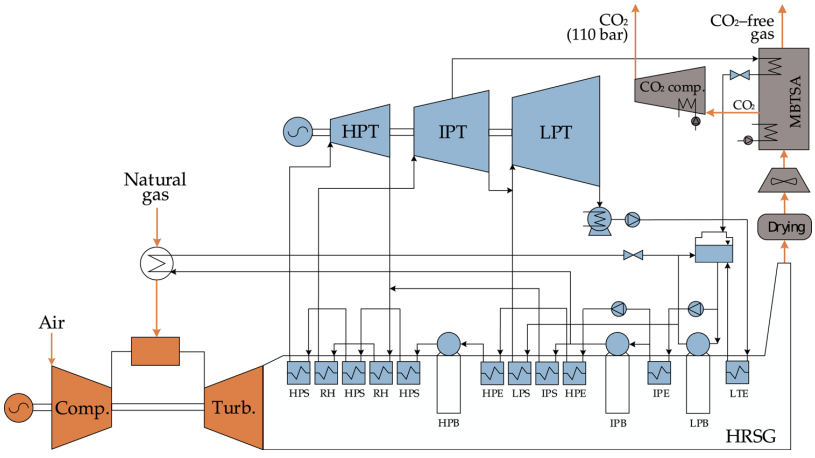

Fig. 3. Layout of the reference NGCC power plant integrated with the MBTSA process. Comp. for air compressor; Turb. for gas turbine; HPT, IPT and LPT for high, intermediate and low pressure turbines, respectively; HRSG for heat recovery steam generator; HPS, IPS, LPS for high, intermediate and low pressure superheaters, respectively; HPE, IPE, LPE for the corresponding economizers, HPB, IPB and LPB for the boilers; and RH for the reheater.

and pressure ranges examined. At 30 °C and 0.0515 bar, which correspond the CO_2 partial pressure at the feed gas conditions, the equilibrium capacity of CO_2 is 3.5 mol/kg, versus 0.4 mol/kg of N_2 at the feed gas conditions (30 °C and 0.996 bar). This confirms the high equilibrium selectivity of the adsorbent, which is beneficial for the MBTSA process, where high purity of the CO_2 product is desired.

The values of the parameters obtained by fitting the isotherms with the Virial model are listed in Table 3. The heat of adsorptions obtained by the Virial fitting is in good agreement with the values obtained from the slope of the Van't Hoff plot, shown in Fig. 5, where the Henry's law constant are plotted against the reciprocal of temperature (Shen et al., 2010; Ruthven, 1984; Yang, 1987).

3.2. MBTSA process performances

Based on the CO_2 adsorption capacity at the feed gas conditions and the corresponding flow of CO_2 that is to be captured, it was possible to make an initial estimation of the amount of sorbent required (in terms of kg/s) and determine the size of the unit. Due to the large amount of flue gas to be processed (over 900 kg/s) it was necessary to employ two MBTSA units, as the gas velocity within the adsorption section must be kept below the minimum fluidization velocity and the size of the column should be limited to realistic values.

A set of simulations was then performed by varying several design parameters and operating conditions, as well as adjusting the system configuration, in order to reach the desired CO_2 purity and capture rate. Details on the system dimensions and operating conditions employed can be found in Appendix B9 . Results of the gPROMS simulations are shown in Figs. 6–9, in terms of N_2 and CO_2 concentration profiles reached at steady state in each section of the MBTSA. In all figures, the horizontal axis represents the position along the height (vertical coordinate) of the corresponding MBTSA section, being zero the bottom of the section, i.e. the sorbent outlet, while the upper limit of the axis corresponds to the top of the section. For clarity purpose, the flow directions of gas and sorbent are also shown on the plots, by the green arrows.

The corresponding temperature profiles, for both the gas and solid phases, are shown in Fig. 10. In order to limit the increase in temperature due to the high heat of adsorption of CO_2, with a consequent reduction in adsorption capacity, it was decided to operate the adsorption section similarly to the cooling section, where heat is removed from the sorbent by indirect heat exchange with cooling water. Nevertheless, an increase in temperature of nearly 20 °C is observed within the adsorption section.

Thanks to the high equilibrium selectivity of the Zeolite 13X, the adsorbent leaving the adsorption section contains a nearly negligible amount of N_2 in the adsorbed phase, which has a beneficial effect on the obtainable CO_2 purity. As it passes through the preheating section the CO_2 loaded adsorbent is heated from 30 °C to approximately 90 °C (solid outlet temperature). The change in temperature is accompanied by a change in CO_2/N_2 ratio in the gas phase (Fig. 7), as part of the adsorbed CO_2 is released by the adsorbent. However, due to the high CO_2 adsorption capacity even at relatively high temperatures, the change in adsorbent loading taking place within the preheating section is very limited. This means that most of the desorption will take place in the desorption section, where the temperature is further increased to 180 °C (Case A) and 207 °C (Case B). In order to direct the gas flow towards the CO_2 extraction line, and thus avoiding upward gas flow within the desorption section, a mild vacuum (0.97 bar) is applied at the bottom of the section (sorbent outlet).

Due to the steepness of the CO_2 isotherm, when leaving the desorption section, the adsorbent loading of CO_2 is still significant (nearly 1 mol/kg). Part of this CO_2 can be removed from the adsorbent and recovered from the top of cooling section, by recirculating a small fraction of the CO_2-free gas from the adsorption section to the cooling section. If the flow or recirculated gas through the cooling section is sufficiently small, the gas leaving from the top will contain mostly CO_2 and can be mixed with the CO_2 product exiting the desorption section without excessively reducing the CO_2 purity.

The total amount of energy required for sorbent regeneration was evaluated by applying the energy balance across the preheating and desorption sections, where the adsorbent is heated to the regeneration temperature. The amount of thermal energy that can be recovered by transferring heat from the hot adsorbent leaving the desorption section to the adsorbent that has to be regenerated, was estimated by analyzing the temperature profiles along the heating and cooling sections, and the corresponding heat exchanged.

As expected, the system behavior is very sensitive to the regeneration temperature, as it directly affects the CO_2 working capacity and thus the amount of adsorbent required. A lower regeneration temperature, which is beneficial when considering heat integration using waste heat from the power plant, implies a less efficient regeneration of the sorbent and thus has to be compensated by increasing the amount of circulating sorbent. As an example of simulation results, two cases employing different regeneration temperatures are presented in Table 3. Better CO_2 purity and capture rate are obtained in the case of higher regeneration temperature (Case B), which also requires 16.3% less adsorbent. When comparing the total amount of thermal energy required, the case using lower regeneration temperature (Case A) seems to be more efficient. However, due to the difference in CO_2 capture rate, the specific energy consumption of the two cases in terms of energy required per unit mass of CO_2 captured does not differ significantly.

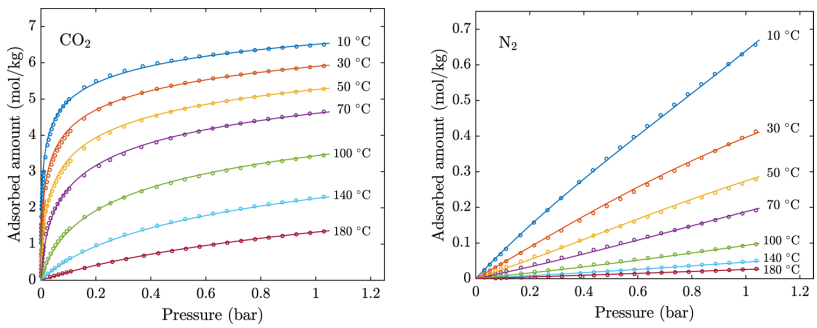

Fig. 4. CO_2 (left) and N_2 (right) adsorption isotherms on Zeolite 13X at temperatures between 10 and 180 °C, and pressures up to 1.05 bar: experimental values (symbols) and fitting with Virial model (lines).

Table 3
Virial model parameters fitting CO_2 and N_2 adsorption isotherms on Zeolite 13X at temperatures between 10 and 180 °C and pressures between 0 and 1.05 bar.

	K_∞ mol kg^{-1} kPa	$-\Delta H$ (kJ/mol)	A_0 (kg mol^{-1})	A_1 (kg K/mol)	B_0 (kg^2 mol^{-1})	B_1 (kg^2 K/mol^2)
CO_2	1.61935×10^{-7}	44.7838	0.4220	7.8371	−0.0485	34.8669
N_2	5.48207×10^{-7}	22.6591	−13.037	3889.5	24.9613	−7213.8

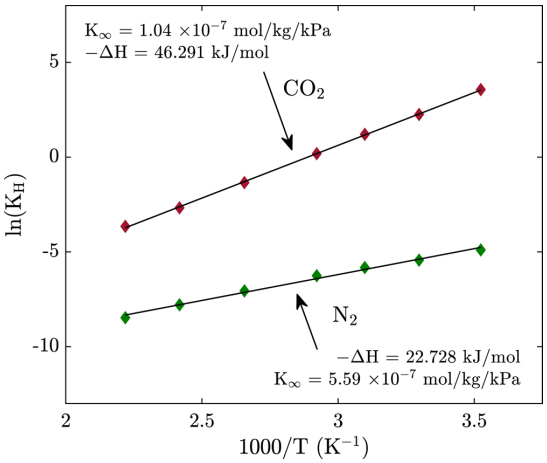

Fig. 5. Van't Hoff plot for estimation of isosteric heat of adsorption: CO_2 in red and N_2 in green. (For interpretation of the references to color in this figure legend, the reader is referred to the web version of this article.)

Table 4

3.3. Results of the power plant integration

The main results of the Thermoflex (Thermoflow Version, 2017) simulations are shown in Table 5, where the following five cases are presented: (i) the NGCC without CO_2 capture as reference case, (ii) the NGCC coupled with a MEA capture process characterized by 90% capture rate (which corresponds to the minimum target process specification), (iii) the NGCC coupled with a MEA capture process with a 95% capture rate, for comparison purposes with the MBTSA system, (iv) the NGCC integrated with the MBTSA case using 180 °C as regeneration temperature (previously referred as Case A), (v) the NGCC integrated with the MBTSA case using 207 °C as regeneration temperature (previously referred as Case B). By comparing the investigated cases, the table shows how the different capture systems affect the power plant performance in terms of net electric efficiency, including a detailed list of the energy use associated to the capture process and power plant auxiliaries.

While the gas cycle is not affected by the capture process, as its operating conditions remain unchanged, the steam cycle suffers from a reduction in power generated, due to the steam bleeding for meeting the heat demand of the capture process. As regard to the MEA cases, low pressure steam is sufficient to provide the required heat, as the reboiler is operated at relatively low temperature (134 °C steam inlet temperature). On the contrary, the MBTSA process requires higher steam extraction pressures, depending on the sorbent regeneration temperature, in order to maintain the minimum pinch point within the heat exchanger. Although the MEA process requires steam at lower pressure, which is beneficial for the steam cycle performances, the total amount of heat to be provided by the steam is 2.5 times higher than for the MBTSA process. The overall reduction in power output due to steam bleeding is smaller when MBTSA process is chosen over the MEA process, confirming that the thermal energy requirement for regeneration is a crucial process parameters to consider when selecting a capture technology (Fernandez et al., 2014). However, when comparing the net electric efficiency of the power plant, no significant difference is observed between the two technologies, causing a reduction of about 7 and 8 percentage points for the MBTSA and the MEA respectively. The reason for this is the higher energy required by MBTSA when comparing the CO_2 capture auxiliaries. In this respect, the higher energy consumption of the MBTSA are associated mainly to: (i) the use of the electric chiller for water removal, (ii) the CO_2 compressor, which uses approximately double amount of energy compared to the MEA case, due to the lower inlet pressure of the CO_2 to be compressed and the

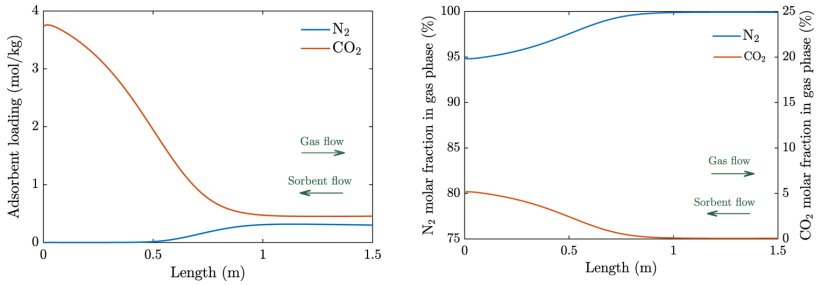

Fig. 6. Adsorbent loading (left) and molar fraction (right) profiles along the vertical coordinate of the adsorption section.

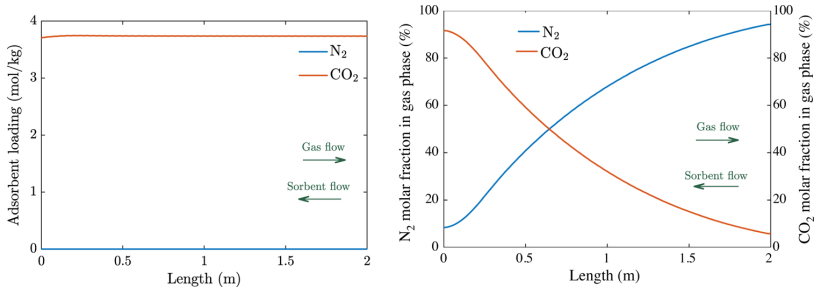

Fig. 7. Adsorbent loading (left) and molar fraction (right) profiles along the vertical coordinate of the preheating section.

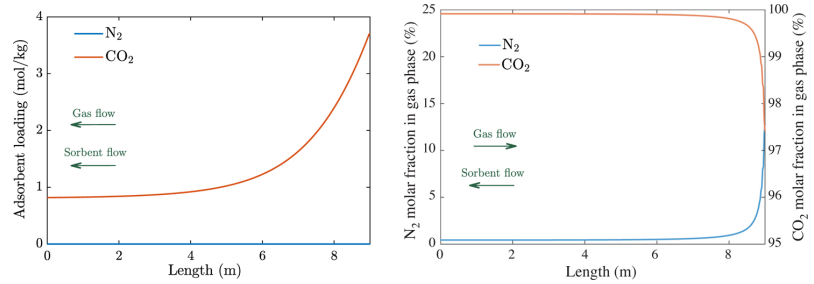

Fig. 8. Adsorbent loading (left) and molar fraction (right) profiles along the vertical coordinate of the desorption section.

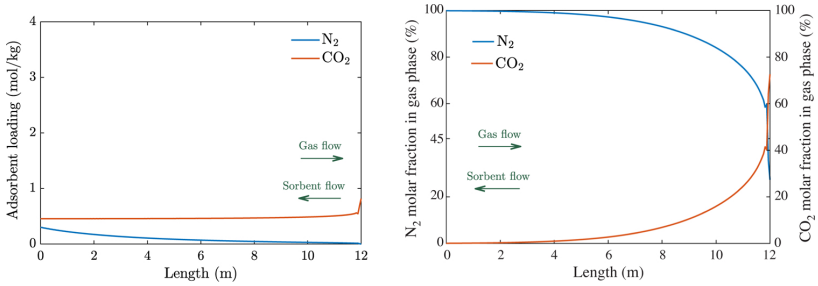

Fig. 9. Adsorbent loading (left) and molar fraction (right) profiles along the vertical coordinate of the cooling section.

higher inlet temperature (180 °C, against 40 °C for the MEA process). A graphical representation of how the individual factors contribute to the total reduction in the net electric efficiency for each case is shown in Fig. 11, where the power loss due to steam extraction is calculated as the difference between the steam turbine power output in the reference NGCC without CO_2 capture and the NGCC with the corresponding capture system.

In terms of net electric efficiency, the values obtained for the MEA process are in line with the results of similar studies available in literature (Lillia et al., 2018; Fernandez et al., 2014). Fernandez et al. (2014) estimated a 8.4 percentage points reduction, versus the 8.0 and 8.4 of this study, corresponding to Case A and Case B respectively. As expected, the higher energy penalty is associated to the MEA process with the higher capture rate (Case B). By increasing the capture rate, the heat input of the extracted steam also increases, with a negative effect on the power output.

With respect to the MBTSA processes, better performances in terms of net electric efficiency are obtained for Case A, in which the steam extracting pressure is lower, with a beneficial effect on the power output of the steam turbines. Despite the worse performance in term of net electric efficiency, Case B of MBTSA process outperform the other four cases evaluated in regards to the amount of CO_2 emitted by the power plant.

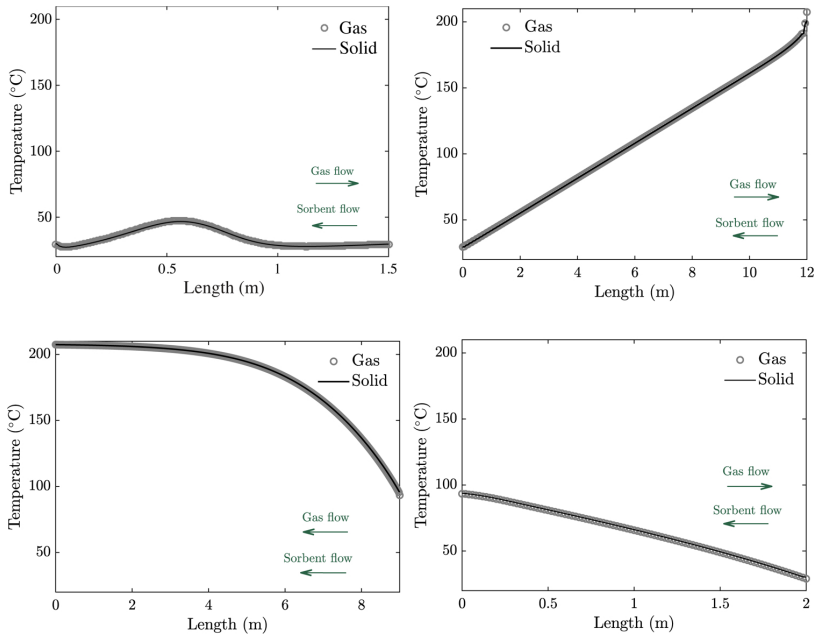

Fig. 10. Temperature profiles along the vertical coordinate of: adsorption section (top left), cooling section (top right), desorption section (bottom left), cooling section (bottom right).

Table 4
Summary of process design and process simulation results for two case studies (values referred to the two MBTSA units).

	Case A	Case B
Amount of circulating sorbent	570 kg/s	490 kg/s
CO_2 working capacity	2.76 mol/$kg_{sorbent}$	3.28 mol/$kg_{sorbent}$
Regeneration temperature	180 °C	207 °C
CO_2 purity (%)	95.1	95.8
CO_2 capture rate (%)	96.0	98.2
Energy required for sorbent regeneration		
–Without heat integration	152.7 MW_{th}	158.7 MW_{th}
–With heat integration	101.2 MW_{th}	100.7 MW_{th}
Specific energy for sorbent regeneration		
–Without heat integration	2.21 MJ/$kg_{CO2captured}$	2.24 MJ/$kg_{CO2captured}$
–With heat integration	1.46 MJ/$kg_{CO2captured}$	1.42 MJ/$kg_{CO2captured}$

4. Conclusions

The application of MBTSA technology for CO_2 capture from a NGCC power plant is evaluated. The performances of the MBTSA process in terms of CO_2 capture rate and CO_2 purity are assessed via dynamic simulations performed in gPROMS software. Input model parameters concerning the adsorbent material were provided by experimentally measuring adsorption isotherms on a pelletized sample of Zeolite 13X.

When designing the MBTSA process, two cases employing different regeneration temperatures (180 °C for Case A and 207 °C for Case B) were compared. In both cases the proposed system is able to meet the process target specifications, being the obtained CO_2 purity 95.1% and 95.8% for Case A and Case B respectively, with corresponding capture rates of 96.0% and 98.2%.

Based on the performed MBTSA simulations, the thermal energy required for sorbent regeneration is estimated. Promising results are obtained when considering internal heat recovery, through which approximately 35% of the total energy required can be saved.

A more comprehensive analysis of the energy consumption associated to the CO_2 capture process is performed by implementing a full plant model of the NGCC integrated with the capture process. The Thermoflex software is used for this purpose. Besides accounting for the effect of steam bleeding on the overall power plant performances, the developed model allows a detailed analysis of the energy penalties associated to the various CO_2 capture auxiliaries (e.g. booster fans, CO_2 compressor, and electric chiller for water removal from flue gas).

Table 5
Results of the power plant integration with the MBTSA and comparison with the MEA capture process.

	Without capture	MEA case A	MEA case B	MBTSA case A	MBTSA case B
Capture efficiency (%)	–	90.0	95.0	96.0	98.2
CO_2 captured (t/h)	–	229.4	242.2	243.2	248.8
CO_2 emitted (t/h)	253.4	23.9	11.2	10.1	4.6
Specific emissions (kg/MWh)	316.0	32.5	15.3	13.2	6.0
GT gross electric power output (MW)	555.3	555.3	555.3	555.3	555.3
ST gross electric power output (MW)	246.5	182.2	178.5	214.8	211.3
Gross power output (MW)	801.8	737.5	733.9	770.1	766.7
Net power output (MW)	792.7	693.1	688.1	692.9	689.0
Net electric efficiency (% LHV)	63.1	55.1	54.7	56.2	55.9
Details on the steam extraction					
Steam extraction temperature (°C)		292	292	395	465
Steam extraction pressure (bar)		3.62	3.62	8.17	13.16
Steam extracted flow (kg/s)		106.8	101.2	38.0	35.9
Heat input (MW)		251.7	265.7	101.2	100.7
Detailed plant auxiliaries					
Gas turbine auxiliaries (MW)	1.071	1.071	1.071	1.071	1.071
Condenser c.w. pump (MW)	0.728	0.423	0.384	0.559	0.569
Condensate forwarding pump (MW)	0.419	0.162	0.147	0.322	0.327
HP feedwater pump (MW)	4.604	4.609	4.609	4.605	4.605
IP feedwater pump (MW)	1.317	1.316	1.316	1.316	1.316
Steam turbine auxiliaries (MW)	0.518	0.383	0.375	0.451	0.444
Miscellaneous auxiliaries (MW)	0.401	0.369	0.367	0.385	0.383
Total CO_2 capture auxiliaries (MW)	0	36.090	37.459	54.493	54.728
Total plant auxiliaries (MW)	9.057	44.422	45.729	63.246	63.490
Detailed CO_2 capture auxiliaries					
Booster fan(s) (MW)		10.827	10.827	10.023	10.008
Electric chiller (MW)				15.330	15.330
Intercooled compressor (MW)		20.479	21.617	28.824	29.077
Cooling water pump (MW)		2.165	2.252	0.316	0.315
Solvent circulation pump (MW)		1.973	2.082		
Condensate pump (MW)		0.014	0.015		
Others (MW)		0.632	0.667		

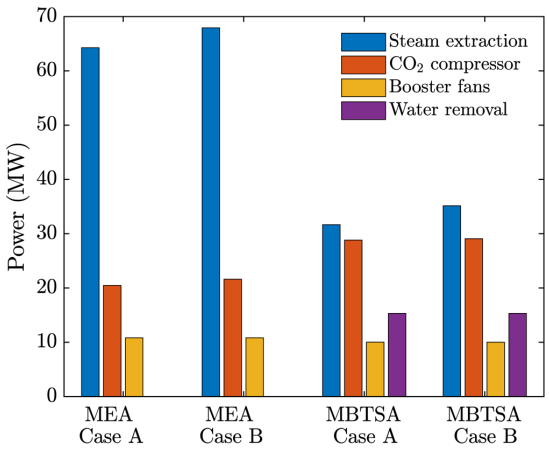

Fig. 11. Individual contribution to the overall duty of the analyzed capture processes.

For comparison purposes, the application of a benchmark capture system was also considered, by suitably modifying the Thermoflex model of the reference NGCC. Interestingly, no significant difference is observed between the proposed MBTSA system and the MEA process: the overall net electric efficiency decreases from 63.1% to 55.1% and 56.2% when applying the capture process to the MEA and the MBTSA respectively. While the MBTSA requires less steam when compared to the MEA system, the latter presents a lower energy penalty associated to the CO_2 capture auxiliaries, compensating the higher effect associated to steam bleeding.

In conclusion, the results show that, based on the assumptions made, the simulated MBTSA process applied to NGCC power plant is suitable for capturing CO_2 at high purity and high capture rate, while being competitive with the state-of-the-art capture process in terms of energy penalties. Considering the much earlier stage of development of this technology in respect with the MEA process, the MBTSA seems to offer a larger potential for process improvement and should be considered for further development. In this respect, dedicated experimental activities are underway including testing of a lab scale MBTSA system.

Acknowledgment

We acknowledge the Research Council of Norway for its financial support through the EDemoTeC project (Grant no. 267873) within the CLIMIT program.

Appendix A. Fuel properties and MEA process specifications

Tables A6 and A7

Table A6
Fuel specification used in the NGCC simulations.

Volumetric composition		
Hydrogen	H_2	0.36 %
Oxygen	O_2	0.07 %
Nitrogen	N_2	3.65 %
Carbon monoxide	CO	0.09 %
Carbon dioxide	CO_2	0.34 %
Methane	CH_4	87 %
Ethane	C_2H_6	8.46 %
Ethylene	C_2H_6	0.03 %
Heating values		
LHV	46280	kJ/kg
HHV	51237	kJ/kg

Table A7
Specification of the MEA capture process.

Parameter	Value
Specific energy input (Fernandez et al., 2014)	3.95 MJ/kg
Cooler exit temperature	40 °C
CO_2 compressor inlet temperature	40 °C
CO_2 compressor inlet pressure	1.6 bar
CO_2 compressor delivery pressure	110 bar
Number of compressor stages	5
Booster fan isentropic efficiency	85%
Booster fan mech. + elec. efficiency	95%
Pumps efficiency	75%
Total gas pressure drop (in absorber)	0.1 bar
Steam pressure at reboiler inlet (Fernandez et al., 2014)	3.05 bar
Steam temperature at reboiler inlet (Fernandez et al., 2014)	134 °C

Appendix B. Main assumptions and remarks on the MBTSA model

The conservation equations describing the moving bed adsorption system are obtained by assuming that mass, velocity and temperature gradients in the radial direction are negligible. The model also assumes ideal gas behavior in the bulk phase, constant cross sectional area, constant velocity of the adsorbent and constant void fraction.

In the resulting one-dimensional balance equations, detailed in Fig. 2, two phases can be distinguished: (i) a gas phase, which exchanges energy and mass with the adsorbent, and only energy with the wall; and (ii) a solid phase, onto which the gas diffuses and adsorbs.

The main model variables are therefore: gas velocity and pressure, gas concentrations of each component in the bulk phase, gas concentrations in the macropores of the adsorbents, adsorbed phase concentrations, temperature of the bulk gas phase and temperature of the solid phase. While the pressure drops are computed using the Ergun equation, the adsorption equilibrium between the gas phase in the macropores and the adsorbed phase is described by the Virial isotherms model.

The adsorption kinetics is predicted with a lumped resistance model based on the linear driving force (LDF) approximation. The exponential temperature dependence typical of activated processes is used to compute the effective diffusivity within the adsorbent. The model equation and parameters used for this purpose are given in Table B8, together with other supplementary equations and correlations used in the simulations.

As previously mentioned, for providing (and removing) the necessary heat to the system, an indirect contact type heat exchanger configuration was assumed. For simplicity, a constant convective heat transfer parameter ($h_{g,hx}$), and fixed temperature of the heat transfer surface along the vertical axis (T_{hx}) were assumed. The hydraulic diameter (D_h) of the adsorbent-gas side (i.e. the ratio between the volume of the adsorbent-gas side and the heat transfer area on the same side, at a given positing along the vertical axis) is adjusted in order to ensure that sufficient heat transfer area is available, thus allowing the adsorbent to reach the desired temperature within the traversed heat exchanger. Numerical values of the assumed heat transfer parameters, system dimensions, and residence times within each sections of the moving bed are given in Table B9.

Table B8
Supplementary equations and model parameters used in the MBTSA simulations.

Correlations	
Molecular diffusivity (Wilke, 1950)	$D_m = \frac{1-y_i}{\sum_{j\neq i}^{n} \frac{y_i}{D_{ij}}}$
Binary diffusivity (Bird et al., 2002)	$D_{ij} = \frac{0.01883T^{3/2}}{P\sigma_{ij}^2\Omega_{D_{ij}}}\sqrt{\frac{1}{M_{w,i}}+\frac{1}{M_{w,j}}}$
Macropore diffusivity (Yang, 1987)	$\frac{1}{D_p} = \tau_p\left(\frac{1}{D_k}+\frac{1}{D_m}\right)$
Knudsen diffusivity (Ruthven, 1984)	$D_k = 97r_p\sqrt{\frac{T}{M_w}}$
Rate of adsorption in micropores	$\frac{D_c}{r_c^2} = \frac{D_c^0}{r_c^2}\exp\left(\frac{Ea}{RT}\right)$
Axial dispersion coefficient	$D_z = \frac{D_m}{\varepsilon_c}(20 + 0.5\,Sc\,Re)$
Axial thermal conductivity of gas	$\lambda = k_g(7 + 0.5Pr\,Re)$
Scherwood number correlation	$Sh = 2.0 + 1.1\,Re^{0.6}\,Sc^{1/3}$
Nusselt number correlation	$Nu = 2.0 + 1.1Re^{0.6}\,Pr^{1/3}$

Dimensionless numbers	Parameters value
Biot, $Bi = \frac{r_p k_f}{\varepsilon_p D_p}$	Bed void fraction (ads. section): $\varepsilon_c = 0.8$
Reynolds, $Re = \frac{\rho_g u d_p}{\mu_g}$	Bed void fraction (other sections): $\varepsilon_c = 0.6$
Schmidt, $Sc = \frac{\mu_g}{\rho_g D_m}$	Parameters of adsorption rate
Prandtl, $Pr = \frac{C_{p,g}\mu_g}{k_g}$	CO_2: $E_a = 15$ kJ/mol; $D_c^0/r^2 = 25\ s^{-1}$
Sherwood, $Sh = \frac{k_f d_p}{D_m}$	N_2: $E_a = 12$ kJ/mol; $D_c^0/r^2 = 10\ s^{-1}$

Table B9
Details on the MBTSA design and parameters.

	MBTSA section			
	Adsorption	Preheating	Desorption	Cooling
Length (m)	1.5	2	9	12
Number of discretization intervals	200	100	400	200
Inlet gas superficial velocity ($m\,s^{-1}$)	1.50			
Cross sectional area (m^2)	254.5	78.5	78.5	78.5
Adsorbent residence time (s)	257	247	1111	1481
Heat transfer coefficient ($W\,m^{-2}\,s^{-1}$)	90	90	90	90
Hydraulic diameter (m)	0.04	0.10	0.10	0.08

References

Anantharaman, R., Bolland, O., Booth, N., van Dorst, E., Ekstrom, C., Fernandez, E.S., Editor, F.F., Macchi, E., Manzolini, G., Nikolic, D., Pfeffer, A., Prins, M., Rezvani, S., Robinson, L., 2011. CESAR-D2.4.3-APPROVED-European Best Practice Guidelines for CO_2 Capture Technologies – EBTF. Technical Report. Alstom UK, NTNU, E.ON, Shell, Vattenfall, TNO, Alstom UK, Polit. di Milano, Univ. of Ulster.

Baksh, M.S.A., Kikkinides, E.S., Yang, R.T., 1992. Lithium type X zeolite as a superior sorbent for air separation. Sep. Sci. Technol. 27, 277–294.

Barrer, R.M., 1981. Sorption in porous crystals: equilibria and their interpretation. J. Chem. Technol. Biotechnol. 31, 71–85.

Bird, R.B., Stewart, W.E., Lightfoot, E.N., 2002. Transport Phenomena, 2nd edition. Wiley, New York.

Chue, K., Kim, J., Yoo, Y., Cho, S., Yang, R., 1995. Comparison of activated carbon and zeolite 13X for CO_2 recovery from flue gas by pressure swing adsorption. Ind. Res. Eng. Chem. 34, 591–598.

Fernandez, E.S., Goetheer, E., Manzolini, G., Macchi, E., Rezvani, S., Vlugt, T., 2014. Thermodynamic assessment of amine based CO_2 capture technologies in power plants based on European benchmarking task force methodology. Fuel 129, 318–329.

Franco, F., Anantharaman, R., Bolland, O., Booth, N., van Dorst, E., Ekstrom, C., Fernandes, E., Macchi, E., Manzolini, G., Nicolic, D., Pfeffer, A., Prins, M., Rezvani, S., Robinson, L., 2011. Test Cases and Preliminary Benchmarking Results from the Three Projects. Technical Report. Alstom UK.

gPROMS Model Builder Version 5.0. Process System Enterprise (PSE), UK.

Grande, C.A., Kvamsdal, H., Mondino, G., Blom, R., 2017. Development of moving bed temperature swing adsorption (MBTSA) process for post-combustion CO_2 capture: initial benchmarking in a (NGCC) context. Energy Procedia 114, 2203–2210.

Hefti, M., Marx, D., Joss, L., Mazzotti, M., 2015. Adsorption equilibrium of binary mixtures of carbon dioxide and nitrogen on zeolites ZSM-5 and 13X. Microporous Mesoporous Mater. 215, 215–228.

Hornbostel, M.D., Bao, J., Krishnan, G., Nagar, A., Jayaweera, I., Kobayashi, T., Sanjurjo, A., Sweeney, J., Carruthers, D., Petruska, M.A., 2013. Characteristics of an advanced carbon sorbent for CO_2 capture. Carbon 56, 77–85.

Kim, K., Park, Y.K., Park, J., Jung, E., Seo, H., Kim, H., Lee, K.S., 2014. Performance comparison of moving and fluidized bed sorption systems for an energy-efficient solid sorbent-based carbon capture process. Energy Procedia 63, 1151–1161.

Kim, K., Son, Y., Lee, W.B., Lee, K.S., 2013. Moving bed adsorption process with internal heat integration for carbon dioxide capture. Int. J. Greenhouse Gas Control 17, 13–24.

Knaebel, K., 2009. Temperature Swing Adsorption System.

Liang, Z., Fu, K., Idem, R., Tontiwachwuthikul, P., 2016. Review on current advances, future challenges and consideration issues for post-combustion CO_2 capture using amine-based absorbents. Chin. J. Chem. Eng. 24, 278–288.

Lillia, S., Bonalumi, D., Grande, C., Manzolini, G., 2018. A comprehensive modeling of the hybrid temperature electric swing adsorption process for CO_2 capture. Int. J. Greenhouse Gas Control 74, 155–173.

Liu, Z., Grande, C.A., Li, P., Yu, J., Rodrigues, A.E., 2011. Multi-bed vacuum pressure swing adsorption for carbon dioxide capture from flue gas. Sep. Purif. Technol. 81, 307–317.

Merel, J., Clausse, M., Meunier, F., 2008. Experimental investigation on CO_2 post-combustion capture by indirect thermal swing adsorption using 13X and 5A zeolites. Ind. Eng. Chem. Res. 47, 209–215.

Mondino, G., Grande, C.A., Blom, R., 2017. Effect of gas recycling on the performance of a

moving bed temperature-swing (MBTSA) process for CO_2 capture in a coal fired power plant context. Energies 10, 745.
Park, Y.J., Lee, S.J., Moon, J.H., Choi, D.K., Lee, C.H., 2006. Adsorption equilibria of O_2, N_2, and Ar on carbon molecular sieve and zeolites 10X, 13X, and LiX. J. Chem. Data Eng. 51, 1001–1008.
Plaza, M.G., Rubiera, F., Pevida, C., 2017. Evaluating the feasibility of a TSA process based on steam stripping in combination with structured carbon adsorbents to capture CO_2 from a coal power plant. Energy Fuels 31, 9760–9775.
Ribeiro, A.M., Sauer, T.P., Grande, C.A., Moreira, R.F.P.M., Loureiro, J.M., Rodrigues, A.E., 2008. Adsorption equilibrium and kinetics of water vapor on different adsorbents. Ind. Eng. Chem. Res. 47, 7019–7026.
Ruthven, D.M., 1984. Principles of Adsorption and Adsorption Processes. John Wiley & Sons.
Shen, C., Grande, C.A., Li, P., Yu, J., Rodrigues, A.E., 2010. Adsorption equilibria and kinetics of CO_2 and N_2 on activated carbon beads. Chem. Eng. J. 160, 398–407.
Shen, C., Liu, Z., Li, P., Yu, J., 2012. Two-stage VPSA process for CO_2 capture from flue gas using activated carbon beads. Ind. Eng. Chem. Res. 51, 5011–5021.
Son, Y., Kim, K., Lee, K.S., 2014. Feasibility study of a moving-bed adsorption process with heat integration for CO_2 capture through energy evaluation and optimization. Energy Fuels 28, 7599–7608.
Taqvi, S.M., LeVan, M.D., 1997. Virial description of two-component adsorption on homogeneous and heterogeneous surfaces. Ind. Eng. Chem. Res. 36, 2197–2206.
Thermoflow Version 27. Termoflow Inc.
Vandervort, C., 2018. Advancements in H class gas turbines and combined cycle power plants. In: ASME Turbo Expo 2018: Turbomachinery Technical Conference and Exposition. American Society of Mechanical Engineers. V003T08A007.
Wilke, C.R., 1950. Diffusional properties of multicomponent gases. Chem. Eng. Prog. 46, 95–104.
Yang, R.T., 1987. Gas Separation by Adsorption Processes. Butterworth-Heinemann.
Zanco, S.E., Mazzotti, M., Gazzani, M., Romano, M.C., Martínez, I., 2018. Modeling of circulating fluidized beds systems for post-combustion CO_2 capture via temperature swing adsorption. AIChE J. 64, 1744–1759.

I&EC research
Industrial & Engineering Chemistry Research

pubs.acs.org/IECR

Article

Production of MOF Adsorbent Spheres and Comparison of Their Performance with Zeolite 13X in a Moving-Bed TSA Process for Postcombustion CO_2 Capture

Giorgia Mondino,* Aud I. Spjelkavik, Terje Didriksen, Shreenath Krishnamurthy, Ruth Elisabeth Stensrød, Carlos A. Grande, Lars O. Nord, and Richard Blom*

Cite This: *Ind. Eng. Chem. Res.* 2020, 59, 7198−7211

Read Online

ACCESS | Metrics & More | Article Recommendations | Supporting Information

ABSTRACT: Well-shaped 300−700 μm spheres of aggregated metal−organic framework CPO-27-Ni crystallites have been produced using a spray-granulation method with cross-bonded alginate as the binder. The spheres are suitable for use in a moving-bed temperature-swing adsorption (MBTSA) process for postcombustion CO_2 capture. The adsorption isotherm data of CO_2, N_2 ,and H_2O have been measured in the temperature intervalof 30−120 °C, and adsorption kinetics have been estimated from breakthrough measurements. The adsorption data together with the physical characteristics of the spheres (pore-size distribution and porosity) have been used to simulate the performance of a MBTSA process utilizing the CPO-27-Ni/alginate spheres as adsorbent and compared to similar simulations using Zeolite 13X spheres. Simulations have been carried out in a natural gas-fired power plant (NGCC) context. The process simulations indicate that the net electric efficiency of the NGCC plant with a MBTSA process utilizing the CPO-27-Ni/alginate spheres is similar to that of a MBTSA process utilizing Zeolite 13X adsorbent, 56.1% and 55.9%, respectively, which are slightly higher than the net efficiency of the benchmark case NGCC with a MEA-based solvent process of 54.7%.

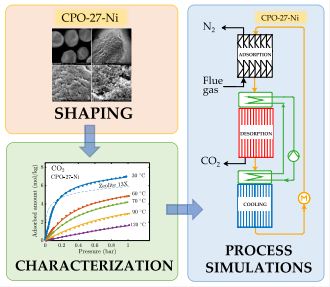

INTRODUCTION

Metal−organic frameworks (MOFs) are a class of microporous materials with large structural and chemical diversity and a high number of potential uses within adsorption-based technologies such as gas storage,[1−10] gas and liquid separation,[11−13] protection against toxic-industry compounds (TICs),[14] heat pumps and chillers,[15,16] water harvesting,[17] antimicrobial treatment,[18] catalysis,[19] and sensors.[20−22] Yet the use of MOFs is negligible commercially, partly due to upscaling and cost issues, and on the more technical side, one of the hindrances for further development is the lack of real testing of shaped MOFs under realistic conditions. Since most technologies require materials with a specific structure, either pellets, spheres, monoliths, or other, it is important that high yield methods for shaping MOFs are developed that maintain the good properties of the starting material but have a higher material density and a shape that gives optimal fluid transport throughout the material during the process. Having this, relevant data for the different applications can be obtained.

MOFs combine an inorganic atom, ion, or cluster with one or more multifunctional organic linkers to build up the porous framework. Some MOFs are only stable at relatively low temperatures and decompose readily when exposed to water, while others are stable under harsh conditions such as in boiling water over prolonged periods.[23] Furthermore, the physical stability of the MOF crystallites toward external pressures and elevated temperatures vary widely, and especially, MOFs having extremely high surface areas are the most sensitive and will collapse at relatively low pressures. Traditional methods for material shaping, such as extrusion and pelletization, involve the use of pressure, which often causes a significant reduction in specific surface area and porosity.[24−26] Therefore, in many cases, soft chemistry methods for MOF shaping are needed that give the wanted structures with the needed physical strength and at the same time maintain the porosity and surface area of the MOF.

When used in CO_2 capture technologies, the adsorbent material should be able to selectively adsorb CO_2 from the targeted gas mixture. In the case where the CO_2 is to be removed from a flue gas, either from power plants (coal or gas fired) or energy intensive industries (cement, steel, waste incinerators), the total pressure of the flue gas is often around 1 atm with 4−30 vol % CO_2, the rest being N_2, O_2, H_2O, and

Special Issue: Carbon Capture and Utilization

Received: November 21, 2019
Revised: March 28, 2020
Accepted: March 30, 2020
Published: March 30, 2020

https://dx.doi.org/10.1021/acs.iecr.9b06387
Ind. Eng. Chem. Res. 2020, 59, 7198−7211

varying amounts (most often in the ppm range) of SO_x, NO_x, and other impurities depending on the combustion source and flue gas cleaning. Disregarding the sulfur- and nitrogen-containing impurities, there are several MOFs that show promising performance for removal of CO_2 at low partial pressures in the presence of water vapor: the CPO-27/MOF-74/M_2(dobdc) (dobdc = 2,5-dioxidobenzene-1,4-dicarboxylate) family with either Mg or Ni as a metal component,[27] UTSA-16,[28] the SiFSIX family with either Cu or Zn as a metal component,[29] and last, but not least, the Diamin-appended mmen-Mg_2(dobpdc) (dobpdc = 4,4′-dioxidobiphenyl-3,3′-dicarboxylate) system,[30] all showing high selectivity for CO_2 over N_2, significant CO_2 capacity at around 10 kPa CO_2 pressure, and also reasonable stable cyclic performance in the presence of water vapor.[31−33]

We have recently developed a soft-chemical method to produce well-shaped MOF spheres based on the use of cross-bonded alginates.[34] With this method, we can produce MOF spheres containing 85−95 wt % MOF (dry basis) with negligible loss in specific surface area except the 10%−15% loss induced by the alginate in the spheres. The method is general but requires that the MOF is stable in water for the time needed to make the spheres, typically around 1 h.

Different processes need different sizes of the spheres. In the search for new promising adsorbent and processes for postcombustion CO_2 capture, we are building a lab-scale moving-bed temperature swing adsorption (MBTSA) unit.[35−38] Such a process will need adsorbent particles having good flowability and average diameters in the 0.3−1.0 mm range to avoid too long intraparticle diffusion pathways causing slow rate of adsorption. We believe spherically shaped particles will best fill these needs. We have recently presented the production and characterization of 2−3 mm spheres of CPO-27-Ni for fixed bed pressure-swing adsorption (PSA) applications.[32,39] In the present Article, we present the properties of CPO-27-Ni spheres and their production by the alginate method using a spray nozzle that gives the droplet size distribution in the range from 0.3 to 0.7 mm suitable for use in a MBTSA process. The method is based on adding the MOF powder to an aqueous alginate solution yielding a homogeneous slurry with low viscosity and the wanted alginate/MOF ratio allowing the slurry to be atomized by use of a suitable spray nozzle before entering a $CaCl_2$ solution. Divalent Ca^{2+} cross binds the alginate, fixating the droplet shape, yielding spherical alginate/MOF/H_2O beads which can be dried under mild conditions yielding dry alginate/MOF spheres. We present the physical characteristics of the spheres (size distribution, porosity, and density) and the adsorption properties relevant for postcombustion CO_2 capture: CO_2, N_2, and H_2O equilibrium isotherms and kinetic parameters estimated from breakthrough curves using the individual components. We have used the data to evaluate the performance of a MBTSA process for postcombustion CO_2 capture in an NGCC context. A comparison has also been done with recently published results obtained using Zeolite 13X spheres as the adsorbent.[38]

EXPERIMENTAL SECTION

Synthesis of CPO-27-Ni Powder. Around 100 g of batch CPO-27-Ni was produced in a 5.5 L autoclave using $Ni(CH_3COO)_2$ $4H_2O$ (99% from Aldrich) and 2,5-dihydroxyterephtalic acid (99.6% from Carbosynth) in an all-water synthesis as described in ref 32. Here, 224.0 g of Ni-acetate and 89.2 g of 2,5-dihydroxyterephtalic acid were separately suspended in 1.5 L of deionized water. The two suspensions were rapidly mixed together under continuous stirring before being introduced to the autoclave equipped with an impeller. The temperature was set to 110 °C, and the rotation speed of the impeller was set to 174 rpm. The reaction time was 71 h before the autoclave was cooled to ambient temperature overnight. After separating the product from the solvent by decantation and centrifugation, the crystalline powder was further washed three times with deionized water (approximately 1.5 L per wash lasting approximately 1 h) before storage as a wet sludge. The solid content of the sludge was estimated to be 24.2 wt % from measuring the mass before and after drying under vacuum overnight at 120 °C. The X-ray pattern (reported in the Supporting Information) is consistent with earlier CPO-27-Ni diagrams in ref 40.

Production of CPO-27-Ni Spheres. Here, 15.9 g of Alginate (Protanal LF10/60 from FMC) was dissolved in 1 L of deionized water and further stirred overnight to ensure a homogeneous solution. Then, 372.7 g of the wet CPO-27-Ni sludge (approximately 90.2 g of dry CPO-27-Ni) was added to the alginate/water solution. An additional 307.5 mL of deionized water was used to wash out the rest of the CPO-27-Ni sludge from the beaker. The slurry was then stirred overnight to ensure homogeneity. The setup used for spray-spheronizing CPO-27-Ni beads is shown in Figures S1 and S2 in the Supporting Information. Using a peristatic pump, the slurry is fed at a speed of 25 mL/min to a 0.5 mm spray nozzle using air at around 4.0 L/min as the atomizing agent. Then, 0.2 M $CaCl_2$ (98% from Aldrich) in deionized water was used as the gelation bath. After approximately 1 h, the spheres were removed from the gelation bath and washed. The washing was done by continuously flowing (approximately 3 L/h) tap water upward through a 1 L glass column with a glass filter keeping the spheres in place. This continuous washing took place for 21 h, and then, the spheres were collected and stored wet in a closed bottle. To find the optimal washing time, small samples of beads were removed from the washing setup after 45 min, 3 h, 21 h, and 45 h. BET analyses of the samples showed that 21 h were needed to reach a stable high specific surface area.

For comparison, a sample of the binderless Zeolite 13X spheres with sphere size distribution from 500 to 900 μm was received from CWK in Germany.

Adsorbent Characterization. *BET and Pore Characterization.* Specific surface areas were estimated from N_2 isotherms recorded at liquid nitrogen temperatures (77 K) using the BET formalism. Sample activation was typically carried out overnight at an external pretreatment unit (BELPREP II vac) at 120 °C under vacuum prior to a short (2 h) pretreatment at the BELSORP mini-instrument. The micropore volume was estimated using the t-plot method based on said N_2 isotherm measurements at 77 K, while larger pores were analyzed using a Hg porosimeter (Micromeritics AutoPore IV 9520) operating from 0.1 Pa to 414 MPa covering the pore diameter range from approximately 360 to 0.003 μm.

Thermal Stability (TG-DSC-MS). The thermal stability of the CPO-27-Ni precursor powder and the shaped beads were analyzed by using a TG-DSC-MS instrument (Netzsch STA 449 F1 instrument equipped with a QMS 403 C MS analyzer). Experiments were carried out using approximately 20 mg of material, a 2 °C/min heating rate, and an air flow of 50 mL/min. First, the samples were heated for 16 h in the air (50 mL/

https://dx.doi.org/10.1021/acs.iecr.9b06387
Ind. Eng. Chem. Res. 2020, 59, 7198−7211

min) at 90 °C to remove volatile components, and then, the samples were heated to 800 °C. Mass changes (TG) and heat transfer within the sample (DSC) as well as analyses of the kinds of volatile components leaving the sample during the process (by mass spectrometry, MS) were recorded. On the basis of the experiments, the thermal stability of the samples was evaluated.

Powder X-ray Diffraction. Powder X-ray diffraction patterns from 2θ = 5−60 of the MOF adsorbents were measured using a PANalytical EMPYREAN diffractometer equipped with a Cu source and Pixel 3D detector.

Scanning Electron Microscopy (SEM). Scanning electron microscopy pictures of the CPO-27-Ni spheres were collected on a FEI Nova NanoSEM 650 instrument.

Single Component Isotherm Measurements. Isotherms of pure CO_2, N_2, and H_2O were collected up to 1 bar (0.04 bar for H_2O) at different temperatures between 30 and 120 °C on a commercial volumetric BELSORP Max instrument (BEL, Japan). Sample activation was typically carried out overnight with an external pretreatment unit (BELPREP II vac) at 120 °C under vacuum prior to a short (2 h) pretreatment with the BELSORP Max instrument as part of the isotherm measurement procedure.

Adsorption Kinetics. Adsorption and desorption experiments were carried out using a dynamic column breakthrough apparatus. The schematic of the apparatus is shown in Figure 1. It consists of gas flow controllers to provide fixed flow rates,

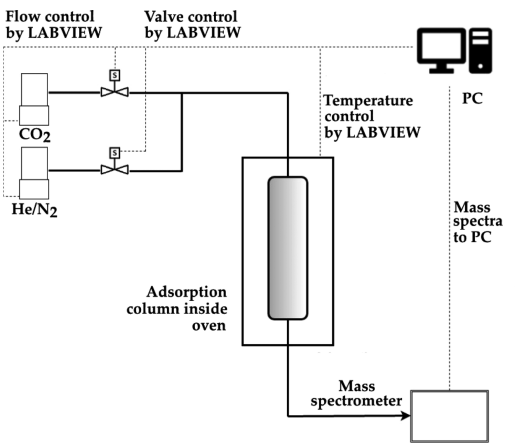

Figure 1. Schematic of the breakthrough setup.

an adsorption column housed in a temperature-controlled oven, and a mass spectrometer to detect the concentration downstream. Initially, the adsorbent column was regenerated under a helium/nitrogen purge of 100 mL/min overnight at 120 °C, and following that, the column was cooled to the experimental temperature of 50 °C. Once thermal equilibrium is reached, a step input in concentration was provided (6.5% CO_2 in He or N_2). The adsorption step was carried out with 17 mL/min of CO_2 and 261 mL/min of He or N_2 gas. After equilibrium was attained, desorption was carried out with the pure carrier gas. Experiments were carried out with two different particle sizes, namely, 300−500 and 500−700 μm. About 1.3 g of the smaller particles and 1.0 g of the larger particles were used in the experiments. Due to the difference in mass, the packed height for the two particle sizes were 7.3 and 4.6 cm, respectively. A thermocouple was also inserted into the packed bed to measure the temperature profile inside the adsorption column.

THEORETICAL BASIS

Modeling of Adsorption Isotherms. Equilibrium data of pure CO_2 and N_2 were fitted using the Virial isotherm model, given by[41,42]

$$P_i = \frac{q_i^*}{K_i}\exp[A_i q_i^* + B_i q_i^{*2} + C_i q_i^{*3}] \tag{1}$$

where subscript i indicates the adsorbate (CO_2 or N_2), of which p_i is the pressure, q_i the amount adsorbed, and K_i the Henry constant. The temperature dependence of the Virial coefficients A_i, B_i, and C_i was expressed by

$$A_i = A_{0,i} + \frac{A_{1,i}}{T_s};\ B_i = B_{0,i} + \frac{B_{1,i}}{T_s};\ C_i = C_{0,i} + \frac{C_{1,i}}{T_s} \tag{2}$$

while the Van't Hoff equation was used for the Henry constant

$$K_i = K_{\infty,i}\exp\left(\frac{\Delta H_i^0}{RT}\right) \tag{3}$$

where $K_{\infty,i}$ is the adsorption constant at infinite temperature, ΔH_i^0 the heat of adsorption at zero coverage, and R the universal gas constant.

The fitting of the experimental data to extract the model parameters was performed on Scilab 6.0.2[43] using the Nelder−Mead optimization routine for minimizing the square of residuals between the experimental data and predicted isotherms, in the whole temperature range simultaneously.

On the basis of the fitting parameters from pure gas measurements, multicomponent adsorption equilibrium can be predicted by applying the following extension of the Virial model[44]

$$P_i = \frac{q_i^*}{K_i}\exp\left[\sum_{j=1}^{N} A_{ij} q_j^* + \sum_{j=1}^{N}\sum_{k=1}^{N} B_{ijk} q_j^* q_k^* + \sum_{j=1}^{N}\sum_{k=1}^{N}\sum_{l=1}^{N} C_{ijkl} q_j^* q_k^* q_l^*\right] \tag{4}$$

where the mixing Virial coefficients are calculated as

$$A_{ij} = \frac{A_i + A_j}{2};\ B_{ijk} = \frac{B_i + B_j + B_k}{3};\ C_{ijkl} = \frac{C_i + C_j + C_k + C_l}{4} \tag{5}$$

Equations 4 and 5 were used in the MBTSA simulations to take into account competitive adsorption of N_2 and CO_2.

Modeling of Moving-Bed Temperature-Swing Adsorption (MBTSA) Process. On the basis of the measured equilibrium and kinetics properties, the use of the CPO-27-Ni spheres in a moving-bed temperature-swing adsorption process for CO_2 capture is evaluated via simulations.

The moving-bed system considered in this study, as schematically shown in Figure 2, consists of a series of units through which the adsorbent circulates while cyclically adsorbing and desorbing CO_2 by means of temperature swing. More specifically, the adsorption of CO_2 from the flue gas occurs within the top unit (adsorption section) where adsorbent and flue gas flow countercurrently to each other,

https://dx.doi.org/10.1021/acs.iecr.9b06387
Ind. Eng. Chem. Res. 2020, 59, 7198−7211

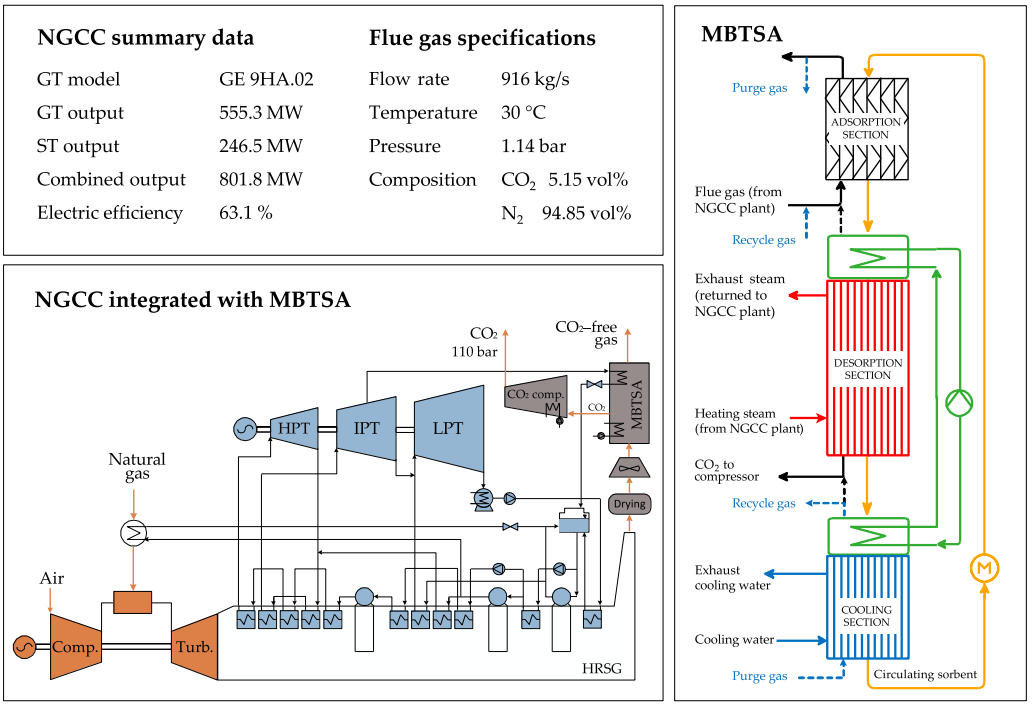

Figure 2. Specifications of the flue gas and reference NGCC power plant (top left), process flow diagram of the NGCC power plant with CO_2 capture (bottom left), and schematic diagram of MBTSA (right). The figure is a modified version of the one presented in ref 38.

with the adsorbent being fed from the top and the gas entering from the bottom.

The adsorbed CO_2 is then released and collected in a high CO_2 purity stream by increasing the temperature of the adsorbent as it passes through the desorption section, the latter being an indirect contact heat exchanger using steam as heating media. The cycle is then closed by indirectly cooling the regenerated adsorbent in the cooling section and returning it to the adsorption section for starting a new cycle. As shown in Figure 2, the system allows for a heat-integration scheme to reduce the external energy demand by recovering heat from the hot particles leaving the desorption section to be used for preheating the adsorbent before entering this section.

For process simulations, a detailed mathematical model of the MBTSA was implemented and solved in the gPROMS Model Builder.[45] Each section of the moving bed is described by a set of coupled partial differential equations distributed over the vertical coordinate, as described below (eqs 6−10).[36−38]

The profiles of the gas phase concentration along the section height are obtained from the mass balance in the gas phase

$$\varepsilon_c \frac{\partial C_i}{\partial t} = \varepsilon_c \frac{\partial}{\partial z}\left(D_z C_T \frac{\partial Y_i}{\partial z}\right) - \frac{\partial (uC_i)}{\partial z} - \frac{(1-\varepsilon_c-\xi)a' K_m}{\mathrm{Bi}/5+1}(C_i - C_{p,i}) \tag{6}$$

where t is time; z the position along the section height; C_i, $C_{p,i}$, and Y_i the concentration in the bulk gas, the concentration in the macropores, and the molar fraction, respectively, (with the index i being either CO_2 or N_2); ε_c the bed void fraction; ξ bed fraction occupied by the structured packing; D_z the axial dispersion; C_T the total concentration; u the gas velocity; a' the adsorbent particle specific area; K_m the film mass transfer coefficient; and Bi the Biot number.

Using the linear driving force (LDF) approximation to express the macropore mass transfer, the mass balance in the macropores is given by

$$\varepsilon_p \frac{\partial C_{p,i}}{\partial t} = \varepsilon_p \frac{15 D_{p,i}}{R_p^{\,2}} \frac{\mathrm{Bi}_i}{5+\mathrm{Bi}_i}(C_i - C_{p,i}) - \rho_p\left(\frac{\partial q_i}{\partial t} + v_s \frac{\partial q_i}{\partial z}\right) - v_s \frac{\partial C_{p,i}}{\partial z} \tag{7}$$

where R_p is the particle radius, $D_{p,i}$ the macropore diffusivity, ρ_p the particle density, Bi_i the Biot number of component i, q_i the concentration of component i in the adsorbed phase, and v_s the velocity of the adsorbent.

Similarly, by expressing the mass transfer rate in the solid phase with a LDF model, the adsorbent loading profiles are computed from the mass balance in the solid phase given by

$$\frac{\partial q_i}{\partial t} + v_s \frac{\partial q_i}{\partial z} = \frac{15 D_{c,i}}{r_c^{\,2}}(q_i^* - q_i) \tag{8}$$

where $D_{c,i}$ is the micropore diffusivity, $15D_c/r_c^2$ the adsorption rate of component i in the micropores, and q_i^* the adsorbed concentration of component i in equilibrium with the corresponding local concentration in the macropore ($C_{p,i}$). As previously mentioned, the adsorption equilibrium is described using the extension of the Virial isotherm model for multicomponent systems (eq 4).

https://dx.doi.org/10.1021/acs.iecr.9b06387
Ind. Eng. Chem. Res. 2020, 59, 7198−7211

Finally, the gas and the adsorbent temperatures (T and T_s) are predicted by solving the energy balances in the gas phase (eq 9) and the energy balance in the solid phase (eq 10), respectively.

$$\varepsilon_c C_T c_v \frac{\partial T}{\partial t} = \frac{\partial}{\partial z}\left(\lambda \frac{\partial T}{\partial z}\right) - u C_T c_p \frac{\partial T}{\partial z} + \varepsilon_c RT \sum \frac{\partial C}{\partial t} - (1 - \varepsilon_c - \xi) a' h_f (T - T_s) - \frac{4 h_{g,hx}}{D_h}(T - T_{hx}) \quad (9)$$

$$[(1 - \varepsilon_c - \xi)\rho_p c_{ps} + \xi \rho_{pk} c_{pk}]\left(\frac{\partial T_s}{\partial t} + v_s \frac{\partial T_s}{\partial z}\right) = \xi \frac{\partial}{\partial z}\left(\lambda_{pk} \frac{\partial T_s}{\partial z}\right) + (1 - \varepsilon_c - \xi) a' h_f (T - T_s) + (1 - \varepsilon_c - \xi)\rho_p \sum \left(-\Delta H_i \left[\frac{\partial q_i}{\partial t} + v_s \frac{\partial q_i}{\partial z}\right]\right) + (1 - \varepsilon_c \xi)\varepsilon_p R T_s \sum \left[\frac{\partial C_{p,i}}{\partial t} + v_s \frac{\partial C_{p,i}}{\partial z}\right] \quad (10)$$

In the previous equations, ΔH_i represents the heat of adsorption, h_f the film heat transfer coefficient between the gas and the solid, $h_{g,hx}$ the convective heat transfer coefficient between the gas and the wall, D_h the hydraulic diameter, T_{hx} the temperature of the heat transfer surface, c_v and c_p the gas specific heat capacities at constant volume and constant pressure, respectively, λ and λ_{pk} the heat axial dispersion coefficient of the gas and the packing, respectively, and R the universal gas constant.

The spatial derivatives of the equations above were discretized applying the centered finite difference method with second-order approximation. The number of discretization intervals was set to 400 for the adsorption and desorption sections, 100 for the preheating section, and 300 for the cooling section. As described in more details in a previous work,[37,38] the gPROMS composite model approach[46] was used to connect the individual sections of the MBTSA in a single flowsheet and solve simultaneously the corresponding model equations, given the appropriate boundary conditions. The dynamic simulations were performed until a steady state was reached, and all results presented here refer to the steady state solution.

Further details on the approach used for model implementation and the underlying model assumptions can be found elsewhere,[37,38] while additional equations and main correlations used for computing mass and heat transfer parameters are reported in the Supporting Information.

Integration of Capture Process with Power Plant. The application of the MBTSA capture process considered in the present study refers to a natural gas combined cycle (NGCC) power plant. The impact of the capture process on the power cycle efficiency was investigated via process simulations. For this purpose, a computational model of the NGCC opportunely modified to accommodate the CO_2 capture unit was used. The model, implemented in THERMOFLEX,[47] was developed in a previously published work[38] with the purpose of performing a detailed analysis of the energy use associated with the various CO_2 capture auxiliaries, as well as allowing a direct and consistent comparison with the benchmark amine-based technology. The main characteristics of the reference NGCC (without CO_2 capture) are given in Figure 2, together with the flue gas specifications used as input to the MBTSA simulations. It should be noted that the composition of the flue gas was simplified to a binary mixture of N_2 and CO_2 in order to reduce the computational time of the moving-bed simulations. Furthermore, due to the large amount of flue gas to be treated, the use of two MBTSA units was assumed. Figure 2 also presents a schematic layout of the simulated NGCC, showing the components that have been added to the reference NGCC to mimic the presence of the MBTSA. Besides the extraction of steam needed for sorbent regeneration (i.e., in the desorption section of the moving bed), the following components are included in the model: (i) a water circuit to provide cooling to the cooling section of the moving bed, (ii) a booster fan to overcome the pressure drops occurring in the adsorption section, (iii) a drying unit to dehydrate the flue gas upstream of the MBTSA, and (iv) an intercooled CO_2 compressor. The details on how the results from the MBTSA simulations were used as basis for the integration, providing the necessary inputs to the power plant simulations, is presented in ref 38.

RESULTS AND DISCUSSION

Adsorbent Properties. We have prepared CPO-27-Ni in an all-water synthesis at a 100 g scale yielding microcrystalline powder (Figure S3). Further, the washed powder was shaped by a spray-spheronization technique at productivities around 100 g/h yielding free-flowing well-shaped 300−700 μm spheres. Comparisons of the physical parameters of the CPO-27-Ni spheres with those of the reference Zeolite 13X sample are given in Table 1. The surface area of the CPO-27-Ni spheres is somewhat lower than that of the water washed precursor CPO-27-Ni powder (1250 m^2/g). The reduction in BET area is somewhat larger than expected from the amount of alginate in the spheres (15.0 wt % on dry basis). It should be noted that extensive washing of the spheres in a continuous flow of water over more than 20 h is needed to reach the BET area noted in Table 1. The long washing time needed is most likely because removal of unreacted precursors stemming both from the MOF synthesis and from the shaping takes a longer time for the beads due to the longer diffusion pathways compared to the micron-sized CPO-27-Ni precursor crystalline powder.

Table 1. Physical Properties of CPO-27-Ni and Zeolite 13X Spheres Used in This Study

	CPO-27-Ni	Zeolite 13X
Sphere diameter distribution (μm)	500−700	500−900
Specific BET area (m^2/g)	960	740
Micropore volume (mL/g)[a]	0.37	0.32
Mesopore volume (mL/g)[b]	0.00	0.09
Macropore volume (mL/g)[b]	0.52	0.28
Sphere density (g/mL)	0.739	0.924
Sphere porosity (%)	38	34

[a]From N_2 adsorption at 77 K using the t-plot method. [b]From Hg-porosimetry accumulated Hg intrusion at 414 MPa. [c]Sphere density = (specific crystal volume + mesopore and macropore volume)$^{-1}$. [d]Sphere porosity = mesopore and macropore volume × sphere density.

Figure 3 shows the SEM pictures of the CPO-27-Ni spheres at different magnifications. The sphericity is not perfect but reflects the droplet shape and gelation kinetics of the process.

https://dx.doi.org/10.1021/acs.iecr.9b06387
Ind. Eng. Chem. Res. 2020, 59, 7198−7211

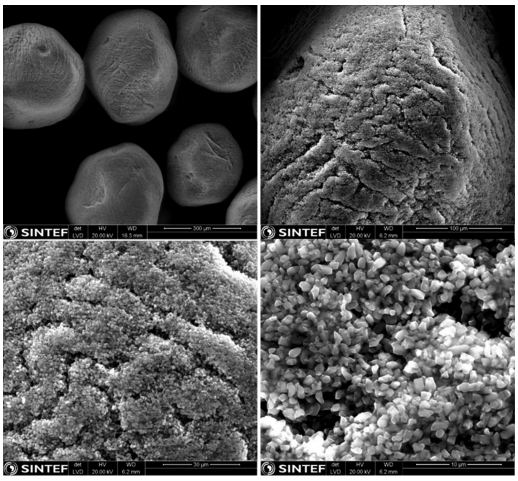

Figure 3. SEM pictures at increasing magnification of the CPO-27-Ni spheres made for MBTSA application.

When we go closer into the sphere surface, we see clearly the individual micron-sized CPO-27-Ni crystallites, but the alginate network that keeps the MOF crystals together stays invisible due to the high acceleration voltage used in the analysis. The CPO-27-Ni crystals are densely packed into aggregates with "ravines" (1−5 μm wide) between the aggregates that might be voids of alginate-rich areas. The

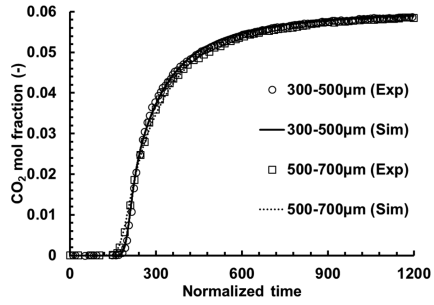

Figure 5. CO_2 breakthrough profiles for different pellet sizes at 50 °C. The x axis is normalized time to show the effect of particle size.

Hg-intrusion analysis shows two domains of filling (Figure S4 and S5, Supporting Information). First, a filling at around 100 μm is most probably filling of the voids between the spheres. No filling is observed between 1 and 10 μm, indicating that the "ravines" observed in the SEM pictures are not voids but more probably cross-bonded alginat-rich areas with no porosity. Lastly, there is filling due to the presence of macropores with the average pore diameter around 120 nm, consistent with the voids between the submicron-sized crystals observed by SEM. Since the crystal size distribution is narrow, also the macropore size distribution is quite narrow.

The Hg-intrusion curve for Zeolite 13X shows a similar pattern: First, a filling of the voids between the spheres, then a macropore filling at around 120 nm, but for this material there

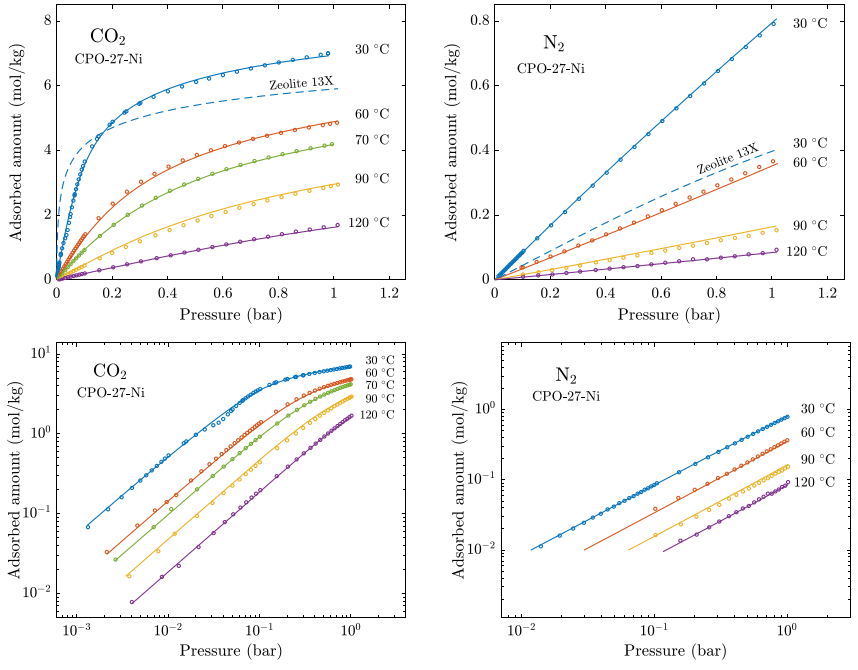

Figure 4. Adsorption isotherms of CO_2 and N_2 on CPO-27-Ni spheres in linear (top) and logarithmic scales (bottom).

https://dx.doi.org/10.1021/acs.iecr.9b06387
Ind. Eng. Chem. Res. 2020, 59, 7198−7211

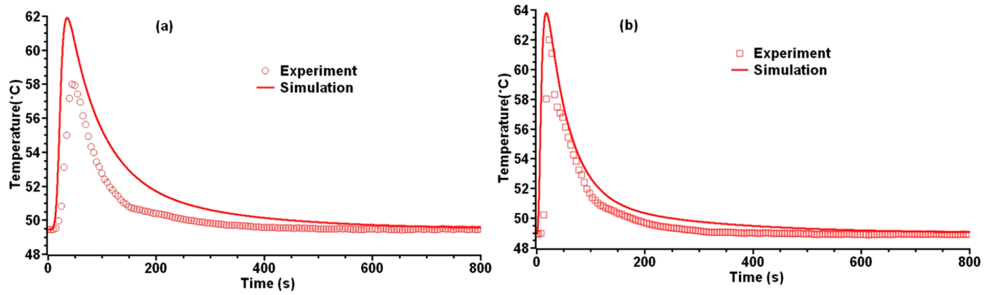

Figure 6. Temperature profile inside the column packed with (a) 300−500 and (b) 500−700 μm CPO-27-Ni spheres.

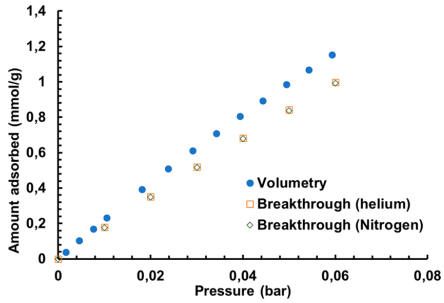

Figure 7. Adsorption capacity of CO_2 on CPO-27-Ni spheres obtained from breakthrough experiments performed at 50 °C, using helium (red box) and nitrogen (green diamond) as carrier gases. Comparison with values extrapolated from volumetric isotherm measurements.

Table 3. Main Design Parameters and Operating Conditions Used in Simulations of the MBTSA Process[a]

	CPO-27-Ni	Zeolite 13X
Height of adsorption section (m)	3.5	1.5
Cross-sectional area in adsorption section (m^2)	254.5	254.5
Column void fraction in adsorption section (−)	0.8	0.8
Cross-sectional area in other sections (m^2)	78.5	78.5
Column void fraction in adsorption section (−)	0.6	0.6
Height of preheating section (m)	3.0	2.0
Height of desorption section (m)	6.0	9.0
Height of cooling section (m)	10	12
Adsorbent residence time/cycle time (min)	26	45
CO_2 extraction pressure (bar)	0.97	0.97
Amount of circulating sorbent (kg/s)	350	245
Regeneration temperature (°C)	132	207

[a]Values referred to a single MBTSA unit.

is also a small mesopore volume of around 0.09 mL/g at around 4−5 nm pore diameter.

The porosities of the CPO-27-Ni and Zeolite 13X spheres are 38% and 34%, respectively, based on mesopore and macropore volumes of 0.52 and 0.37 mL/g, respectively, from the Hg-porosimetry analysis. Sphere densities are estimated to 0.74 and 0.92 g/mL, respectively. The differences in sphere densities reflect the difference in the crystallographic densities of the precursor CPO-27-Ni and Zeolite 13X crystals, 1.2 and 1.404 g/mL, respectively,[48,49] and also that the macropore volume of the spray-spheronized CPO-27-Ni adsorbent is higher than that of the Zeolite 13X spheres. We believe the extra porosity is a consequence of the spray method used and that lower porosities might be achieved using other droplet-forming methods and/or alginate types or contents. Minimizing the sphere mesoporosity and macroporosity is important to further increase the volumetric CO_2 capacity of the adsorbent and consequently reduce the size of the MBTSA process. The crystalline densities should be regarded as the maximum sphere densities achievable of the respective materials that cannot be exceeded without partial destruction of the crystal lattice.

The TG-DSC traces of CPO-27-Ni precursor powder and CPO-27-Ni/alginate beads are indistinguishable (Figures S6 and S7). However, we know from previously published work with MOF/alginate spheres that the alginate itself starts decomposing at around 135 °C.[50]

Adsorption Equilibrium. The adsorption isotherms of CO_2 and N_2 measured on the CPO-27-Ni spheres are shown in Figure 4, while H_2O isotherms are given in Figure S8 in the Supporting Information. In Figure 4, the isotherms at 30 °C are compared with the corresponding Zeolite 13X isotherms published in a previous work.[38] Although the highest measured CO_2 uptake (recorded at 100 kPa and 30 °C) of the MOF is higher than on Zeolite 13X, the CO_2 capacity of CPO-27-Ni is significantly lower when compared at low partial pressures relevant for postcombustion capture applications where the adsorption of CO_2 is typically carried out at low temperature and low CO_2 partial pressure. Further the isotherm of CO_2 in CPO-27-Ni is less steep than that of Zeolite 13X. On the other hand, CPO-27-Ni adsorbs significantly less CO_2 than Zeolite

Table 2. Summary of Kinetics Experiments on CPO-27-Ni Spheres

Conditions						
Spheres size (μm)	Carrier gas	$D_{molecular}$ ($\times 10^{-5}$ m^2/s)	$D_{Knudsen}$ ($\times 10^{-5}$ m^2/s)	K	k_{LDF} (s^{-1})	Tortuosity
300−500	He	7.0	2.2	301	4.41	3.3
300−500	N_2	1.9	2.2	293	2.66	3.4
500−700	He	7.0	2.2	500	1.56	2.8

https://dx.doi.org/10.1021/acs.iecr.9b06387
Ind. Eng. Chem. Res. 2020, 59, 7198−7211

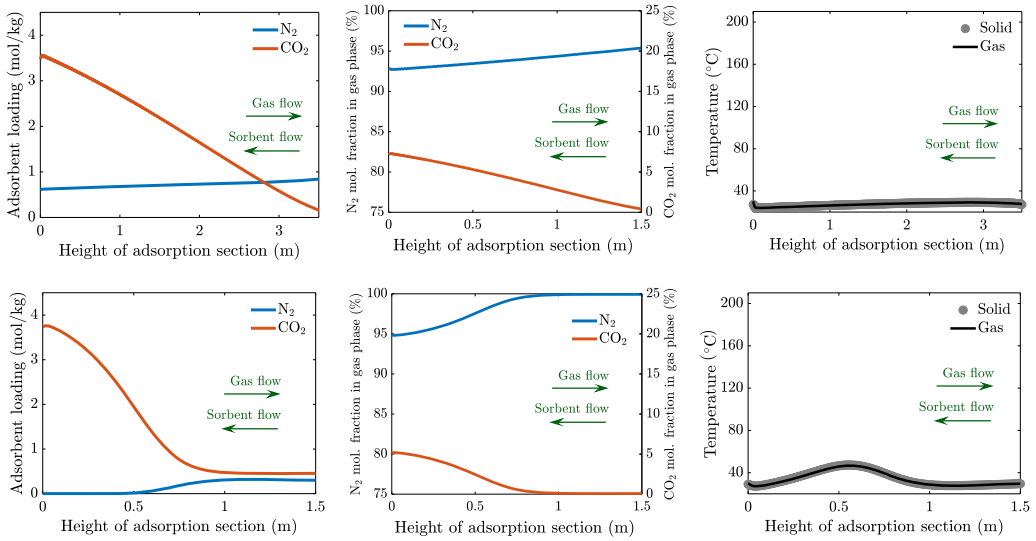

Figure 8. Adsorbent loading, molar fractions, and temperature profiles along the height of the adsorption section of the moving bed using CPO-27-Ni spheres (top plots) and Zeolite 13X (bottom plots). The flue gas flows countercurrently to the adsorbent: position zero corresponds to the bottom of the section, i.e., flue gas inlet and adsorbent outlet.

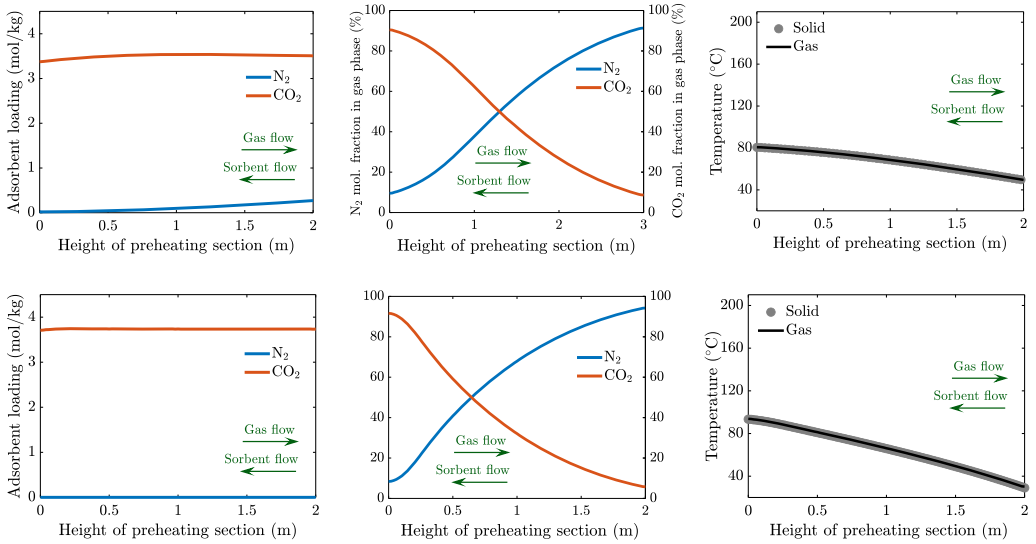

Figure 9. Adsorbent loading, molar fractions, and temperature profiles along the preheating section of the moving bed using CPO-27-Ni (top plots) and Zeolite 13X (bottom plots). Position zero corresponds to outlet of the adsorbent (bottom of the section).

13X also at high temperature and close to atmospheric pressure, i.e., at desorption (regeneration) conditions in a temperature swing capture process, which means that for a given regeneration temperature a higher level of regeneration can be achieved with the MOF. Figure 4 also shows the results of the fitting with the Virial model obtained by simultaneous nonlinear regression of the data in the whole temperature range. The fitted parameters are reported in the Supporting Information together with the corresponding values of the Zeolite 13X.[38] The obtained heat of adsorption of CO_2 is lower for CPO-27-Ni (37.4 kJ/mol) than for Zeolite 13X (44.8 kJ/mol), which is beneficial in terms of limiting the energy requirement of the capture process. The estimated heat of adsorption for the CPO-27-Ni spheres is close to previously reported values of 38−39 kJ/mol for powder samples.[27,51]

Adsorption Kinetics. Figures 5 and 6 show the CO_2 adsorption breakthrough trace and the temperature profiles with different pellet sizes using helium as the carrier gas. The

https://dx.doi.org/10.1021/acs.iecr.9b06387
Ind. Eng. Chem. Res. 2020, 59, 7198−7211

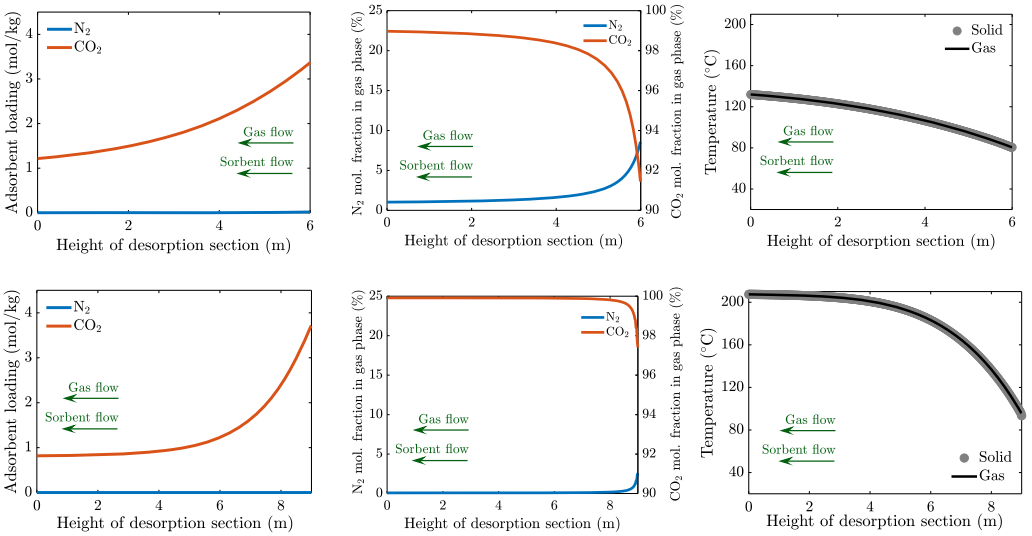

Figure 10. Adsorbent loading, molar fractions, and temperature profiles along the desorption section of the moving bed (top plots) and Zeolite 13X (bottom plots). The flue gas flows countercurrently to the adsorbent: Position zero corresponds to the bottom of the section, i.e., CO_2 extraction point, and sorbent outlet.

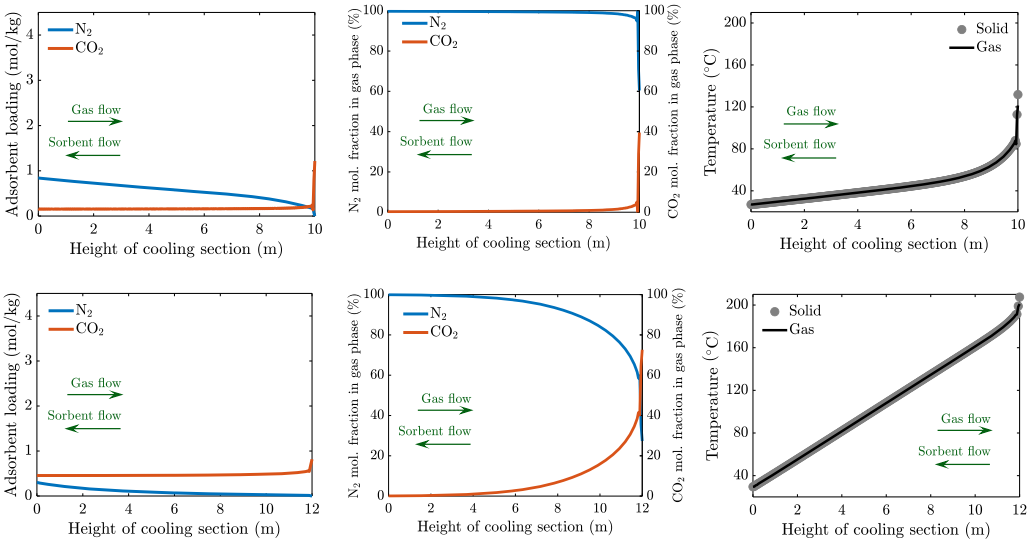

Figure 11. Adsorbent loading, molar fractions, and temperature profiles along the cooling section of the moving bed using CPO-27-Ni spheres (top plots) and Zeolite 13X (bottom plots). Position zero corresponds to the bottom of the section, i.e., inlet of recirculation gas, and sorbent outlet.

CO_2 trace for the larger particles is more spread out than that of the smaller particles indicating that the mass transfer is a function of the particle size. This is consistent with earlier data concluding that the adsorption of CO_2 in CPO-27-Ni is governed by diffusion in the macropores.[39,52,53]

Using the desorption trace, a mass balance was performed to obtain the adsorption isotherm up to 6 kPa as described by Brandani et al.[54] As helium gas is considered inert, the capacity curve obtained is equivalent to a single component isotherm. The capacity value obtained at 6 kPa CO_2 pressure was 1 mmol/g. This is about 15% less than the "extrapolated" value from single component isotherms from the volumetric measurements as seen in Figure 7. This difference can be attributed to the different regeneration conditions used in the two experiments. The competitive isotherm of CO_2 in the presence of nitrogen showed that at 50 °C, the nitrogen does not affect the adsorption of CO_2. This may not be the case at low temperatures, where the competition could be stronger.

https://dx.doi.org/10.1021/acs.iecr.9b06387
Ind. Eng. Chem. Res. 2020, 59, 7198−7211

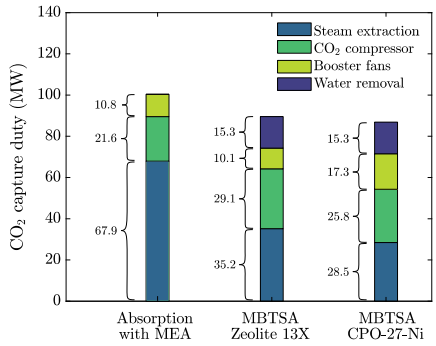

Figure 12. Individual contributions to the overall capture duty. Comparison of the MBTSA process with CPO-27-Ni, MBTSA with Zeolite 13X, and the amine-based process.

In order to extract the kinetic parameters from the breakthrough curves, a nonisothermal, nonisobaric 1D model was then used to fit the experimental profiles.[55] The model equations are described in the Supporting Information. The residual between the simulated and experimental adsorption breakthrough profiles was minimized by fitting the isotherm parameters, the LDF coefficient, and the heat transfer coefficient values.

In the first step, the helium experiment was analyzed. For nonadsorbing helium, the affinity coefficient and heat of adsorption values were taken as zero, and the LDF coefficient was kept as 1000 s^{-1}. The fitting of the breakthrough experiments was carried out in MATLAB.[56] The results from the modeling are shown in Figures 5 and 6 and summarized in Table 2. In general, there is a good agreement between the experimental and simulated profiles.

The ratio of the LDF coefficient values for the smaller and larger pellets was found to be 2.8, which is slightly higher than the ratio of the square of the average particle diameters (2.25). With respect to the different carrier gas, the ratios of the estimated LDF constants were similar to the ratio of the respective macropore diffusivity values. In these experiments, the total pressure was constant and hence, for the macropore diffusivity is a combination of Knudsen and molecular diffusivities and given by

$$\frac{1}{D_{\text{macro}}} = \frac{1}{D_{\text{molecular}}} + \frac{1}{D_{\text{Knudsen}}} \tag{11}$$

The molecular and the Knudsen diffusivity values were calculated by the correlations given in eqs 12 and 13. The 9/13 in the Knudsen diffusivity value is the Derjaguin correction factor.[57] The breakthrough experiments were coupled with independent mercury intrusion experiments which gave the porosity and pore radius. The LDF correlation was then rearranged to extract the values of the tortuosity which are provided in the same table. For the smaller pellets, the tortuosity value was found to be 1.8 ± 0.1, and for the large pellets, it was 1.4 ± 0.1.

$$D_{\text{molecular}} = \frac{0.001858T^{1.5}}{P\sigma^2\Omega}\sqrt{\frac{1}{M1} + \frac{1}{M2}} \tag{12}$$

$$D_{\text{Knudsen}} = \frac{9}{13}(0.97)r_{\text{Pore}}\sqrt{\frac{T}{M}} \tag{13}$$

Simulations of MBTSA for CO_2 Capture Using CPO-27-Ni Spheres and Comparison with Zeolite 13X. As basis for the design of the MBTSA with CPO-27-Ni, the process developed in a previous work using Zeolite 13X was taken as the initial configuration. A series of simulations was then performed by iteratively adjusting certain design parameters until desired process performances were achieved. In this respect, a minimum of 95% CO_2 purity and 90% CO_2 capture rate were set as targets. The list of design parameters that were modified and their final values used in the simulations presented here are reported in Table 3, together with the corresponding values of the original parameters from the zeolite case.

In terms of constraints to be taken into account when adjusting the operating conditions, a major difference between the zeolite and the MOF cases was on the choice of the regeneration temperature; while no limitation was imposed in the zeolite study, a temperature of 133 °C was set as the maximum desorption temperature for the CPO-27-Ni case in order to avoid potential degradation of the adsorbent. As suggested by the isotherm plots in Figure 4, this means that the adsorbent will still contain a significant amount of CO_2 adsorbed (above 1 mol/kg) when leaving the desorption section. In other words, only part of the captured CO_2 will be recovered as a result of a temperature increase occurring within

Table 4. Main Simulation Results of MBTSA with CPO-27-Ni and Integration of Capture Process with NGCC Power Plant[a]

	NGCC without CO_2 capture	NGCC with amine-based process (MEA)	NGCC with MBTSA, Zeolite 13X	NGCC with MBTSA, CPO-27-Ni
CO_2 purity (%)		99.9	95.8	98.9
CO_2 capture efficiency (%)		95.0	98.2	92.6
Heat input to capture unit (MW_{th})		266	101	125
Specific heat input ($MJ/kg_{CO2captured}$)		3.95	1.42	1.89
NGCC emissions (t_{CO2}/h)	253	11.2	4.6	18.8
CO_2 captured (kg/h)	–	242	249	240
NGCC specific emissions (kg/MWh)	316	15	6	24
NGCC gross power output (MW_{el})	802	734	767	773
GT gross electric power output (MW_{el})	555	555	555	555
ST gross electric power output (MW_{el})	246	179	211	218
CO_2 capture auxiliaries (MW)		37.5	54.7	60.1
NGCC net electric efficiency (%)	**63.1**	**54.7**	**55.9**	**56.1**

[a]Comparison with Zeolite 13X study[38] and capture with amine-based capture process.[38]

https://dx.doi.org/10.1021/acs.iecr.9b06387
Ind. Eng. Chem. Res. 2020, 59, 7198−7211

the desorption section. However, the remaining CO_2 can be recovered by further purging the adsorbent while traversing the subsequent cooling section. For this purpose, a small fraction (approximately 5 wt %) of the CO_2-free product gas from the adsorption section is recirculated to the cooling section, where it flows countercurrently to the adsorbent inducing further desorption of CO_2. The flow of recirculated gas through the cooling section also serves to maintain the pressure inside the column close to atmospheric pressure, as the cooling of the adsorbent would otherwise promote adsorption of the surrounding gas, and thus a decrease in pressure in the bulk phase. As a result of this recirculation through the cooling section, a small gas stream (approximately 7 wt % of the feed gas) containing a certain amount of CO_2 will be released from the top of the cooling section. As shown in Figure 2 (dashed blue stream lines), the released gas is then recycled and mixed with the flue gas feeding the adsorption section, with the purpose of improving the recovery of CO_2, by simultaneously increasing the CO_2 partial pressure in the feed gas. For simplicity, it is assumed that the recycled gas is cooled to the feed gas temperature before mixing. A similar strategy was adopted in the zeolite case, with the difference that the resulting product gas from the cooling (shown in dashed black line in Figure 2) section was directly mixed with the CO_2 product obtained from the desorption section, rather than being mixed with the feed gas.

The simulation results in terms of concentration and temperature profiles along the height of each moving-bed section are shown in Figure 8−11 and compared with the profiles obtained using Zeolite 13X. One of the main differences between the two cases concerns the shape of the concentration profiles in the adsorption section. As CPO-27-Ni presents a more spread profile, it was necessary to increase the length of the adsorption to 3.5 m (versus the original 1.5 m of the zeolite case), leading to higher pressure drops. The reason for this is related to the difference in the CO_2 adsorption isotherms of the two adsorbents at the feed gas conditions, which are steeper in the zeolite. Another difference that can be observed by looking at Figure 8 is the higher amount of N_2 coadsorbing with CO_2 on CPO-27-Ni, as result of the lower equilibrium selectivity of CPO-27-Ni compared to Zeolite 13X. However, this does not affect the purity of the CO_2 product (which is collected from the desorption section), as the N_2 desorption occurs within the preheating section (Figure 9). Here, the adsorbent undergoes a first increase in temperature, which induces a shift in adsorption equilibrium: Most of the adsorbed N_2 is released to the gas phase with the accompanying gas being removed from the top, while simultaneously, the CO_2 concentration in the gas phase increases without a significant change in the adsorbed concentration. In a similar way as for the gas recovered from the cooling section, the gas released from the preheating section is recycled to the feed gas (shown as dashed black line in Figure 2), being approximately 1 wt % of the total flow rate. The majority of CO_2 is then desorbed as a result of further heating of the adsorbent occurring in the desorption section (Figure 10). By setting a mild vacuum (0.97 bar) as evacuation pressure, the released gas is collected at the bottom, where high CO_2 purity is achieved. Lastly, adsorbent cooling is carried out in the cooling section (Figure 11), where a small stream of nearly pure N_2 recirculated from the adsorption section is used as purge gas to further regenerate the adsorbent from the remaining CO_2. As previously mentioned, the fraction of recirculated gas was approximately 5% of the total CO_2-free gas leaving the adsorption section.

As shown in Figures 8−11 and reported in Table 3, the advantage of the zeolite of having a shorter adsorption section is offset by the need for longer cooling and desorption sections, due to their higher regeneration temperature. In fact, with respect to sorbent inventory, the process using zeolite is outperformed by CPO-27-Ni: despite circulating a lower amount of material in terms of kg/s, the total amount of adsorbent required (i.e., the amount of adsorbent that is processed in one cycle) is 43% higher due to the much longer residence time of the zeolite.

Energetic Performance of Capture Process and Results of Power Plant Integration. On the basis of the results obtained with the MBTSA simulations, the amount of thermal energy required for sorbent regeneration was computed and used as input to the NGCC model simulations. The results of the power plant integration are summarized in Figure 12 and Table 4, together with a comparison with the reference NGCC plant (without capture), the benchmark amine-based process, and the reference moving-bed process using zeolite.

Very similar performances are obtained for the two MBTSA processes (Zeolite 13X and CPO-27-Ni) in terms of overall power cycle efficiency, causing approximately a 7%-point reduction in net electric efficiency, compared to an 8%-point capture penalty of the amine-based process. As shown graphically in Figure 12, one of the main differences between the moving-bed and amine-based systems is the need for drying the flue gas prior to the capture process when using solid sorbents, with the energy penalty associated with the drying process. Another factor playing in favor of the MEA process is the slightly higher pressure at which CO_2 is separated, which implies lower energy consumption by the CO_2 compressor. On the other hand, the MBTSA processes present a significantly lower heat demand for sorbent regeneration and hence a lower power loss associated with the steam extraction.

When comparing the zeolite-based process with the MOF-based process, the higher energy penalty due to the pressure drops in the CPO-27-Ni system is compensated by the lower reduction in power output associated with steam bleeding. In fact, despite requiring a slightly higher amount of energy for sorbent regeneration (both in terms of total heat input and specific heat per kg of CO_2 captured), CPO-27-Ni allows extraction of steam at lower pressure, which is beneficial for the steam cycle performance. Details on the steam extraction conditions and flow rates can be found in the Supporting Information.

CONCLUSIONS

We have prepared CPO-27-Ni/alginate spheres suitable for use in a moving-bed temperature-swing adsorption (MBTSA) process for postcombustion CO_2 capture. The shaped spheres maintain most of the CO_2 capacity of the CPO-27-Ni precursor powder but have better flow characteristics needed to avoid clogging in a MBTSA reactor. The MOF spheres have been compared with Zeolite 13X spheres of similar size. The two adsorbents have similar CO_2 capacities in mmol/g units, but the CPO-27-Ni/alginate spheres have lower volumetric CO_2 capacity due to the intrinsic lower crystallographic density of CPO-27-Ni compared to Zeolite 13X and to the larger macropore volume of the former because of the shaping

https://dx.doi.org/10.1021/acs.iecr.9b06387
Ind. Eng. Chem. Res. 2020, 59, 7198−7211

method used. Despite this difference, simulation of the two adsorbents in a MBTSA process for capturing CO_2 from an NGCC power plant indicate that the CPO-27-Ni spheres have lower energy requirements compared to Zeolite 13X, the main reason being a lower temperature needed for regeneration. Due to the high hydrophilicity of both adsorbents, a drying step of the flue gas is needed before the CO_2 capture process. Despite this extra process, the simulations show that the MBTSA process utilizing either adsorbent perform slightly better than a solvent-based MEA process in terms of energy requirements.

Further improving the shaping process used for CPO-27-Ni, especially minimizing the macropore volume of the spheres and thus increasing their volumetric CO_2 uptake, will further improve the performance of the MBTSA process. In particular, this will reduce the process footprint which is one of the major challenges with adsorbent-based processes.

■ ASSOCIATED CONTENT

Supporting Information

The Supporting Information is available free of charge at https://pubs.acs.org/doi/10.1021/acs.iecr.9b06387.

Setup used for MOF shaping; details on X-ray diffraction; Hg-intrusion and TG-DSC-MS analyses; tabulated data of CO_2, N_2, and H_2O isotherms; water isotherms plots; model equations used for modeling breakthrough curves; and additional equations used in the MBTSA simulations (PDF)

■ AUTHOR INFORMATION

Corresponding Authors

Giorgia Mondino − *Department of Energy and Process Engineering, NTNU − Norwegian University of Science and Technology, Trondheim, Norway*; Email: giorgia.mondino@ntnu.no

Richard Blom − *SINTEF Industry, 0314 Oslo, Norway*; orcid.org/0000-0001-8675-0774; Email: richard.blom@sintef.no

Authors

Aud I. Spjelkavik − *SINTEF Industry, 0314 Oslo, Norway*

Terje Didriksen − *SINTEF Industry, 0314 Oslo, Norway*

Shreenath Krishnamurthy − *SINTEF Industry, 0314 Oslo, Norway*; orcid.org/0000-0002-9584-6804

Ruth Elisabeth Stensrød − *SINTEF Industry, 0314 Oslo, Norway*

Carlos A. Grande − *SINTEF Industry, 0314 Oslo, Norway*; orcid.org/0000-0002-9558-5413

Lars O. Nord − *Department of Energy and Process Engineering, NTNU − Norwegian University of Science and Technology, Trondheim, Norway*

Complete contact information is available at: https://pubs.acs.org/10.1021/acs.iecr.9b06387

Author Contributions

The manuscript was written through contributions of all authors. All authors have given approval to the final version of the manuscript.

Funding

We acknowledge financial support from the CLIMIT program of the Norwegian Research Council for funding the EDeMoTeC project (Grant 267873).

Notes

The authors declare no competing financial interest.

■ ACKNOWLEDGMENTS

We want to thank Martin F. Sunding at SINTEF Materials Physics for recording the SEM pictures.

■ ABBREVIATIONS

CCR2 = CC chemokine receptor 2
CCL2 = CC chemokine ligand 2
CCR5 = CC chemokine receptor 5
TLC = thin layer chromatography
TG-DSC-MS = thermogravimetry and differential scanning calorimetry coupled with mass spectroscopy
GT = gas turbine
ST = steam turbine

■ NOMENCLATURE

A_i = first Virial coefficient of component i, kg mol^{-1}
a' = specific area of adsorbent particle, m^2 m^{-3}
B_i = second Virial coefficient of component i, kg mol^{-1}
Bi_i = Biot number of component i
C_i = third Virial coefficient of component i, kg mol^{-1}
C_i = concentration of component i in bulk gas phase, mol m^{-3}
$C_{p,i}$ = concentration of component i in the macropores, mol m^{-3}
c_p = molar specific heat of gas mixture at constant pressure, J mol^{-1}K^{-1}
$c_{p,s}$ = specific heat of solid phase, J kg^{-1}K^{-1}
C_T = total gas concentration in bulk phase, mol m^{-3}
c_v = molar specific heat of gas mixture at constant volume, J mol^{-1} K^{-1}
$D_{c,i}$ = micropores/crystals diffusivity of component i, m^2 s^{-1}
D_h = hydraulic diameter, m
D_{Knudsen} = Knudsen diffusivity, m^2 s^{-1}
D_{macro} = diffusivity in macropores, m^2 s^{-1}
$D_{\text{molecular}}$ = molecular diffusivity, m^2 s^{-1}
$D_{p,i}$ = macropore diffusivity of component i, m^2 s^{-1}
D_z = axial dispersion coefficient, m^2 s^{-1}
K_i = equilibrium constant of component i, mol kg^{-1} bar^{-1}
K_{eq}^{∞} = equilibrium constant at infinite temperature, mol kg^{-1} bar^{-1}
h_f = film heat transfer coefficient between the gas and the particle, J s^{-1} m^{-2} K^{-1}
$h_{g,hx}$ = film heat transfer coefficient between the gas and the wall, J s^{-1}m^{-2} K^{-1}
K_m = film mass transfer coefficient, m s^{-1}
$M1$ = molecular weight of components 1, g mol^{-1}
$M2$ = molecular weight of components 1, g mol^{-1}
P = pressure, Pa
P_i = partial pressure of component i, bar
q_i = adsorbed phase concentration of component i, mol kg^{-1}
q_i^* = adsorbed concentration of component i at equilibrium with the gas, mol kg^{-1}
R = ideal gas constant, J K^{-1} mol^{-1}
r_c = crystals/micropore radius, m
r_{pore} = macropores radius, m
R_p = particle radius, m
t = time, s
T = temperature of the gas phase, K
T_{hx} = temperature of the wall, K

https://dx.doi.org/10.1021/acs.iecr.9b06387
Ind. Eng. Chem. Res. 2020, 59, 7198−7211

T_s = temperature of the solid phase, K
u = superficial gas velocity, m s^{-1}
v_s = velocity of the solid phase, m s^{-1}
z = axial coordinate in the moving bed, m
Y_i = molar fraction of component i

GREEK SYMBOLS

ΔH_i^0 = isosteric heat of adsorption of component i, J mol^{-1}
ε_c = column void fraction
ε_p = particle porosity
λ = heat axial dispersion coefficient, J m^{-1} s^{-1} K^{-1}
λ_{pk} = heat axial dispersion coefficient of structured packing, J m^{-1} s^{-1} K^{-1}
ξ = volumetric fraction of structured packing
ρ_p = particle density, kg m^{-3}
ρ_{pk} = density of structured packing, kg m^{-3}
σ = Lennard-Jones parameter (collision diameter), Å
Ω = dimensionless collision integral of binary diffusivity

REFERENCES

(1) Eddaoudi, M.; Kim, J.; Rosi, N.; Vodak, D.; Wachter, J.; O'Keeffe, M.; Yaghi, O. M. Systematic design of pore size and functionality in isoreticular MOFs and their application in methane storage. *Science* **2002**, *295*, 469.
(2) Rosi, N. L.; Eckert, J.; Eddaoudi, M.; Vodak, D. T.; Kim, J.; O'Keeffe, M.; Yaghi, O. M. Hydrogen storage in microporous metal-organic frameworks. *Science* **2003**, *300*, 1127.
(3) Morris, R.; Wheatley, P. S. Gas storage in nanoporous materials. *Angew. Chem., Int. Ed.* **2008**, *47*, 4966.
(4) Sculley, J.; Yuan, D.; Zhou, H.-C. The current status of hydrogen storage in metal-organic frameworks-updated. *Energy Environ. Sci.* **2011**, *4*, 2721.
(5) Gangu, K. K.; Maddila, S.; Mukkamala, S. B.; Jonnalagadda, S. B. Characteristics of MOF, MWCNT and graphene containing materials for hydrogen storage: A review. *J. Energy Chem.* **2019**, *30*, 132.
(6) Makal, T. A.; Li, J.-R.; Lu, W.; Zhou, H.-C. Methane storage in advanced porous materials. *Chem. Soc. Rev.* **2012**, *41*, 7761.
(7) Peng, Y.; Krungleviciute, V.; Eryazici, I.; Hupp, J. T.; Farha, O. K.; Yildirim, T. Methane storage in metal-organic frameworks: Current records, surprise findings, and challenges. *J. Am. Chem. Soc.* **2013**, *135*, 11887.
(8) Mason, J. A.; Veenstra, M.; Long, J. R. Evaluating metal-organic frameworks for natural gas storage. *Chem. Sci.* **2014**, *5*, 32.
(9) Gomez-Gualdron, D. A.; Wilmer, C. E.; Farha, O. K.; Hupp, J. T.; Snurr, R. Q. Exploring the limits of methane storage and delivery in nanoporous materials. *J. Phys. Chem. C* **2014**, *118*, 6941.
(10) Shen, J.; Sulkowski, J.; Beckner, M.; Dailly, A. Effects of textural and surface characteristics of metal-organic frameworks on the methane adsorption for natural gas vehicular application. *Microporous Mesoporous Mater.* **2015**, *212*, 80.
(11) Bastin, L.; Barcia, P. S.; Hurtado, E. J.; Silva, J. A. C.; Rodrigues, A. E.; Chen, B. L. A microporous metal-organic framework for separation of CO2/N2 and CO2/CH4 by fixed-bed adsorption. *J. Phys. Chem. C* **2008**, *112*, 1575.
(12) Adil, K.; Belmabkhout, Y.; Pillai, R. S.; Cadiau, A.; Bhatt, P. M.; Assen, A. H.; Maurin, G.; Eddaoudi, M. Gas/vapour separation using ultra-microporous metal-organic frameworks: insight into the structure/separation relationship. *Chem. Soc. Rev.* **2017**, *46*, 3402.
(13) Ahmad, R.; Wong-Foy, A. G.; Matzger, A. J. Microporous coordination polymers as selective sorbents for liquid chromatography. *Langmuir* **2009**, *25*, 11977.
(14) Hindocha, S.; Poulston, S. Study of the scale-up, formulation, ageing and ammonia adsorption capacity of MIL-100(Fe), Cu-BTC and CPO-27(Ni) for use in respiratory protection filters. *Faraday Discuss.* **2017**, *201*, 113.
(15) de Lange, M. F.; Zeng, T.; Vlugt, T. J. H.; Gascon, J.; Kapteijn, F. Manufacture of dense CAU-10-H coatings for application in adsorptive driven heat pumps: optimization and characterization. *CrystEngComm* **2015**, *17*, 5911.
(16) Teo, H. W. B.; Chakraborty, A.; Kayal, S. Formic acid modulated (fam) aluminium fumarate MOF for improved isotherms and kinetics with water adsorption: Cooling/heat pump applications. *Microporous Mesoporous Mater.* **2018**, *272*, 109.
(17) Trapani, F.; Polyzoidis, A.; Loebbecke, S.; Piscopo, C. G. On the general water harvesting capability of metal-organic frameworks under well-defined climatic conditions. *Microporous Mesoporous Mater.* **2016**, *230*, 20.
(18) Quiros, J.; Boltes, K.; Aguado, S.; de Villoria, R. G.; Vilatela, J. J.; Rosal, R. Antimicrobial metal-organic frameworks incorporated into electrospun fibers. *Chem. Eng. J.* **2015**, *262*, 189.
(19) Jiao, L.; Wang, Y.; Jiang, H. L.; Xu, Q. Metal-organic frameworks as platforms for catalytic applications. *Adv. Mater.* **2018**, *30* (37), 1703663.
(20) Shekhah, O.; Liu, J.; Fischer, R. A.; Woll, C. MOF thin films: existing and future applications. *Chem. Soc. Rev.* **2011**, *40*, 1081.
(21) Stavila, V.; Talin, A. A.; Allendorf, M. D. MOF-based electronic and optoelectronic devices. *Chem. Soc. Rev.* **2014**, *43*, 5994.
(22) Wales, D. J.; Grand, J.; Ting, V. P.; Burke, R. D.; Edler, K. J.; Bowen, C. R.; Mintova, S.; Burrows, A. D. Gas sensing using porous materials for automotive applications. *Chem. Soc. Rev.* **2015**, *44*, 4290.
(23) Low, J. J.; Benin, A. I.; Jakubczak, P.; Abrahamian, J. F.; Faheem, S. A.; Willis, R. R. Virtual high throughput screening confirmed experimentally: porous coordination polymer hydration. *J. Am. Chem. Soc.* **2009**, *131* (43), 15834.
(24) Kusgens, P.; Zgaverdea, A.; Fritz, H. G.; Siegle, S.; Kaskel, S. Metal-organic frameworks in monolithic structures. *J. Am. Ceram. Soc.* **2010**, *93*, 2476.
(25) Tagliabue, M.; Rizzo, C.; Millini, R.; Dietzel, P. D. C.; Blom, R.; Zanardi, S. Methane storage on CPO-27-Ni pellets. *J. Porous Mater.* **2011**, *18*, 289.
(26) Hong, W. Y.; Perera, S. P.; Burrows, A. D. Manufacturing of metal-organic framework monolits and their application in CO2 adsorption. *Microporous Mesoporous Mater.* **2015**, *214*, 149.
(27) Dietzel, P. D. C.; Besikiotis, V.; Blom, R. Application of metal–organic frameworks with coordinatively unsaturated metal sites in storage and separation of methane and carbon dioxide. *J. Mater. Chem.* **2009**, *19*, 7362.
(28) Xiang, S.; He, Y.; Zhang, Z.; Wu, H.; Zhou, W.; Krishna, R.; Chen, B. Microporous metal-organic framework with potential for carbon dioxide capture at ambient conditions. *Nat. Commun.* **2012**, *3* (1), 954.
(29) Nugent, P.; Belmabkhout, Y.; Burd, S. D.; Cairns, A. J.; Luebke, R.; Forrest, K.; Pham, T.; Ma, S.; Space, B.; Wojtas, L.; Eddaoudi, M.; Zaworotko, M. J. Porous materials with optimal adsorption thermodynamics and kinetics for CO2 separation. *Nature* **2013**, *495*, 80.
(30) McDonald, T. M.; Mason, J. A.; Kong, X.; Bloch, E. D.; Gygi, D.; Dani, A.; Crocella, V.; Giordanino, F.; Odoh, S. O.; Drisdell, W. S.; Vlaisavljevich, B.; Dzubak, A. L.; Poloni, R.; Schnell, S. K.; Planas, N.; Lee, K.; Pascal, T.; Wan, L. F.; Prendergast, D.; Neaton, J. B.; Smit, B.; Kortright, J. B.; Gagliardi, L.; Bordiga, S.; Reimer, J. A.; Long, J. R. Cooperative insertion of CO_2 in diamine-appended metal-organic frameworks. *Nature* **2015**, *519* (7543), 303.
(31) Kizzie, A. C.; Wong-Foy, A. G.; Matzger, A. J. Effect of humidity on the performance of Microporous Coordination Polymers as adsorbents for CO2 capture. *Langmuir* **2011**, *27* (10), 6368.
(32) Dasgupta, S.; Divekar, S.; Aarti; Spjelkavik, A. I.; Didriksen, T.; Nanoti, A.; Blom, R. Adsorption properties and performance of CPO-27-Ni/alginate spheres during multicycle pressure-vacuum-swing adsorption (PVSA) CO_2 capture in the presence of moisture. *Chem. Eng. Sci.* **2015**, *137*, 525.
(33) Masala, A.; Vitillo, J. G.; Mondino, G.; Grande, C. A.; Blom, R.; Manzoli, M.; Marshall, M.; Bordiga, S. CO_2 capture in dry and wet conditions in UTSA-16 metal-organic framework. *ACS Appl. Mater. Interfaces* **2017**, *9*, 455.

https://dx.doi.org/10.1021/acs.iecr.9b06387
Ind. Eng. Chem. Res. 2020, 59, 7198−7211

(34) Spjelkavik, A. I.; Aarti; Divekar, S.; Didriksen, T.; Blom, R. Forming MOFs into spheres by use of molecular gastronomy methods. *Chem. - Eur. J.* **2014**, *20*, 8973−8978.
(35) Berg, C. Hypersorption process for separation of light gases. *Trans. AIChE* **1946**, *XLII*, 665.
(36) Grande, C. A.; Kvamsdal, H.; Mondino, G.; Blom, R. Development of moving bed temperature swing adsorption (MBTSA) process for post-combustion CO_2 capture: Initial benchmarking in a NGCC context. *Energy Procedia* **2017**, *114*, 2203.
(37) Mondino, G.; Grande, C. A.; Blom, R. Effect of gas recycling on the performance of a moving bed temperature swing (MBTSA) process for CO_2 capture in a coal fired power plant context. *Energies* **2017**, *10*, 745.
(38) Mondino, G.; Grande, C. A.; Blom, R.; Nord, L. O. Moving bed temperature swing adsorption for CO2 capture from a natural gas combined cycle power plant. *Int. J. Greenhouse Gas Control* **2019**, *85*, 58.
(39) Krishnamurthy, S.; Blom, R.; Ferrari, M. C.; Brandani, S. Adsorption and diffusion of CO2 in CPO-27−Ni beads. *Adsorption* **2019**, DOI: 10.1007/s10450-019-00162-x.
(40) Dietzel, P. D. C.; Panella, B.; Hirscher, M.; Blom, R.; Fjellvag, H. Hydrogen adsorption in a nickel based coordination polymer with open metal sites in the cylindrical cavities of the desolvated framework. *Chem. Commun.* **2006**, *9*, 959.
(41) Lopes, F. V.; Grande, C. A.; Ribeiro, A. M.; Oliveira, E. L.; Loureiro, J. M.; Rodrigues, A. E. Enhancing capacity of activated carbons for hydrogen purification. *Ind. Eng. Chem. Res.* **2009**, *48*, 3978.
(42) Grande, C. A.; Lopes, F. V.; Ribeiro, A. M.; Loureiro, J. M.; Rodrigues, A. E. Adsorption of Off-Gases from Steam Methane Reforming (H_2, CO_2, CH_4, CO and N_2) on Activated Carbon. *Sep. Sci. Technol.* **2008**, *43*, 1338.
(43) *Scilab*, version 6.0.2; Scilab Enterprises, 2019. http://www.scilab.org (accessed April 2020).
(44) Taqvi, S. M.; LeVan, M. D. Virial description of two-component adsorption on homogeneous and heterogeneous surfaces. *Ind. Eng. Chem. Res.* **1997**, *36*, 2197.
(45) *gPROMS Model Builder*, version 5.0; Process System Enterprise (PSE), 2017.
(46) Liu, Z.; Grande, C. A.; Li, P.; Yu, J.; Rodrigues, A. E. Multi-bed Vacuum Pressure Swing Adsorption for carbon dioxide capture from flue gas. *Sep. Purif. Technol.* **2011**, *81*, 307.
(47) *Thermoflow package*, version 27.0; Thermoflow, Inc., 2017.
(48) Elsayed, E.; Al-Dadah, R.; Mahmoud, S.; Anderson, P. A.; Elsayed, A.; Youssef, P. G. CPO-27(Ni), aluminium fumarate and MIL-101(Cr) MOF materials for adsorption water desalination. *Desalination* **2017**, *406*, 25−36.
(49) Friedrich, D.; Mangano, E.; Brandani, S. Automatic estimation of kinetic and isotherm parameters from ZLC experiments. *Chem. Eng. Sci.* **2015**, *126*, 616−624.
(50) Lee, D. W.; Didriksen, T.; Olsbye, U.; Blom, R.; Grande, C. A. Shaping of metal-organic framework UiO-66 using alginates: effect of operation variables. *Sep. Purif. Technol.* **2020**, *235*, 116182.
(51) Queen, W. L.; Hudson, M. R.; Bloch, E. D.; Mason, J. A.; Gonzalez, M. I.; Lee, J. S.; Gygi, D.; Howe, J. D.; Lee, K.; Darwish, T. A.; James, M.; Peterson, V. K.; Teat, S. J.; Smit, B.; Neaton, J. B.; Long, J. R.; Brown, C. M. Comprehensive study of carbon dioxide adsorption in the metal-organic frameworks M2(dobdc) (M= Mg, Mn, Fe, Co, Ni, Cu, Zn). *Chem. Sci.* **2014**, *5*, 4569−4581.
(52) Hu, X.; Brandani, S.; Benin, A. I.; Willis, R. R. Development of a semiautomated zero length column technique for carbon capture applications: study of diffusion behavior of CO_2 in MOFs. *Ind. Eng. Chem. Res.* **2015**, *54*, 5777.
(53) Liu, J.; Wang, Y.; Benin, A. I.; Jakubczak, P.; Willis, R. R.; LeVan, M. D. CO_2/H_2O adsorption equilibrium and rates on metal−organic frameworks: HKUST-1 and Ni/DOBDC. *Langmuir* **2010**, *26*, 14301.
(54) Brandani, F.; Ruthven, D. M.; Coe, C. G. Measurement of Adsorption Equilibrium by the Zero Length Column (ZLC) Technique Part 1: Single-Component Systems. *Ind. Eng. Chem. Res.* **2003**, *42*, 1451−1461.
(55) Rajagopalan, A. K.; Avila, A. M.; Rajendran, A. Do adsorbent screening metrics predict process performance? A process optimization based study for post-combustion capture of CO_2, *Int. Int. J. Greenhouse Gas Control* **2016**, *46*, 76−85.
(56) *MATLAB*, version 9.7; The MathWorks, Inc., 2019.
(57) Hu, X.; Mangano, E.; Friedrich, D.; Ahn, H.; Brandani, S. Diffusion mechanism of CO_2 in 13X zeolite beads. *Adsorption* **2014**, *20*, 121.

https://dx.doi.org/10.1021/acs.iecr.9b06387
Ind. Eng. Chem. Res. 2020, 59, 7198−7211

Evaluation of MBTSA Technology for CO_2 Capture from Waste-to-Energy Plants

Giorgia Mondino[a,b,*], Carlos A. Grande[b], Richard Blom[b], Lars O. Nord[a]

[a] *NTNU - Norwegian University of Science and Technology, Department of Energy and Process Engineering, Trondheim, Norway*
[b] *SINTEF Industry, P.O. Box 124 Blindern, N0314 Oslo, Norway*

Abstract

Moving bed temperature swing adsorption (MBTSA) is a promising technology for CO_2 capture from flue gases. In a MBTSA unit, a selective adsorbent material is circulated between a low-temperature stage where it removes CO_2 from the flue gas and a higher-temperature zone where it desorbs CO_2 at higher purity. The main benefits of MBTSA are low pressure drops in the adsorption zone and the possibility to heat the adsorbent faster than standard adsorption technologies. This work evaluated via process simulations the use of the MBTSA technology for CO_2 capture from an industrial-scale waste-to-energy plant. To assess the technology with realistic parameters, we measured heat transfer coefficients in the heating section of a new MBTSA demonstrator unit using activated carbon spheres. The heating device was produced by 3D printing, and has rectangular channels on the gas-solid side rotated at 45° to facilitate solid flow. The heat transfer coefficients increased with the flow rate of activated carbon particles, and the highest value of 120 W/m^2K was measured for a sorbent mass flux of 3.5 kg/m^2s. This information was used as input for the process simulations, and allowed a tailored and realistic design of an MBTSA unit capturing more than 90% of the exhaust CO_2 with a purity above 95%. The rather high specific energy duty of the process (5.7 MJ/kg CO_2) can be attributed to the low adsorption capacity of the activated carbon. In this respect, significant improvements can be expected by employing adsorbents with higher adsorption capacity and selectivity, such as zeolites or metal-organic frameworks.

Keywords: carbon capture and storage (CCS), TSA, solid sorbent, activated carbon, process simulation, waste incinerator, heat transfer coefficient

1. Introduction

The production of municipal solid waste is expected to keep increasing as a result of the rapid grow of population and living standards around the world (Kaza et al., 2018). Waste-to-energy plants represent a key technology to manage the increasing quantities of solid waste, reduce the

*Corresponding author
Email address: giorgia.mondino@sintef.no (Giorgia Mondino)

methane emissions associated with landfilled waste, and satisfy the rising energy demand (Brunner and Rechberger, 2015). In addition, the integration of waste-to-energy plants with Carbon Capture and Storage (CCS) technologies has the potential to make waste a net-zero or even negative emission energy source (Kearns, 2019, Haaf et al., 2020, Turan et al., 2021).

In the context of post-combustion CO_2 capture, adsorption-based processes are considered a promising alternative to the current benchmark technology based on amine solutions, which suffers from high energy consumption and environmental as well as corrosion issues related to solvent degradation (Sjostrom and Krutka, 2010, Bui et al., 2018). Adsorption-based processes make use of porous solids capable of: i) removing the CO_2 from the flue gas by selectively adsorbing it onto their surface and ii) releasing the adsorbed CO_2 when subjected to a change of pressure or temperature. The former property enables the separation of the CO_2 from the rest of the flue gas components, while the latter is responsible for the regeneration of the adsorbent, enabling a cyclic operation and permitting the recovery of CO_2 in a high purity stream. When the regeneration of the adsorbent is carried out by reducing the pressure of the system, the process is referred to as Pressure Swing Adsorption (PSA) or Vacuum Swing Adsorption (VSA), depending on the operating pressure, while the term Temperature Swing Adsorption (TSA) is used to indicate processes where the adsorbent is regenerated by an increase in temperature upon external heat supply. In large-scale post-combustion capture applications, the CO_2 has to be purified from low-concentration, low-pressure and high volume flow rate flue-gases and regeneration via temperature swing seems to be the most appropriate option (Ruthven, 1984, Wankat, 2006, Bui et al., 2018).

In conventional TSA processes, the adsorbent is normally shaped as beads or pellets and packed in a series of columns that cyclically alternate between the adsorption and regeneration steps. One of the main drawbacks of fixed bed processes in applications involving large flow rates, such as post-combustion capture, is the high pressure drop occurring across the packed-bed, unless the adsorbent pellets are replaced by especially shaped adsorbents (e.g., honeycomb monolith, hollow fibers, spaced sheets)(Akhtar et al., 2014, Rezaei and Webley, 2010, Masala et al., 2017, Farmahini et al., 2021). Another important factor hampering the commercialization of TSA systems for post-combustion CO_2 capture is that a large temperature swing is often required (Zanco et al., 2018, Morales-Ospino et al., 2021) to achieve the demanding product specifications in terms of both CO_2 purity and recovery (Joss et al., 2017). These large temperature swings do not only imply high energy penalties and parasitic losses, but also lead to long cycle times due to the poor heat transfer within the packed bed (Bonjour et al., 2004, Plaza et al., 2017, Zanco et al., 2021). This, in turn, results in large sorbent inventories, low process productivity, and large system footprints, which makes conventional TSA processes less competitive with respect to other post-combustion technologies (Bonjour et al., 2005, Rezaei and Webley, 2010, Zanco et al., 2017, 2021).

One way to overcome the aforementioned challenges is by performing the adsorption-desorption cycle in a moving bed system, rather than in the traditional fixed bed configuration (Knaebel, 2005). In the moving bed process, the temperature swing is achieved by circulating the adsorbent through sections at different temperatures. Each of these sections has a specific purpose and corresponds to a different step: adsorption, desorption and cooling. In contrast with fixed bed processes in which the same column is operated at variable conditions according to the cycle schedule, each section of the moving bed system can be designed and operated according to its specific purpose.

This offers interesting opportunities for system optimization, aiming, for example, to reduce the pressure drop within the adsorption section, or to enhance heat transfer in the desorption and cooling sections, so that a more compact design and higher productivity can be achieved. Furthermore, the MBTSA offers the possibility to internally recover part of the heat needed for sorbent regeneration and thus reduce the external energy duty of the process (Knaebel, 2005, Kim et al., 2013, Morales-Ospino et al., 2021). Another major feature distinguishing moving bed from fixed bed processes is that the former can be operated at steady state, avoiding complex cycle scheduling (Plaza et al., 2017, Kim et al., 2013) and the parasitic losses associated with intermittent heating/cooling of the heat exchanger walls (Bonjour et al., 2004, 2005). The possibility to operate in steady state is also an advantage in terms of process control and integration (Kim et al., 2013), which is particularly relevant within post combustion applications where: (i) the flow rate and composition of flue gases from the upstream power plant can vary over time (Montañés et al., 2018, Rúa et al., 2020), (ii) the power cycle can be appositely modified to supply the heat required by the capture process (Mondino et al., 2019)

The the concept of moving bed was first introduced in the '40s by Berg (1945) for fractionating hydrocarbons. Only recently the same concept has been applied for CO_2 capture purposes, first by Knaebel (2005) who suggested the use of hot flue gas for indirect sorbent heating, and later by Hornbostel and co-workers (Hornbostel et al., 2013, 2015, Hornbostel, 2016), who tested a large bench scale moving bed system employing steam for direct heating of the adsorbent. Pilot-scale design and testing of a moving-bed process for CO_2 capture was performed also by (Okumura et al., 2014, 2017), who used an amine impregnated adsorbent regenerated by low temperature steam. The main advantage of direct sorbent heating is that it is possible to achieve fast heat transfer rates due to intense mixing between sorbent particles and heating fluid. However, this type of configuration prevents the use of sorbents materials that are incompatible with the heat transfer fluid and compromises the use of internal heat recovery, which is crucial to minimize the process energy use. In this context, the group of Kim et al. (Kim et al., 2013, 2014, Son et al., 2014) proposed a moving bed process with an internal heat integration scheme, where part of the energy required for sorbent regeneration is recovered from the heat generated during the adsorption step using indirect-contact heat exchangers. The same type of indirect-contact heat exchanger for MBTSA processes was employed in the recent study carried out by (Morales-Ospino et al., 2021), who confirmed that internal heat recovery is crucial to limit the process energy penalty.

The success of this heat integration is largely dependent on the performance of the indirect-contact heat exchanger employed to provide and remove heat from the sorbent. In particular, the estimation of the sorbent-side heat transfer coefficient is crucial for the design of the MBTSA system because it represents the limiting thermal resistance between the gas/adsorbent phases and the heating/cooling fluid. The convective heat transfer to the flowing sorbent is determined by several factors, including the flow pattern, particle mixing, contact area between sorbent and hot surfaces, as well as the sorbent residence time. The effective heat transfer is therefore affected not only by the geometry of the system (e.g., tube arrangements and shape, hydraulic diameters, pitching) or operating conditions (e.g., temperatures of heating/cooling fluid, flow rates), but also by specific properties of the bulk solid that influence its flowability (e.g., particle shape, size, density). Several studies investigated the heat transfer mechanisms in moving bed heat exchangers employing bulk solids as working fluid, both computationally (Campbell, 1990, Lee et al., 1998,

Isaza et al., 2015) and experimentally (Niegsch et al., 1994, Baird et al., 2008, Al-Ansary et al., 2012, Baumann and Zunft, 2015). As an example, the recent works by Qoaider et al. (2017), Dai et al. (2020) analyzed how different materials, including glass beads, corundum, sand, basalt or mixtures thereof, result in different flow characteristics. Other studies focused on different system geometries and configurations, considering for example moving packed beds with and without gas flow (Baird et al., 2008), or comparing horizontal tubes, vertical tubes, parallel plates, and finned tubes (Al-Ansary et al., 2012). The influence of the tube shapes on the local heat transfer has also been investigated by Tian et al. (2020), who compared circular cross-sectioned tubes with elliptical shaped ones. One of the conclusions from the surveyed literature is that the convective heat transfer coefficient of flowing solid particles in moving bed heat exchangers is case-specific and hard to estimate without experimental data (Obuskovic, 1988).

Another factor hindering the development of the MBTSA technology is the lack of an established method to design a process for a given flue gas specification. The design of an MBTSA system is a complex task that involves a large number of inter-related process parameters such as the choice of adsorbent material, process configuration, size and geometry of the different components, and operating conditions. In this context, process modelling and simulation is an essential tool for the conceptualization and analysis of new MBTSA systems. Provided that the model captures all relevant physical mechanisms, process simulations can be used to evaluate the system performance under different conditions. This, in turn, can help the designer to gain a better understanding of the process and serve as a basis to improve the design until the desired performance targets are met. In view of these advantages, process simulation has been a popular tool for the design of post-combustion PSA/VSA (Liu et al., 2011, Krishnamurthy et al., 2014, Farmahini et al., 2021) and TSA cycles (Plaza et al., 2017, Joss et al., 2017, Lillia et al., 2018). By contrast, modeling and simulation of MBTSA processes has lagged behind due to the early stage of development of this technology. In fact, only a handful of recent computational studies attempted to design and evaluate the performance of the MBTSA process for CO_2 capture in coal-fired power plants (Kim et al., 2013, Son et al., 2014, Mondino et al., 2017, Morales-Ospino et al., 2021) and natural gas combined cycle power plants (Mondino et al., 2019, 2020). However, to the knowledge of the authors', the utilization of the MBTSA technology for CO_2 capture in waste-to-energy plants has not been studied yet.

The aim of the present work is to design and evaluate an MBTSA process for capturing CO_2 from an industrial-scale waste-to-energy power plant. To assess the technology with realistic parameter values, we have measured heat transfer coefficients in the heating section of a new MBTSA demonstrator unit using activated carbon spheres with 0.7 mm diameter. In addition, a detailed computational model previously developed by the authors (Mondino et al., 2020) has been extended to include the experimentally measured heat transfer coefficients and to account for the internal heat recovery achieved by coupling the preheating and precooling sections. The feasibility of the proposed MBTSA process is evaluated based on different performance indicators including system footprint, energy duty, CO_2 separation performance, and process productivity.

2. Heat transfer measurements

A series of experiments were carried out in a lab-scale apparatus replicating a full MBTSA process with the aim to analyze the heat transfer performance of the desorption section.

2.1. Experimental apparatus

The MBTSA apparatus, schematically shown in Figure 1, is composed of three main sections, namely the adsorption, the desorption and the cooling sections, through which the adsorbent circulates in a continuous manner. The adsorbent is released into the adsorption section at a controlled flow rate from a feeding system placed at the top (ZD22B Standard Feeder, ThreeTec, Switzerland). The adsorption section consists of a 1.5 m high, 5 cm internal diameter polycarbonate column filled with structured packing that ensures uniform distribution of the sorbent flow.

After passing through the adsorption section, the sorbent enters a rotary valve (ACS valve, CI series) activated by a three-phase induction motor connected to the power supply by a WEG frequency inverter (CFW500 vector inverter/series). The rotary valve discharges the sorbent into the desorption section indicated as "measuring section" in Figure 1. This part consists of a series of three heat exchanger modules (shell-and-tube), in which the sorbent is indirectly heated by a thermal fluid. More specifically, the adsorbent moves downwards in the shell-side of the heat exchanger while the heating media flows within the horizontal tubes in a cross-flow mode. In addition, the lateral surfaces of the heat exchanger modules are insulated with a glass wool layer to limit the heat losses to the surroundings.

Each heat exchanger module contains a bundle of 55 horizontal tubes through which the heating fluid is distributed in a multi-pass configuration. As shown on the bottom left side of Figure 1, the tubes present an inner circular cross section (6 mm in diameter) and an outer squared cross section with a square side of 8 mm. Such configuration and tube shape were adopted to ensure good contact between the sorbent particles and the heating surface, enhancing the heat transfer rate. In particular, staggered horizontal tube arrangements promote a better particle mixing in comparison with vertical tubes or plate configurations (Takeuchi, 1996, Baumann and Zunft, 2015, Tian et al., 2020), especially when the tube pitch is narrow (Baumann et al., 2014). Furthermore, using a squared cross-section alleviates the local formation of stagnant and void zones above and below the tubes, respectively. This phenomenon typically occurs on circular tubes and limits the performance of the heat exchanger (Niegsch et al., 1994, Baumann and Zunft, 2015). The numerical values of the geometrical parameters of the heat exchanger are listed in Table 1.

Water is used as thermal fluid, supplied by a SE-6 JULABO heating circulator. The temperature of the water at the heat exchanger inlet is controlled by adjusting the set point on the heating circulator. The flow rate is measured with a turbine flow meter (F110P-AU model, HP series, KEM - Germany) installed between the heating circulator and the heat exchanger. The mass flow rate cannot be directly controlled as it depends on the balance between the pressure drop in the circuit and the charateristic of the Julabo circulator pump.

The sorbent temperature is measured with four thermocouples located at different positions within the heat exchangers, see Figure 1 (top left). The thermocouples are installed within the spacers separating the modules to ensure a good contact with the bulk of the sorbent flow. Four additional thermocouples are used to measure the water temperature at the inlet and outlet of each

heat exchanger module. All thermocouples are connected to a data acquisition system to record the temperature data in a LabVIEW interface (LabVIEW). Moreover, a series of powder level sensors are installed within the spacers separating the heat exchanger modules and connected to the LabVIEW program for monitoring the level of adsorbent inside the heat exchangers and ensure that the bed is packed during operation.

The bottom outlet of the heating section is connected to an adjustable transport screw driven by a stepper motor (M1343031, LAM Technologies) that discharges the sorbent into the cooling section. The speed of the screw is adjusted through the LabView program while monitoring the powder level indicators so that the level of adsorbent inside the heat exchanger can be kept as desired.

The cooling section is similar to the heating one, but has only two modules and employs water as cooling media supplied by a Jualbo CORIO™ CD-300F Refrigerated Circulator. After passing through the cooling section, the sorbent finally reaches a collector funnel at the bottom of the unit from which it is transported back to the top feeder by means of a vacuum conveyor system.

Table 1: Geometry and material properties of the heat exchanger used for the heat transfer measurements.

Parameter	Symbol	Unit	Value
Number of modules	N_{mod}	-	3
Number of tubes per module	N_{t}	-	55
Number of passes (water side)[a]	N_{pass}	-	5
Number of tubes per pass (water side)	$N_{\mathrm{t,pass}}$	-	11
Internal tube diameter	$d_{\mathrm{t,int}}$	m	0.006
External tube square side	$s_{\mathrm{t,ext}}$	m	0.008
Single tube length	l_{t}	m	0.1
Total tube length	$l_{\mathrm{t,tot}}$	m	16.50
Heat transfer area - water side	A_{w}	m^2	0.311
Heat transfer area - sorbent side	A_{s}	m^2	0.528
Cross flow area - sorbent side[b]	$A_{\mathrm{cf,s}}$	mm^2	6857
Cross flow area - water side[c]	$A_{\mathrm{cf,w}}$	mm^2	311
Tubes material	-	-	TiAl6V4
Specific heat capacity of TiAl6V4	$c_{p,\mathrm{t}}$	J/kg K	526
Thermal conductivity of TiAl6V4	k_{t}	W/m K	6.6
Density of TiAl6V4	ρ_{t}	$\mathrm{kg/m}^3$	4420

[a] The flow is directed into separate passes by four baffles placed in the lateral heads
[b] Calculated as the volume available for the sorbent flow divided by the module height
[c] Calculated as the internal cross section of a single tube multiplied by the number of tubes per pass

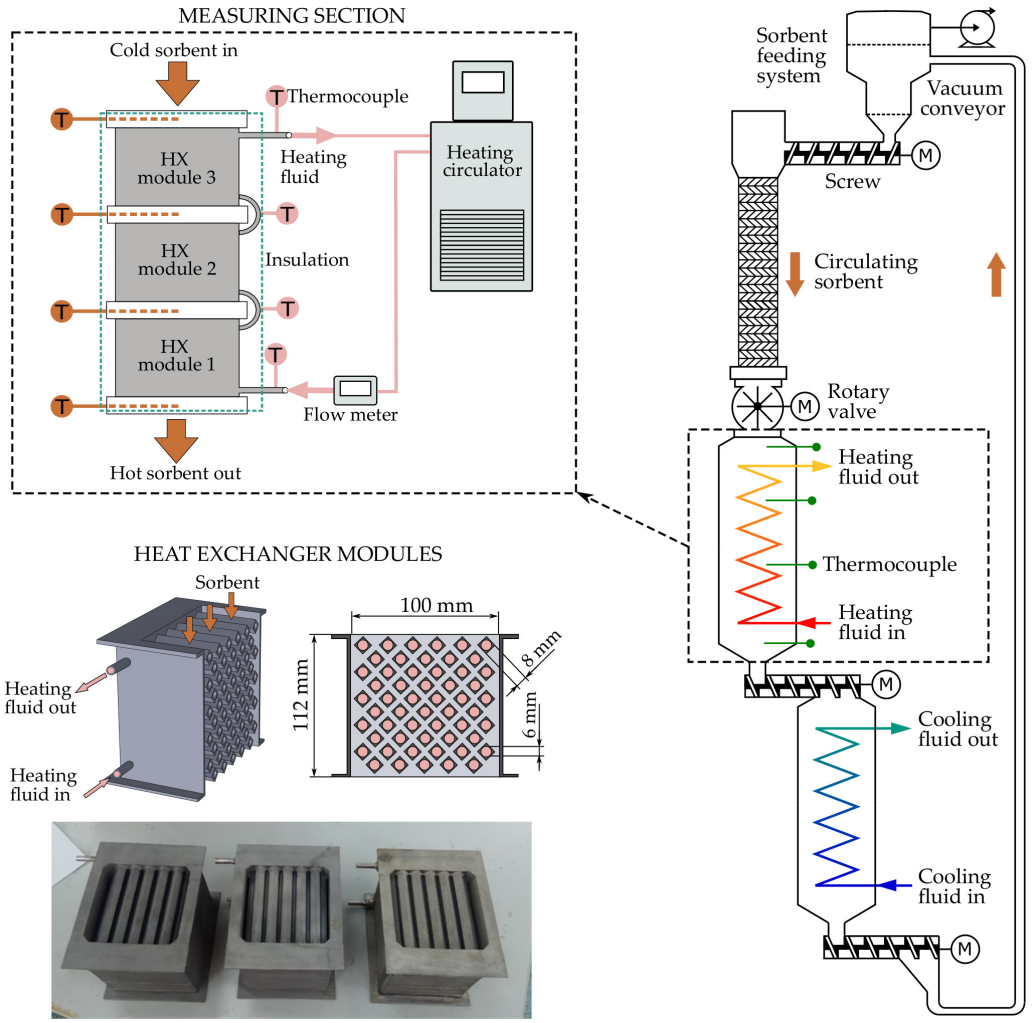

Figure 1: Experimental set-up used for heat transfer measurements: schematic diagram of the lab-scale moving bed (right), details on the measuring section (top left) and heat exchanger modules with a sectioned three-dimensional view, a cross-section and a picture of the three modules (bottom left).

2.2. Experimental procedure

The heat transfer measurements were carried out using an activated carbon shaped as 0.5–1.0 mm spherical beads supplied by Blücher (Germany). The physical properties of the adsorbent are summarized in Table 2. The system was loaded with approximately 10 kg of adsorbent. As previously mentioned, the adsorbent flow rate is controlled by the upper feeding system through a double screw that can be operated at different rotational rates. As the actual feeding rate does not only depend on the apparatus specifications, but also on the type of sorbent material and its flowing properties, the feeding system was calibrated prior to the experiments. To this aim, the sorbent flow rates were measured at different rotating speeds of the feed screw within the experimental range (7–24 g/s).

All experimental data were collected upon reaching steady state, which was assessed by monitoring the system temperatures via the LabVIEW interface. The sorbent feeding system was activated starting from the lowest flow rate and operated for several minutes until a new steady state was reached. At this point, the temperature measurement were recorded in LabVIEW. The sorbent flow rate was then changed to the next set point and the procedure was repeated. Each data point was obtained by averaging the readings over a period of time to reduce the influence of instantaneous random fluctuations.

Table 2: Physical properties of the adsorbent material.

Parameter	Value	Unit
Adsorbent type	Activated carbon*	–
Particle shape	Spherical beads	–
Particle diameter†	0.7	mm
Bulk density	452	kg/m^3
Particle density†	904	kg/m^3
Heat capacity†	880	kJ/kg K
Particle porosity†	0.50	–

* Provided by Blücher (Germany).
† Input value for the MBTSA simulations.

2.3. Determination of the heat transfer coefficient

The heat transfer coefficient is determined from the governing equations of the heat exchangers. The main assumptions underlying this analysis are: steady-state operating conditions, one-dimensional flow, negligible changes in the potential and kinetic energy of the fluids, constant transport properties, no fouling on internal heat exchanger surfaces, uniform heat transfer coefficients, and negligible heat loss to the surroundings. The latter assumption was verified by estimating the heat loss due to the natural convection of air on the vertical surfaces exposed to the surrounding. Based on the actual temperature of the exposed insulation layer and the room temperature, the heat loss was estimated to be less than 1 % of the total heat transfer rate in all cases.

Under the assumption of negligible heat loss, the heat transfer from the water is equal to the heat transfer to the sorbent. If, in addition, the specific heat of water is assumed to be constant, the heat flow rate can be calculated from the measured data according to:

$$\dot{Q} = \dot{m}_{\mathrm{w}} c_{p,\mathrm{w}} (T_{\mathrm{w,in}} - T_{\mathrm{w,out}}), \tag{1}$$

where the subscript w stands for water.

Using the mean logarithmic temperature difference approach (Cengel et al., 1998), the heat transfer rate can be related to the heat transfer resistances as:

$$\dot{Q} = \frac{\Delta T_{\mathrm{LM}}}{R_{\mathrm{tot}}}, \tag{2}$$

where R_{tot} is the total heat transfer resistance and ΔT_{LM} is the logarithmic mean temperature difference for the counter-flow arrangement. The total thermal resistance, R_{tot}, is the sum of the contributions due to internal convection (water-side), conduction across the tube walls, and external convection (sorbent-side). The average heat transfer coefficient between the flowing sorbent and the tube walls, h_{s}, can be solved from:

$$R_{\mathrm{tot}} = R_{\mathrm{w}} + R_{\mathrm{t}} + R_{\mathrm{s}} = \frac{1}{A_{\mathrm{w}} h_{\mathrm{w}}} + \frac{\ln(d_{\mathrm{t,ext}}/d_{\mathrm{t,int}})}{2\pi k_{\mathrm{t}} l_{\mathrm{t,tot}}} + \frac{1}{A_{\mathrm{s}} h_{\mathrm{s}}}, \tag{3}$$

where the subscript t stands for tubes and s for sorbent, whereas A_{s} is the heat transfer area on the sorbent side, given by:

$$A_{\mathrm{s}} = 4 s_{\mathrm{t,ext}}\, l_{\mathrm{t}}\, N_{\mathrm{mod}}\, N_{\mathrm{t}}. \tag{4}$$

Concerning the internal convective resistance (water side), the heat transfer area A_{w} is calculated directly from the system geometry as:

$$A_{\mathrm{w}} = 2\pi r_{\mathrm{t,int}}^2\, l_{\mathrm{t,tot}}, \tag{5}$$

where $l_{\mathrm{t,tot}}$ is the total length of tubes in the heat exchanger and $r_{\mathrm{t,int}}$ is the internal tube diameter. Moreover, the internal heat transfer coefficient, h_{w}, is estimated from an empirical correlation. As the water flow is laminar in all the tests (Reynolds numbers between 1178–1638), the following correlation for internal laminar flow was adopted (Cengel et al., 1998):

$$\mathrm{Nu} = \frac{h_{\mathrm{w}} d_{\mathrm{t,int}}}{k_{\mathrm{w}}} = 3.66 + \frac{0.065(d_{\mathrm{t,int}}/l_{\mathrm{t}})\,\mathrm{Re}\,\mathrm{Pr}}{1 + 0.04[(d_{\mathrm{t,int}}/l_{\mathrm{t}})\,\mathrm{Re}\,\mathrm{Pr}]^{2/3}} \tag{6}$$

The water conductivity, k_{w}, and the dimensionless numbers appearing in the correlation were evaluated at the bulk mean water temperature (i.e., arithmetic average of the temperature at the inlet and outlet).

Lastly, the tube walls resistance, R_{t}, was directly calculated from the thermal properties of the tube material (TiAl6V4 alloy) and the system geometry. For this purpose, the square profile of the tubes (with a side length $s_{\mathrm{t,ext}}$) was converted into an equivalent circular profile (with diameter $d_{\mathrm{t,ext}}$) with the same cross-sectional area as the actual profile.

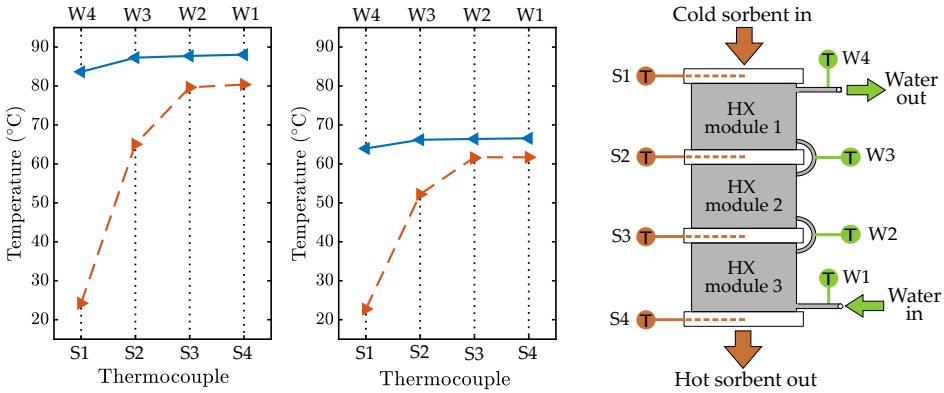

Figure 2: On the left, example of experimental results obtained for two test runs: Plot of the measured sorbent and water temperatures. On the right, schematic diagram of the experimental set-up indicating the position of each thermocouple.

2.4. Experimental results

An example of the collected temperature data is shown in Figure 2, where the points in the plots correspond to the temperatures sensed by the thermocouple, as specified in the schematic diagram on the right side. It was observed that, in all the experiments performed, the largest adsorbent temperature gain is achieved within the first module, while only a small fraction of heat is exchanged in the second and third modules. Furthermore, the change in temperature experienced by the water, is only a few degrees in the first module and almost negligible in the second and third ones. It was therefore decided to estimate the heat transfer coefficient using only the data corresponding to the first module, where the majority of the heat exchange takes place and the results have the least uncertainty.

The numerical values of the measured temperatures and the thermal parameters used to estimate the heat transfer coefficient are reported in Table 3. The estimated heat transfer rate, $\dot{Q}$, ranged between 249 W and 629 W, corresponding to tests 4 and 9, respectively. With regards to the thermal resistances, the convection on the sorbent-side was always the dominating resistance, ranging between 72 and 82 % of the total thermal resistance, while the conductive resistance of the tube walls ranged between 1.8 and 2.7 %.

The convective heat transfer coefficient on the sorbent side was computed for each operating point according to Eq. (3), and the results were plotted against the velocity of the solid particles in Figure 3. As expected, the heat transfer coefficient increases with the solid velocity (Niegsch et al., 1994, Al-Ansary et al., 2012, Baumann and Zunft, 2015), while no dependence was observed on the solid temperature. The measured heat transfer coefficients ranged between 69 and 117 W/m^2 K with an uncertainty below 8% in all cases, which was evaluated using the law of propagation of uncertainty (Farrance and Frenkel, 2012). The trend of the experiments suggests that even higher values might be achieved by operating the system at higher solid velocities. However, this hypothesis could not be verified due to the limitations of the experimental apparatus.

In order to correlate the experimental results, the heat transfer coefficient and solid velocity

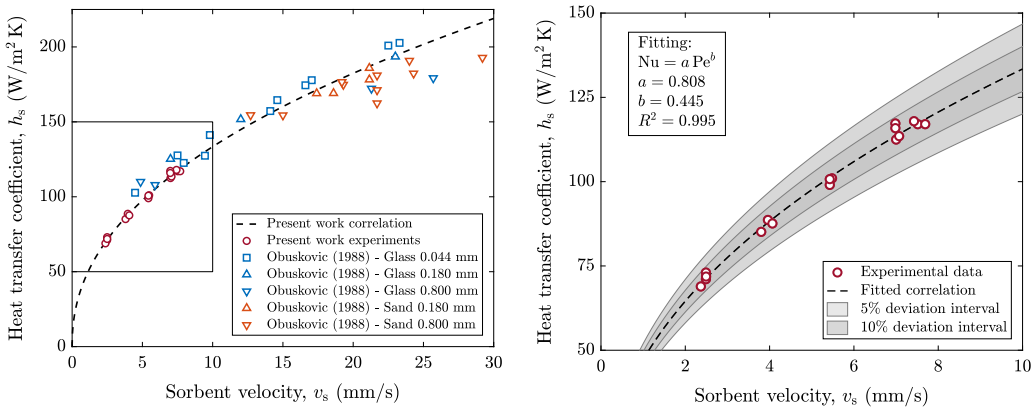

Figure 3: Experimental heat transfer coefficients and fitted correlation (right). Comparison of the heat transfer coefficients measured in this work against the values reported by Obuskovic (1988) for a single tube immersed in a moving bed operated with glass and sand particles of different diameters (left).

were expressed in terms of dimensionless quantities. The dependence of the heat transfer coefficient on: (i) gas thermal conductivity, (ii) bulk density, (iii) sorbent heat capacity, (iv) solid velocity, and (v) tube external side can be expressed as:

$$f(h_s,\, k_g,\, \rho_b,\, c_{p,s},\, v_s,\, s_{t,ext}) = 0. \tag{7}$$

Since this relationship involves 6 variables and 4 physical dimensions (i.e., time, length, mass, and temperature), dimensional analysis yields two independent dimensionless groups:

$$g(\mathrm{Nu},\, \mathrm{Pe}) = 0, \tag{8}$$

where

$$\mathrm{Nu} = \frac{h_s s_{t,ext}}{k_g} \tag{9}$$

is the Nusselt number and

$$\mathrm{Pe} = \frac{\rho_b c_{p,s} v_s s_{t,ext}}{k_g} \tag{10}$$

is the Péclet number. The Nusselt and Péclet numbers can be interpreted as the dimensionless heat transfer coefficient and solid velocity, respectively. Using these dimensionless numbers, the experimental results were correlated by means of regression analysis, and the following equation was obtained:

$$\mathrm{Nu} = a\,\mathrm{Pe}^b = 0.808\,\mathrm{Pe}^{0.445}. \tag{11}$$

This correlation is used to estimate the heat transfer rate within the full-scale MBTSA model described in the following section. As shown in Figure 3 (right), the relative deviation between the heat transfer coefficients determined experimentally and the values predicted by Equation (11) is below 5% for all cases. In addition, the coefficient of determination obtained from the regression

analysis is $R^2 = 0.995$. This suggests that the proposed correlation is adequate to predict the heat transfer coefficient for flowing adsorbent particles within cross-flow shell-and-tube heat exchangers, provided that the they are geometrically similar and operated within the range of particle velocities considered in these experiments.

In addition, Figure 3 (left) compares the heat transfer coefficients measured in this work against those reported by Obuskovic (1988) for a single tube immersed in a moving bed of solid particles. The heat transfer coefficients obtained for the activated carbon particles considered in this work are comparable with those obtained by Obuskovic (1988) for glass and sand particles of different diameters. In addition, the variation of the heat transfer coefficient with the velocity of the solid particles follows the same trend as the data from Obuskovic (1988). In particular, the exponent of the Péclet number obtained in the present work ($b = 0.455$), see Equation (11), agrees well with the exponent reported by Obuskovic (1988) for their low-velocity experiments ($b = 0.4$), and with the theoretical value suggested by Mickley and Fairbanks (1955) for an homogeneous moving bed of infinitesimally small particles ($b = 0.5$).

Finally, the heat transfer coefficients measured in this work are significantly higher than those typically encountered in fixed bed configurations. For example, Marx et al. (2016) reported heat transfer coefficients between 20 and 40 W/m^2 K when performing TSA experiments on a indirectly-heated packed bed filled with a zeolite 13X adsorbent shaped as spherical beads with diameters between 1.6 and 2.0 mm. Similarly, Bonjour et al. (2002) obtained heat transfer values up to 50 W/m^2 K when measuring the heat transfer performance of a coaxial packed bed heat exchanger filled with activated carbon beads of 0.65 mm mean diameter. This confirms that the moving bed configuration has the potential to address one of the main limitations of the fixed bed TSA process, namely, the low productivity due to the slow heating and cooling of the adsorbent.

Table 3: Overview of experimental results: measured data and calculated heat transfer parameters

			Test ID																
			1	2	3	4	5	6	7	8	9	10	11	12	13	14	15	16	17
Sorbent																			
Flow rate	$\dot{m}_s$	g/s	7.72	7.72	16.99	7.34	16.82	16.82	21.70	23.29	23.84	7.73	11.78	12.28	21.92	12.60	23.02	21.65	21.65
Mass flux	J_s	kg/m^{2}s	1.13	1.13	2.48	1.07	2.45	2.45	3.16	3.40	3.48	1.13	1.72	1.79	3.20	1.84	3.36	3.16	3.16
Velocity	v_s	mm/s	2.49	2.49	5.48	2.37	5.43	5.43	7.00	7.51	7.69	2.49	3.80	3.96	7.07	4.07	7.43	6.98	6.98
Inlet temp.	$T_{s,in}$	°C	25.1	24.2	26.4	22.7	24.9	26.7	27.7	28.8	26.4	21.2	24.4	22.6	26.9	23.2	25.9	31.0	27.5
Outlet temp.	$T_{s,out}$	°C	66.2	65.1	55.8	52.2	45.5	46.0	43.5	52.0	51.1	66.6	60.8	59.0	53.5	48.2	41.2	45.8	43.2
Water																			
Inlet temp.	$T_{w,in}$	°C	87.5	87.3	85.7	66.2	65.3	65.3	64.7	84.7	84.6	87.3	86.7	86.4	84.9	65.7	64.2	64.9	64.5
Outlet temp.	$T_{w,out}$	°C	84.2	83.6	80.6	64.0	62.0	62.1	61.2	79.2	78.9	83.7	82.4	81.8	79.4	62.8	60.5	61.7	61.0
Flow rate	$\dot{m}_w$	g/s	27.65	25.09	25.21	26.57	26.58	26.58	26.59	26.51	26.51	25.67	25.68	25.69	25.70	27.07	27.09	27.08	27.09
Velocity	v_w	mm/s	91.88	83.39	83.72	87.16	87.16	87.16	87.16	87.96	87.96	85.31	85.31	85.31	85.31	88.79	88.79	88.79	88.79
Density	ρ_w	kg/m^3	967	968	968	980	981	981	981	969	969	968	968	968	969	980	981	981	981
Viscosity	μ_w	mPa s	0.326	0.326	0.332	0.428	0.433	0.433	0.435	0.335	0.335	0.326	0.329	0.330	0.334	0.431	0.438	0.435	0.437
Heat capacity	$c_{p,w}$	J/kg K	4202	4202	4201	4188	4187	4187	4187	4200	4200	4202	4202	4202	4201	4187	4187	4187	4187
Conductivity	k_w	W/m K	0.671	0.671	0.670	0.656	0.656	0.656	0.655	0.670	0.670	0.671	0.671	0.671	0.670	0.656	0.655	0.655	0.655
Reynolds	Re	-	1638	1483	1466	1198	1185	1185	1178	1528	1526	1517	1507	1504	1485	1212	1193	1202	1197
Prandtl	Pr	-	2.04	2.04	2.08	2.73	2.77	2.77	2.78	2.10	2.10	2.04	2.06	2.06	2.09	2.75	2.80	2.78	2.79
Nusselt	Nu	-	5.19	5.08	5.09	5.17	5.17	5.17	5.17	5.14	5.14	5.11	5.11	5.11	5.11	5.19	5.19	5.19	5.19
Heat balance																			
Heat load	$\dot{Q}$	W	385.1	383.2	544.6	248.8	361.3	352.7	387.5	609.4	629.4	386.9	465.1	498.6	597.2	323.9	423.5	362.9	396.9
Mean log ΔT	ΔT_{LM}	-	37.05	37.82	40.87	25.21	27.54	26.54	26.88	40.91	42.25	37.82	39.74	41.28	41.07	27.09	28.37	24.41	26.92
HTC water	h_w	W/m^{2}K	581.0	568.0	568.1	565.4	564.9	564.9	564.7	574.4	574.3	571.0	570.8	570.7	570.4	567.6	567.0	567.3	567.1
HTC sorbent	h_s	W/m^{2}K	73.0	71.1	101.0	68.9	99.0	100.7	112.5	117.0	117.0	71.9	85.1	88.6	113.5	87.6	117.9	117.3	115.9
Thermal resistances																			
Total	R_{tot}	K/kW	96.19	98.70	75.03	101.30	76.24	75.27	69.38	67.13	67.13	97.76	85.45	82.79	68.76	83.65	66.98	67.25	67.83
Water side	R_w	K/kW	16.60	16.98	16.98	17.06	17.07	17.07	17.08	16.79	16.79	16.89	16.90	16.90	16.91	16.99	17.01	17.00	17.01
Tubes walls	R_t	K/kW	1.79	1.79	1.79	1.79	1.79	1.79	1.79	1.79	1.79	1.79	1.79	1.79	1.79	1.79	1.79	1.79	1.79
Sorbent side	R_s	K/kW	77.80	79.93	56.26	82.45	57.37	56.40	50.51	48.54	48.54	79.08	66.76	64.10	50.06	64.86	48.18	48.46	49.03
% water side	R_w	%	17.3	17.2	22.6	16.8	22.4	22.7	24.6	25.0	25.0	17.3	19.8	20.4	24.6	20.3	25.4	25.3	25.1
% tubes walls	R_t	%	1.9	1.8	2.4	1.8	2.3	2.4	2.6	2.7	2.7	1.8	2.1	2.2	2.6	2.1	2.7	2.7	2.6
% sorbent side	R_s	%	80.9	81.0	75.0	81.4	75.3	74.9	72.8	72.3	72.3	80.9	78.1	77.4	72.8	77.5	71.9	72.1	72.3

3. Application of the MBTSA process to a waste-to-energy plant

3.1. Case study definition

The second part of this study considers the application of the MBTSA process to capture CO_2 from a Combined Heat and Power (CHP) waste-to-energy plant with a net power output of 16.8 MW_{el} and a thermal output of 64.6 MW_{th}. The power plant was modeled in Thermoflex software (Thermoflow Version 27) using a built-in waste-to-energy plant model. The flue gas specification required to design the MBTSA process were obtained by simulating the plant at its nominal operating point. In order to reduce the computational effort of the MBTSA simulations, the composition of the exhaust gas was simplified to a binary mixture of N_2 and CO_2, assuming that: (i) the flue gas is dried prior to the capture process, and (ii) O_2 and Ar behave similarly to N_2 in terms of adsorption equilibrium and kinetics (Plaza et al., 2014, 2017). The resulting flue gas specifications, used as input for designing and simulating the MBTSA process, are listed in Table 4.

Table 4: Flue gas specifications of the waste-to-energy CHP plant.

Parameter	Value	Unit
Mass flow rate	55.9	kg/s
Temperature	30	°C
Pressure	101.5	kPa
Simplified composition:		
molar fraction of CO_2	11	%
molar fraction of N_2	89	%

3.2. Adsorbent material

The adsorbent used for the case study was the same activated carbon employed in the heat transfer experiments. The physical properties of the adsorbent used as basis for the MBTSA process simulations are summarized in Table 2. In addition, the adsorption equilibrium data for CO_2 and N_2 were measured experimentally and fitted with a suitable adsorption isotherm model as described below.

Pure-component isotherms of CO_2 and N_2 were measured on a sample of the activated carbon using a volumetric adsorption apparatus (Belsorp Max, MicrotracBEL, Japan). The data were collected at six different temperatures between 30 and 150 °C. Prior to the measurements, overnight degassing of the sample was performed at 150 °C and vacuum conditions.

The experimental isotherms data were fitted with a Virial model truncated at its second term (Barrer, 1981, Grande et al., 2008):

$$P_i = \frac{q_i^*}{K_{\mathrm{H},i}} \exp(A_i q_i^* + B_i q_i^{*2}), \tag{12}$$

where subscript i indicates the adsorbate (CO_2 or N_2), P_i is the partial pressure, q_i^* the amount adsorbed at equilibrium, and $K_{\mathrm{H},i}$ the Henry's law constant. The temperature dependence of the

Table 5: Virial model parameters fitting CO_2 and N_2 adsorption isotherms on the activated carbon at temperatures between 30 and 150 °C and pressures up to 105 kPa.

	K_H^∞ mol/kg kPa	$-\Delta H$ kJ/mol	A_0 kg/mol	A_1 K kg/mol	B_0 kg^2/mol^2	B_1 K kg^2/mol^2
CO_2	$2.6969 \cdot 10^{-7}$	30.006	−4.3235	1474.0	1.4239	−465.20
N_2	$5.5486 \cdot 10^{-7}$	21.934	−22.982	7121.1	51.644	−15756

Virial coefficients A_i and B_i was expressed by

$$A_i = A_{0,i} + \frac{A_{1,i}}{T_s} \quad \text{and} \quad B_i = B_{0,i} + \frac{B_{1,i}}{T_s}, \tag{13}$$

while the dependence of the Henry's law constant with temperature was given by the Van't Hoff equation:

$$K_{H,i} = K_{H,i}^\infty \exp\left(\frac{-\Delta H_i}{RT_s}\right), \tag{14}$$

where $K_{H,i}^\infty$ is the adsorption constant at infinite temperature, ΔH_i the heat of adsorption at zero coverage, and R the universal gas constant.

The values of the fitted Virial model parameters are summarized in Table 5, and they serve as basis for prediction of adsorption equilibrium in the MBTSA model, where the multi-component extension of the Virial model (Taqvi and LeVan, 1997, Grande et al., 2008, Shen et al., 2010) is implemented to account for competitive adsorption of the two gases (see Appendix A).

The results of the CO_2 and N_2 isotherms measurements together with the isotherms fitting are shown in Figure 4. As expected, the adsorption capacity of CO_2 is higher than that of N_2 in the whole temperature and pressure ranges examined. Nevertheless, the equilibrium selectivity expressed as

$$s_{CO_2/N_2} = \frac{q_{CO_2}/p_{CO_2}}{q_{N_2}/p_{N_2}} \tag{15}$$

and calculated at the feed gas conditions is just above 11. This value is significantly lower than that of other widely used CO_2 capture adsorbents, such as 13X and 5A zeolites, for which the selectivity can be as high as 96 and 90, respectively (Merel et al., 2008). Indeed, the CO_2 adsorption capacity at the feed gas conditions (11 kPa and 30 °C) is much lower for the activated carbon, being less than 0.4 mol/kg, compared to a value larger than 2 mol/kg for the zeolites (Cavenati et al., 2004, Mulloth and Finn, 1998).

With regards to the heat of adsorption, the values obtained by fitting the CO_2 and N_2 isotherms are in agreement with literature data reported for other carbon adsorbents (Lopes et al., 2009, Plaza et al., 2017, Mondino et al., 2017).

3.3. MBTSA process configuration

The MBTSA process configuration considered in this work is illustrated in Figure 5. The system comprises five main sections through which the adsorbent circulates, namely the adsorption,

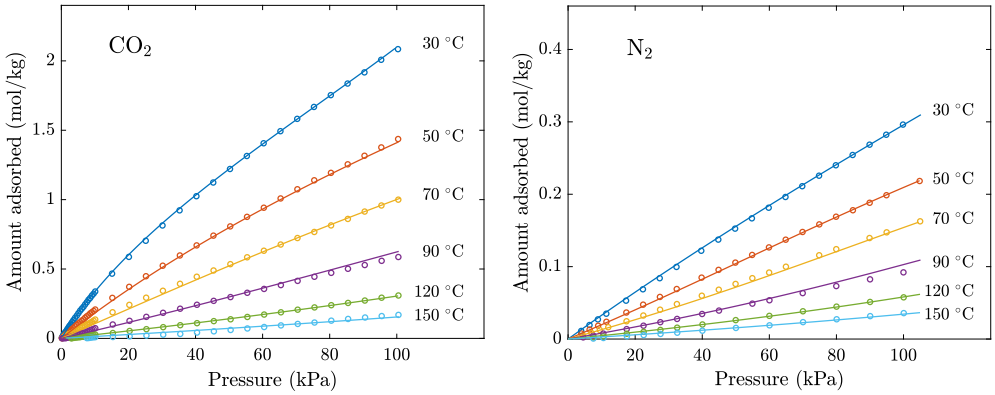

Figure 4: CO_2 and N_2 adsorption isotherms on the activated carbon: measured data (dots) and model fitting (continuous lines).

preheating, desorption, precooling and cooling sections. The separation of the CO_2 from the rest of the flue gas takes place within the adsorption section, where the gas flows upwards in a countercurrent way with respect to the adsorbent that moves downwards. While the CO_2 is preferentially adsorbed onto the activated carbon, the non-adsorbing N_2 is vented to the atmosphere from the top outlet of the adsorption section. In order to ensure uniform distribution of the sorbent flow, the adsorption section is filled with structured packing consisting of corrugated and perforated metal plates, similar to those used in absorption columns.

The adsorbent reaching the bottom outlet of the adsorbent section is loaded with CO_2 and needs to be regenerated. The thermal energy required for sorbent regeneration is provided within the preheating and desorption sections, both operated as indirect-contact heat exchangers. The preheating section is used first to heat the adsorbent to a certain extent by means of internally recovered heat, while the desorption section is used to provide additional heat to the sorbent until reaching the target desorption temperature. The desorbing CO_2 is collected in a CO_2-rich stream at the bottom end of the desorption section. Light vacuum (about 90 kPa) is applied to assist the desorption and direct the desorbing gas towards the extraction point.

The remaining sections, precooling and cooling, are used to bring the adsorbent back down to the adsorption temperature. If complete regeneration is not achieved within the desorption section, the remaining CO_2 is recovered by purging the adsorbent in the cooling and precooling sections with a small fraction of the CO_2-free product. Ultimately, the regenerated adsorbent is transported back to the top of the unit, closing the cycle.

3.4. Design of the MBTSA process

Based on the given flue gas specifications and adsorbent characteristics, the MBTSA process was designed to achieve a CO_2 purity of at least 95 % and a capture rate higher than 90 %, as typically required in CCS application (Nord and Bolland, 2020, Joss et al., 2017).

The design of the MBTSA process was accomplished using the one-dimensional model documented by the authors in previous publications (Mondino et al., 2017, 2019, 2020). The model is

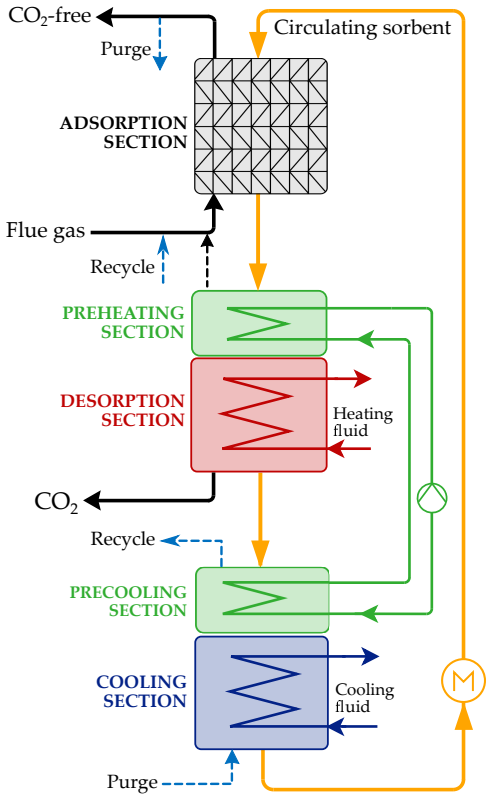

Figure 5: Schematic diagram of the simulated MBTSA process.

based on the mass, energy and momentum balances applied to the different MBTSA sections, and it was implemented in the gPROMS environment (gPROMS Model Builder Version 6.0). Compared to previous works, the model was extended to include the equations of the heating/cooling media of the heat exchangers and to accommodate the sorbent-side heat transfer coefficients determined experimentally. The complete set of model equations, together with the underlying assumptions, is reported in Appendix A.

Several design parameters including the system dimensions (height and diameter of each section) and operating conditions (amount of circulating sorbent, adsorption and desorption temperatures, and CO_2 extraction pressure) were adjusted until the target CO_2 purity and capture rate were achieved. The design parameters of the final configuration are listed in Table 6. A very large amount of sorbent (650 kg/s) relative to the flue gas (56 kg/s) was required because of the low CO_2 capacity of the adsorbent. The limited working capacity of the adsorbent was partially compensated by adopting a large temperature swing. In particular, the cooling and regeneration temperatures, i.e., the minimum and maximum temperatures experienced by the adsorbent, were 18 °C and 184 °C, respectively.

Table 6: MBTSA design and process parameters.

Operating conditions		
Sorbent regeneration temperature	184	°C
Sorbent cooling temperature	18	°C
CO_2 extraction pressure	90	kPa
Inlet gas sup. velocity	0.41	m/s
Void fraction in adsorption section	0.7	-
Void fraction in other sections	0.5	-
System dimensions		
Diameter in adsorption section	12.8	m
Diameter in other sections	13.3	m
Height of adsorption section	0.9	m
Height of preheating section	0.4	m
Height of desorption section	0.8	m
Height of precooling section	0.4	m
Height of cooling section	0.6	m
Total height	3.1	m
Sorbent inventory		
Amount of circulating sorbent	650	kg/s
Sorbent mass flux in heat exchangers	4.7	kg/m^2s
Sorbent residence time	4.2	min
Heating/cooling fluids		
Specific heat capacity	4.2	kJ/kg K
Density	1000	kg/m^3
Flow rate in preheat./precool. sections	160.6	kg/s
Flow rate in desorption section	267.6	kg/s
Flow rate in cooling section	267.6	kg/s
Inlet temperature in desorption section	187	°C
Inlet temperature in cooling section	10	°C

With regards to the system dimensions, the length and diameter of the adsorption section were selected as a trade-off to reduce the footprint of the column and limit the gas and sorbent velocities to avoid fluidization, guarantee a sufficient residence time, and limit the pressure drop. The cross section area of the other sections (preheating, desorption, precooling and cooling) was determined by scaling up the heat exchanger modules of the experimental apparatus to the actual sorbent flow rate, while maintaining the same tube shape and diameter (i.e., same heat transfer area per unit volume). The length was then adjusted so that the desired temperatures were reached by the end of the section.

3.5. Simulation results - Concentration and temperature profiles

Figure 6 shows the computed concentration and temperature profiles along the five MBTSA sections, where the left and right limits of the plot correspond to the bottom of the cooling section and the top of the adsorption section, respectively. In agreement with this representation, the adsorbent flows from the right to the left in each section and the feed gas flows from the left to the right within the adsorption section.

As seen in the adsorbent loading profile within the adsorption section, a significant amount of nitrogen is also adsorbed along with the CO_2. This is in agreement with the adsorption equilibrium data and corresponding selectivity, which was estimated to be as low as 11. More specifically, at the bottom end of the adsorption section, i.e., at the gas feeding point, the fraction of nitrogen in the adsorbed phase is approximately 39% of the total, corresponding to a specific loading around 0.26 mol/kg, versus a CO_2 loading of 0.42 mol/kg. Furthermore, as seen in the temperature profile of the adsorption section, the effect of the heat of adsorption is modest and causes an increase in the adsorbent temperature of about 9 °C. As expected, in the adsorption section the maximum temperature is reached at the gas feeding point, where the adsorption driving force is the highest. The reason for the limited impact of this non-isothermal effect can be attributed to the high sorbent-to-gas ratio associated to the low adsorption capacity.

Most of the adsorbed nitrogen is released from the adsorbed phase as the temperature increases along the preheating section, i.e., moving from right to left along the plot, while the CO_2 loading remains approximately constant due to its stronger affinity on the adsorbent. The gas that is being desorbed within the preheating section is removed from the top and re-mixed with the feed gas (see Figure 5). As the N_2 is removed, and the adsorbent temperature increases, the CO_2 fraction in the gas phase gradually increases towards the bottom end of the preheating section. The same trend continues in the desorption section, where the adsorbent temperature is further increased to the target regeneration temperature (184 °C) and CO_2 molar fraction in the gas phase reaches a maximum value of 97.2% at the bottom end of the section, i.e., the CO_2 extraction point.

As depicted in Figure 6, the adsorbent still contains a certain amount of CO_2 (about 0.07 mol/kg) when entering the following section for precooling. To further regenerate the adsorbent and recover this CO_2, a fraction of the CO_2-free product (approximately 15% of the total flow rate on a weight basis) was used to counter-currently purge the adsorbent within the cooling and precooling sections. The use of this purge gas is also important to avoid the formation of low pressure zones induced by the decrease in temperature, thus maintaining the pressure close to atmospheric.

In addition to the gas and sorbent temperature profiles, the bottom plot in Figure 6 also shows the temperature of the heating and cooling fluids along the corresponding sections. In an attempt to maximize the internal heat recovery, the flow rate of the heat transfer media was tuned so that its heat capacity rate was as close as possible to that of the sorbent-gas side and the temperature difference along the heat exchanger was approximately constant.

3.6. Simulation results - Overall system performance

The MBTSA process was evaluated in terms of several performance indicators, and the results are reported in Table 7. The CO_2 purity corresponds to the molar fraction of CO_2 in the CO_2-rich

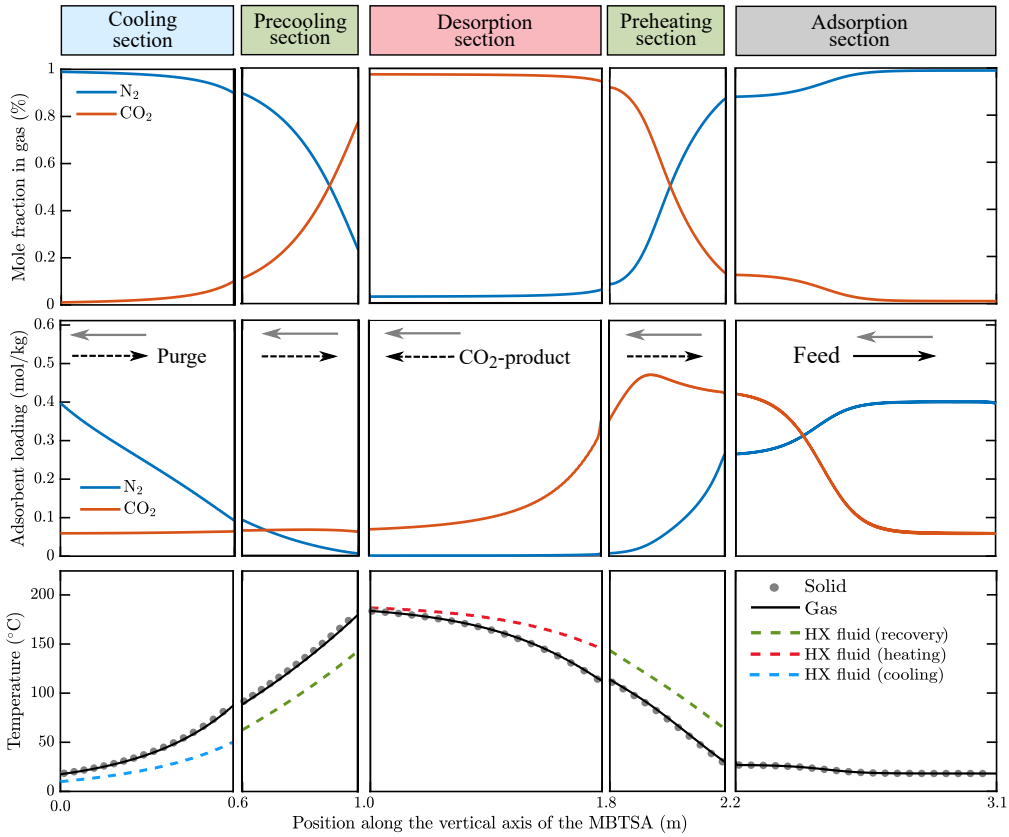

Figure 6: Concentration and temperature profiles for each section of the MBTSA system. Position 0 m corresponds to bottom of the cooling section and position 3.1 m to the top of the adsorption section. The black and gray arrows represent the direction of the gas and sorbent flows, respectively.

product,

$$\text{CO}_2 \text{ purity} = \frac{\dot{n}_{\text{CO}_2,\text{CO}_2\text{-rich gas}}}{\dot{n}_{\text{tot,CO}_2\text{-rich gas}}} \cdot 100, \tag{16}$$

while the capture rate is obtained from an overall system mass balance as the ratio between the amount of CO_2 in the CO_2-rich product (i.e., moles of CO_2 captured per unit time) and the amount of CO_2 in the flue gas (i.e., amount of CO_2 fed to the system per unit time),

$$\text{CO}_2 \text{ capture rate} = \frac{\dot{n}_{\text{CO}_2,\text{CO}_2\text{-rich gas}}}{\dot{n}_{\text{tot,flue gas}}} \cdot 100. \tag{17}$$

The process productivity was calculated as the ratio between the mass flow rate of CO_2 in the CO_2-rich product and the total sorbent inventory,

$$\text{Productivity} = \frac{\dot{m}_{\text{CO}_2,\text{CO}_2\text{-rich gas}}}{\dot{m}_{\text{s}} \cdot t_{\text{cycle}}}. \tag{18}$$

Table 7: Summary of simulations results.

Main performance indicators		
CO_2 purity	97.2	%vol
CO_2 capture rate	90.8	%vol
CO_2 captured	8.26	kg/s
Sorbent flow rate	650	kg/s
Process productivity	181	$kg_{CO_2}/t_s h$
Specific energy duty	5.7	MJ/kg_{CO_2}
Heat loads in MBTSA sections		
Preheating (internal recovery)	54.2	MW
Desorption (external heating)	47.0	MW
Precooling (internal recovery)	54.2	MW
Cooling (external cooling)	45.8	MW

The sorbent inventory is the amount of adsorbent needed to complete a full cycle and is calculated as the product of sorbent flow rate and the total cycle time (sum of residence time in each section). Lastly, the specific energy duty refers to the amount of thermal energy required to capture one kilogram of CO_2, and it was calculated by dividing the heat flow rate provided in the desorption section by the amount of CO_2 captured per unit time,

$$\text{Specific energy duty} = \frac{\dot{Q}_{\text{desorption section}}}{\dot{m}_{\text{CO}_2,\text{CO}_2\text{-rich gas}}}. \tag{19}$$

In spite of the low adsorbent selectivity, the designed MBTSA process was able to meet the desired target performance in terms of purity and capture rate, the obtained values being 97.2% and 90.8%, respectively. With regards to the energy use, the process requires 5.7 MJ/kg_{CO_2}, which is higher than other values reported in the literature for TSA capture processes achieving high CO_2 purity and recovery. For example, a value of 4.28 MJ/kg_{CO_2} has been reported for a heat-integrated fixed-bed TSA system employing Zeolite 13X (Joss et al., 2017), while Merel et al. (2008) estimated 4.5 MJ/kg_{CO_2} when using 5A zeolite. A slightly lower value (3.59 MJ/kg_{CO_2}) was reported by Plaza et al. (2017) referring to a TSA system based on structured carbon adsorbent and steam stripping. Nevertheless, the specific energy duty estimated in the present study is approximately three times higher than that of a similar case study previously documented by the authors (Mondino et al., 2019), where zeolite 13X was employed to capture CO_2 from a natural gas combined cycle (Mondino et al., 2019). The relatively higher energy duty can be explained by the much lower working capacity of the activated carbon (0.36 mol/kg) compared to that of the zeolite (2.8 mol/kg) which implies larger sorbent inventory and contributes to the parasitic duty associated to the sorbent heat capacity. In addition, to compensate for the low adsorption capacity towards CO_2, a high desorption temperature was adopted, which also led to an increase in the process energy requirement.

On the other hand, the simulated process seems to be very promising in terms of productivity,

the obtained value being 181 $kg_{CO_2}/t_s h$. Such high process productivity can be attributed to the short cycle time (4.22 min) associated with the fast heating and cooling of the adsorbent. For comparison, Bonjour and co-workers calculated a productivity of 22.4 $kg_{ethane}/t_s h$ for a fixed bed TSA process with indirect heating for gaseous pollutant treatment (Bonjour et al., 2005). In the context of post-combustion CO_2 capture, Plaza et al. (2017) reported a productivity of 35-40 $kg_{CO_2}/t_s h$ when using carbon honeycomb monoliths in a fixed bed process with direct heating, while Joss et al. (2017) obtained a productivity between 30 and 60 $kg_{CO_2}/t_s h$ for an indirect heated TSA process using zeolite 13X achieving similar performance in terms of energetic consumption (about 4 MJ/t_{CO_2}), purity (above 95%), and capture rate (above 90%).

4. Conclusions

The heat transfer coefficient of a heat exchanger used for sorbent heating in an MBTSA system was determined in a lab scale apparatus. For this purpose, an activated carbon material shaped in spherical beads was circulated through a set of cross-flow shell-and-tube heat exchanger modules at different operating conditions (sorbent velocity and heating fluid temperature). The analysis of the results revealed a direct dependence between the heat transfer coefficient and sorbent flow rate, while no dependence was observed on sorbent temperature. The trend of the experimental results suggested that operating the system at higher sorbent flow rates could lead to even higher heat transfer coefficients. In any case, the heat transfer coefficients obtained (69–117 $W/m^2 K$) are significantly higher than those typically encountered in fixed bed configurations (10–50 $W/m^2 K$). This confirmed that the moving bed configuration has the potential to address one of the main limitations of the fixed bed TSA process, namely, the low productivity due to the slow heating and cooling of the adsorbent.

The results of the experimental campaign were used to develop a correlation for the sorbent-side heat transfer coefficient in terms of the Nusselt and Péclet numbers. This correlation was incorporated into an MBTSA computational model, which was then used to design and analyze an MBTSA process for an industrial-scale waste-to-energy CHP plant. The adsorbent material was the same commercial activated carbon used in the heat transfer experiments. Despite the low selectivity of the adsorbent, the proposed MBTSA process was able to achieve high CO_2 purity (97.2 %) and capture rate (90.8%), at the expense of adopting a high regeneration temperature (187 °C) and solid-to-gas ratio (11.6 kg of adsorbent per kg of flue gas). These two factors led to a rather high energy consumption (5.7 MJ/kg_{CO_2}) compared with the values reported in literature for other adsorbents. Nevertheless, the designed MBTSA system was able to achieve high process productivity (181 $kg_{CO_2}/t_{ads} h$). This can be attributed to the fast temperature swings associated with the high sorbent-side heat transfer coefficient of the moving bed configuration. Overall, the simulation results indicate that the MBTSA technology is suited to capture CO_2 at high purity and recovery, while achieving higher process productivity than fixed bed TSA processes. However, the energy performance of the capture process was relatively poor, especially considering that 53.5% of the heat required to regenerate the adsorbent was provided by internal heat recovery. In this regard, it is believed that the thermal energy required may be significantly reduced by replacing the activated carbon material by other adsorbents having higher capacity and selectivity towards CO_2, such as zeolites or metal-organic frameworks.

Nomenclature

Latin symbols

a	Fitting constant	-
a'	Particle specific area	m^2/m^3
A_i	First single-component Virial coefficients	kg/mol
A_{ij}	First multi-component Virial coefficients	kg/mol
$A_{0,i}$	Fitting constants of the first Virial coefficients	kg/mol
$A_{1,i}$	Fitting constants of the first Virial coefficients	K kg/mol
$A_{\mathrm{cf,s}}$	Cross-flow area of the sorbent side	m^2
$A_{\mathrm{cf,w}}$	Cross-flow area of the water side	m^2
A_{s}	Heat transfer area of the sorbent side	m^2
A_{w}	Heat transfer area of the water side	m^2
b	Fitting constant	-
B_i	Second single-component Virial coefficients	kg^2/mol^2
B_{ijk}	Second multi-component Virial coefficients	kg^2/mol^2
$B_{0,i}$	Fitting constants of the second Virial coefficients	kg^2/mol^2
$B_{1,i}$	Fitting constants of the second Virial coefficients	K kg^2/mol^2
Bi_i	Biot number of the adsorbent particles for component i	-
$c_{p,\mathrm{f}}$	Specific heat capacity of the heating/cooling fluid	J/kg K
$c_{p,\mathrm{g}}$	Specific heat capacity of the gas mixture	J/kg K
$c_{p,\mathrm{pk}}$	Specific heat capacity of packing material	J/kg K
$c_{p,\mathrm{s}}$	Specific heat capacity of the adsorbent	J/kg K
$c_{p,\mathrm{t}}$	Specific heat capacity of the heat exchanger tubes	J/kg K
$c_{p,\mathrm{w}}$	Specific heat capacity of water	J/kg K
$\hat{c}_p$	Molar heat capacity of the gas mixture at constant pressure	J/mol K
$\hat{c}_v$	Molar heat capacity of the gas mixture at constant volume	J/mol K
C_i	Molar concentration of component i in the gas phase	mol/m^3
$C_{\mathrm{p},i}$	Molar concentration of component i in the macropores	mol/m^3
C_{T}	Total molar concentration of the gas phase	mol/m^3
d_{p}	Particle diameter	m
$d_{\mathrm{t,ext}}$	Equivalent external diameter of the tubes	m
$d_{\mathrm{t,int}}$	Internal diameter of the tubes	m
D_{c}^0	Micropore limiting diffusivity at infinite temperature	m^2/s
D_{ij}	Binary molecular diffusivity of components (i, j)	m^2/s
$D_{\mathrm{Kn},i}$	Knudsen diffusivity of component i	m^2/s
$D_{\mathrm{m},i}$	Molecular diffusivity of component i	m^2/s

$D_{\mathrm{p},i}$	Macropore diffusivity of component i	m^2/s
$D_{z,i}$	Axial dispersion coefficient of component i	m^2/s
$E_{\mathrm{a},i}$	Activation energy of micropore diffusion of component i	J/mol
h_{gs}	Heat transfer coefficient between gas and solid	$\mathrm{W/m^2\,K}$
h_{ft}	Heat transfer coefficient between fluid and tube walls	$\mathrm{W/m^2\,K}$
h_{gt}	Heat transfer coefficient between gas and tube walls	$\mathrm{W/m^2\,K}$
h_{s}	Heat transfer coefficient on the sorbent side	$\mathrm{W/m^2\,K}$
h_{w}	Heat transfer coefficient on the water side	$\mathrm{W/m^2\,K}$
J_{s}	Sorbent mass flux	$\mathrm{kg/m^2\,s}$
$k_{\mathrm{f,i}}$	Film mass transfer coefficient of component i	m/s
k_{g}	Thermal conductivity of the gas mixture	W/m K
k_{w}	Thermal conductivity of water	W/m K
$K_{\mathrm{H},i}$	Henry's law constant of component i	mol/kg Pa
$K^{\infty}_{\mathrm{H},i}$	Henry's law constant at infinite temperature	mol/kg Pa
l_{t}	Length of a single tube	m
$l_{\mathrm{t,tot}}$	Total length of the tubes	m
L_{x}	Tube length along flow direction	m
L_{z}	Section length along vertical axis	m
$\dot{m}$	Mass flow rate	mol/s
$\dot{m}_{\mathrm{s}}$	Mass flow rate of sorbent	mol/s
$\dot{m}_{\mathrm{w}}$	Mass flow rate of water	mol/s
M_{w}	Molecular weight	kg/mol
$\dot{n}$	Molar flow rate	mol/s
N_{mod}	Number of heat exchanger modules	-
N_{pass}	Number of passes per module	-
N_{t}	Number of tubes per module	-
$N_{\mathrm{t,pass}}$	Number of tubes per pass	-
Nu	Nusselt number	-
P	Total pressure of the gas mixture	Pa
P_i	Partial pressure of component i	Pa
Pe	Péclet number	-
Pr	Prandtl number	-
q_i	Adsorbed concentration of component i	mol/kg
q^*_i	Adsorbed concentration of component i at equilibrium	mol/kg
$\dot{Q}$	Heat flow rate	W
r_{c}	Micropore radius	m

r_p	Particle radius	m
r_{pore}	Macropore radius	m
$r_{t,int}$	Internal radius of the tubes	m
R	Ideal gas constant	J/K mol
R_t	Heat transfer resistance of the tubes	K/W
R_{tot}	Total heat transfer resistance	K/W
R_s	Heat transfer resistance on the sorbent side	K/W
R_w	Heat transfer resistance on the water side	K/W
Re	Reynolds number	-
s_{CO_2/N_2}	Adsorbent selectivity of carbon dioxide over nitrogen	-
$s_{t,ext}$	External side length of the tubes	m
Sc_i	Schmidt number of component i	-
Sh_i	Sherwood number of component i	-
t	Time	s
t_{cycle}	Cycle time of the MBTSA process	s
T	Temperature of the gas	K
T_f	Temperature of the heating/cooling fluid	K
T_s	Temperature of the sorbent particles	K
T_t	Temperature of the heat exchanger tubes wall	K
T_w	Temperature of the water	K
u	Superficial velocity of the gas	m/s
u_f	Velocity of the heating/cooling fluid	m/s
v_s	Velocity of the adsorbent	m/s
v_w	Velocity of water	m/s
Y_i	Molar fraction of component i	-
z	Coordinate along the section height	m

Greek symbols

α_{gt}	Ratio of external surface area of tubes to gas-solid volume	m^2/m^3
$\alpha_{t,ext}$	Ratio of external surface area of tubes to fluid volume	m^2/m^3
$\alpha_{t,int}$	Ratio of internal surface area of tubes to fluid volume	m^2/m^3
ΔH_i	Heat of adsorption of component i	J/mol
ΔT_{LM}	Logarithmic mean temperature difference	K
ε	Column void fraction	-
ε_p	Particle porosity	-
λ_g	Axial heat dispersion coefficient of the gas mixture	W/m K

λ_{pk}	Axial heat dispersion coefficient of the packing	W/m K
μ_g	Dynamic viscosity of the gas mixture	Pa s
μ_w	Dynamic viscosity of water	Pa s
ξ	Packing porosity factor	-
ρ_f	Density of the heating/cooling fluid	kg/m^3
ρ_g	Density of the gas mixture	kg/m^3
ρ_p	Density of the adsorbent particles	kg/m^3
ρ_{pk}	Density of the packing	kg/m^3
ρ_t	Density of the heat exchanger tubes	kg/m^3
ρ_w	Density of water	kg/m^3
σ_{ij}	Lennard-Jones parameter of binary diffusivity	m
τ_p	Particle tortuosity	-
$\Omega_{D_{ij}}$	Dimensionless collision integral of binary diffusivity	-

Abbreviations

CCS	Carbon Capture and Storage
CFDM	Centered Finite Difference Method
CHP	Combined Heat and Power
GHG	Greenhouse Gases
HTC	Heat Transfer Coefficient
HX	Heat Exchanger
LDF	Linear Driving Force
MBTSA	Moving Bed Temperature Swing Adsorption
PSA	Pressure Swing Adsorption
TSA	Temperature Swing Adsorption
VSA	Vacuum Swing Adsorption

Acknowledgments

We acknowledge the Research Council of Norway for its financial support through the EDemoTeC project (Grant no. 267873) within the CLIMIT program.

Appendix A. MBTSA model equations

The MBTSA process is described by means of a one-dimensional mathematical model obtained by applying the mass, momentum and energy balances to the different sections (adsorption, preheating, desorption, precooling and cooling), each of which is connected to the adjacent ones through appropriate boundary conditions. Although the numerical value of certain design parameters (e.g., void fraction, section height, etc.) and operating conditions differ from section to section, the model equations and the underlying assumptions are the same for each section: negligible gradients in the radial direction, constant cross sectional area, constant sorbent velocity, uniform and constant void fraction, and ideal gas behavior in the bulk phase.

Transport equations

The gas phase concentration profiles along the section height are predicted by solving the mass balance in the gas phase for each species:

$$\varepsilon_{\mathrm{c}}\frac{\partial C_i}{\partial t}+\frac{\partial (uC_i)}{\partial z}=\varepsilon_{\mathrm{c}}\frac{\partial}{\partial z}\left(D_{z,i}C_{\mathrm{T}}\frac{\partial Y_i}{\partial z}\right)-\frac{(1-\varepsilon_{\mathrm{c}}-\xi)\,a'k_{\mathrm{f},i}}{\mathrm{Bi}_i/5+1}(C_i-C_{\mathrm{p},i}), \tag{A.1}$$

where the index i corresponds to each component of the gas mixture, t is the time; z the position along the section height; C_i, $C_{\mathrm{p},i}$, and Y_i the concentration in the bulk gas, the concentration in the macropores, and the molar fraction in the bulk gas, respectively; ε_{c} the column void fraction; ξ the volume fraction occupied by structured packing; $D_{z,i}$ the axial dispersion coefficient; u the superficial gas velocity; a' the adsorbent particle specific area; $k_{\mathrm{f},i}$ the film mass transfer coefficient; and Bi_i the Biot number. In addition, C_{T} is the total concentration in the bulk gas, and it is computed with the ideal gas equation of state:

$$C_{\mathrm{T}}=\sum_i C_i=\frac{P}{RT}, \tag{A.2}$$

where P and T are the pressure and temperature in the bulk gas, respectively, and R is the universal gas constant.

Using the linear driving force (LDF) approximation to express the mass transfer rate from the bulk gas to the pores, and from the pores to the adsorbed phase, the mass balance in the macropores is given by:

$$\varepsilon_{\mathrm{p}}\frac{\partial C_{\mathrm{p},i}}{\partial t}+v_{\mathrm{s}}\frac{\partial C_{\mathrm{p},i}}{\partial z}=\varepsilon_{\mathrm{p}}\frac{15D_{\mathrm{p},i}}{r_{\mathrm{p}}^2}\frac{\mathrm{Bi}_i}{5+\mathrm{Bi}_i}\left(C_i-C_{\mathrm{p},i}\right)-\rho_{\mathrm{p}}\frac{15D_{\mathrm{c},i}}{r_c^2}\left(q_i^*-q_i\right), \tag{A.3}$$

where r_{p} is the particle radius, $D_{\mathrm{p},i}$ the macropore diffusivity, ρ_{p} the particle density, q_i the adsorbed concentration of component i, and v_{s} the velocity of the adsorbent.

Similarly, the mass balance in the solid phase is given by:

$$\frac{\partial q_i}{\partial t}+v_{\mathrm{s}}\frac{\partial q_i}{\partial z}=\frac{15D_{\mathrm{c},i}}{r_{\mathrm{c}}^2}\left(q_i^*-q_i\right), \tag{A.4}$$

where $15D_{\mathrm{c},i}/r_{\mathrm{c}}^2$ is treated as a single parameter representing the adsorption rate of component i, and q_i^* is the adsorbed concentration of component i in equilibrium with the corresponding local concentration in the macropore ($C_{\mathrm{p},i}$). The adsorption equilibrium is described with the multi-component extension of the Virial isotherm model (Taqvi and LeVan, 1997, Grande et al., 2008) that takes into account competitive adsorption of the different species in the gas mixture:

$$P_i=\frac{q_i^*}{K_{\mathrm{H},i}}\exp\left[\sum_{j=1}^{N}A_{ij}q_j^*+\sum_{j=1}^{N}\sum_{k=1}^{N}B_{ijk}q_j^*q_k^*\right] \tag{A.5}$$

where the mixing Virial coefficients are calculated based on the fitting parameters from pure component measurements (Table 5) as:

$$A_{ij} = \frac{A_i + A_j}{2} \quad \text{and} \quad B_{ijk} = \frac{B_i + B_j + B_k}{3}. \tag{A.6}$$

The pressure gradient along the sections was computed using the Ergun equation (Ergun, 1952):

$$\frac{\partial P}{\partial z} = \frac{150\mu_{\mathrm{g}}(1-\varepsilon_{\mathrm{c}})^2}{\varepsilon_{\mathrm{c}}^3 d_{\mathrm{p}}^2} u + \frac{1.75(1-\varepsilon_{\mathrm{c}})\rho_{\mathrm{g}}}{\varepsilon_{\mathrm{c}}^3 d_{\mathrm{p}}} u|u|, \tag{A.7}$$

where P is the total pressure in the bulk gas, d_{p} is the particle diameter, μ_{g} is the gas viscosity, and ρ_{g} the gas density.

The gas and adsorbent temperatures (T and T_{s}) are computed from the energy balance in the gas phase and solid phases, respectively:

$$\varepsilon_{\mathrm{c}} C_{\mathrm{T}} \hat{c}_v \frac{\partial T}{\partial t} + u C_{\mathrm{T}} \hat{c}_p \frac{\partial T}{\partial z} = \frac{\partial}{\partial z}\left(\lambda_{\mathrm{g}} \frac{\partial T}{\partial z}\right) + \varepsilon_{\mathrm{c}} RT \sum_i \frac{\partial C_i}{\partial t} - (1-\varepsilon_{\mathrm{c}} - \xi)\, a' h_{\mathrm{gs}} (T - T_{\mathrm{s}}) - \alpha_{\mathrm{gt}} h_{\mathrm{gt}} (T - T_{\mathrm{t}}) \tag{A.8}$$

$$\begin{aligned}\left[(1-\varepsilon_{\mathrm{c}}-\xi)\rho_{\mathrm{p}} c_{p,\mathrm{s}} + \xi \rho_{\mathrm{pk}} c_{p,\mathrm{pk}}\right]\left(\frac{\partial T_{\mathrm{s}}}{\partial t} + v_{\mathrm{s}} \frac{\partial T_{\mathrm{s}}}{\partial z}\right) &= \xi \frac{\partial}{\partial z}\left(\lambda_{\mathrm{g_{pk}}} \frac{\partial T_{\mathrm{s}}}{\partial z}\right) + (1-\varepsilon_{\mathrm{c}}-\xi)\, a' h_{\mathrm{gs}} (T - T_{\mathrm{s}}) + \\ (1-\varepsilon_{\mathrm{c}}-\xi)\rho_{\mathrm{p}} \sum_i \left(-\Delta H_i \left[\frac{\partial q_i}{\partial t} + v_{\mathrm{s}} \frac{\partial q_i}{\partial z}\right]\right) &+ (1-\varepsilon_{\mathrm{c}}-\xi)\varepsilon_{\mathrm{p}} R T_{\mathrm{s}} \sum_i \left[\frac{\partial C_{\mathrm{p},i}}{\partial t} + v_{\mathrm{s}} \frac{\partial C_{\mathrm{p},i}}{\partial z}\right]\end{aligned} \tag{A.9}$$

In the previous equations, ΔH_i represents the heat of adsorption of component i, h_{gs} the film heat transfer coefficient between the gas and the solid, h_{gt} the convective heat transfer coefficient between the gas and the tubes wall, α_{gt} the heat transfer area per unit volume, T_{s} the temperature of the sorbent, T_{t} the temperature of the tubes wall, $\hat{c}_v$ and $\hat{c}_p$ the gas molar heat capacities at constant volume and constant pressure, respectively, $c_{p,\mathrm{s}}$ the specific heat capacity of the sorbent, $c_{p,\mathrm{pk}}$ the specific heat capacity of the packing, ρ_{pk} the density of the packing, λ_{g} the heat axial dispersion coefficient of the gas, and λ_{pk} the heat axial dispersion coefficient of the packing.

In addition, in the sections operated as indirect-contact heat exchanger, the temperature of the tubes wall (T_{t}) and the temperature of the heating/cooling fluid (T_{f}) are respectively given by:

$$\rho_{\mathrm{t}} c_{p,\mathrm{t}} \frac{\partial T_{\mathrm{t}}}{\partial t} = \alpha_{\mathrm{t,ext}} h_{\mathrm{gt}} (T - T_{\mathrm{t}}) - \alpha_{\mathrm{t,int}} h_{\mathrm{ft}} (T_{\mathrm{t}} - T_{\mathrm{f}}) \quad \text{and} \tag{A.10}$$

$$\rho_{\mathrm{f}} c_{p,\mathrm{f}} \frac{\partial T_{\mathrm{f}}}{\partial t} + u_{\mathrm{f}} \rho_{\mathrm{f}} c_{p,\mathrm{f}} \frac{L_z}{L_x} \frac{\partial T_{\mathrm{f}}}{\partial z} = -\alpha_{\mathrm{t,int}} h_{\mathrm{ft}} (T_{\mathrm{f}} - T_{\mathrm{t}}), \tag{A.11}$$

where the subscript t refers to the tubes wall, the subscript f refers to the heating/cooling fluid, $\alpha_{\mathrm{t,ext}}$ and $\alpha_{\mathrm{t,int}}$ are the external and internal heat transfer areas per unit of fluid volume, h_{ft} is the convective heat transfer coefficient between the heating/cooling fluid and the heat exchanger tubes, and the ratio L_x/L_z is the distance travelled by the heating/cooling fluid per unit of height.

Equation (A.10) was derived assuming that the thermal conduction resistance of the walls is negligible, while taking into account the effect of the thermal capacity of the heat exchanger walls. On the other hand, Equation (A.11) was derived considering a heat exchanger with a cross-flow shell-and-tube configuration, whereby the heating/cooling fluid flows within horizontal tubes. To this end, the energy balance was applied to a single tube along the direction of the fluid flow (x). The horizontal coordinate (x) was then converted to the axial coordinate along the section (z) by assuming a linear dependence of the tube length (L_x) with respect to the section length (L_z).

Transport parameters

The axial dispersion coefficients ($D_{z,i}$) controlling the diffusion term of the gas mass balances, Equation (A.1), are obtained from the correlation proposed by Wakao and Funazkri (1978):

$$D_{z,i} = \frac{D_{\mathrm{m},i}}{\varepsilon_{\mathrm{c}}}(20 + 0.5\ \mathrm{Sc}_i\,\mathrm{Re}), \tag{A.12}$$

where the Schmidt and Reynolds numbers are defined as

$$\mathrm{Sc}_i = \frac{\mu_{\mathrm{g}}\rho_{\mathrm{g}}}{D_{\mathrm{m},i}} \quad \text{and} \quad \mathrm{Re} = \frac{\rho_{\mathrm{g}} u\, d_{\mathrm{p}}}{\mu_{\mathrm{g}}}, \tag{A.13}$$

with ρ_{g} and μ_{g} being the gas density and viscosity, respectively, and d_{p} the particle diameter. The molecular diffusivities ($D_{\mathrm{m},i}$) are approximated with the Wilke correlation (Wilke, 1950):

$$D_{\mathrm{m},i} = \frac{1 - Y_i}{\sum_{j\neq i}^{n} \frac{Y_i}{D_{ij}}}. \tag{A.14}$$

where the binary diffusivity (D_{ij}) is given by (Bird et al., 2002):

$$D_{ij} = \frac{0.01883\ T^{3/2}}{P\ \sigma_{ij}^2\ \Omega_{D_{ij}}} \sqrt{\frac{1}{M_{\mathrm{w},i}} + \frac{1}{M_{\mathrm{w},j}}}, \tag{A.15}$$

with M_{w} being the molecular weight of the gas species, σ_{ij} the Lennard-Jones parameter, and $\Omega_{D_{ij}}$ the diffusion collision integral.

The source term of the gas mass balances, Equation (A.1), involves the film mass transfer coefficients ($k_{\mathrm{f},i}$) and the Biot number of the adsorbent particles (Bi_i). The former is estimated with the Sherwood number correlation proposed by Wakao and Funazkri (1978):

$$\mathrm{Sh}_i = \frac{k_{\mathrm{f},i} d_{\mathrm{p}}}{D_{\mathrm{m},i}} = 2.0 + 1.1\mathrm{Re}^{0.6}{\mathrm{Sc}_i}^{1/3}, \tag{A.16}$$

while the Biot number is defined as

$$\mathrm{Bi}_i = \frac{r_{\mathrm{p}} k_{\mathrm{f},i}}{\varepsilon_{\mathrm{p}} D_{\mathrm{p},i}}, \tag{A.17}$$

where r_{p} is the particle radius, ε_{p} is the particle porosity and $D_{\mathrm{p},i}$ the macropore diffusivity. The macropore diffusivity is computed using the relation proposed by Yang (1987):

$$\frac{1}{D_{\mathrm{p},i}} = \tau_{\mathrm{p}} \left(\frac{1}{D_{\mathrm{Kn},i}} + \frac{1}{D_{\mathrm{m},i}}, \right) \tag{A.18}$$

where τ_{p} is the particle tortuosity, and D_{Kn} is the Knudsen diffusivity, which is computed according to (Ruthven, 1984):

$$D_{\mathrm{Kn},i} = \frac{2}{3} r_{\mathrm{pore}} \sqrt{\frac{8}{\pi} \frac{R\,T}{M_{\mathrm{w},i}}}. \tag{A.19}$$

Moreover, the rate of adsorption of each component ($15 D_{\mathrm{c},i}/r_{\mathrm{c}}^2$), appearing in Equations (A.3) and (A.4), is assumed to have a dependency on temperature given by an Arrhenius equation:

$$\frac{15 D_{\mathrm{c},i}}{r_{\mathrm{c}}^2} = \frac{15 D_{\mathrm{c},i}^0}{r_c^2} \exp\left(\frac{-E_{\mathrm{a},i}}{RT}\right), \tag{A.20}$$

where the term $15D^0_{c,i}/r_c^2$ represents the adsorption rate at infinite temperature and $E_{a,i}$ the activation energy of micropore/crystal diffusion.

In analogy with mass dispersion in the gas phase, the axial thermal dispersion coefficient (λ_g) appearing in the gas energy balance, Equation (A.8), is obtained from the empirical correlation proposed by Wakao et al. (1979):

$$\lambda_g = k_g(7 + 0.5\,\mathrm{Pr}\,\mathrm{Re}), \tag{A.21}$$

where the Prandtl number is defined as

$$\mathrm{Pr} = \frac{c_{p,g}\mu_g}{k_g}, \tag{A.22}$$

with k_g being the gas thermal conductivity. In addition, the convective heat transfer coefficient between gas and solid (h_{gs}) is computed with the Nusselt number correlation proposed by Wakao et al. (1979):

$$\mathrm{Nu} = \frac{h_{gs}d_p}{k_g} = 2.0 + 1.1\mathrm{Re}^{0.6}\mathrm{Pr}^{1/3}. \tag{A.23}$$

Lastly, the convective heat transfer coefficient on the sorbent-side of the heat exchanger ($h_{gt} \equiv h_s$) was computed with the correlation developed from the heat transfer measurements, see Equation (11) in the main text.

References

Akhtar, F., Andersson, L., Ogunwumi, S., Hedin, N., Bergström, L., 2014. Structuring adsorbents and catalysts by processing of porous powders. Journal of the European Ceramic Society 34, 1643–1666.

Al-Ansary, H., El-Leathy, A., Al-Suhaibani, Z., Jeter, S., Sadowski, D., Alrished, A., Golob, M., 2012. Experimental study of a sand–air heat exchanger for use with a high-temperature solar gas turbine system. Journal of Solar Energy Engineering 134.

Baird, M.H.I., Rama Rao, N.V., Tackie, E., Vahed, A., 2008. Heat transfer to a moving packed bed of nickel pellets. The Canadian Journal of Chemical Engineering 86, 142–150.

Barrer, R.M., 1981. Sorption in porous crystals: equilibria and their interpretation. Journal of Chemical Technology and Biotechnology 31, 71–85.

Baumann, T., Zunft, S., 2015. Development and performance assessment of a moving bed heat exchanger for solar central receiver power plants. Energy Procedia 69, 748–757.

Baumann, T., Zunft, S., Tamme, R., 2014. Moving bed heat exchangers for use with heat storage in concentrating solar plants: a multiphase model. Heat transfer engineering 35, 224–231.

Berg, C.H., 1945. Adsorption process and apparatus.

Bird, R.B., Stewart, W.E., Lightfoot, E.N., 2002. Transport Phenomena. Second Edition. Wiley, New York.

Bonjour, J., Chalfen, J.B., Meunier, F., 2002. Temperature swing adsorption process with indirect cooling and heating. Industrial & engineering chemistry research 41, 5802–5811.

Bonjour, J., Clausse, M., Meunier, F., 2005. A tsa process with indirect heating and cooling: parametric analysis and scaling-up to practical sizes. Chemical Engineering and Processing: Process Intensification 44, 969–977.

Bonjour, J., Rocha, L., Bejan, A., Meunier, F., 2004. Dendritic fins optimization for a coaxial two-stream heat exchanger. International Journal of Heat and Mass Transfer 47, 111–124.

Brunner, P.H., Rechberger, H., 2015. Waste to energy–key element for sustainable waste management. Waste management 37, 3–12.

Bui, M., Adjiman, C.S., Bardow, A., Anthony, E.J., Boston, A., Brown, S., Fennell, P.S., Fuss, S., Galindo, A., Hackett, L.A., 2018. Carbon capture and storage (ccs): the way forward. Energy & Environmental Science 11, 1062–1176.

Campbell, C.S., 1990. Rapid granular flows. Annual Review of Fluid Mechanics 22, 57–90.

Cavenati, S., Grande, C.A., Rodrigues, A.E., 2004. Adsorption equilibrium of methane, carbon dioxide, and nitrogen on zeolite 13x at high pressures. Journal of Chemical & Engineering Data 49, 1095–1101.

Cengel, Y.A., Klein, S., Beckman, W., 1998. Heat transfer: a practical approach. volume 141. WBC McGraw-Hill Boston.

Dai, Y.L., Liu, X.J., Xia, D., 2020. Flow characteristics of three typical granular materials in near 2d moving beds. Powder Technology 373, 220–231.

Ergun, S., 1952. Fluid flow through packed columns. Chem. Eng. Prog. 48, 89–94.

Farmahini, A.H., Krishnamurthy, S., Friedrich, D., Brandani, S., Sarkisov, L., 2021. Performance-based screening of porous materials for carbon capture. Chemical Reviews 121, 10666–10741.

Farrance, I., Frenkel, R., 2012. Uncertainty of measurement: a review of the rules for calculating uncertainty components through functional relationships. The Clinical Biochemist Reviews 33, 49.

gPROMS Model Builder Version 6.0, 2019. Process System Enterpise (PSE). UK.

Grande, C.A., Lopes, F.V., Ribeiro, A.M., Loureiro, J.M., Rodrigues, A.E., 2008. Adsorption of off-gases from steam methane reforming (H_2, CO_2, CH_4, co and N_2) on activated carbon. Separation Science and Technology 43, 1338–1364.

Haaf, M., Anantharaman, R., Roussanaly, S., Ströhle, J., Epple, B., 2020. Co2 capture from waste-to-energy plants: Techno-economic assessment of novel integration concepts of calcium looping technology. Resources, Conservation and Recycling 162, 104973.

Hornbostel, M., 2016. Pilot-Scale Evaluation of an Advanced Carbon Sorbent-Based Process for Post-Combustion Carbon Capture. Report. SRI International, Menlo Park, CA (United States).

Hornbostel, M.D., Bao, J., Krishnan, G., Nagar, A., Jayaweera, I., Kobayashi, T., Sanjurjo, A., Sweeney, J., Carruthers, D., Petruska, M.A., 2013. Characteristics of an advanced carbon sorbent for CO_2 capture. Carbon 56, 77–85.

Hornbostel, M.D., Krishnan, G.N., Sanjurjo, A., 2015. Falling microbead counter-flow process for separating gas mixtures.

Isaza, P.A., Warnica, W.D., Bussmann, M., 2015. Co-current parallel-plate moving bed heat exchanger: An analytical solution. International Journal of Heat and Mass Transfer 87, 616–624.

Joss, L., Gazzani, M., Mazzotti, M., 2017. Rational design of temperature swing adsorption cycles for post-combustion co 2 capture. Chemical Engineering Science 158, 381–394.

Kaza, S., Yao, L., Bhada-Tata, P., Van Woerden, F., 2018. What a Waste 2.0: a Global Snapshot of Solid Waste Management to 2050. World Bank Publications.

Kearns, D.T., 2019. Waste-to-Energy with CCS: A Pathway to Carbon-Negative Power Generation.

Kim, K., Park, Y.K., Park, J., Jung, E., Seo, H., Kim, H., Lee, K.S., 2014. Performance comparison of moving and fluidized bed sorption systems for an energy-efficient solid sorbent-based carbon capture process. Energy Procedia 63, 1151–1161.

Kim, K., Son, Y., Lee, W.B., Lee, K.S., 2013. Moving bed adsorption process with internal heat integration for carbon dioxide capture. International Journal of Greenhouse Gas Control 17, 13–24.

Knaebel, K.S., 2005. Temperature swing adsorption system. US Patent 8353978B2.

Krishnamurthy, S., Haghpanah, R., Rajendran, A., Farooq, S., 2014. Simulation and optimization of a dual-adsorbent, two-bed vacuum swing adsorption process for co2 capture from wet flue gas. Industrial & Engineering Chemistry Research 53, 14462–14473.

LabVIEW, 2019. National Instruments. USA.

Lee, W., Youn, S., Park, S., 1998. Finite element analysis of the flow and heat transfer of solid particles in moving beds. International journal of energy research 22, 1145–1155.

Lillia, S., Bonalumi, D., Grande, C., Manzolini, G., 2018. A comprehensive modeling of the hybrid temperature electric swing adsorption process for CO_2 capture. International Journal of Greenhouse Gas Control 74, 155–173.

Liu, Z., Grande, C.A., Li, P., Yu, J., Rodrigues, A.E., 2011. Multi-bed vacuum pressure swing adsorption for carbon dioxide capture from flue gas. Separation and Purification Technology 81, 307–317.

Lopes, F.V., Grande, C.A., Ribeiro, A.M., Oliveira, E.L., Loureiro, J.M., Rodrigues, A.E., 2009. Enhancing capacity of activated carbons for hydrogen purification. Industrial & engineering chemistry research 48, 3978–3990.

Marx, D., Joss, L., Hefti, M., Mazzotti, M., 2016. Temperature swing adsorption for postcombustion co_2 capture: single-and multicolumn experiments and simulations. Industrial & Engineering Chemistry Research 55, 1401–1412.

Masala, A., Vitillo, J.G., Mondino, G., Martra, G., Blom, R., Grande, C.A., Bordiga, S., 2017. Conductive zsm-5-based adsorbent for co2 capture: active phase vs monolith. Industrial & Engineering Chemistry Research 56, 8485–8498.

Merel, J., Clausse, M., Meunier, F., 2008. Experimental investigation on CO_2 post-combustion capture by indirect thermal swing adsorption using 13x and 5a zeolites. Industrial & Engineering Chemistry Research 47, 209–215.

Mickley, H.S., Fairbanks, D.F., 1955. Mechanism of heat transfer to fluidized beds. AIChE Journal 1, 374–384.

Mondino, G., Grande, C.A., Blom, R., 2017. Effect of gas recycling on the performance of a moving bed temperature-swing (MBTSA) process for CO_2 capture in a coal fired power plant context. Energies 10, 745.

Mondino, G., Grande, C.A., Blom, R., Nord, L.O., 2019. Moving bed temperature swing adsorption for CO_2 capture from a natural gas combined cycle power plant. International Journal of Greenhouse Gas Control 85, 58–70.

Mondino, G., Spjelkavik, A.I., Didriksen, T., Krishnamurthy, S., Stensrød, R.E., Grande, C.A., Nord, L.O., Blom, R., 2020. Production of mof adsorbent spheres and comparison of their performance with zeolite 13x in a moving-bed tsa process for postcombustion CO_2 capture. Industrial & Engineering Chemistry Research 59, 7198–7211.

Montañés, R.M., Flø, N.E., Nord, L.O., 2018. Experimental results of transient testing at the amine plant at technology centre mongstad: Open-loop responses and performance of decentralized control structures for load changes. International Journal of Greenhouse Gas Control 73, 42–59.

Morales-Ospino, R., Santos, V.N., Lima Jr, A.R., Torres, A.E.B., Vilarrasa-García, E., Bastos-Neto, M., Cavalcante Jr, C.L., Azevedo, D.C., Marques, C.R., de Aquino, T.F., 2021. Parametric analysis of a moving bed temperature swing adsorption (mbtsa) process for postcombustion co_2 capture. Industrial & Engineering Chemistry Research .

Mulloth, L.M., Finn, J.E., 1998. Carbon dioxide adsorption on a 5A zeolite designed for CO_2 removal in spacecraft cabins. Report. National Aeronautics and Space Administration, Ames Research Center.

Niegsch, J., Köneke, D., Weinspach, P.M., 1994. Heat transfer and flow of bulk solids in a moving bed. Chemical Engineering and Processing: Process Intensification 33, 73–89.

Nord, L.O., Bolland, O., 2020. Carbon Dioxide Emission Management in Power Generation. John Wiley & Sons.

Obuskovic, N.S., 1988. Heat transfer between moving beds of solids and a vertical tube. Ph.D. thesis. Oregon State University.

Okumura, T., Ogino, T., Nishibe, S., Nonaka, Y., Shoji, T., Higashi, T., 2014. Co2 capture test for a moving-bed system utilizi g low-temperature steam. Energy Procedia 63, 2249–2254.

Okumura, T., Yoshizawa, K., Nishibe, S., Iwasaki, H., Kazari, M., Hori, T., 2017. Parametric testing of a pilot-scale design for a moving-bed co2 capture system using low-temperature steam. Energy Procedia 114, 2322–2329.

Plaza, M.G., González, A.S., Pevida, C., Rubiera, F., 2014. Influence of water vapor on co2 adsorption using a biomass-based carbon. Industrial & Engineering Chemistry Research 53, 15488–15499.

Plaza, M.G., Rubiera, F., Pevida, C., 2017. Evaluating the feasibility of a TSA process based on steam stripping in combination with structured carbon adsorbents to capture CO_2 from a coal power plant. Energy & Fuels 31, 9760–9775.

Qoaider, L., Thabit, Q., Kiwan, S., 2017. Performance assessment of a moving-bed heat exchanger with a sensible heat transfer medium for solar central receiver power plants, in: 2017 8th International Renewable Energy Congress (IREC), IEEE. pp. 1–5.

Rezaei, F., Webley, P., 2010. Structured adsorbents in gas separation processes. Separation and Purification Technology 70, 243–256.

Ruthven, D.M., 1984. Principles of adsorption and adsorption processes. John Wiley & Sons.

Rúa, J., Bui, M., Nord, L.O., Mac Dowell, N., 2020. Does ccs reduce power generation flexibility? a dynamic study of combined cycles with post-combustion co2 capture. International Journal of Greenhouse Gas Control 95, 102984.

Shen, C., Grande, C.A., Li, P., Yu, J., Rodrigues, A.E., 2010. Adsorption equilibria and kinetics of CO_2 and N_2 on activated carbon beads. Chemical Engineering Journal 160, 398–407.

Sjostrom, S., Krutka, H., 2010. Evaluation of solid sorbents as a retrofit technology for co2 capture. Fuel 89, 1298–1306.

Son, Y., Kim, K., Lee, K.S., 2014. Feasibility study of a moving-bed adsorption process with heat integration for CO_2 capture through energy evaluation and optimization. Energy & Fuels 28, 7599–7608.

Takeuchi, H., 1996. Particles flow pattern and local heat transfer around tube in moving bed. AIChE journal 42, 1621–1626.

Taqvi, S.M., LeVan, M.D., 1997. Virial description of two-component adsorption on homogeneous and heterogeneous surfaces. Industrial & Engineering Chemistry Research 36, 2197–2206.

Thermoflow Version 27, 2017. Termoflow Inc.

Tian, X., Yang, J., Guo, Z., Wang, Q., Sunden, B., 2020. Numerical study of heat transfer in gravity-driven particle flow around tubes with different shapes. Energies 13.

Turan, G., Zapantis, A., Kearns, D., Tamme, E., Staib, C., Zhang, T., Burrows, J., Gillespie, A., Havercroft, I., Rassool, D., Consoli, C., Liu, H., 2021. Global Status of CCS 2021. Report. Global CCS Institute, Melbourne, Australia.

Wakao, N., Funazkri, T., 1978. Effect of fluid dispersion coefficients on particle-to-fluid mass transfer coefficients in packed beds: correlation of sherwood numbers. Chemical Engineering Science 33, 1375–1384.

Wakao, N., Kaguei, S., Funazkri, T., 1979. Effect of fluid dispersion coefficients on particle-to-fluid heat transfer coefficients in packed beds: correlation of nusselt numbers. Chemical engineering science 34, 325–336.

Wankat, P.C., 2006. Separation process engineering. Pearson Education.

Wilke, C.R., 1950. Diffusional properties of multicomponent gases. Chemical Engineering Progress 46, 95–104.

Yang, R.T., 1987. Gas separation by adsorption processes. volume 1. World Scientific.

Zanco, S.E., Ambrosetti, M., Groppi, G., Tronconi, E., Mazzotti, M., 2021. Heat transfer intensification with packed open-cell foams in tsa processes for co2 capture. Chemical Engineering Journal , 131000.

Zanco, S.E., Joss, L., Hefti, M., Gazzani, M., Mazzotti, M., 2017. Addressing the criticalities for the deployment of adsorption-based co2 capture processes. Energy Procedia 114, 2497–2505.

Zanco, S.E., Mazzotti, M., Gazzani, M., Romano, M.C., Martínez, I., 2018. Modeling of circulating fluidized beds systems for post-combustion CO_2 capture via temperature swing adsorption. AIChE Journal 64, 1744–1759.